

UNIVERSITY OF SHEFFIELD

PHD. THESIS

**Nuclear Spin Phenomena in III-V
and II-VI Semiconductor Quantum
Dots**

Author:

Gautham Rangunathan

Registration No: 150122834

Supervisor:

Dr. Evgeny CHEKHOVICH

Second Supervisor:

Prof. Maurice SKOLNICK

LOW DIMENSIONAL STRUCTURES AND DEVICES (LDSD)
GROUP

DEPARTMENT OF PHYSICS AND ASTRONOMY

October 2019

Abstract

This thesis contains experimental observations of fundamental nuclear spin properties in single self-assembled quantum dots (QDs). Using optically detected nuclear magnetic resonance (NMR) techniques, we investigate both the dense quadrupolar nuclear spin system of III-V InGaAs/GaAs dots and for the first time the dilute nuclear spin bath of II-VI CdTe/ZnTe QDs at large external magnetic fields. Non-resonant optical pumping can be used to demonstrate dynamic nuclear polarisation (DNP) of the spin bath ($> 60\%$) and changes in the nuclear magnetisation can be probed through changes in the hyperfine shifts of the spectral exciton emission lines. We present the first direct measurement of DNP in the CdTe/ZnTe QD system containing only a few hundred nuclear spins. We observe a robust nuclear polarisation formed via quantum well states and a system governed by a strong Knight field (from the confined electron) as well as spectral wandering effects due to charge fluctuations in the environment.

Using a newly developed continuous wave (cw) NMR technique as a tool for QD structural analysis, the structure of single, self-assembled QDs (with only 10^5 nuclei) in different InGaAs/GaAs samples were determined. The first measurement of NMR signal from low strain nuclei revealed shallow, disc-like shapes for the QDs with the electron wavefunction penetrating significantly into the weakly strained surrounding GaAs barrier layers.

Finally, we compare the nuclear spin bath properties for an InGaAs/GaAs QD with and without a resident electron. Using cw radiofrequency excitation with a spectral shape of a frequency comb, the underlying homogenous nuclear linewidth could be extracted from the large strain induced inhomogeneous broadening. By all indications, the presence of a single electron spin trapped in a QD has a detrimental effect on the nuclear spin bath due to cotunnelling with electrons in the Fermi sea and the Knight field.

Acknowledgements

There are many people in the Low Dimensional Structures and Devices (LDSD) group at the University of Sheffield without whom this PhD. would not have been possible. There were those that I was lucky enough to work with directly who helped improve my knowledge and experimental skills and those whose company made the four years a fruitful experience.

Firstly I need to thank my supervisor Evgeny Chekhovich whose determination and drive meant that we were able to perform a vast array of experiments in my time in the lab. I learnt a lot and with an ever present supervisor, guidance was always able whenever I needed it. It is quite impressive how automated the measurements are in the lab and how this unique combination of hardware, Labview and Mathematica have been developed to perform such complicated experiments.

I am very grateful also to the other small sub-group of people that worked directly in our lab on the nuclear spin work. When I first started my PhD., it was intended that I was to succeed Andreas Waeber as he was finishing his. He helped me more than I could possibly ask for, where he was always available to help in the lab, with data analysis through Mathematica scripts and of course allowing me to settle in to the work. This was all while he was in the process of writing up his own thesis and it is why (I now realise) I am so thankful. Additionally, I am very grateful to have had George Gillard as my own successor, who through his time at Sheffield was already very competent and capable in the lab and I am sure I have learned as much from him as he from me, just through discussions of the experiments. Thanks to our visitor Jakub Kobak from the University of Warsaw who is the entire reason that Chapter 4 of this thesis was possible. Though his time here was short, we managed to write a paper together and performed so many experiments in a challenging material system. Thanks also to Ata Ulhaq and Ian Griffiths for all our discussions and collaborations. Thanks also to the other individuals allowing for the smooth running of the experiments including the technicians, members of the workshop, those responsible for the growth and processing of the samples, our theory

collaborator Ceyhun Bulutay and for the TEM processing Richard Beanland. Last but not least, the experiments only worked at all thanks to Chris Vickers and Philip Taylor, whose door we would knock on every Tuesday and Friday to see if they had any spare liquid helium lying around.

LDSO is certainly a unique research group with a such a large number of people and the huge amount of success for many decades. This is undoubtedly due to the leadership of Maurice Skolnick who somehow manages to keep on top of it all and produce continued success. We had many interesting discussions in our fortnightly meetings and together with Mark Fox, always provided useful comments on the work. Thanks to all the members of the ever changing LDSO group and in particular (but not limited to) Dominic Hallett, Tom Lyons, Joe Maguire, Luca Sortino, David Hurst, Lucy Rodriguez, Catherine Phillips, Charles Whittaker, Zofia Bishop, Alistair Brash, Andrew Foster, Rikki Coles, John O'Hara, Qingqing Duan, Jasminder Sidhu, Stefan Schwarz, Scott Dufferwiel, Luis Martins, Guiseppe Buonaiuto, Deivis Vaitiekus, Robbie Schofield, Chris Bentham, David Price, Panaiot Zotev, Alessandro Catanzaro, Ruggero Emmanuele, Charlotte Ovenden, Toby Dowling, Daniel Gillard, Sam Sheldon and Mahmoud Jalalimehrabad for all our discussions in the Austin room or on a Friday evening. It is all of you that I will remember as LDSO.

Finally I would like to thank my friends and family for their support and allowing me to take my mind off the grind that is academic life. Particularly thanks to my parents, my brother and his wife and my two little nieces, who always made me smile.

Publications and Conferences

Papers

G. Rangunathan, J. Kobak, G. Gillard, W. Pacuski, K. Sobczak, J. Borysiuk, M. S. Skolnick, and E. A. Chekhovich. “Direct Measurement of Hyperfine Shifts and Radio Frequency Manipulation of Nuclear Spins in Individual CdTe/ZnTe Quantum Dots”, *Physical Review Letters*, 122(9):096801, March 2019, doi: 10.1103/PhysRevLett.122.096801.

A. M. Waeber, G. Gillard, **G. Rangunathan**, M. Hopkinson, P. Spencer, D. A. Ritchie, M. S. Skolnick, and E. A. Chekhovich. “Pulse control protocols for preserving coherence in dipolar-coupled nuclear spin baths”, *Nature Communications*, 10(1):3157, July 2019, doi: 10.1038/s41467-019-11160-6.

Conference Presentations

G. Rangunathan, A. M. Waeber, M. Hopkinson, I. Farrer, D. A. Ritchie, J. Nilsson, R. M. Stevenson, A. J. Bennett, A. J. Shields, M. S. Skolnick, and E. A. Chekhovich. “NMR Study of electron-nuclear spin interactions in negatively charged InGaAs/GaAs quantum dots”, *UK Semiconductors 2016*, Sheffield, UK; July 2016.

G. Rangunathan, A. M. Waeber, M. Hopkinson, I. Farrer, D. A. Ritchie, J. Nilsson, R. M. Stevenson, A. J. Bennett, A. J. Shields, M. S. Skolnick and E. A. Chekhovich. “Structural analysis of InGaAs/GaAs quantum dots using inverse NMR spectra”, *The Rank Prize Symposium on Solid State Nano-Photonics for Quantum Science and Technology*, Grasmere, UK; September 2017.

G. Rangunathan, J. Kobak, G. Gillard, W. Pacuski, M. S. Skolnick and E. A. Chekhovich. “Direct probing and manipulation of the nuclear spins in individual II-VI CdTe/ZnTe quantum dots”, *UK Semiconductors 2018*, Sheffield, UK; July 2018.

Conference Posters

G. Rangunathan, A. M. Waeber, M. Hopkinson, I. Farrer, D. A. Ritchie, J. Nilsson, R. M. Stevenson, A. J. Bennett, A. J. Shields, M. S. Skolnick and E. A. Chekhovich. “Structural analysis of InGaAs/GaAs quantum dots using inverse NMR spectra”, *Quantum Dot Day 2017*, Edinburgh, UK; January 2017.

G. Rangunathan, J. Kobak, G. Gillard, W. Pacuski, M. S. Skolnick and E. A. Chekhovich. “Direct probing and manipulation of the nuclear spins in individual II-VI CdTe/ZnTe quantum dots”, *Quantum Dot Day 2018*, Sheffield, UK; January 2018.

G. Rangunathan, J. Kobak, G. Gillard, W. Pacuski, M. S. Skolnick and E. A. Chekhovich. “Direct probing and manipulation of the nuclear spins in individual II-VI CdTe/ZnTe quantum dots”, *Quantum Dot 2018*, Toronto, Canada; June 2018.

G. Rangunathan, A. M. Waeber, M. Hopkinson, I. Farrer, D. A. Ritchie, J. Nilsson, R. M. Stevenson, A. J. Bennett, A. J. Shields, M. S. Skolnick and E. A. Chekhovich. “Structural analysis of InGaAs/GaAs quantum dots using inverse NMR spectra”, *Quantum Dot 2018*, Toronto, Canada; June 2018.

Contents

Abstract	i
Acknowledgements	ii
Publications and Conferences	iv
List of Figures	ix
List of Tables	xxiii
List of Acronyms	xxiv
1 Introduction	1
1.1 Motivation for using quantum dots	2
1.2 Outline of this thesis	4
2 Optically active self assembled quantum dots	6
2.1 Quantum dot sample growth	7
2.2 Electronic states and optical properties of quantum dots	10
2.2.1 Excitons and optical selection rules	14
2.2.2 Exciton fine structure	16
2.2.3 Charged excitons and biexcitons	18
2.2.4 Quantum dots in electric fields	20
2.2.5 Quantum dots in magnetic fields	22
2.3 Interactions with nuclear spins in quantum dots	24
2.3.1 Coupling of electron and nuclear spins: the hyperfine interaction	25
2.3.2 Nuclear magnetic dipole-dipole interaction	27
2.3.3 Quadrupolar energy levels of nuclei in strained systems	28
2.3.4 Overhauser and Knight fields due to hyperfine interaction	31
2.3.5 Nuclear magnetic resonance and spin relaxation	35
3 Experimental techniques	41
3.1 Self assembled quantum dot samples	42
3.1.1 Ungated InGaAs/GaAs quantum dot “In-flush” sample	42
3.1.2 InGaAs/GaAs quantum dot diode “Low Temp Cap” sample	44
3.2 Sample control and cryostat	46
3.3 Optical photoluminescence spectroscopy	49

3.4	Nuclear magnetic resonance techniques	53
3.4.1	Optically detected NMR: the Pump-RF-Probe technique	53
3.4.2	Inverse NMR technique	56
3.4.3	Frequency combs	60
3.4.4	NMR hardware	62
4	Nuclear spin properties of single CdTe/ZnTe quantum dots	65
4.1	Comparison of nuclear environment in II-VI and III-V quantum dots	66
4.2	CdTe/ZnTe self assembled quantum dot samples	68
4.3	Experimental hardware changes to measure nuclear spin properties in CdTe/ZnTe dots	71
4.4	Experimental observations in CdTe/ZnTe QD sample A	72
4.4.1	Large spectral shifts in continuous wave spectra	72
4.4.2	Electron and hole g-factors and assignment of the sign of nuclear spin polarisation	74
4.5	Basic properties of the dynamic nuclear polarisation in CdTe/ZnTe dots: power and magnetic field dependence	77
4.6	Nuclear spin dynamics in CdTe/ZnTe dots	80
4.7	Optically detected NMR spectra of CdTe/ZnTe dots	83
4.8	Summary	86
5	Structural analysis of InGaAs/GaAs quantum dots using optically detected NMR	88
5.1	Calibration measurements for inverse NMR experiments	89
5.1.1	Pump and probe pulse parameter calibration	90
5.1.2	Nuclear spin lifetime	93
5.1.3	Radiofrequency pulse parameter calibration for cw NMR	94
5.2	Inverse NMR CT spectra example	101
5.3	Comparison of all inverse NMR CT spectra	104
5.4	Novel 3-band inverse NMR technique to measure ST spectra	107
5.5	TEM image analysis of InGaAs/GaAs QD samples	113
5.6	Summary	117
6	Effect of a single electron on the nuclear spin properties in an InGaAs/-GaAs quantum dot	119
6.1	Bias dependant photoluminescence spectra and Overhauser shift of InGaAs quantum dots	120
6.2	Bias dependant nuclear spin lifetime of InGaAs quantum dots	123
6.3	Inhomogeneous linewidth measurement using NMR spectra	127
6.4	Homogeneous linewidth measurement using frequency combs	132
6.4.1	Frequency comb technique	132
6.4.2	Measurement of homogeneous NMR linewidths	134
6.5	Summary	137
7	Conclusion	139

A Appendix: Spectral wandering in CdTe/ZnTe quantum dots	141
B Appendix: Estimate of the average chemical composition of the InGaAs QDs	144
C Appendix: Entire dataset for high resolution inverse NMR CT spectra	148
D Appendix: 3-band inverse NMR ST spectra data correction	151
Bibliography	157

List of Figures

2.1 Illustration of quantum dot growth. The left panel shows how the lattice mismatch between the GaAs substrate (blue) and the InGaAs film (red) creates strain in Stranski-Krastanov (SK) dots. The right panel shows how the growth progresses in SK dots: 1) the initial GaAs substrate, 2) monolayers of InGaAs are deposited onto the substrate and grow layer by layer (similar to Frank-van der Merwe growth), 3) the growth then proceeds by forming islands (as in Volmer Weber growth), 4) Finally the dots are capped with the substrate material (GaAs) to achieve a good confinement potential. 8

2.2 Schematic diagram of a typical Schottky diode hetrostructure. Top panel shows the contents of each layer (not to scale). A highly n-doped region forms the back contact of the diode and provides a large number of free electrons at the fermi energy. Bottom panel shows the conduction and valence band edges for each of the layers. This illustrates the confined QD states, the blocking barrier above the dot layer to prevent charges reaching the surface. As a gate voltage V_G is applied, the confined QD levels can be tuned with respect to the Fermi level, thus allowing electrons to tunnel into the QD from the n-doped layer. Adapted from [1] 9

2.3 Band structure diagram of a bulk GaAs semiconductor near the centre of the Brillouin zone. The conduction band (red) only has a single band whose minima is separated in energy with the valence band edge (blue) by a bandgap E_g . There are 3 sub bands in the valence band - the heavy hole (HH), the light hole (LH) and the split off (SO) band which is offset by the spin orbit splitting Δ of a few hundred meV. The HH and LH bands are degenerate at the the Γ point ($k = 0$) but for $k \neq 0$, the LH band gets increasingly further in energy than the HH band with respect to the conduction band edge. 11

- 2.4 The band gaps and important energy offsets in the InGaAs/GaAs self assembled quantum dot system at liquid helium temperatures. a) the confinement in the growth direction is strong and the potential acts like a finite square well leading to discrete energy levels. b) the confinement is weaker in the lateral x - y plane and can be treated as a 2D parabolic potential. Due to the cylindrical symmetry in the x - y plane, there are 1, 2, 3... pairs of opposing spin electrons or holes for the $s, p, d...$ states. Only the heavy hole states are considered in this figure. The electron ground state energy level is offset from the minimum in the InGaAs conduction band edge by $E_{1e}^{offs} \approx 400$ -500 meV and the heavy hole state is offset by $E_{1hh}^{offs} \approx 70$ -100 meV from the maximum in the valence band edge. The intershell separation between the s and p -shells are $E_e^{s-p} = 15$ -60 meV for the electron and $E_{hh}^{s-p} = 10$ -40 meV for the heavy holes. All values are approximate (from [2-4]) and the actual numbers vary significantly between individual dots. 13
- 2.5 Schematic diagram to show the non-resonant excitation of carriers in a quantum dot. If non resonant excitation is applied in the wetting layer (WL), electrons from the valence band are excited into the conduction band leaving behind holes. Nearby carriers are quickly captured into the higher QD shells and subsequently relax into the lower shells non-radiatively. Finally the electrons/holes recombine and emit a photon which can be detected optically. 15
- 2.6 Correction terms and fine structure of the neutral exciton in self assembled QDs (not to scale). Quantum confinement in the dot creates discrete energy levels and the neutral exciton is formed when a single electron-hole pair populates the dot. The Coulomb interaction lowers the exciton transition energy by the exciton binding energy $E_{X_0}^B = 10 - 30$ meV in InGaAs dots. The spin-orbit interaction (caused by reduced symmetry) splits the p -type hole bands into the heavy hole (HH) and light hole (LH) states with a HH-LH splitting E_{HL} of several tens of meV. The exchange interaction between the electron and hole causes the splitting of bright (antiparallel spins that are optically active) and dark (parallel spins that do not interact with photons) exciton states. The isotropic part splits the bright states from the dark by the electron-hole exchange energy $\delta_0 = 100 - 300$ μ eV and mixes the dark states with splitting $\delta_D = 0 - 100$ μ eV. The anisotropic exchange interaction, which changes considerably based on asymmetry in the formation of the dot, causes the fine structure splitting between the bright excitons $\delta_B = 40 - 200$ μ eV [5]. The pure bright states $|\downarrow\uparrow\rangle$ and $|\uparrow\downarrow\rangle$ are circularly polarised (σ^+/σ^-) but due to the mixing of the states, the observed bright exciton states at zero external magnetic field are linearly polarised (Π^X/Π^Y). 17

- 2.7 Illustrative energy level diagram of the various exciton types in a quantum dot. The electron spin is represented by a red single arrow and hole spin by a blue double arrow. The biexciton (XX) to exciton (X^0) cascade is shown on the left panel and the XX state is not at twice the X^0 energy with respect to the ground state because of the biexciton binding energy E_{XX}^B caused by the Coulomb interaction. The states here are shown in a circular polarisation basis which is the case for large external magnetic fields in Faraday configuration. The middle panel shows the two possible configurations for the positive trion X^+ and the right panel shows the negative trion X^- . Each spin state for the trions couples to only one circular polarisation of light. The energies are not to scale and unlike the schematic energy levels shown here, the transitions of the trion states are shifted in energy with respect to the X^0 transition. 19
- 2.8 Effect of the electric field on the exciton transitions measured using the diode sample used in this work. As the bias is changed, the different charged states of the dot (X^0 and X^-) are observed and the plotted datapoints are the energies of the peaks as the bias is changed. This bias dependent photoluminescence spectra was taken at an external magnetic of 8T in Faraday geometry and using a low power non-resonant excitation so there are two Zeeman split components of each exciton. As the electric field changes, it can be seen that the energies of all 4 lines are shifted (mostly in a linear fashion but a small quadratic curvature is visible). The inset shows a close up of the low energy X^0 line along with a quadratic fit (fitting parameters are shown in Section 3.1.2) of the quantum confined Stark effect. 21
- 2.9 Schematic diagram illustrating the effect of an external magnetic field (\mathbf{B}) on the fine structure of a neutral exciton X^0 . At 0 field, the bright states B^\pm are split from the dark states D^\pm by energy δ_0 due to the isotropic exchange interaction. The eigenstates B^+ or B^- are linearly polarised (Π^x, Π^y). In Faraday geometry (field along optical axis), the bright states B^\pm are split into pure states $|\pm 1\rangle$ (eg. $|+1\rangle = |\downarrow\uparrow\rangle$) which are circularly polarised (σ^+, σ^-), while the dark states are optically forbidden. In Voigt geometry (field perpendicular to optical axis), both bright and dark states become optically active with linearly polarised components. Adapted from [6]. 23
- 2.10 a) Energy level diagram for a single nucleus with spin $I = 3/2$. When a magnetic field B_z is applied, the degeneracy of the $I = 3/2$ is lifted and 4 states are observed equally separated by the Larmor frequency ω_L . Including the effects of the quadrupolar interaction perturbatively, the STs are strongly modified in first order ($\omega_Q^{(1)}$) whereas the CT is only affected weakly in second order ($\omega_Q^{(2)}$). b) Schematic diagram of the three observed peaks in the nuclear resonance spectrum of a single nucleus that occur due to the energy levels shown in a) for a spin $I = 3/2$ nucleus. c) Schematic diagram of the inhomogeneously broadened NMR spectra for a spin $I = 3/2$ isotope where the signal from all nuclei of a given isotope are summed. The linewidth of the CT is narrower than the ST for a wide range of magnetic fields because of the weak second order $\omega_Q^{(2)}$, but the STs are broad because of the large variation in $\omega_Q^{(1)}$ across the QD. 32

2.11	The quantum dot electron-nuclear spin system showing the reciprocal interaction between the electron and nuclear spins through the Overhauser and Knight fields caused by the hyperfine interaction.	33
2.12	Simple illustration of an NMR experiment for a spin half nucleus. In an external static magnetic field B_z , the two Zeeman split nuclear levels are separated by the Larmor frequency ω_L . The population of the two levels can be manipulated using an oscillating transverse rf field B_x , oscillating at frequency ω_{rf} and is resonantly driven when $\omega_{rf} = \omega_L$	36
2.13	Representation of the a) longitudinal and b) transverse spin relaxation mechanisms on the Bloch sphere. The arrows represent the magnetization vector at various points in time and the left panel shows the longitudinal relaxation (characterized by the lifetime T_1) to the horizontal plane ($M_0 = 0$) from an initial magnetization $M_{(t=0)}$ along z and the right panel shows the transverse relaxation (governed by the coherence time T_2), which does not change the z component of the magnetization.	38
3.1	a) Optical microscope image of the surface of the sample grown using the In-flush technique (4 by 2 mm in dimensions). b) Zoomed in section of the sample marked by the red rectangle in a) where the QDs studied in this work were found. The features visible on the surface are markers which can be used as a reference when relocating specific dots. c) Bright field TEM image of a cross section of the “In-flush” sample with 3000 times magnification. The asymmetric DBR cavity is clearly visible around the dot layer (courtesy of Richard Beanland). d) Representative PL spectrum of a dot measured in this work at an external magnetic field of $B_z = 8$ T. The excitation power of the non-resonant laser is $1 \mu\text{W}$, the polarisation is linear and the wavelength of the laser is 850 nm. The dominant exciton line is the Zeeman split neutral exciton (X^0), but other exciton lines from the same dot are also visible (X^+ and XX).	43
3.2	a) Optical microscope image of the surface of the “Low Temp Cap” p-i-n diode sample. The 10 by 10 array of apertures are labelled and can be used to easily relocate a particular QD. The two dark spots towards the top are used for bonding of the wires to the diode to allow for bias tuning. b) The current-voltage (IV) curve measured for one of the diodes shows characteristic diode behaviour. The data was measured with no optical illumination and at $T = 4.2$ K. c) Annular dark field TEM images to show the cross section of the sample with 80000 times magnification. A thin InAs layer is just visible as the bright layer beneath the AlGaAs superlattice. . .	45

- 3.3 Simplified schematic diagram of the cryogenic system. The cryostat holds a liquid He reservoir that allows for the use of a superconducting magnet with fields up to 8 T along the vertical axis. A laser can pass through the system and is focussed onto the sample surface with an aspheric lens, which is also used to collect the emitted dot signal. The sample is mounted on a non magnetic holder that can be positioned precisely using 3 piezoelectric nanopositioners. The sample is not in contact with the liquid He, but instead is contained within an insert tube filled with a low pressure He gas used for exchange gas cooling. There is a copper coil near the sample used to apply radiofrequency excitations to the quantum dots and another coil used as a pickup coil to monitor the waveforms. Wires are fed through the cage structure and the electrical components can be controlled externally through the electrical connectors at the top of the insert. A breadboard housing important optical components sits on top of the cryostat and the structure is damped to minimize vibrations and maintain optical alignment. 47
- 3.4 Diagram of experimental setup for optical photoluminescence spectroscopy. Two diode lasers are used to realize the pump-probe technique and pass through shutters and a series of polarisation optics via single mode (SM) fibres to create a high power, circularly polarised pump laser that polarises the nuclear spin bath and a low power, linear probe laser that detects the quantum dot signal. The emitted signal from the sample is directed through a high resolution double spectrometer and onto a CCD to measure the spectra. Also, the laser power and the location on the sample can be monitored by deflecting part of the beam onto a power meter and an imaging camera respectively. The components located on the breadboard above the cryostat are shown by the dotted rectangle. 50
- 3.5 Schematic illustration of the Pump-RF-Probe technique used for optically detected NMR measurements. The initially randomly fluctuating nuclear spins are polarised by a high power pump laser. Nuclei of a particular isotope are depolarised by applying a cw radiofrequency excitation and the final nuclear spin state is detected optically in the PL spectra with a low power probe laser. A change in splitting in the PL spectra is observed as the nuclear polarisation is altered. 54
- 3.6 PL spectra recorded using the pump-probe technique from the X^0 transition of a quantum dot from the In-flush sample at $B_z = 8$ T. The sample is pumped with different polarisations of light for a few seconds before recording the spectra and a clear Overhauser shift ΔE_{OHS} is visible. With linear pumping, the Zeeman splitting is 1.124 meV and under σ^+ (σ^-) pumping, a shift of $\Delta E_{OHS} = +125\mu\text{eV}$ ($-125\mu\text{eV}$) is observed. 55

- 3.7 Schematic comparison of the saturation and inverse NMR techniques for quadrupolar nuclei with the example case chosen as spin $I = 3/2$. a) Shows how the populations (green bars) of the various spin states of a single nuclear isotope follow the Boltzmann distribution after strong optical pumping (with polarisation of $\sim 70\%$) and with no rf applied. b) Using the saturation NMR method, a narrow band with width w_{sat} is applied for a sufficient time in resonance with the $1/2 \leftrightarrow 3/2$ ST and equalizes the populations between these two states. The other spin states are unaffected. c) If a single broadband cw pulse is applied covering all three transitions (spectrum indicated by the blue rf waveform) the populations of all 3 states are equalized. d) In the inverse NMR method, two broad rf bands are applied separated by a gap of width w_{gap} . When applied to the ST, all levels are affected and the populations are equalized separately for two groups of levels $m \leq +1/2$ and $m = +3/2$, resulting in a larger overall change in polarisation and enhancement of the detected NMR signal. 59
- 3.8 Schematic illustration of the generation of a rf frequency comb that is used in inverse NMR experiments. First, in a) we consider a simple case of two rf sine waves with frequency f_{car} and f_{mod} being modulated. b) A high and low frequency side band is formed either side of f_{car} and are separated by f_{mod} . c) Now, we consider modulating the carrier with an arbitrary waveform, which has a frequency comb shape that consists of a large number of closely spaced modes. d) Again high and low frequency sidebands are formed. e) This final frequency comb waveform approximates a spectral frequency band and can be arbitrarily positioned for use in inverse NMR experiments. 61
- 3.9 Circuit diagram for the applied rf waveform in inverse NMR experiments. Two sets of carriers and envelopes are stored in arbitrary waveform generators. The final shape of the waveform is created using external analogue mixers and a summator and then passed through a 30 W amplifier. This amplified rf field is applied through an rf coil placed near the sample via a variable length of 50 Ω coaxial cable to ensure broadband matching. The reflected signal (through the directional coupler) and the transmitted signal (through the pickup coil) can be monitored with a signal analyser. 63

- 3.10 Transmitted radiofrequency waveform detected using a signal analyser via the pickup coil, which was used to measure the ^{75}As isotope in the In-flush sample. The gap is centered on the ^{75}As resonance frequency at $B_z = 8$ T which is 58.576 MHz and the total width of the band is 18 MHz and the gap width is 12 kHz. Left panel: The transmitted waveform on a linear amplitude scale and a broad frequency scale with a span of about 20 MHz (inset shows a zoomed in spectra with span ≈ 100 kHz to explicitly monitor the narrow gap). Right panel: The same transmitted waveform as the left panel but shown with a logarithmic amplitude scale. The matching can not be perfect across the whole 18 MHz range but on the log scale, the entire band is flat to within about ~ 2 dB. There is a small rf power within the gap due to imperfections with the amplifier but the power spectral density of the band is at least 30 dB (1000 times) larger than the power density within the gap (see inset of right panel). The waveforms appear as bands because the modes of the frequency comb are closely spaced - here a mode spacing of $f_{MS} = 125$ Hz was used. 64
- 4.1 Schematic illustration comparing the nuclear spin baths in semiconductor quantum dots. On the left (in blue) is the dense nuclear spin bath found in InGaAs/GaAs dots and all the quadrupolar nuclear spins $I \geq 3/2$ are shown with thick arrows. On the right (in brown) is the dilute nuclear spin bath found in CdTe/ZnTe dots, which are smaller (contain less nuclei) and only a fraction of them possess a nuclear spin; most nuclei have no spin $I = 0$ (shown as grey dots) and the few nuclei with a spin are spin $I = 1/2$ isotopes (depicted with thin arrows). 67
- 4.2 Broad range photoluminescence spectra taken from the CdTe/ZnTe QD samples used in this work at $B_z = 0$ T using 405 nm excitation. a) Sample A contains a low density of single dot lines and b) Sample B has a higher density of dots (the inset shows the magnified signal from the single dot region) accompanied by a quantum well. 69
- 4.3 a) Bright field transmission electron microscopy (TEM) image of a cross section of Sample B. The dark regions indicate the presence of CdTe and the arrows show the approximate boundaries of two regions representing single CdTe quantum dots. b) Energy-dispersive X-ray (EDX) image of the same region as a) with the red dots (cadmium nuclei) showing there is an inhomogeneity in the distribution of cadmium atoms. An almost horizontal (with $\sim 2^\circ$ tilt) layer rich in Cd is seen in the EDX image and is attributed to the quantum well layer in Sample B. 70

- 4.4 a) Continuous wave (cw) PL spectra of the neutral exciton X^0 of a single CdTe/ZnTe QD from sample A at $B_z = 4$ T using a non-resonant 532 nm excitation and a power of 2.2 mW. b) Similar cw PL spectra of a dot in sample B with 200 μ W, 561 nm excitation at $B_z = 2.5$ T. Circularly polarised light was used and blue circles represent σ^- excitation and the red squares represent σ^+ excitation. For sample A, a clear change in splitting is visible of $(E_Z^{\sigma^-} - E_Z^{\sigma^+})/2 \approx -22$ μ eV which is unrelated to nuclear spin effects, but for sample B a small change of $(E_Z^{\sigma^-} - E_Z^{\sigma^+})/2 \approx 1.5$ μ eV is measured when the data is fit with Gaussian lineshapes and is related to the nuclear spin polarisation. 73
- 4.5 a) Continuous wave PL spectra of the neutral exciton in a single dot in sample A at $B_z = 8$ T using σ^- (blue dashed lines) and σ^+ (red solid lines) excitation. a) At high power $P_{exc} = 400$ μ W, two Zeeman split bright exciton states are observed and b) at low power $P_{exc} = 7$ μ W, both bright and dark exciton states are seen. Note \uparrow/\downarrow represents the hole spin and \uparrow/\downarrow the electron spin projection. 75
- 4.6 a) Pump-probe PL spectra of the neutral exciton X^0 in a single dot in sample B at $B_z = 2.5$ T using σ^- (blue circles, fit shown by solid lines) and σ^+ (red squares, fit shown by dashed lines), under excitation with a 561 nm laser. b) Pump-probe measurement cycle timing diagram used for CdTe/ZnTe dots. 78
- 4.7 a) The detected X^0 Zeeman splitting E_Z as a function of the pump power for a single dot from sample B, measured at $B_z = 2.5$ T using the pump-probe scheme and pumped with a 561 nm laser with polarisation σ^- (blue circles) or σ^+ (red squares). The maximum Overhauser shifts observed at high power were $\Delta E_Z^{\sigma^-,max} \approx +2.3$ μ eV and $\Delta E_Z^{\sigma^+,max} \approx -2.4$ μ eV. b) The total X^0 PL intensity (sum of the Zeeman split components), measured under cw conditions. The PL signal from the dot saturates at ≈ 50 μ W under both σ^+/σ^- excitation. 79
- 4.8 The detected change in splitting between σ^- and σ^+ pumping $((E_Z^{\sigma^-} - E_Z^{\sigma^+})/2)$ of X^0 as a function of the external magnetic field (in Faraday configuration) for a single dot from sample B using the pump-probe scheme. 80
- 4.9 a) Nuclear spin polarisation buildup dynamics in a single CdTe/ZnTe QD from sample B using the pump-probe scheme at $B_z = 2.5$ T. The characteristic buildup time under σ^- pumping (blue, open symbols) is $\tau_{buildup} = 0.9_{-0.5}^{+1.3}$ ms and under σ^+ pumping (red, solid symbols) is $\tau_{buildup} = 1.5_{-1.0}^{+3.0}$ ms, where the 95 % confidence intervals are quoted. b) Nuclear spin polarisation decay in the dark of the same QD. A combined exponential fit gives the characteristic decay time $\tau_{decay} = 4.3_{-1.6}^{+2.5}$ s. c) Pump-probe measurement cycle timing diagram used for buildup dynamics where an extra linear erase pulse prevents buildup of DNP between cycles. d) Pump-probe timing diagram for decay dynamics measurement. 82
- 4.10 Schematic illustration of the shape of the rf waveform applied to excite both cadmium isotopes for the NMR spectra measurements in CdTe/ZnTe dots. 84

- 4.11 Optically detected NMR spectra at $B_z = 2.5$ T for the Cd and Te isotopes in two single CdTe/ZnTe quantum dots: a) QD1 and b) QD2 in sample B. Both σ^- (thin blue line) and σ^+ (thick red line) pumping are shown and the width of the rf waveform, which indicates the spectral resolution (also shown with horizontal bars), was 63 kHz (dotted line) or 174 kHz (solid line). The dashed horizontal lines show the measured splitting without any rf and indicate the “background” level of splitting and the “off resonant” spectra show a measurement with f_{RF} between ~ 25.3 and ~ 26.2 MHz where no nuclear isotopes are present. c) Pump-rf-probe measurement cycle timing diagram used to measure NMR spectra. 85
- 5.1 Dependence of the Zeeman splitting on the angle of a rotatable quarter wave plate (QWP). The data was measured on the neutral exciton X^0 line in a pump-probe scheme using the In-flush sample at $B_z = 8$ T. The other experimental parameters were $P_{\text{Pump}} = 1$ mW, $T_{\text{Pump}} = 6$ s, $P_{\text{Probe}} = 0.25$ μ W and $T_{\text{Probe}} = 30$ ms. With linear pumping Π , the Zeeman splitting is ~ 1.124 meV and under σ^+ (σ^-) pumping with a corresponding QWP angle of 54° (-46°), a shift of $\Delta E_{OHS} \approx +125$ μ eV (-125 μ eV) is observed. 90
- 5.2 a) Dependence of the Zeeman splitting on the pump pulse duration T_{Pump} under both σ^+ (red solid squares) and σ^- (blue open squares) pumping at $B_z = 8$ T for a single dot in the In-flush sample. Inset shows the pump-probe-erase timing diagram used for this measurement only. A clear buildup in the Overhauser shift is observed and the vertical line shows the chosen pump time of $T_{\text{Pump}} = 6$ s for NMR experiments. The other experimental parameters for this measurement were $P_{\text{Pump}} = 1$ mW, $P_{\text{Probe}} = 0.25$ μ W and $T_{\text{Probe}} = 10$ ms. b) Effect of the duration and power of the probe pulse on the Zeeman splitting. Three different probe powers were applied and both σ^+ (solid symbols) and σ^- (open symbols) pumping with $T_{\text{Pump}} = 6$ s and $P_{\text{Pump}} = 1$ mW are shown. A clear decay of the nuclear polarisation is observed which is faster for larger probe powers. Here, the vertical line shows the chosen probe time of $T_{\text{Probe}} = 40$ ms at a probe power of $P_{\text{Probe}} = 1$ μ W for NMR experiments. 92
- 5.3 Dependence of the Zeeman splitting on the wait time T_{Wait} in the dark between the pump and probe pulse (shown schematically in the inset) under both σ^+ (red solid squares) and σ^- (blue open squares) pumping at $B_z = 8$ T for a single dot in the In-flush sample. The other experimental parameters were $P_{\text{Pump}} = 1$ mW, $T_{\text{Pump}} = 6$ s, $P_{\text{Probe}} = 1$ μ W and $T_{\text{Probe}} = 30$ ms. . . . 93
- 5.4 Nuclear resonance spectra schematic of the four studied isotopes in a single self assembled InGaAs/GaAs quantum dot at $B_z = 8$ T. There are narrow central transition peaks corresponding to the $-\frac{1}{2} \leftrightarrow +\frac{1}{2}$ spin states of each isotope. There are two satellite transitions for the spin $I = 3/2$ isotopes for Ga and As, but eight for the $I = 9/2$ isotope of ^{115}In 95

- 5.5 Calibration measurement to determine the total spectral width of each isotope in the In-flush sample at $B_z = 8$ T using σ^- pumping only. The change in Overhauser shift ΔE_{OHS} is between the “no gap” measurement where a single band of width w_{Band} depolarises the isotope and a “gap” measurement where a gap is introduced in the band. The gap widths (and length of rf pulse T_{RF}) used were 400 kHz (4.4 s) for ^{75}As (left panel), 200 kHz (3 s) for $^{115}\text{In} + ^{69}\text{Ga}$ centred on the ^{115}In resonance frequency (middle panel) and 100 kHz (1.28 s) for ^{71}Ga 96
- 5.6 The difference in Overhauser shift ΔE_{OHS} produced by the “no gap” and “gap” waveforms (which provides the amplitude of the CT NMR signal) as the duration of the rf pulse T_{RF} is varied. The data is taken for each isotope in the In-flush sample at $B_z = 8$ T using σ^- pumping only. The chosen widths of the gap are similar to those used in the high resolution inverse NMR CT spectra i.e. 30 kHz for ^{75}As (left panel), 30 kHz for ^{115}In (middle panel) and 10 kHz for ^{71}Ga 100
- 5.7 The change in Overhauser shift ΔE_{OHS} observed by applying a single rf band only (“no gap”) to depolarise the entire isotope as the length of the rf pulse T_{RF} is varied. This measurement allow us to determine the total Overhauser shift per isotope: $37 \mu\text{eV}$ for ^{75}As (left panel), $69 \mu\text{eV}$ for $^{115}\text{In} + ^{69}\text{Ga}$ (middle panel) and $17 \mu\text{eV}$ for ^{71}Ga . The data is taken for each isotope in the In-flush sample at $B_z = 8$ T using σ^- pumping only. 101
- 5.8 The optical pump pulse polarises all isotopes and the populations of the nuclear spin states for a spin $I = 3/2$ follow the Boltzmann distribution where most nuclei are initialised into the $I_z = +3/2$ for σ^- pumping. The “no gap” waveform depolarises all nuclei of a specific isotope so the populations of all states are the same. The “gap” waveform (with the gap centred on the CT) creates a population probability distribution with different probability values based on I_z and a change in the Overhauser shift is detected due to nuclei within the gap. The final NMR signal is obtained by taking the change in splitting between the “no gap” minus “gap” measurements as f_{Gap} moves across the resonance. For σ^+ pumping the changes in splitting are reversed and the final NMR signal is from “gap” minus “no gap”. 102
- 5.9 Inverse NMR CT spectra of ^{115}In in the In-flush sample at $B_z = 8$ T using σ^- pumping only. The “No Gap” waveform provides a background level of splitting and the change in splitting observed when applying a $w_{\text{Gap}} = 18$ kHz (which is the resolution and shown by the horizontal bar) provides the NMR signal. a) shows the unfiltered Zeeman splitting and b) shows the data filtered with a Gaussian averaging filter with a filter width of $w_{\text{Gap}}/3 = 6$ kHz. Also shown in b) is an example of a Gaussian fit which is used to extract the approximate width of the peak w_{inh} 103
- 5.10 High resolution central transition (CT) NMR spectra of all nuclear isotopes in both InGaAs/GaAs QD samples. All spectra were taken at $B_z = 8$ T and using σ^- polarized pumping. The horizontal bars indicate the resolution which in these experiments are given by the width of the gap in the inverse NMR radiofrequency waveform and differ by isotope ($w_{\text{Gap}} = 4$ kHz for both Ga isotopes, $w_{\text{Gap}} = 12$ kHz for ^{75}As and $w_{\text{Gap}} = 18$ kHz for ^{115}In). 105

- 5.11 Comparison of the 2 and 3 band inverse NMR technique. a) Schematic illustration of the shape of the NMR signal from a spin $I = 3/2$ quadrupolar nuclear isotope. A narrow central transition ($I_z = +\frac{1}{2} \leftrightarrow -\frac{1}{2}$) is accompanied by 2 broad satellite transitions ($I_z = +\frac{3}{2} \leftrightarrow +\frac{1}{2}$ or $-\frac{3}{2} \leftrightarrow -\frac{1}{2}$) due to the strain distribution in single quantum dots. b) The shape of the inverse NMR radiofrequency waveform used to manipulate the isotope to measure the CT spectra. Two broad bands that are wide enough to cover the entire resonance are accompanied by a narrow gap and the central frequency of the gap f_{Gap} is moved across the CT resonance peak to measure the CT signal. c) The shape of the rf waveform for the new 3-band inverse NMR technique used to measure the STs. The gap between the bands is large and if the gap overlaps the CT transition, a 3rd narrow CT band ($w_{\text{CTband}} < w_{\text{Gap}}$) is applied to saturate the CT signal. The position of the 3rd band f_{CTband} remains fixed and the width of the 3rd band is chosen to cover at least 90% of the CT resonance peak. 108
- 5.12 The inverse NMR ST spectra of ^{71}Ga in the Low Temp Cap sample. Both pump polarizations are shown for both 2 and 3 band techniques and a clear reduction in peak amplitude is visible in the 3 band measurement due to saturation of the CT signal. All spectra were taken at $B_z = 8$ T with a gap width (resolution) of $w_{\text{Gap}} = 600$ kHz. 109
- 5.13 Inverse NMR satellite transition (ST) spectra of all nuclear isotopes in both QD samples using the novel 3-band inverse NMR technique and pumping with either σ^+ or σ^- circularly polarized pumping. All spectra were taken at $B_z = 8$ T and an inverse NMR gap width of $w_{\text{Gap}} = 600$ kHz which is the resolution of the spectra. Top Panel: ST spectra from a single QD in the sample grown with In-flush. Bottom Panel: ST spectra from a dot in the Low Temp Cap sample. The shaded lines at frequency 58.84 MHz, 75.37 MHz, 82.52 MHz and 104.85 MHz indicate the width of the CT-band used to saturate the CT of each of the 4 nuclear isotopes: ^{75}As ($w_{\text{CTband}} = 503$ kHz), ^{115}In ($w_{\text{CTband}} = 81$ kHz), ^{69}Ga ($w_{\text{CTband}} = 39$ kHz) and ^{71}Ga ($w_{\text{CTband}} = 39$ kHz) respectively. 110
- 5.14 a) Transmission electron microscope (TEM) 002 dark field images of a cross section of the In-flush sample with 50000 times magnification. Both larger pyramidal shaped dots and shallower disc like dots both visible. b) Shows a magnified TEM image of a shallow dot and c) a large dot in the In-flush sample with 150000 times magnification. 114

- 5.15 a) Annular dark field TEM image of Low Temp Cap sample with 2.5×10^6 times magnification. An indium layer is clearly visible (as the bright layer), but no obvious quantum dot like structures are found. b) Very high resolution TEM image of InAs layer in the Low Temp Cap sample with 6×10^6 magnification. The image growth axis and in plane axis are labelled with dimensions and these values are used for the axes scales in the plots in c) and d). c) In plane variation of ρ_{In} calculated from the intensity values of the high resolution TEM image (shown in b)) of the Low Temp Cap sample. Note that $\rho_{In} = 0$ corresponds to pure GaAs and $\rho_{In} = 1$ is pure InAs. d) The variation of the fraction of In ρ_{In} in the growth direction by averaging over rows of pixels in the high resolution TEM image (shown in b)). Thanks to Richard Beanland from the University of Warwick for the TEM images. 115
- 6.1 Bias dependant photoluminescence spectra of a single dot from the Low Temp Cap sample at $B_z = 8$ T with low power ($0.3 \mu\text{W}$) non-resonant 850 nm excitation. a) PL map showing the appearance of different exciton (X^0 and X^-) states as the bias is changed. b) The measured PL amplitudes and c) the detected linewidths of each exciton line as the bias is changed. 121
- 6.2 Dependence of the Zeeman splitting on the bias applied during the pump pulse V_{Pump} under both σ^+ (red solid squares) and σ^- (blue open squares) pumping at $B_z = 8$ T for a single dot in the Low Temp Cap sample. The vertical line shows the optimal pump bias of $V_{\text{Pump}} = 1.28$ V (which induces the largest Overhauser shift) used in NMR experiments. The other experimental parameters for this measurement were $P_{\text{Pump}} = 1$ mW, $T_{\text{Pump}} = 6.8$ s, $P_{\text{Probe}} = 0.25 \mu\text{W}$ and $T_{\text{Probe}} = 10$ ms. 123
- 6.3 Bias dependence of the nuclear spin lifetime for a single InGaAs QD in the Low Temp Cap sample. The exponential decay of the nuclear polarisation is measured and the extracted T_1 times from the fit are plotted as the sample is kept at different biases in the dark V_{Dark} . Three distinct charging states of the QD are observed with long nuclear $T_1 > 10^4$ s for the empty (0e) and doubly charged (2e) states and a smaller $T_1 > 560$ s for a singly charged dot (1e). The other experimental parameters for this measurement were $B_z = 8$ T, $P_{\text{Pump}} = 1$ mW, $T_{\text{Pump}} = 10$ s, $P_{\text{Probe}} = 0.25 \mu\text{W}$ and $T_{\text{Probe}} = 25$ ms. Note that all T_1 values $> 10^4$ s are estimated values since long delay times $T_{\text{Wait}} > 900$ s were not explicitly measured. 124
- 6.4 Schematic illustration of a nuclear spin flip via cotunnelling with the electron reservoir in the Fermi sea. The nuclear spin (black arrow) may be flipped without changing the confined electron spin (red arrow) with the energy difference ΔE_N 1) provided by electron-hole annihilation or 2) absorbed by electron-hole excitation in the Fermi reservoir. Adapted from [7]. 126

- 6.5 Schematic illustration of an electron mediated nuclear spin flip. Two distant nuclear spins (black arrows) that overlap the electron wavefunction (shaded orange area) and with a small difference in energy (shown within the dashed circles) can exchange their spins via a virtual second order spin flip with the electron spin (red arrow). This redistributes the nuclear spin polarisation and causes a faster decay of the nuclear spin lifetime in the 1-electron charging plateau. Adapted from [7]. 127
- 6.6 a) Inverse NMR CT spectra of ^{71}Ga for a single dot in the Low Temp Cap sample for an empty dot ($V_{\text{Dark}} = 1.64$ V, brown squares) and a singly charged dot ($V_{\text{Dark}} = 1.732$ V, blue circles). The inset shows a magnified version of the 0e peak. The data was taken at $B_z = 8$ T using σ^- pumping and the gap widths used in the inverse NMR waveform were $w_{\text{Gap}} = 6$ kHz for the 0e peak and $w_{\text{Gap}} = 140$ kHz for the 1e peak (shown by the horizontal bars). b) Timing diagram for NMR spectra measurements illustrating the bias values used for the various pulses in the cycle. By changing the bias applied in the dark V_{Dark} , we control the QD charge state during the rf pulse. 128
- 6.7 a) Inverse NMR CT spectra of ^{71}Ga for a single dot in the Low Temp Cap sample for different dark biases across the 1e plateau. The data was taken at $B_z = 8$ T using σ^- pumping and the gap widths used in the inverse NMR waveform were $w_{\text{Gap}} = 40$ kHz for $V_{\text{Dark}} = 1.716$ V and $V_{\text{Dark}} = 1.754$ V and $w_{\text{Gap}} = 140$ kHz for $V_{\text{Dark}} = 1.720$ V, $V_{\text{Dark}} = 1.732$ V and $V_{\text{Dark}} = 1.44$ V. b) A subset of the data shown in Figure 6.3 of how the nuclear spin lifetime T_1 varies across the 1e plateau. The vertical lines (with the corresponding colours) show the different V_{Dark} values used to measure the NMR spectra and their relative positions in the 1e plateau. c) The extracted NMR CT linewidths w_{inh} (FWHM from Gaussian fitting) for the different biases across the 1e plateau. 130
- 6.8 Schematic diagram to illustrate the frequency comb technique to measure the homogeneous linewidth w_{hom} of a nuclear spin ensemble. a) The inhomogeneously broadened NMR lineshape (with width w_{iso}) of a quadrupolar nuclear isotope (black line) showing both the central transition (CT, $I_z : -\frac{1}{2} \leftrightarrow \frac{1}{2}$) and the satellite transitions (ST, $I_z : -\frac{3}{2} \leftrightarrow -\frac{1}{2}$ or $+\frac{1}{2} \leftrightarrow +\frac{3}{2}$) is actually the spectral sum of a large number of individual nuclear transitions with width w_{hom} (red lines). Shown in green is the applied rf excitation in the shape of a frequency comb with a mode spacing f_{MS} and a width w_{comb} that covers the entire resonance ($w_{\text{comb}} > w_{\text{iso}}$). b, c) By changing the mode spacing f_{MS} we can experimentally determine the underlying homogeneous linewidth w_{hom} due to the effect on the rf induced nuclear spin depolarisation time. The two extreme cases are shown: b) either $w_{\text{hom}} > f_{\text{MS}}$, so all nuclear transitions are driven by the rf (and we observe fast depolarisation) or c) $w_{\text{hom}} < f_{\text{MS}}$, so some nuclear transitions (dashed red line) do not overlap with any of the modes of the comb and the depolarisation rate is slow. When the depolarisation begins to slow down, we can estimate w_{hom} because $w_{\text{hom}} \sim f_{\text{MS}}$. Adapted from [8]. 133

- 6.9 The change in the ^{71}Ga nuclear spin polarisation ΔE_{OHS} as the duration T_{RF} of the applied rf frequency comb is changed. Different modes spacings of the frequency comb f_{MS} are shown and a clear slow down of the nuclear spin depolarisation is observed for large f_{MS} whilst the sample is kept in a) the 0e state ($V_{\text{Dark}} = 1.64$ V) and b) the centre of the 1e plateau ($V_{\text{Dark}} = 1.732$ V) in the dark during the rf pulse. The data is taken at $B_z = 8$ T and using σ^- pumping and the solid lines show the exponential fitting. 135
- 6.10 Two-dimensional density plot of how the Overhauser shift changes ΔE_{OHS} due to ^{71}Ga depolarisation with different mode spacing f_{MS} of the frequency comb and different durations of the rf pulse T_{RF} . The f_{MS} at which the depolarisation slows down gives an estimate of the homogeneous linewidth w_{hom} (indicated by black arrows) and this occurs a) for an empty dot ($V_{\text{Dark}} = 1.64$ V) at $w_{\text{hom}} \approx 400$ Hz and b) for a singly charged dot ($V_{\text{Dark}} = 1.732$ V) at a much larger $w_{\text{hom}} \approx 50000$ Hz. 136
- A.1 The observed variation in the PL energy of the neutral X^0 state as a function of wall clock time passed in the lab, during NMR measurements. The average energies of the two Zeeman split peaks are plotted for two separate QDs in sample B. 142
- C.1 The inverse NMR CT spectra of all 4 isotopes for both samples. The spectra were taken at $B_z = 8$ T and using σ^- pumping. The horizontal and vertical scales of each row (isotope) are set to be identical so that the equivalent lineshapes can be compared for a specific isotope between samples. 149
- D.1 Schematic illustration of various gap positions relative to the 3rd CT band in inverse 3-band NMR measurements. 152
- D.2 Raw uncorrected data (solid lines) of the satellite transition (ST) NMR spectra from all nuclear isotopes in both QD samples using the new 3-band inverse NMR technique and pumping with either σ^+ or σ^- circularly polarised pump. Also shown in thin dashed lines are the corrected NMR ST dataset using the data correction procedure described in this appendix. All spectra were taken at $B_z = 8$ T and an inverse NMR gap width of 600 kHz which is the resolution of the spectra. Top Panel: ST spectra from the sample grown with In-flush. Bottom Panel: ST spectra from the sample capped at low temperature. The shaded lines at frequency 58.84 MHz, 75.37 MHz, 82.52 MHz and 104.85 MHz indicate the width of the CT-band used to saturate the CT of each of the 4 nuclear isotopes: ^{75}As ($w_{\text{CTband}} = 503$ kHz), ^{115}In ($w_{\text{CTband}} = 81$ kHz), ^{69}Ga ($w_{\text{CTband}} = 39$ kHz) and ^{71}Ga ($w_{\text{CTband}} = 39$ kHz) respectively. 156

List of Tables

2.1	Important parameters relating to all of the nuclear isotopes found in the samples used in this work. The values are given for both the InGaAs system and for the CdTe/ZnTe system. Note that these are the stable naturally occurring isotopes which possess non-zero nuclear spin I . The hyperfine constants A for Ga and As are taken from [9] and for In, Cd and Te are averaged over the stable isotopes of the same element and taken from [10]. The other parameters are from [11].	34
5.1	List of all important experimental parameters used for the cw inverse NMR spectra measurements in the In-flush sample at $B_z = 8$ T. To account for the skewness in the ^{75}As lineshape, the 3rd band is offset to lower frequencies by $\dagger 100$ kHz, see Appendix C.	98
5.2	List of all important experimental parameters used for the cw inverse NMR spectra measurements in the Low Temp Cap sample at $B_z = 8$ T. To account for the skewness in the ^{75}As lineshape, the 3rd band is offset to lower frequencies by $\ast 30$ kHz, see Appendix C.	99
5.3	The inhomogeneous linewidths (FWHM) of CT peaks (w_{inh}) from fitting NMR CT spectra and the normalised integrated CT signal (ΔE_{CT}) for all isotopes in both InGaAs/GaAs QD samples.	105
6.1	The inhomogeneous linewidths (FWHM) of CT peaks (w_{inh}) at different dark biases V_{Dark} across the 1e plateau from fitting the inverse NMR ^{71}Ga CT spectra for the Low Temp Cap sample.	131
B.1	The experimentally measured total OHS (ΔE_{OHS}) and the normalised integrated CT signal (ΔE_{CT}) for In and Ga in both InGaAs/GaAs QD samples (using σ^- pumping only at $B_z = 8$ T). Note that ΔE_{OHS} for ^{113}In and ^{69}Ga is a combined value due to the total OHS from both isotopes. . .	144
C.1	The chosen widths of the third CT saturation band w_{CTband} (in units of [kHz]) of each of the isotopes in the two samples used in this work. To account for the skewness in the ^{75}As lineshape, the 3rd band is offset to lower frequencies (compared to the ^{75}As CT frequency) by $\ast 30$ kHz for the Low temp cap sample and $\dagger 100$ kHz for the In-flush sample.	150

List of Acronyms

QM	Quantum Mechanics
NV	Nitrogen Vacancy
QD	Quantum Dot
GaAs	Gallium Arsenide
InAs	Indium Arsenide
InGaAs	Indium Gallium Arsenide
CdTe	Cadmium Telluride
ZnTe	Zinc Telluride
NMR	Nuclear Magnetic Resonance
MBE	Molecular Beam Epitaxy
MOVPE	Metal Organic Vapour Phase Epitaxy
FM	Frank-van der Merwe
VW	Volmer-Weber
SK	Stranski-Krastanov
WL	Wetting Layer
DBR	Distributed Bragg Reflector
CB	Conduction Band
VB	Valence Band
HH	Heavy Hole
LH	Light Hole
QCSE	Quantum Confined Stark Effect
EFG	Electric Field Gradient
OHS	Overhauser shift
DNP	Dynamic Nuclear Polarisation
rf	Radio Frequency
cw	Continuous Wave
ML	Mono Layer
HWP	Half Wave Plate

QWP	Quarter Wave Plate
CCD	Charge Coupled Device

Chapter 1

Introduction

In the last century or so, quantum mechanics (QM) has become one of the fundamental pillars of our understanding of the universe. Its philosophically unintuitive statements have been confirmed by numerous ground-breaking experiments. Though originally developed to understand the properties of sub-atomic particles, research in the last few decades has steered towards harnessing the properties of quantum systems to store, process and transmit information.

The development of computation has certainly been a fascinating journey undertaken by human kind. Since the pioneering work by Charles Babbage on the ‘Analytical Engine’ through the concepts proposed by Alan Turing on computational algorithms to the modern day micro chips containing billions of transistors. The number of atoms that are required to form a transistor is continuously decreasing and clearly at some point there is a limit to the computing power of such ‘classical computers’. However, if the strange properties of quantum mechanics can be controlled to create a ‘quantum computer’, certain tasks could be solved far more efficiently than even the most powerful classical counterpart.

The first proposals to use quantum effects to create a computer were made by Richard Feynman [12] and others [13–15]. These quantum computers would be able to compute certain problems such as Shor’s prime factorization [16], Grover’s list search [17] and the ‘quantum random walk’ [18] algorithms much more efficiently by scaling polynomially with time (as opposed to exponentially for their classical counterparts). Such a computer would be based around quantum bits or ‘qubits’. In contrast to the classical bits which can only be in the state “0” or “1”, a qubit is written as $\Psi = a|0\rangle + b|1\rangle$ and is a linear combination of both $|0\rangle$ and $|1\rangle$ states. This wavefunction Ψ is probabilistically defined so that the normalisation condition holds for the probability amplitudes $|a|^2 + |b|^2 = 1$.

The fundamental requirements of a qubit to realise a fault tolerant quantum computer were set out by the DiVincenzo criteria [19] and later summarised [20] into 3 more general categories:

- scalability - it should be possible to create many qubits with the ability to control each one individually, without the cost of external resources (including space, time and energy) growing exponentially,
- universal logic - a finite set of universal quantum logic gates should exist to control all necessary computing operations,
- correctability - the system is able to be efficiently initialized into and measured from a specific quantum state.

These categories are difficult to implement all together as they require a strong interaction for fast initialisation and readout but enough isolation from the surrounding environment for long coherence times so that a state can be stored in ‘memory’. DiVincenzo also added additional criteria regarding the ability to convert between a ‘stationary qubit’ and a ‘flying qubit’ (such as a photon) so that small quantum circuits can communicate with each other to form larger quantum computers.

Several directions of research have ensued to find systems that can be used as the hardware for quantum computers [20] including individual atomic ions trapped by electric fields [21–23], nuclear spins in liquid solutions [24–26], superconducting Josephson junctions [27–29], single impurities in crystals such as silicon [30–32] or Nitrogen Vacancy (NV) centres in diamond [33–35] and last but not least quantum dots (QDs). QDs confine charge carriers (electrons and holes) in all 3 spatial directions and can be formed in a variety of ways such as electrostatic confinement [36], colloidal crystals in solution [37], fluctuations at crystal boundaries [38, 39] and self assembled QDs due to lattice mismatch [1, 40].

1.1 Motivation for using quantum dots

Throughout the work presented in this thesis, only samples containing self assembled QDs were studied and most experimental results will be from an individual dot. It is beyond the scope of this brief background to provide a complete comparison between all of the potential qubit candidates stated above (for more information see [20]). Instead only the advantages and disadvantages of the self assembled QD system shall be discussed.

The most commonly studied compound semiconductor self assembled QD systems use III–V materials such as Indium Arsenide (InAs) or Gallium Arsenide (GaAs). The lattice mismatch between InAs and GaAs causes a strain driven random growth process (see Chapter 2.1). The single most important feature of these materials is that they have strong light-matter interactions. Both InAs and GaAs are direct bandgap semiconductors and there exists a strong optical transition [41] between the electron in the highest occupied energy level (Valence band) and the lowest unoccupied level (Conduction band). This allows photons to be absorbed and emitted very efficiently from the dots and they have been identified as excellent single photon sources [42–45]. The spin degree of freedom of an electron trapped in a QD is a good candidate for Divincenzo’s ‘stationary qubit’ and the polarisation of the emitted photons can carry this information and act as ‘flying qubits’, thus creating quantum networks. This well studied material system also benefits from years of development in growth and processing techniques allowing for advanced nano-fabrication technology. Since they are grown within a semiconductor matrix, additional structures can be incorporated around the QD such as diodes [1, 46] for electrical charge control, cavities [47] to enhance the optical coupling and waveguides [48, 49] for transporting of photons within the crystal (leading to so called ‘on-chip’ integration).

However, there are also significant difficulties in taking these promising attributes and having a developed, working quantum computer. Firstly, the carriers confined within a QD can interact with phonons in the crystal lattice [50] which leads to dephasing. Moreover, the self assembly process occurs randomly so the size and quantity of the grown QDs varies across the surface of the crystal and each dot will emit at a different wavelength. Whilst attempts have been made to deterministically control the sites at which QDs are grown [51–53], the resulting dots are unsatisfactory since their optical properties are not as good as randomly positioned dots. Finally, the confined spin in a self assembled QD is not isolated from its surroundings; there are a large number (approximately 10^5 in InGaAs/GaAs QDs) of fluctuating quadrupolar nuclear spins which create a time varying nuclear magnetic field which again causes decoherence of the carrier spin [10, 54–57]. Whilst some of the issues such as the site control of dots may be improved through clean growth conditions, some issues like the presence of a fluctuating nuclear spin bath are an inherent part of the III-V quantum dot system and can not be removed in a simple way.

1.2 Outline of this thesis

The work contained within this thesis is to primarily understand the fundamental properties of the nuclear spins in single self assembled QDs. The aim is to manipulate and control the nuclear spins so that a more stable environment is created for the confined carrier. The nuclei are optically polarised and manipulated using specially designed nuclear magnetic resonance (NMR) techniques and the NMR signal can be detected optically by looking at the effect of the nuclear field on the electron spin states.

Typically there are two routes to decrease the amplitude of the nuclear spin bath fluctuation: either align all the spins so that they don't fluctuate (i.e. polarise the nuclear spins) or use a system with less nuclear spins. For the former, high degrees of nuclear polarisation can be already be achieved in InGaAs/GaAs [10, 58, 59] and GaAs/AlGaAs QDs [9] and we use this fact as part of our pump-probe scheme (see Chapter 3), which is integral to optical detection of NMR. For the latter, it has been shown in group IV semiconductors such as isotopically controlled phosphorus in silicon that the electron spin coherence time can be enhanced by many orders of magnitude [60] when isotopes with no nuclear spins are used. As part of the work presented in this thesis (see Chapter 4), we look at an intermediary system of II–VI Cadmium Telluride on Zinc Telluride (CdTe/ZnTe) QDs, where most nuclei are spin free but still have good optical properties comparable to III–V dots.

A brief description of the contents of each chapter is summarized below. After some initial background and explanations of the experimental methods used, there are three chapters containing separate, novel pieces of experimental research:

- Chapter 2 presents some of the basic concepts associated with self assembled QDs including the growth procedure, electron, hole and nuclear spin properties. Also included are the various ways in which the spins can be manipulated including electric, magnetic and radiofrequency fields.
- Chapter 3 outlines the key experimental methods and equipment used throughout this work. The most important techniques of photoluminescence (PL) spectroscopy and optically detected NMR are explained as well as the necessary hardware required (including the cryostat, optical setup and radiofrequency components).

- In Chapter 4, the first direct measurement of the nuclear Overhauser field in the dilute nuclear spin bath system of CdTe/ZnTe QDs is presented together with important properties such as the time dynamics, pump power and magnetic field dependence. Together with this, the first detection of Cd and Te NMR signals in these materials are also presented, indicating a system with a large Knight field due to the confined electron and significant charge fluctuations.
- In Chapter 5, the structure of individual InGaAs/GaAs QDs using NMR spectra and TEM images is analyzed. Since the nuclei are coupled to the strain within the QD, important structural information of individual QDs may be determined from NMR spectroscopy such as the chemical composition and the strain distribution. A novel 3-band inverse NMR technique is developed and previously undetectable signals from nuclei in low strain regions are able to be measured.
- In Chapter 6, direct experimental comparisons are shown between the neutral InGaAs/GaAs QD and a single electron charged state. Spatial inhomogeneity in the electron-nuclear spin interaction is studied and the additional electron provides an additional pathway to depolarise the nuclear spins.
- Chapter 7 contains the key conclusions and possible directions of future research from the experimental results.

Chapter 2

Optically active self assembled quantum dots

All experimental work in this thesis is conducted on semiconductor samples of individual optically active, self assembled quantum dots. As the wording suggests, there are several important characteristics to this system. The ‘quantum dot’ (QD) refers to the fact that carrier spins (such as electrons or holes) are confined in all 3 spatial dimensions leading to atom-like, discrete spacing between energy levels. ‘Optically active’ means that both an electron and a hole are confined together and the system can be populated by an incoming photon as well as recombine and emit a photon. ‘Self assembled’ describes how the growth procedure occurs spontaneously and randomly driven by the crystal lattice mismatch.

The samples studied in Chapters 5 and 6 contain the most commonly studied system of InGaAs QDs on a GaAs substrate and the material system used in Chapter 4 is the potentially promising alternative of CdTe QDs on a ZnTe substrate. All samples were grown using molecular beam epitaxy (MBE) but in this chapter, the concepts and the growth procedure will be introduced through the InGaAs/GaAs QD system only. Most of the discussion will also apply to CdTe/ZnTe QDs but any differences in growth methods or specific properties will be included directly within Chapter 4.

Here, the fabrication techniques required to create self assembled QD samples are discussed. The basic properties of this system are explored including the energy level structure/transitions and finally the way the energy levels change with external fields is described. Though the work in this thesis primarily concerns the nuclear spin properties, it is essential to understand the electronic properties first because as we will see, the two

systems are inherently intertwined. The interactions between the electron and nuclear system is then discussed along with spin relaxation mechanisms.

2.1 Quantum dot sample growth

The first discovery of 3 dimensional confinement in semiconductor nanocrystals was made by Ekimov [61]. Various types of QDs have already been discussed in Chapter 1, but optically active QDs are fabricated primarily using epitaxial techniques such as molecular beam epitaxy (MBE) [62] or metal organic vapour phase epitaxy (MOVPE) [63].

The word epitaxy refers to depositing layers of material onto a crystalline substrate along a specific crystal axis. The QD samples used throughout this thesis were grown with MBE. An MBE reactor consists of a very high vacuum chamber attached to a series of cells containing pure elements such as In, Ga or As. Upon heating, these elements sublime and can be directed into beams of gaseous atoms that are fed into the vacuum chamber. To grow InAs QDs, beams of In and As condense onto the surface of a crystalline GaAs substrate wafer and react to form (mono)layers of InAs. The crucial next step to create 3 dimensional confinement occurs because of the lattice mismatch between the InAs film and the GaAs substrate (approx. 7 %) which leads to strain between nuclei in the two materials.

The growth can then proceed in one of three distinct ways [64] depending on the surface tensions of the film/substrate:

- monolayer by monolayer - Frank-van der Merwe (FM) growth [65],
- island growth - Volmer-Weber (VW) [66],
- a combination of the above methods where initially layers are grown, then islands are formed - Stranski-Krastanov (SK) [67].

For the self assembled QDs studied in this work, the dots grow randomly via the SK growth mechanism and there is a distribution in the size and energies of the dots depending on various growth parameters such as pressure, temperature and deposition rates. Typically InGaAs QDs have a diameter of about 20 nm and a height of 5 nm. The islands form on top of the flat layer (called the wetting layer (WL)) as a way of relaxing the energy due to strain in the growth direction and clean, defect-free QDs can form [68] provided the energy

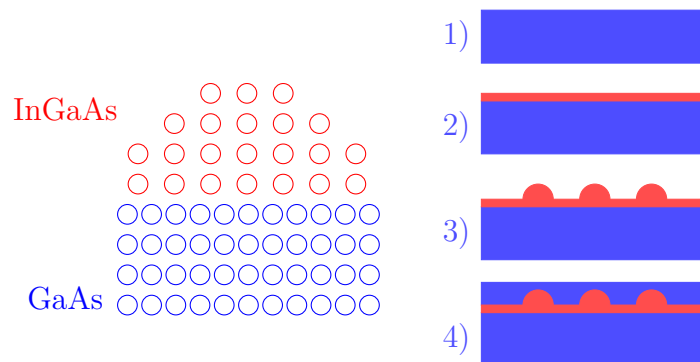


FIGURE 2.1: Illustration of quantum dot growth. The left panel shows how the lattice mismatch between the GaAs substrate (blue) and the InGaAs film (red) creates strain in Stranski-Krastanov (SK) dots. The right panel shows how the growth progresses in SK dots: 1) the initial GaAs substrate, 2) monolayers of InGaAs are deposited onto the substrate and grow layer by layer (similar to Frank-van der Merwe growth), 3) the growth then proceeds by forming islands (as in Volmer Weber growth), 4) Finally the dots are capped with the substrate material (GaAs) to achieve a good confinement potential.

bandgap of the film (InAs) is smaller than that of the substrate (GaAs). Furthermore, the InAs islands are capped (see Figure 2.1) with the substrate material (GaAs) to achieve a good confinement potential [6]. This provides a better optical signal by moving the interface between substrate and air further away from the QD layer. Also, this prevents the formation of non-radiative pathways via surface state recombination which would suppress the QD emission. It is worth mentioning that the system is usually labelled as an InGaAs QD since a significant amount of alloying can take place. Even if the intended film layer is purely InAs, intermixing between the InAs and GaAs layers occurs via surface diffusion [69, 70] and the final island will be composed of some combination of In and Ga atoms. Experimental evidence for this process is discussed in Chapter 5, where NMR techniques are used to analyze the structure of InGaAs QDs.

The fabrication techniques for III-V semiconductor materials are now quite advanced through 30 years of development and the QD layer can be embedded within more sophisticated heterostructures. The emission of the light from the QD can be enhanced (in the growth direction) by growing distributed Bragg reflector (DBR) layers around the dots. This consists of alternating layers of materials with different refractive index (such as GaAs/AlGaAs). Light is partially reflected at the boundary between each layer and this leads to constructive interference which can be tuned to enhance the emission at a particular wavelength. To ensure light is emitted from the system in one direction, for example the $+\hat{z}$ direction up from the dot layer, an asymmetric set of GaAs/AlGaAs DBR pairs are grown with more pairs below and less pairs above the dots. This forms a planar microcavity consisting of two reflective “mirrors” that enhances the signal from the dots by

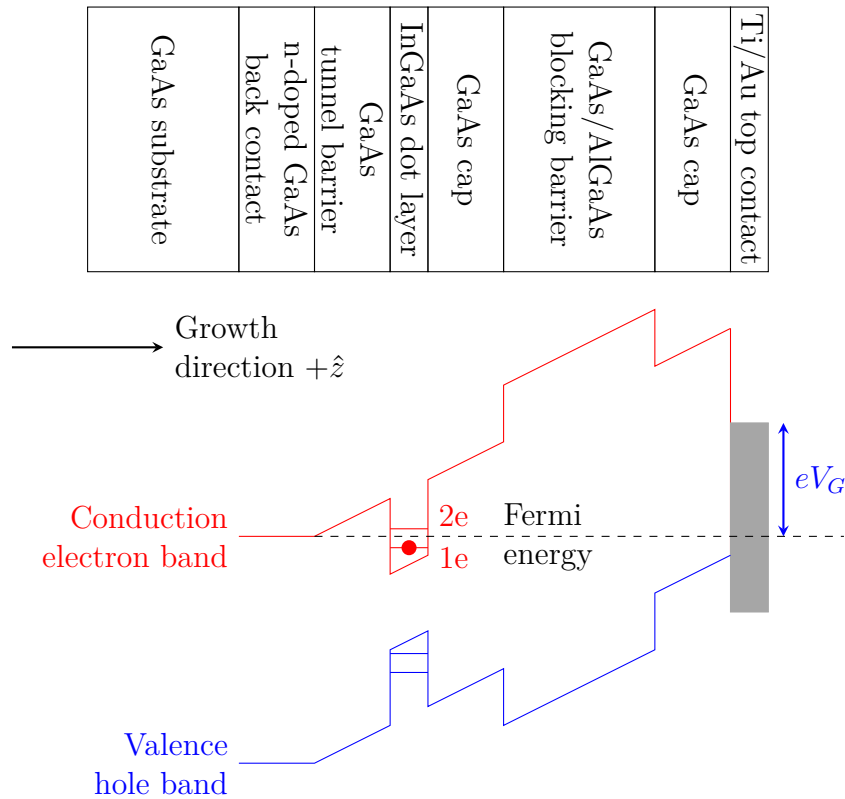


FIGURE 2.2: Schematic diagram of a typical Schottky diode heterostructure. Top panel shows the contents of each layer (not to scale). A highly n-doped region forms the back contact of the diode and provides a large number of free electrons at the Fermi energy. Bottom panel shows the conduction and valence band edges for each of the layers. This illustrates the confined QD states, the blocking barrier above the dot layer to prevent charges reaching the surface. As a gate voltage V_G is applied, the confined QD levels can be tuned with respect to the Fermi level, thus allowing electrons to tunnel into the QD from the n-doped layer. Adapted from [1]

overcoming the total internal reflection caused by the large refractive index of GaAs. The top surface is a partially reflective mirror, which allows some light to escape and improves the extraction efficiency of the signal.

Another important feature that can be achieved through fabrication techniques is charge tuning [71, 72] where the number of electrons and/or holes in the QD can be controlled by changing the bias voltage and embedding the system in a Schottky diode structure [73]. This involves growing a highly n-doped region below the dot layer separated by an undoped tunnelling barrier. The n-layer acts as a back contact for the diode and behaves as a metallic conductor with many free electrons (also referred to as the Fermi sea). Above the dots, a superlattice of alternating AlAs/GaAs is grown (which is faster to grow than an AlGaAs layer) and since AlAs has a larger bandgap than GaAs, it acts as a blocking barrier and prevents carriers flowing to the surface of the heterostructure (and prevents injection of electrons from the top contact). Finally, a layer of Titanium/Gold is grown

on the surface which acts as a top contact for the diode, which has to be semi transparent to allow for the QD signal to be collected.

A depiction of the heterostructure and the band gaps of the various layers of the diode are shown in Figure 2.2. When a gate voltage V_G is applied between the top contact and the back contact, the electric field in the vertical direction can be controlled and this allows the tuning of the QD energy level with respect to the Fermi level of the electrons in the Fermi sea (of the back contact). Depending on the voltage applied and the level of doping, when the Fermi level is close to the ground state of the QD, an electron can tunnel into the dot from the Fermi sea and the dot will be occupied by a single electron. By changing the bias, we can control the charge state of the dot so that it may be unoccupied, charged with a single electron or with 2 electrons. Under reverse bias ($V_G < V_{1e}$), the Fermi energy of the reservoir is below the lowest lying energy level of the QD and no electrons tunnel into the dot. As the forward bias is raised to $V_{1e} \leq V_G \leq V_{2e}$, one electron can tunnel into the dot because the lowest QD level is below the Fermi energy (this configuration is shown in Figure 2.2 where the dot is occupied by a single electron). Further electrons are blocked by the Coulomb repulsion of the electron that is already present in the dot. A further forward voltage of $V_G > V_{2e}$ is required to overcome the effect of this “Coulomb blockade” and then a second electron can also tunnel into the dot [74].

2.2 Electronic states and optical properties of quantum dots

Quantum confinement of the carriers in the QD region occurs because of a mixing of two different materials with different bandgaps. The bandgap of pure GaAs bulk material at liquid helium temperatures is ≈ 1.52 eV [75]. The bandgap of the InGaAs QD region (and hence the confinement potential) depends strongly on the ratio of In to Ga [76] with more indium reducing the band gap and also depends on the strain distribution and the temperature [77, 78]. At low temperatures, the direct bandgap of pure InAs is ≈ 0.43 eV [79]. The structure of the band alignment between InGaAs and GaAs is of type I, meaning that the conduction band (CB) edge of the QD region is lower compared to the bulk GaAs and the valence band (VB) edge is higher, both of which act to reduce the bandgap and provide confinement for both electrons and holes. In the InGaAs region, discrete atom-like energy levels are observed as opposed to the continuous band-like density of states in the bulk semiconductor.

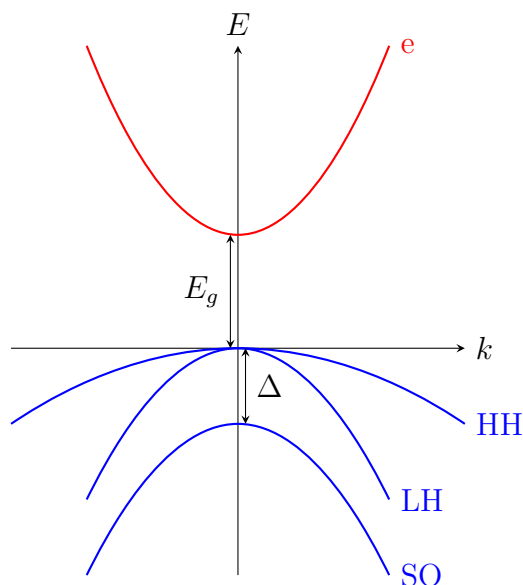


FIGURE 2.3: Band structure diagram of a bulk GaAs semiconductor near the centre of the Brillouin zone. The conduction band (red) only has a single band whose minima is separated in energy with the valence band edge (blue) by a bandgap E_g . There are 3 sub bands in the valence band - the heavy hole (HH), the light hole (LH) and the split off (SO) band which is offset by the spin orbit splitting Δ of a few hundred meV. The HH and LH bands are degenerate at the the Γ point ($k = 0$) but for $k \neq 0$, the LH band gets increasingly further in energy than the HH band with respect to the conduction band edge.

The CB is created by the underlying highest unoccupied orbitals of the atoms that form the semiconductor. The bands of energy form when the individual atoms are brought close together like in a semiconductor lattice and their discrete atomic levels become continuous bands of allowed energies. In the case of III-V materials, the CB contains predominantly s -type electrons with no orbital angular momentum ($\hat{\mathbf{L}} = 0$) and the VB has predominantly hybridised p -type electrons (or holes if the electron has been excited to the CB) with angular momentum $\hat{\mathbf{L}} = 1$ [10, 80] and some contribution from the d -orbitals [81]. The total angular momentum ($\hat{\mathbf{J}}$) is the sum of the orbital ($\hat{\mathbf{L}}$) and spin ($\hat{\mathbf{S}}$) angular momentum:

$$\hat{\mathbf{J}} = \hat{\mathbf{L}} + \hat{\mathbf{S}}. \quad (2.1)$$

By choosing the quantization axis to be parallel to the QD growth axis ($+\hat{z}$), the total angular momentum of the CB electron is simply $j_e = s_e = 1/2$ with a projection $m_{j,e} = \pm 1/2$, which corresponds to the spin up/down electron states (which shall hereby be labelled \uparrow / \downarrow).

For the VB hole, the situation is more complex because there are 3 distinct projections $m_{l,h} = [1, 0, -1]$ for a $l_h = 1$ state. Now, because the orbital angular momentum is no longer zero, the effects of the spin-orbit interaction dictate the band structure for the hole states. The spin-orbit interaction [80] originates from the fact that if the electron moves with respect to some potential (such as the electric field due to the nucleus), it will experience an effective magnetic field acting on its magnetic moment. This field is parallel to the orbital angular momentum of the electron and it shifts the energy of the electron magnetic moment depending on the orientation of the electron spin¹. The spin-orbit interaction has a form that is proportional to $\hat{\mathbf{L}} \cdot \hat{\mathbf{S}}$, so the spin $\hat{\mathbf{S}}$ and orbital momentum $\hat{\mathbf{L}}$ are inherently linked and the only conserved quantity now is the total angular momentum $\hat{\mathbf{J}}$ for $J = 3/2$ particles.

The eigenvalues of $\hat{\mathbf{J}}$ for the holes are $j_h = 3/2$ and $j_h = 1/2$ and each of these states have spin projections of half-integer values. For the $j_h = 3/2$ band, the projections may be $m_{j,h} = [+3/2, +1/2, -1/2, -3/2]$ and for the $j_h = 1/2$ band, also referred to as the split-off (SO) band, $m_{j,h}^{so} = [+1/2, -1/2]$. The split-off band is separated in energy from the $j_h = 3/2$ by the spin-orbit splitting of $\Delta \approx 350$ meV for InGaAs QDs [82]. Furthermore states with $m_{j,h}^{hh} = [+3/2, -3/2]$ in the $j_h = 3/2$ sub band are referred to as heavy hole (HH) states and those with $m_{j,h}^{lh} = [+1/2, -1/2]$ and $j_h = 3/2$ are called light holes (LH). In the bulk semiconductor, the HH and LH states are degenerate at the centre of the Brillouin zone (also referred to as the Γ point where $k = 0$, see Figure 2.3). But in self assembled QDs, the degeneracy is lifted due to strain and quantum confinement effects and typically there is a HH-LH splitting E_{HL} of several tens of meV [10]. The lowest energy state (ground state) is mainly of HH type (though can have a light hole character in some cases[83]) and transitions involving the CB electrons and the HHs are the most important and dominant interactions, but anisotropy in the shape and rotational symmetry breaking [84, 85] can cause HH-LH mixing and transitions to the light hole states are possible with different probabilities [5].

To summarize the VB states, the holes are split into 3 sub-bands where the split-off band can usually be neglected because it is relatively far in terms of energy from the heavy hole/light hole bands. In self assembled QDs, the heavy hole band is the ground state and is the most important when considering optical transitions with the CB electron, but there can be significant mixing between the heavy hole and light hole states due to asymmetry in the growth process.

¹in Atomic Physics, the spin-orbit interaction is responsible for the fine structure splitting of atomic energy levels

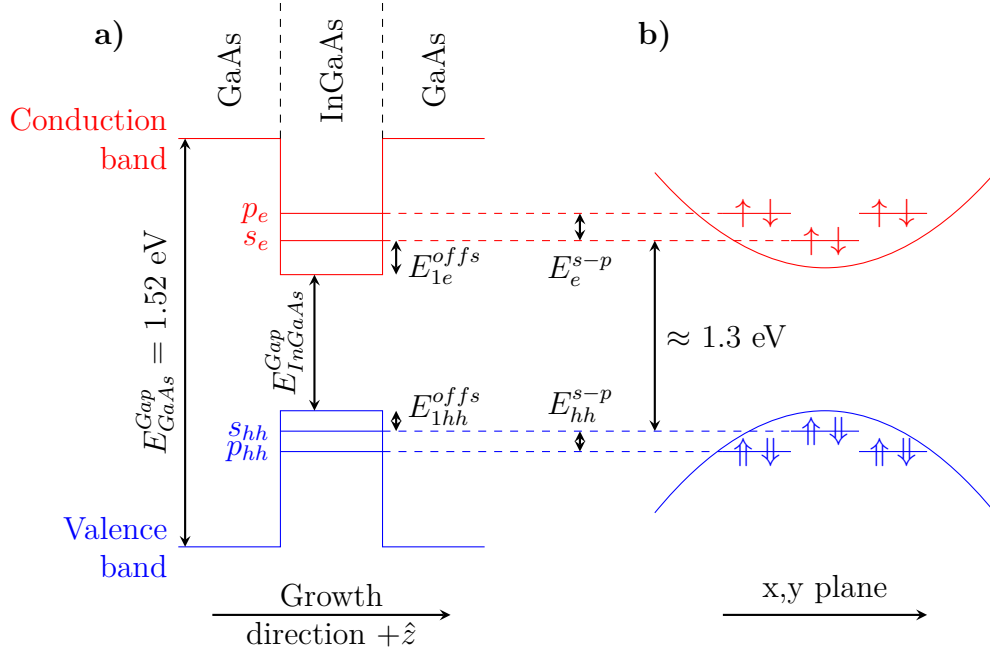


FIGURE 2.4: The band gaps and important energy offsets in the InGaAs/GaAs self assembled quantum dot system at liquid helium temperatures. a) the confinement in the growth direction is strong and the potential acts like a finite square well leading to discrete energy levels. b) the confinement is weaker in the lateral x - y plane and can be treated as a 2D parabolic potential. Due to the cylindrical symmetry in the x - y plane, there are 1, 2, 3... pairs of opposing spin electrons or holes for the $s, p, d...$ states. Only the heavy hole states are considered in this figure. The electron ground state energy level is offset from the minimum in the InGaAs conduction band edge by $E_{1e}^{offs} \approx 400$ -500 meV and the heavy hole state is offset by $E_{1hh}^{offs} \approx 70$ -100 meV from the maximum in the valence band edge. The intershell separation between the s and p -shells are $E_e^{s-p} = 15$ -60 meV for the electron and $E_{hh}^{s-p} = 10$ -40 meV for the heavy holes. All values are approximate (from [2-4]) and the actual numbers vary significantly between individual dots.

As discussed in Section 2.1, the width of self assembled QDs is typically larger than the height by a factor of ~ 5 . So the confinement is much stronger in the growth direction [10] than the x - y plane and the confinement potential can be considered separately [2]. In the growth direction, the confinement can be approximately modelled by a finite square well and in the lateral dimensions, a 2D parabolic potential [86] can be used, which gives cylindrically symmetric orbitals (s, p, d etc.) similar to atomic energy levels except only in the two x - y dimensions. A summary of the band structure and the energy levels due to the confining potentials can be found in Figure 2.4. If we denote the energy levels as $s, p, d...$ in the vertical direction and treat the z confinement as a fixed energy offset, due to the cylindrical symmetry in the x - y plane, additional sub-shells are formed analogous to the atom. Considering the optically active configurations of these degenerate sub-shells

[87], an *s*-shell may accommodate 1 opposing spin pair of electrons (or holes), a *p*-shell can accommodate 2 spin pairs and a *d*-shell can hold 3 pairs.

2.2.1 Excitons and optical selection rules

As has been established thus far, self assembled QDs provide quantum confinement in all 3 dimensions to a nano-scale volume and thus create discrete atom-like energy levels for electrons and holes. At room temperature, this system would be overwhelmed by thermal excitations (phonons with energy $k_B T$, where $k_B = 1.38 \times 10^{-23}$ J/K is the Boltzmann constant and T is the temperature in Kelvin) which would promote electrons to the higher energy states. For InGaAs/GaAs and GaAs/AlGaAs systems, the electrons and holes would escape from the dot entirely. All our experiments (see Section 3) are performed at liquid helium temperatures of 4 K and such cryogenic temperatures (typically < 50 K) ensure that the spacing between the discrete energy levels are sufficiently larger than the thermal energy of the electrons. So if a single electron or hole is generated within the QD it will only occupy the lowest energy states.

The InGaAs/GaAs QD system used in this work contains direct bandgap semiconductors and so interact strongly with photons of light without the need to absorb additional energy from the crystal in terms of phonons. The system may be driven “resonantly” where a photon (with energy equal to the difference in energy between the two levels) excites an electron from the VB to the CB leaving behind a heavy hole in the VB. The bound pair of electron and hole is called an exciton and can be treated as an electrically neutral quasi-particle in its own right. The main reason the individual electron and hole are treated as an exciton and not separate is because of the strong confinement in the volume of the QD. This reduces exciton scattering and narrows the homogeneous linewidth (first seen in 1982 [88]) and in fact optical linewidths of QDs can be very narrow and reach the radiative lifetime limit [89]. There is an additional effect which is caused by the direct Coulomb and exchange interaction between the negatively charged electron and the positive hole. The Coulomb attraction is responsible for the exciton binding energy (and is enhanced by the QD confinement) which lowers the exciton transition energy by about 10-30 meV in InGaAs QDs [90, 91] and is considerably larger than the bulk binding energy of excitons (in GaAs, the binding energy is 4.2 meV [92]).

Another way in which the system may be populated optically is called “non-resonant” excitation, where a photon of higher energy than the QD resonance is absorbed and an electron-hole pair is created in higher order states such as the *p* (referred to as *p*-shell

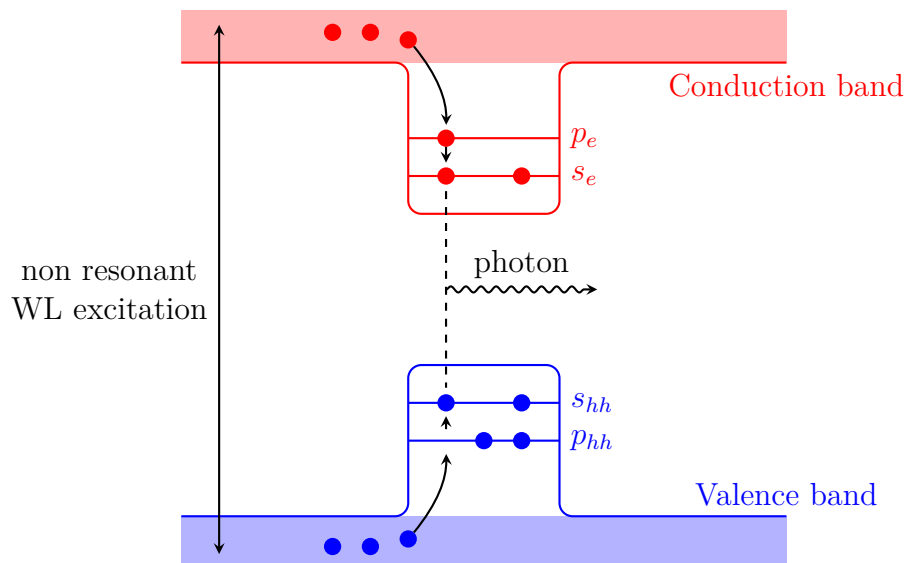


FIGURE 2.5: Schematic diagram to show the non-resonant excitation of carriers in a quantum dot. If non resonant excitation is applied in the wetting layer (WL), electrons from the valence band are excited into the conduction band leaving behind holes. Nearby carriers are quickly captured into the higher QD shells and subsequently relax into the lower shells non-radiatively. Finally the electrons/holes recombine and emit a photon which can be detected optically.

excitation) or d energy levels or even the wetting layer/barrier. These carriers are then captured by the QD very quickly (on a picosecond timescale) and this relaxation process occurs much faster than the radiative lifetime of the ground state of the QD exciton (nanosecond timescale [1]). The exciton can be detected optically as the carriers finally recombine and emit a photon with the same energy as the exciton's resonant excitation energy (see Figure 2.5). This is useful because the incoming non-resonant laser light will have a different energy (frequency) than the light emitted by the QD exciton and allows the observer to easily identify emission lines from single or multiple dots in non-resonant photoluminescence (PL) spectra. If the laser has the same energy as the dot, scattered laser light needs to be suppressed to differentiate it from the actual emission from the QD exciton. There are techniques to achieve this such as cross polarisation, where excitation is with a linear polarised laser and detection with an orthogonal linear polarisation would suppress the scattered laser and is used for example in detecting resonance fluorescence signals [93].

Due to parity and angular momentum conservation rules, only certain transitions are “allowed” when exciting a QD optically. Concerning parity [74], between the bands, only states with the same orbital angular momentum are allowed (such as $s_e \leftrightarrow s_{hh}$ or $p_e \leftrightarrow p_{hh}$) and within a band relaxation takes place between states whose orbital angular momenta differ by ± 1 ($s_e \leftrightarrow p_e$). The angular momentum of an electron in the QD is altered

when a photon is absorbed by a value of ± 1 depending on whether σ^+/σ^- (left or right circular) polarised light is used. This is because the photon itself has a total angular momentum of magnitude 1 and to conserve angular momentum, this photon must induce this change in angular momentum in the created exciton. Hence, the neutral exciton state (denoted X^0) can consist of two circularly polarised states whose spins are anti-parallel: the $J = m_{j,e} + m_{j,h}^{hh} = -1/2 + 3/2 = +1$ state (which can also be labelled $|\uparrow\downarrow\rangle$ ²) and the $J = m_{j,e} + m_{j,h}^{hh} = +1/2 - 3/2 = -1$ ($|\downarrow\uparrow\rangle$) and they are collectively known as “bright excitons” because they are optically allowed. The parallel spin configurations with $J = \pm 2$ (either $|\uparrow\uparrow\rangle$ or $|\downarrow\downarrow\rangle$) are called “dark excitons” and they are optically disallowed as they would require twice the angular momentum transfer of a single photon.

These selection rules discussed so far assume an idealised system. In practice, the self assembly process is unclean and leads to asymmetry in the dots (even of atomic scale [94]) and significant HH-LH mixing can occur (as discussed in Section 2.2) and also the QD quantization can be tilted slightly with respect to the incoming laser. Therefore these rules are relaxed in a real system and forbidden transitions can be observed [4] such as the dark neutral exciton states using low power optical excitation [59].

2.2.2 Exciton fine structure

Fine structure in the ground state exciton occurs due to the exchange interaction between the electron and the hole spin [4]. The fine structure is also affected by the Zeeman interaction when an additional field is applied and furthermore by the nuclear spins via the Overhauser shift, but we will limit our discussion here to an unpolarised nuclear spin bath. The effect of the exchange interaction takes into account the orientation of the spins and adds correction terms to the energy level diagram through shifts and splittings of the exciton states.

Asymmetry in the self assembly process (even at an atomic scale) can cause an irregular elongation in the shape of a real QD and it causes mixing of the two bright excitons and the two dark excitons due to the exchange interaction [5]. So at zero external magnetic field, the pure circularly polarised states are mixed together and the total angular momentum is no longer a good quantum number. The bright exciton states become linearly polarised and are not degenerate with the following eigenstates for the bright excitons

²Here the single arrows $\uparrow\downarrow$ represent the electron spin with spin projection $s_z = 1/2$ and the double arrows $\uparrow\downarrow$ represent the heavy hole spins with projection of the total momentum $j_z = 3/2$

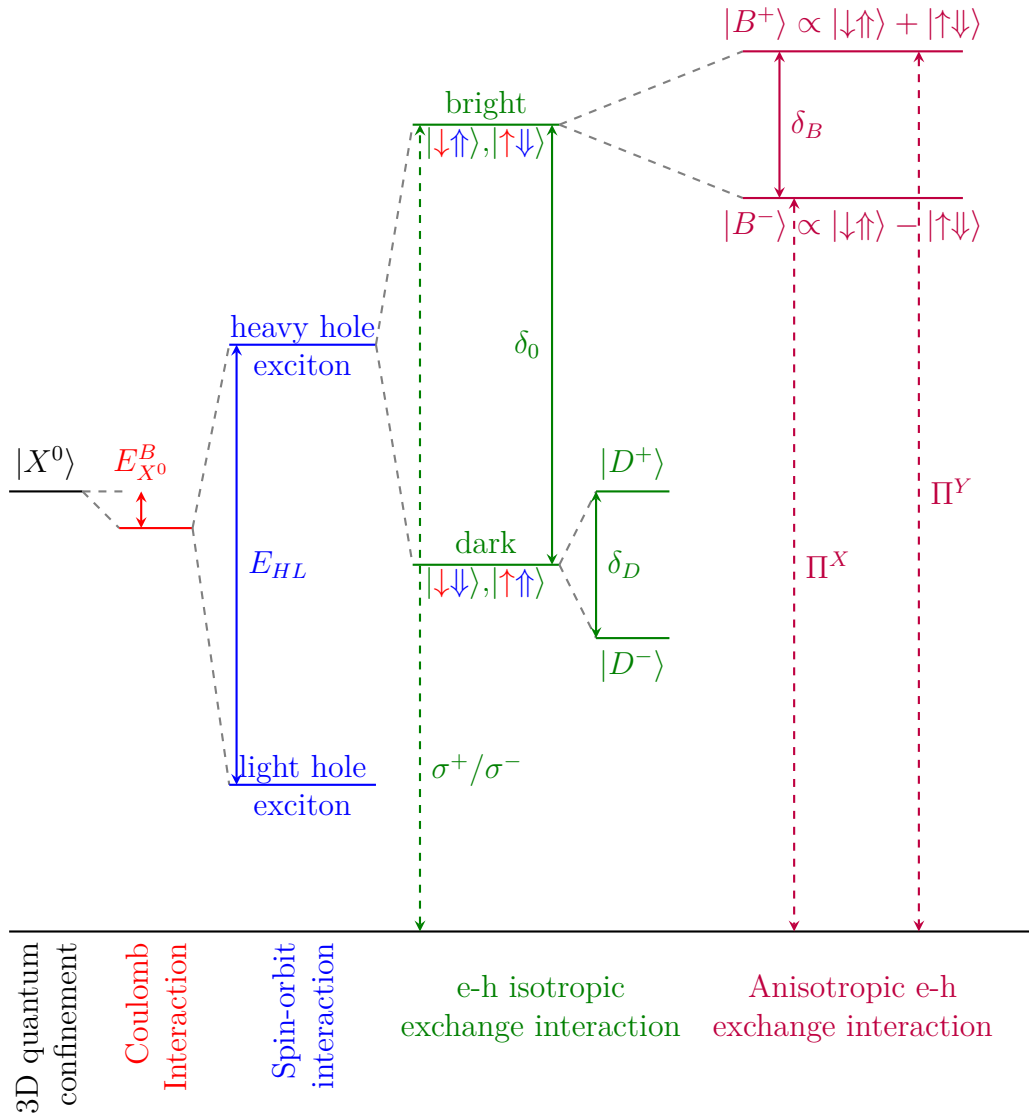


FIGURE 2.6: Correction terms and fine structure of the neutral exciton in self assembled QDs (not to scale). Quantum confinement in the dot creates discrete energy levels and the neutral exciton is formed when a single electron-hole pair populates the dot. The Coulomb interaction lowers the exciton transition energy by the exciton binding energy $E_{X^0}^B = 10 - 30$ meV in InGaAs dots. The spin-orbit interaction (caused by reduced symmetry) splits the p -type hole bands into the heavy hole (HH) and light hole (LH) states with a HH-LH splitting E_{HL} of several tens of meV. The exchange interaction between the electron and hole causes the splitting of bright (antiparallel spins that are optically active) and dark (parallel spins that do not interact with photons) exciton states. The isotropic part splits the bright states from the dark by the electron-hole exchange energy $\delta_0 = 100 - 300$ μeV and mixes the dark states with splitting $\delta_D = 0 - 100$ μeV . The anisotropic exchange interaction, which changes considerably based on asymmetry in the formation of the dot, causes the fine structure splitting between the bright excitons $\delta_B = 40 - 200$ μeV [5]. The pure bright states $|\downarrow\uparrow\rangle$ and $|\uparrow\downarrow\rangle$ are circularly polarised (σ^+/σ^-) but due to the mixing of the states, the observed bright exciton states at zero external magnetic field are linearly polarised (Π^X/Π^Y).

$$|B^\pm\rangle = \frac{1}{\sqrt{2}}(|\downarrow\uparrow\rangle \pm |\uparrow\downarrow\rangle), \quad (2.2)$$

and dark excitons

$$|D^\pm\rangle = \frac{1}{\sqrt{2}}(|\downarrow\downarrow\rangle \pm |\uparrow\uparrow\rangle). \quad (2.3)$$

Two types of exchange interaction may be considered: a short range isotropic interaction which is characterized by the probability of finding the electron and hole in the same part of space and a long range anisotropic interaction where the electron and hole are not in the same space. The isotropic part is present in all dots and gives rise to a splitting between the bright and dark exciton pairs called the electron-hole exchange energy $\delta_0 = 100 - 300 \mu\text{eV}$. It also creates a small splitting between the two dark exciton (D^+ and D^-) states $\delta_D = 0 - 100 \mu\text{eV}$. The anisotropic part of the exchange interaction varies strongly from dot to dot and splits the two bright exciton states (B^+ and B^-) by the fine structure splitting $\delta_B = 40 - 200 \mu\text{eV}$.

The effects of the exchange interaction on the energy levels of the neutral exciton are summarized in Figure 2.6 alongside the effect of the spin orbit interaction from Section 2.2. Optical emission of the biexciton state also shows a fine structure splitting at zero magnetic field but unlike the exciton (due to the initial state of the transition), it arises from the final X^0 state of recombination [4]. The charged trion states show no fine structure splitting at zero magnetic field. The exchange and coulomb interactions do renormalise the transition energies of the trions [10], but because the initial state is a single electron or hole and it interacts with a spin singlet pair of holes or pair of electrons, according to Kramer's degeneracy theorem [5, 95], there is no exchange energy.

2.2.3 Charged excitons and biexcitons

Additional types of exciton can be formed within self assembled QDs by generating further carriers in the QD. The dot may naturally be occupied by an extra electron or hole by growing the appropriate doping layer near the dot and with the appropriate doping concentration and tunnelling barrier, the carriers can tunnel into the QD so that there is on average one additional electron/hole [96, 97]. Alternatively, the dots can be tuned into various charge states by adjusting the voltage in a diode structure and changing the Fermi level of the sea of electrons relative to the QD energy [71, 72] (see Section 2.1).

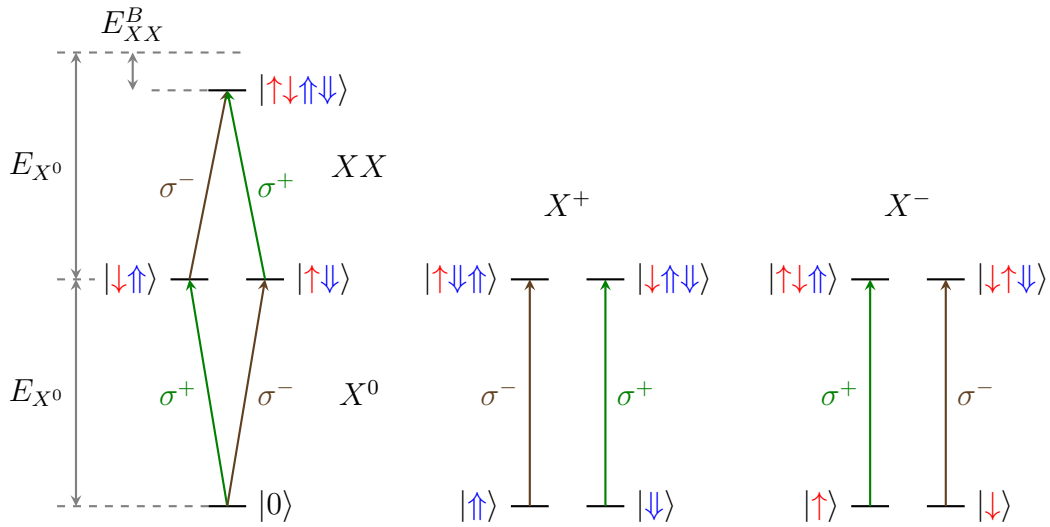


FIGURE 2.7: Illustrative energy level diagram of the various exciton types in a quantum dot. The electron spin is represented by a red single arrow and hole spin by a blue double arrow. The biexciton (XX) to exciton (X^0) cascade is shown on the left panel and the XX state is not at twice the X^0 energy with respect to the ground state because of the biexciton binding energy E_{XX}^B caused by the Coulomb interaction. The states here are shown in a circular polarisation basis which is the case for large external magnetic fields in Faraday configuration. The middle panel shows the two possible configurations for the positive trion X^+ and the right panel shows the negative trion X^- . Each spin state for the trions couples to only one circular polarisation of light. The energies are not to scale and unlike the schematic energy levels shown here, the transitions of the trion states are shifted in energy with respect to the X^0 transition.

The different types of excitons are summarized in Figure 2.7. The lowest energy states in the CB and VB of the QD can both contain two carriers (as long as they have opposite spin projections), so it is possible to form a 4-particle state known as a biexciton (called XX or $2X$, $|\uparrow\downarrow\uparrow\downarrow\rangle$) with a total spin $J = 0$. It is not possible to go directly from the biexciton state to the ground state due to the selection rules. A single electron-hole pair of the biexciton recombine to form the neutral exciton X^0 which can then subsequently recombine to the ground state. Also, the energy difference from the XX to X^0 transition is less than that of the X^0 recombination energy because in the same way that an exciton forms, the Coulomb interaction between the two excitons leads to a biexciton binding energy. Since the biexciton state feeds into the exciton state, it can only be created by high optical excitation powers. So in a photoluminescence spectrum XX appears at lower energies to the X^0 line (by a few meV in InGaAs dots) and has a strong (quadratic) dependence on the optical power for above bandgap excitation [6].

Using tunnelling techniques, a single electron may occupy the QD ground state and this allows for the manipulation and study of single carriers. When such a QD is excited optically, an additional electron hole pair is generated and this leads to the formation of

a different type of exciton known as the negatively charged trion (X^- , such as $|\uparrow\downarrow\uparrow\rangle$ or $|\downarrow\uparrow\downarrow\rangle$). The QD may initially contain an extra hole instead and this creates a positively charged trion (X^+ , such as $|\uparrow\downarrow\uparrow\rangle$ or $|\downarrow\uparrow\downarrow\rangle$). The trion states interact with opposite circular polarisations of light, so it is possible to “pump” the system into a particular spin state by repeatedly injecting photons of one polarisation. The charged trions are shifted in energy from the X^0 transition line because of the different magnitudes of the Coulomb interaction felt by the carriers. The X^- line is found towards lower energies (by a few meV) and the X^+ line can vary but is usually found towards higher energies for InGaAs QDs [98, 99].

2.2.4 Quantum dots in electric fields

The energy level structure and the selection rules discussed so far were for single QDs without the influence of external fields. The excitons in self assembled QDs are influenced by both electric and magnetic fields. Here we start by looking at the effect of a DC electric field.

Due to imperfections in the self assembly process, Ga atoms are not evenly distributed across the InGaAs QDs. The electron and hole in a QD are vertically aligned in space with the hole being localized towards the top of the dot which is rich in In and the electron found towards the bottom [100]. So typically a quantum dot possess a finite permanent electric dipole moment p even when there is no external electric field ($F = 0$).

The DC electric field F modifies the band structure of the layers surrounding the QD - as an illustration, see Figure 2.2. The bending of the bands alters the distance between the hole and the electron thus changes the emission energy. The carriers are still strongly localised because of the difference in bandgap between the InAs QD layer and the surrounding GaAs. The shift in the transition energy with electric fields is called the quantum confined Stark effect (QCSE) and was first observed in 1984 in semiconductor materials [101]. The energy shift ΔE_{QCSE} has both linear and quadratic terms and can be written [102]

$$\Delta E_{QCSE} = E_0 - p \cdot F - \beta F^2, \quad (2.4)$$

where E_0 is the energy at zero electric field, and β is the electric polarisability in the direction of the field. This equation was used to fit the neutral exciton line in the p-i-n diode sample (see Section 3.1.2) used in this work and can be seen in Figure 2.8. As the bias in this diode structure is changed, the shift due to the QCSE is clearly observed.

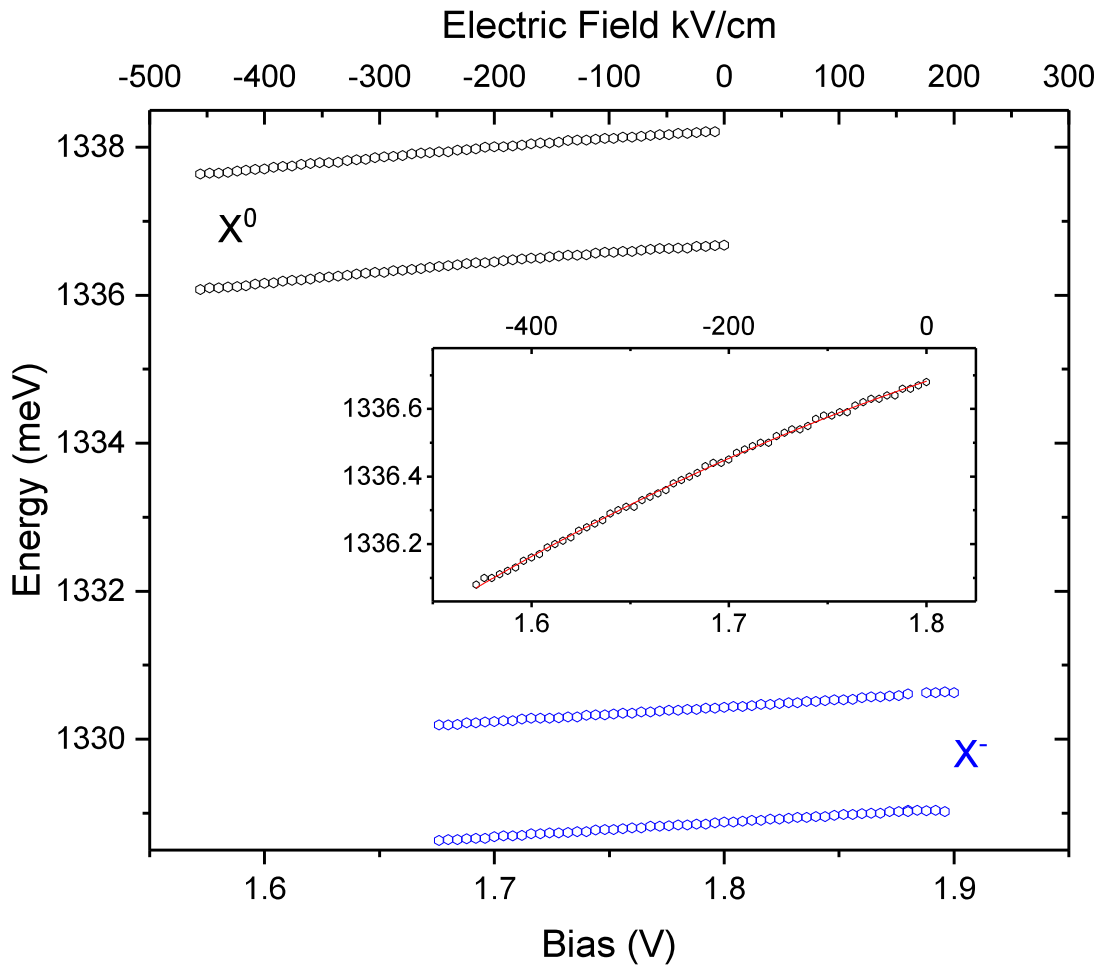


FIGURE 2.8: Effect of the electric field on the exciton transitions measured using the diode sample used in this work. As the bias is changed, the different charged states of the dot (X^0 and X^-) are observed and the plotted datapoints are the energies of the peaks as the bias is changed. This bias dependent photoluminescence spectra was taken at an external magnetic of 8T in Faraday geometry and using a low power non-resonant excitation so there are two Zeeman split components of each exciton. As the electric field changes, it can be seen that the energies of all 4 lines are shifted (mostly in a linear fashion but a small quadratic curvature is visible). The inset shows a close up of the low energy X^0 line along with a quadratic fit (fitting parameters are shown in Section 3.1.2) of the quantum confined Stark effect.

The QCSE can be used to find the separation of the electron and hole [100] but the main application comes from its ability to tune the transition energy. The range of tuning is limited by the electron and hole tunnelling out of the QD before they can recombine but it is possible in some diode devices with large bandgap barriers to observe upto 25 meV Stark shifts [103]. The tuning is of fundamental interest in various applications such as being used to create interference between two remote QDs [104] or bringing a QD into resonance with a cavity [105].

An AC electric field may also be used to shift the energy of QD transitions. This is usually

applied using a high power (quasi-) resonant laser and the shift depends on the frequency and strength of the AC field. The important aspect of this so-called “optical Stark effect” is that the shift depends on the polarisation of the transition and can be used to remove the fine structure splitting by only shifting one of the eigenstates [106].

2.2.5 Quantum dots in magnetic fields

In an external magnetic field, the individual spin components are split due to the Zeeman effect in which the exciton’s spin interacts with the external \mathbf{B} field. The general form of this Zeeman interaction [107] between an electron (S_e) and heavy hole (J_h) spin with a magnetic field in an arbitrary direction can be written

$$\hat{\mathcal{H}}_{Zeeman} = \mu_B \sum_{i=x,y,z} \left(g_{e,i} S_{e,i} - \frac{g_{h,i}}{3} J_{h,i} \right) B_i, \quad (2.5)$$

where μ_B is the Bohr magneton and g_e and g_h are the electron and hole g-factors. The different exciton spin components are split in energy depending on their alignment with the magnetic field. There is also a spin-independent shift of the exciton states to higher energy in a quadratic fashion with respect to increasing the magnetic field. This is called the diamagnetic shift [108] and is caused by the squeezing of the wavefunction due to strong geometrical confinement and is characterized by the diamagnetic constant γ_2 .

The orientation of the magnetic field is very important and we can characterize the observations into two sets of geometry. The first type is called “Faraday geometry” and describes the situation where the magnetic field is oriented parallel to the optical axis ($+\hat{z}$). All experimental work presented in this thesis where an external magnetic field was applied, was done in Faraday geometry and for convenience, the optical path for the excitation laser and collection of the signal was also aligned to $+\hat{z}$. The second type is called “Voigt geometry” and here the external magnetic field is perpendicular to the growth axis.

A summary of the effects of an external magnetic field on the energy levels of a neutral exciton in both Faraday and Voigt configurations is given in Figure 2.9. The field applied along the growth axis gradually transforms the eigenstates that are initially linear at zero field into the circularly polarised components $|+1\rangle = |\downarrow\uparrow\rangle$ and $|-1\rangle = |\uparrow\downarrow\rangle$. This happens when the effect of the Zeeman splitting becomes larger than the fine structure splitting $\Delta E_{Zeeman} > \delta_B$. We can explicitly write out the emission energies of the excitonic states in Faraday geometry. For the bright excitons,

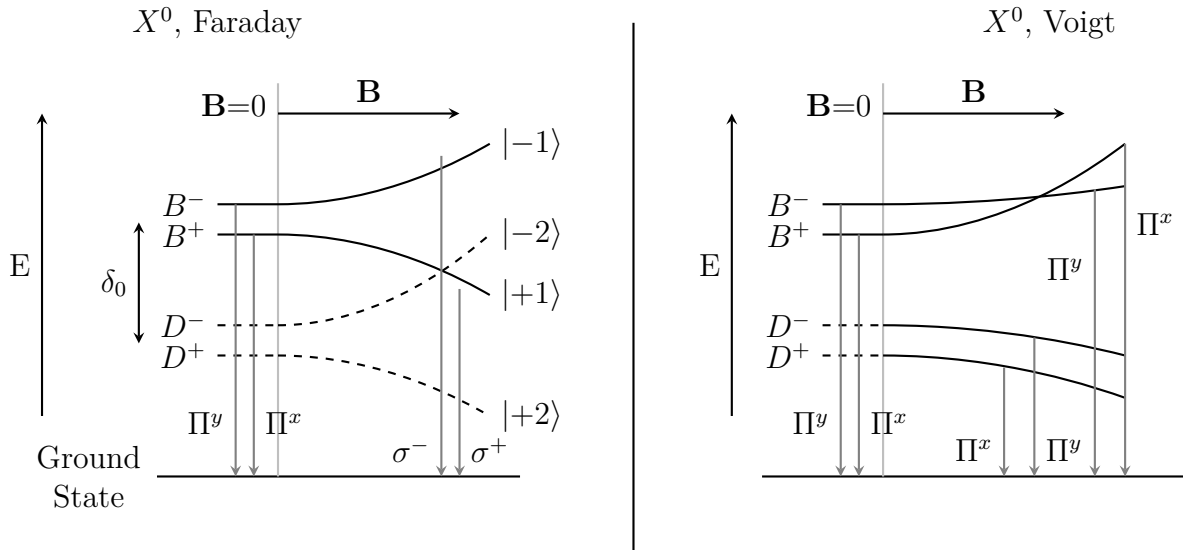


FIGURE 2.9: Schematic diagram illustrating the effect of an external magnetic field (\mathbf{B}) on the fine structure of a neutral exciton X^0 . At 0 field, the bright states B^\pm are split from the dark states D^\pm by energy δ_0 due to the isotropic exchange interaction. The eigenstates B^+ or B^- are linearly polarised (Π^x, Π^y). In Faraday geometry (field along optical axis), the bright states B^\pm are split into pure states $|\pm 1\rangle$ (eg. $|+1\rangle = |\downarrow\uparrow\rangle$) which are circularly polarised (σ^+, σ^-), while the dark states are optically forbidden. In Voigt geometry (field perpendicular to optical axis), both bright and dark states become optically active with linearly polarised components. Adapted from [6].

$$E_B = E_0 + \frac{\delta_0}{2} \pm \frac{1}{2} \sqrt{\delta_B^2 + \mu_B^2 (g_{h,z} - g_{e,z})^2 B_z^2 + \gamma_2 B_z^2}, \quad (2.6)$$

and for dark excitons

$$E_D = E_0 - \frac{\delta_0}{2} \pm \frac{1}{2} \sqrt{\delta_D^2 + \mu_B^2 (g_{h,z} + g_{e,z})^2 B_z^2 + \gamma_2 B_z^2}, \quad (2.7)$$

where E_0 is the band gap energy of the QD at zero field, δ_0 is the electron hole exchange energy, δ_B (δ_D) is the bright (dark) exciton fine structure splitting. Note that we use these equations to calculate the g factors for the II-VI CdTe/ZnTe QD system in Chapter 5.

By contrast, in Voigt geometry, the in-plane field mixes the bright and dark states as there is no longer a rotational symmetry and the dark states can now be observed. There are no longer clear bright and dark states and instead there are 4 linearly polarised carrier states.

Typically, the g-factors do vary from sample to sample because they depend on the size, shape, strain and chemical composition [109]. The magnitude of the g-factors for the electron and hole in the InGaAs QDs have previously been measured to be $|g_{e,z}| = 0.60$ and $|g_{h,z}| = 0.53$ in Faraday geometry [110]. In Voigt geometry, it can be seen that the electron

g-factor is similar ($|g_{e,x}| = 0.54$) but the hole g-factor is much smaller ($|g_{h,x}| = 0.08$) and this is due to the anisotropic confinement in QDs and depends on its shape [110].

It is important to note that for non-resonant excitation and using a Faraday configuration, it is possible to initialize the spin state of a carrier. If a trion state is used, such as X^- , the two zeeman split components are spectrally separated and the spin state can be identified as it only couples to one circular polarisation of light. This allows for the spin pumping scheme by repeatedly injecting photons of one circular polarisation for the preparation of a spin state to a high fidelity [111]. This is in contrast to the Voigt configuration where both vertical and horizontal transitions are allowed and a spin pumping mechanism is only possible with resonant excitation [1].

2.3 Interactions with nuclear spins in quantum dots

The QD system described thus far has concentrated on the exciton spin states and it has been implied that the system is well isolated due to the strong confinement of the carrier. In a real QD system however, the wavefunction of the trapped electron can penetrate significantly into the surrounding material and also impurities and trapped charges near the dot can interact with the dot carrier. But primarily the most important interaction in the InGaAs self assembled QD system is with the surrounding nuclear spins. There are approximately 10^5 nuclei in a single dot and all of them carry a quadrupolar nuclear spin. This creates the central spin problem [10] where a large and fluctuating nuclear spin bath is linked with the electron spin. This also applies to the II-VI QD system, but the nuclear isotopes have no quadrupolar moment (all spin $I = 1/2$) and there are fewer nuclei by a factor of about 100 (see Chapter 4). Here we look at some of the basic properties of the nuclear spins and their interaction with the electron and holes in a III-V QD.

We start by writing out the total Hamiltonian $\hat{\mathcal{H}}_T$ for nuclear spins in a solid [112]

$$\hat{\mathcal{H}}_T = \hat{\mathcal{H}}_Z + \hat{\mathcal{H}}_{hf} + \hat{\mathcal{H}}_{dd} + \hat{\mathcal{H}}_Q, \quad (2.8)$$

which contains four terms. Here, we will briefly describe the effects of each term in our QD system where the electron is confined and more general overviews can be found in the relevant texts [113, 114]. The first term is the Zeeman interaction for nuclei interacting with an external magnetic field pointing along the $+\hat{z}$ axis B_z (and is analogous to the Zeeman effect in Section 2.2.5 for the exciton) and can be written as

$$\hat{\mathcal{H}}_Z = - \sum_j \gamma_{N_j} I_z^j B_z, \quad (2.9)$$

where the sum is over all nuclei j in the QD and I_z is the nuclear spin. γ_N is the nuclear gyromagnetic ratio and is related to the nuclear magneton³ μ_N by $\gamma_N = g_N \mu_N / \hbar$, where g_N is the nuclear g-factor (we have set Planck's constant $\hbar = 1$). Since the nuclear magneton is much smaller than the equivalent factor for the electron (the Bohr magneton μ_B), the energy splitting of the nuclear spin states due to the Zeeman interaction is negligible with respect to the electron Zeeman splitting [10].

The second term $\hat{\mathcal{H}}_{hf}$ in Equation 2.8 is the hyperfine coupling of the electron and nuclear spins and is discussed in Section 2.3.1. The third term $\hat{\mathcal{H}}_{dd}$ describes the magnetic dipolar interaction between nuclei (see Section 2.3.2) and finally $\hat{\mathcal{H}}_Q$ is the quadrupolar coupling between nuclear spins and electric field gradients in QDs (see Section 2.3.3).

2.3.1 Coupling of electron and nuclear spins: the hyperfine interaction

In the field of Atomic Physics, the hyperfine interaction describes how the energy of a magnetic moment of a nuclear spin changes due to the presence of a magnetic field caused by the electron possessing an orbital (and spin) angular momentum. Here, we have a system where a trapped electron spin has a wavefunction which overlaps with a mesoscopic number of nuclear sites. The hyperfine Hamiltonian can be written as $\hat{\mathcal{H}}_{hf} = \hat{\mathcal{H}}_{hf}^{fc} + \hat{\mathcal{H}}_{hf}^{an} + \hat{\mathcal{H}}_{hf}^{orb}$, where the isotropic Fermi-contact part of the Hamiltonian is $\hat{\mathcal{H}}_{hf}^{fc}$, the anisotropic part $\hat{\mathcal{H}}_{hf}^{an}$ is a long range interaction and behaves like a dipole-dipole coupling, and $\hat{\mathcal{H}}_{hf}^{orb}$ is the orbital interaction. The contact part is dominant when there is a physical overlap between the periodic part of the Bloch wave function of the electron and the nuclear lattice site. This is important for s-shell orbitals such as the electrons in the conduction band of a QD where the orbital angular momentum is zero. The anisotropic part is more important for the hole spins in the valence band which occupy p-type bands which have only a small wavefunction amplitude at the site of a nucleus [10].

The Fermi-contact hyperfine interaction between an electron spin $S_z^e = \sigma^e/2$ ⁴ and the nuclei in a dot can be written [113, 115]

³which is defined in terms of the fundamental constants $\mu_N = \frac{e\hbar}{2m_p}$, where e is the charge of an electron and m_p is the mass of a proton

⁴where σ^e is the Pauli matrix operator

$$\hat{\mathcal{H}}_{hf}^{fc} = \frac{\nu_0}{2} \sum_j A_j |\psi(\mathbf{r}_j)|^2 (2I_z^j S_z^e + [I_+^j S_-^e + I_-^j S_+^e]), \quad (2.10)$$

where $\nu_0 = a_0^3$ is the volume of a unit cell and a_0 is the lattice constant, A_j is the hyperfine constant, I^j and \mathbf{r}_j are the nuclear spin and position of the j th nucleus and ψ is the normalized electron envelope wavefunction. The first term in the parentheses of Equation 2.10 shifts the energies of the electron spin and acts as an effective magnetic field felt by the electron [95]. This is called the Overhauser shift [116] and we will see that the reciprocal process also occurs, where the average electron spin acts as an effective magnetic field for each nucleus (called the Knight field [117]). The second term is the electron-nuclear spin flip-flop and this allows for the transfer of polarisation between the two systems and can lead to dynamic nuclear polarisation (DNP) [56], electron [118] or nuclear spin dephasing [55, 113].

The hyperfine constant A_j depends on the nuclear isotope and the electron wavefunction at the nuclear site $|\psi(0)|^2$ which depends on the material. It can be defined as [119, 120]

$$A_j = (2\mu_0/3)\hbar\gamma_{N_j}g_e\mu_B|\psi(0)|^2, \quad (2.11)$$

where μ_0 is the vacuum permeability, $g_e \approx 2$ is the free electron g-factor and μ_B is the Bohr magneton. The hyperfine constants and other important values are shown for various isotopes in Table 2.1.

In QDs, the hole spins are more robust than in a bulk semiconductor due to the strong confinement and discrete energy levels. The anisotropic part of the hyperfine interaction causes a dipole-dipole like interaction between the p -type hole spins S^h and the nuclear spins. For this to be energetically possible, there needs to be some amount of valence band mixing β (where $|\beta| \ll 1$) which mixes the heavy hole and light hole states [10]. As we have seen in Section 2.2, there is a HH-LH splitting E_{HL} of tens of meV in InGaAs QDs due to the spin-orbit interaction but valence band mixing can occur because of anisotropy in the shape of QDs. Now, a mixed spin state needs to be considered with a contribution from both heavy and light holes

$$\widetilde{\left| \pm \frac{3}{2} \right\rangle} = \frac{1}{\sqrt{1+|\beta|^2}} \left(\left| \pm \frac{3}{2} \right\rangle + \beta \left| \mp \frac{1}{2} \right\rangle \right). \quad (2.12)$$

The anisotropic part of the hyperfine interaction between the hole and nuclear spins can then be written [10]

$$\hat{\mathcal{H}}_{hf}^{an} = \nu_0 \sum_j \frac{A_j^h}{1 + \beta^2} |\psi(\mathbf{r}_j)|^2 \left(I_z^j S_z^h + \frac{|\beta|}{\sqrt{3}} [I_+^j S_-^h + I_-^j S_+^h] \right), \quad (2.13)$$

where A_j^h is the hole dipole-dipole hyperfine constant. This equation has a similar form to the contact hyperfine interaction but it has been shown that the hole coupling is much smaller $A_j^h/A_j \sim 0.1$ [121, 122]. Also, the constants A_j^h are negative for cations (In and Ga) and positive for anions (As) (from NMR data [122]) and an explanation of this phenomena is that there is a small contribution from the d -type orbitals in the valence band as well as the mainly p -type orbitals.

The nuclear orbital interaction $\hat{\mathcal{H}}_{hf}^{orb}$ describes the spin-orbit coupling between a non relativistic charged particle in the presence of a nuclear magnetic dipole [112]. It is another term that together with $\hat{\mathcal{H}}_{hf}^{an}$ affects carriers in the valence band (holes) that have a non-zero orbital angular momentum. The Hamiltonian can be written

$$\hat{\mathcal{H}}_{hf}^{orb} = \frac{\mu_0}{4\pi} \sum_j 2\mu_B \gamma_N \frac{\mathbf{L}_j \cdot \mathbf{I}^j}{|\mathbf{r} - \mathbf{r}_j|^3}, \quad (2.14)$$

where μ_0 is the permeability of free space and \mathbf{L}_j is the total orbital angular momentum of the hole and \mathbf{r}_j is the position of the nuclear site.

2.3.2 Nuclear magnetic dipole-dipole interaction

The most important interaction within the nuclear spin bath itself is the nuclear dipolar interaction where the magnetic moments of two individual nuclear spins interact. We have already seen a Hamiltonian of dipolar type when describing the anisotropic part of the hyperfine interaction $\hat{\mathcal{H}}_{hf}^{an}$ which was a dipolar coupling between the hole and nuclear spins. Here we describe the interaction between two nuclear spins I and J with gyromagnetic ratios γ_I and γ_J [112, 113],

$$\hat{\mathcal{H}}_{dd} = \frac{\mu_0}{4\pi} \sum_{i \neq j} \frac{\gamma_I \gamma_J}{r_{ij}^3} \left(\mathbf{I}^i \cdot \mathbf{J}^j - 3 \frac{(\mathbf{I}^i \cdot \mathbf{r}_{ij})(\mathbf{J}^j \cdot \mathbf{r}_{ij})}{r_{ij}^2} \right), \quad (2.15)$$

where r_{ij} is the displacement vector of one spin from another. This process allows the transfer of the nuclear polarisation through the material via dipole-dipole spin flips in a process called nuclear spin diffusion [10]. Due to this dipolar interaction, a nucleus will experience a weak fluctuating local magnetic field from the other nuclei. Through the non spin conserving (non secular) part of the dipolar Hamiltonian, the spin can be transferred to the crystal and in general not conserved [113]. But even at zero external magnetic field, the Knight field and the nuclear quadrupolar interaction can suppress the nuclear spin diffusion. This is because the resonance frequencies of each nucleus are shifted and the dipolar coupling strength may not be enough to induce a spin flip.

The strength of the dipolar coupling between nuclei decays inversely to the cube of the distance between nuclei. So the coupling is strong between adjacent nuclear sites and weak when the nuclei are further away. It is possible to have enhanced coupling between far away nuclei via a virtual transition with the electron spin and is a limiting mechanism to the lifetime of the nuclear spin polarisation at certain biases in a diode sample [7].

When a significant external magnetic field is applied, only the secular (spin conserving) part of the dipolar interaction is non-zero, as it commutes with the Zeeman Hamiltonian [112]. Hence, we obtain a static part $\propto I_z J_z$ and a flip-flop term $\propto [I_+ J_- + I_- J_+]$ that acts on nuclei of the same isotope. Only the homonuclear dipolar (same isotope) interaction remains at large fields because the Zeeman splittings are quite different between the different isotopes and so the heteronuclear dipolar interaction is suppressed.

2.3.3 Quadrupolar energy levels of nuclei in strained systems

In self assembled InGaAs QDs, all naturally occurring stable nuclear isotopes possess a quadrupolar moment Q because their nuclear spin quantum numbers are all $I > 1/2$. Due to the growth process of these dots being driven by strain, there are substantial local deformations. The local elastic strain tensor ϵ_{ij} gives rise to an electric field gradient (EFG) with traceless tensor V_{ij} and the two are related via the 4th rank gradient elastic tensor S_{ijkl} [123, 124]

$$V_{ij} \equiv \frac{\partial^2 V}{\partial x_i \partial x_j} = \sum_{k,l=1}^3 S_{ijkl} \epsilon_{kl}, \quad (2.16)$$

where V is the electrostatic crystal field potential. Note that the sum in Equation 2.16 is chosen to be over the axes x, y, z which are the cubic crystallographic axes (with the z

direction aligned to the growth direction [001]). For cubic crystals (such as the zincblende lattice in GaAs and InGaAs), there are only three independent components of the gradient elastic tensor S_{11} and S_{44} and the traceless property of V_{ij} [125], leads to a trivially related 3rd non-zero component $S_{12} = -S_{11}/2$. The components for the electric field gradient then become $V_{zz} = S_{11}\epsilon_B$ and $V_{xy} = 2S_{44}\epsilon_{xy}$ (along with cyclic permutations [126]) with biaxial strain defined as $\epsilon_B = \epsilon_{zz} - (\epsilon_{xx} + \epsilon_{yy})/2$.

Let us consider a situation where we take only the Zeeman and the quadrupolar interaction terms from Equation 2.8. This simplified scenario is suitable for understanding the self-assembled QD system where these two effects are dominant. The quadrupolar moment of the nuclei in QDs interact with the EFG and results in a specific set of energy levels and features in the magnetic resonance spectra [113, 127–129]. The Hamiltonian $\hat{\mathcal{H}}_N$, that describes the quadrupolar nuclear spin states of a single nuclear species in the presence of a static external magnetic field can be written

$$\hat{\mathcal{H}}_N = \hat{\mathcal{H}}_Z + \hat{\mathcal{H}}_Q. \quad (2.17)$$

Note that this Hamiltonian describes a single species unlike Equation 2.8 which is summed over all nuclear isotopes. The first term is the Zeeman interaction between nuclear spin $\hat{\mathbf{I}}$ and an external magnetic field \mathbf{B} ,

$$\hat{\mathcal{H}}_Z = -\gamma\hbar\hat{\mathbf{I}} \cdot \mathbf{B}, \quad (2.18)$$

where γ is the nuclear gyromagnetic ratio and \hbar is Planck's constant.

The second term is the quadrupolar Hamiltonian

$$\hat{\mathcal{H}}_Q = \frac{e^2qQ}{4I(2I-1)} \left(3\hat{I}_Z^2 - \hat{\mathbf{I}}^2 + \frac{\eta}{2}(\hat{I}_X^2 - \hat{I}_Y^2) \right), \quad (2.19)$$

where e is the charge of an electron, $q \equiv V_{zz}/e$ is the EFG parameter, Q is the electric quadrupole moment of the nucleus and $\eta = \frac{V_{XX}-V_{YY}}{V_{ZZ}}$ is the EFG asymmetry parameter. Note that Equation 2.19 is in the basis of X, Y, Z which are the principal axes (eigenvectors) for the symmetric EFG tensor V_{ij} (and is generally different from the x, y, z crystallographic axes used in Equation 2.16). Finally the EFG components satisfy $|V_{ZZ}| \geq |V_{YY}| \geq |V_{XX}|$ so $0 \leq \eta \leq 1$.

For the case of high magnetic fields (which is the case for the majority of experiments presented here), the Zeeman part of the Hamiltonian is the dominant effect and the quadrupolar part can be treated as a perturbation. In Faraday geometry, with a magnetic field B_z applied along the Oz axis, we define the angle between B_z and the EFG principal axis OZ to be θ and for simplicity, we assume cylindrical symmetry of the EFG so $\eta = 0$. Next, we introduce the Larmor ω_L and the quadrupolar frequency ω_Q (which characterize the strength of the Zeeman and quadrupolar interaction respectively) as

$$\omega_L = -\gamma B_z \quad \text{and} \quad \omega_Q = \frac{3e^2qQ}{\hbar 2I(2I-1)} \quad (2.20)$$

and by using second order perturbation theory[113], the energy difference between adjacent energy levels in zeroth, first and second order is given by

$$\Delta E^{(0)} = E_{I_z+1}^{(0)} - E_{I_z}^{(0)} = \hbar\omega_L \quad (2.21)$$

$$\Delta E^{(1)} = E_{I_z+1}^{(1)} - E_{I_z}^{(1)} = \frac{1}{2}\hbar\omega_Q(3\cos^2\theta - 1)(I_z + \frac{1}{2}) \quad (2.22)$$

$$\begin{aligned} \Delta E^{(2)} = E_{I_z+1}^{(2)} - E_{I_z}^{(2)} = & -\hbar\left(\frac{\omega_Q^2}{16\omega_L}\right)\sin^2\theta\left[I_z(2I_z+1)(17\cos^2-1)\right. \\ & + I(I+1)(1-12\cos^2\theta) \\ & + 4\cos^2\theta(5I_z^2+10I_z+6) \\ & \left. - (I_z^2+2I_z+\frac{3}{2})\right]. \end{aligned} \quad (2.23)$$

If there were no quadrupolar effects (using only the zeroth order term $\Delta E^{(0)}$), the nuclear resonance would purely be determined by the Zeeman interaction and there would be a single frequency at the Larmor frequency ω_L . If the EFG is uniaxial and pointing along B_z (i.e. $\theta = 0$), then $\Delta E^{(1)} = \hbar\omega_Q(I_z + \frac{1}{2})$ and $\Delta E^{(2)} = 0$, so there would simply be $2I$ equally spaced lines separated by ω_Q . In general $\Delta E^{(1)} \gg \Delta E^{(2)}$ and for the central transition (CT, $I_z : -\frac{1}{2} \leftrightarrow \frac{1}{2}$), $\Delta E^{(1)} = 0$, so the CT is only weakly affected in second order by the quadrupolar interaction. The side transitions (STs) are affected by both $\Delta E^{(1)}$ and $\Delta E^{(2)}$ but the the second order effect $\Delta E^{(2)}$ on the side transitions is negligible.

The effects of this perturbative approach on the energy level structure of a spin $I = 3/2$ isotope (such as ^{75}As , ^{69}Ga or ^{71}Ga) is summarized in Figure 2.10, where the first order quadrupolar correction to the frequency $\omega_Q^{(1)} = \Delta E^{(1)}/\hbar$. $\omega_Q^{(1)}$ is negative for $I_z = -3/2$ and positive for $I_z = +1/2$, hence the $-\frac{3}{2} \leftrightarrow -\frac{1}{2}$ ($+\frac{1}{2} \leftrightarrow +\frac{3}{2}$) ST appears on the low

(high) frequency side of the CT. The second order correction $\omega_Q^{(2)} = \Delta E^{(2)}/\hbar$ has only been shown for the CT and is much weaker than $\omega_Q^{(1)}$.

The quadrupolar interaction in self assembled QDs suppress the dipolar nuclear spin flips by changing the energy level spacing between adjacent nuclei. This reduces the nuclear spin diffusion in strained samples [130]. There is also a mismatch in the energy levels with dot nuclei compared to atoms in the surrounding bulk, which suppresses the nuclear spin diffusion from the dot to the surrounding material [10].

2.3.4 Overhauser and Knight fields due to hyperfine interaction

We have seen how the electron and nuclear spin systems in self assembled QDs are inherently linked via the strong confinement of the electron and the hyperfine interaction with the nuclei. The electron spin state can be initialized with circularly polarised light or with resonant optical excitation. The spin state is transferred to the nuclei through the hyperfine interaction and the polarised nuclear spins create an effective magnetic field (Overhauser field) that the electron experiences. The polarised electron also acts back on the nuclei via the Knight field. The system can be summarized as in Figure 2.11.

Since there are 10^5 nuclear spins interacting with the electron, we can consider the average nuclear spin polarisation $\langle I_z^j \rangle$ which provides an effective magnetic field of [10]

$$B_N = \frac{\nu_0 \sum_j A_j |\psi(\mathbf{r}_j)|^2 \langle I_z^j \rangle}{g_e \mu_B}. \quad (2.24)$$

So the total magnetic field felt by the electron is the sum of the external field and the Overhauser field $B_{\text{Tot}} = B_z + B_N$. This provides an additional shift in the electron energy level splitting (as well as the Zeeman splitting) known as the Overhauser shift (OHS) and can be written as

$$E_{OHS} = \hbar \omega_{OHS} = \mu_B g_e B_N. \quad (2.25)$$

Using these ideas, it is clear that the average nuclear spin polarisation can be probed by looking at changes in the Zeeman splitting of an exciton's optical transition lines. All of the experimental work presented here relies on optically detecting nuclear spin polarisation via changes in the OHS as the nuclear spins are manipulated using radiofrequency fields.

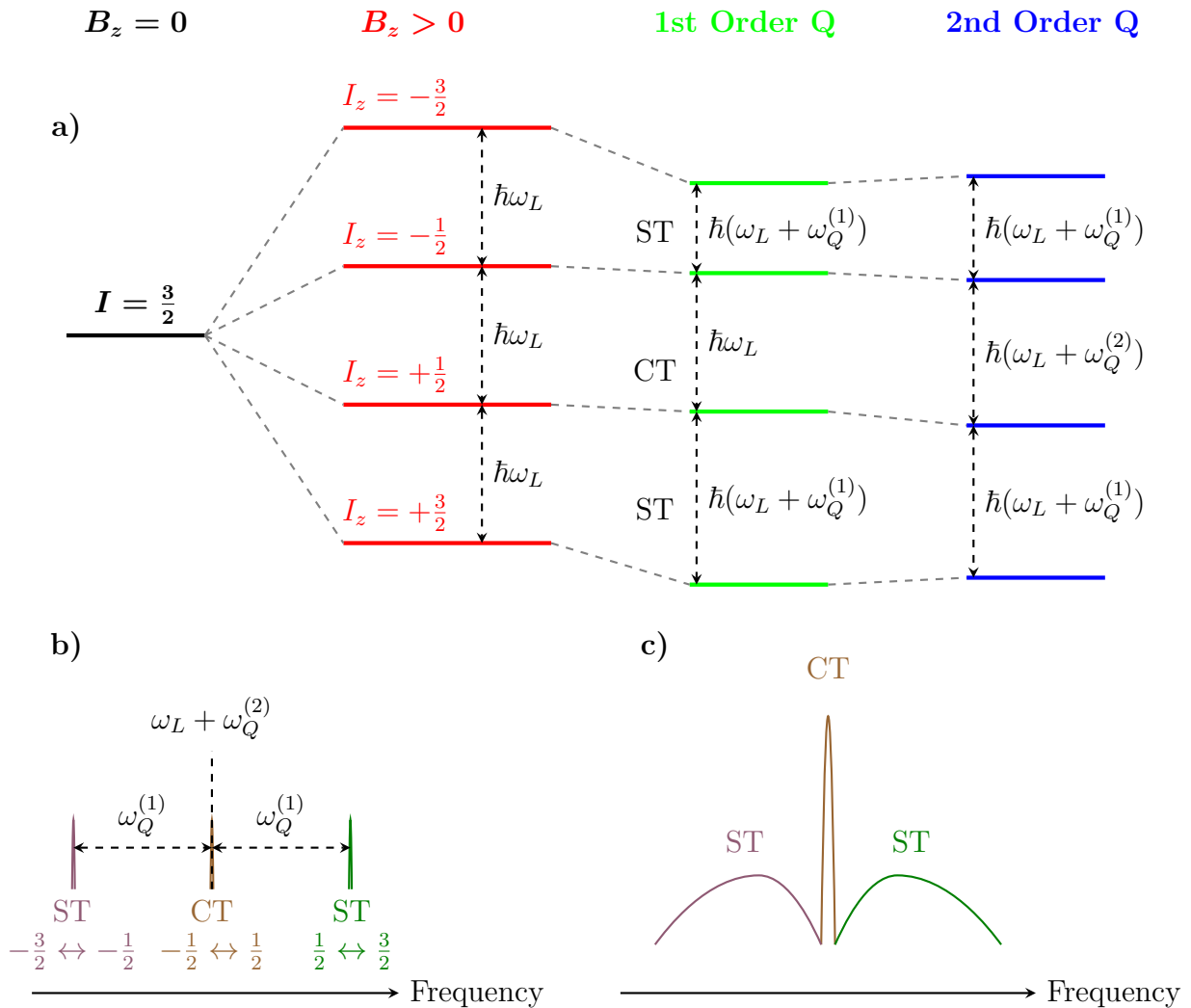


FIGURE 2.10: a) Energy level diagram for a single nucleus with spin $I = 3/2$. When a magnetic field B_z is applied, the degeneracy of the $I = 3/2$ is lifted and 4 states are observed equally separated by the Larmor frequency ω_L . Including the effects of the quadrupolar interaction perturbatively, the STs are strongly modified in first order ($\omega_Q^{(1)}$) whereas the CT is only affected weakly in second order ($\omega_Q^{(2)}$). b) Schematic diagram of the three observed peaks in the nuclear resonance spectrum of a single nucleus that occur due to the energy levels shown in a) for a spin $I = 3/2$ nucleus. c) Schematic diagram of the inhomogeneously broadened NMR spectra for a spin $I = 3/2$ isotope where the signal from all nuclei of a given isotope are summed. The linewidth of the CT is narrower than the ST for a wide range of magnetic fields because of the weak second order $\omega_Q^{(2)}$, but the STs are broad because of the large variation in $\omega_Q^{(1)}$ across the QD.

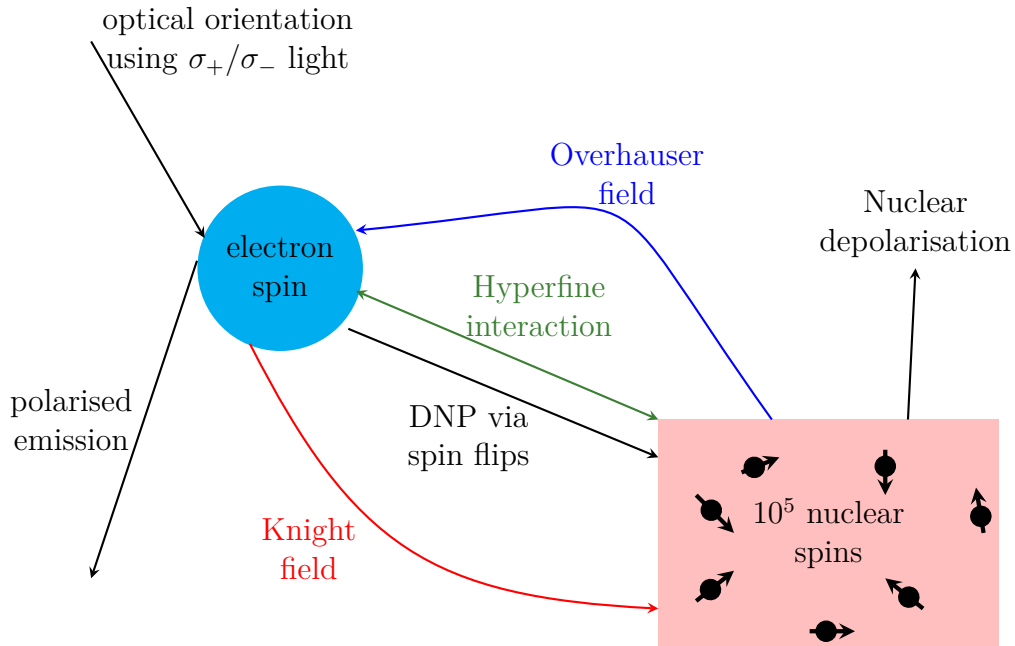


FIGURE 2.11: The quantum dot electron-nuclear spin system showing the reciprocal interaction between the electron and nuclear spins through the Overhauser and Knight fields caused by the hyperfine interaction.

The Knight field is the reciprocal part of the hyperfine interaction to the Overhauser field. As implied by Figure 2.11, the average electron spin $\langle S_z^e \rangle$ also acts as an effective magnetic field on the nuclear spins. We can write the time averaged Knight field as [10]

$$B_e = f_e \frac{\nu_0 A_j}{g_N \mu_N} |\psi(\mathbf{r}_j)|^2 \langle S_z^e \rangle, \quad (2.26)$$

which acts on an individual nuclear spin j and $f_e \in [0, 1]$ is the filling factor for the occupation of the dot by the electron. The hyperfine interaction energy of the Knight field is much smaller than the Overhauser field because the ratio $\mu_B/\mu_N \approx 2000$ and the Knight field is “split” among multiple nuclear spins. The amplitude of the Knight field varies with the electron wavefunction, so a nucleus near the centre of a dot experiences a larger Knight field acting on it than one near the edges. Experimental values for B_e are found to be in the mT range [131, 132].

Dynamic nuclear polarisation (DNP) is the process of building up the nuclear spin polarisation via the transfer of spin from the electron. In our self assembled dots, the electron spin polarisation is built up using a large optical excitation power and circularly polarised light. The electron then transfers its spin to the nuclei through the hyperfine interaction - specifically the spin flip-flop term. If the electron spin can be reinitialized at a sufficiently high rate, the nuclear spins in the QD can be aligned preferentially in one direction to

Isotope	Nuclear spin I	Natural Abundance %	Hyperfine constant A (μeV)	Gyromagnetic ratio $\gamma/2\pi$ (MHz/T)	Quadrupolar moment Q ($\times 10^{-30}$ Qm ²)
⁷⁵ As	3/2	100	43.5	7.315	31.4
¹¹³ In	9/2	4.3	56	9.365	79.9
¹¹⁵ In	9/2	95.7	56	9.385	81.0
⁶⁹ Ga	3/2	60.1	43.1	10.248	17.1
⁷¹ Ga	3/2	39.9	54.8	13.021	10.7
¹¹¹ Cd	1/2	12.8	-30	-9.07	-
¹¹³ Cd	1/2	12.22	-30	-9.49	-
¹²³ Te	1/2	0.89	-45	-11.23	-
¹²⁵ Te	1/2	7.07	-45	-13.55	-

TABLE 2.1: Important parameters relating to all of the nuclear isotopes found in the samples used in this work. The values are given for both the InGaAs system and for the CdTe/ZnTe system. Note that these are the stable naturally occurring isotopes which possess non-zero nuclear spin I . The hyperfine constants A for Ga and As are taken from [9] and for In, Cd and Te are averaged over the stable isotopes of the same element and taken from [10]. The other parameters are from [11].

achieve significant non-equilibrium polarisation. It is possible to create the spin flips in neutral exciton states but this requires the dark states and is efficient when a magnetic field can overcome the exchange splitting δ_0 [133]. Additionally, the spin flip can occur through the electron spin in a charged trion state. Build-up of DNP can occur through non resonant excitation and large optical powers (many times the photoluminescence saturation power [134]) are required which suggest that delocalized electrons can induce spin flips as well.

For a fully polarised spin bath, the expression for the maximum OHS simplifies to a sum over all isotopes of the spin and hyperfine constants. For example, for pure GaAs, the maximum OHS is $E_{OHS}^{max} = I_{Ga}A_{Ga} + I_{As}A_{As} = 137 \mu\text{eV}$ with an equivalent field of $B_N^{max} \approx 5$ T [120]. Note that the values for the hyperfine constants together with the important parameters associated with the main nuclear isotopes in our samples are listed in Table 2.1.

The nuclear field fluctuates about a mean value $\langle B_N \rangle$ and these fluctuations can be treated as an effective magnetic field $\delta B_N = \sqrt{\langle B_N^2 \rangle - \langle B_N \rangle^2}$ which has a Gaussian distribution [55]. These fluctuations are not negligible because of the mesoscopic scale of the nuclear

spin system and is the dominant ensemble decay mechanism [54, 55] for the electron spin at zero external field and cryogenic temperatures as the electron “sees” a random orientation of the fluctuating field (known as the frozen fluctuation model).

In reality the nuclear polarisation never reaches a maximally polarised state. More than 50% polarisation is now routinely observed [59, 115, 135] in a variety of III-V systems and upto 80% has been observed in GaAs/AlGaAs dots [9]. The maximum value is limited by the complicated many body interaction present in the electron-nuclear coupled system and is balanced by the rate at which the nuclear polarisation can be built up and the various loss mechanisms (such as the intrinsic nuclear spin lattice relaxation or spin diffusion to the surrounding nuclei out of the dot).

At zero external field, it is possible to build up DNP because the Knight field [131] (which is larger than the local dipolar field) suppresses the nonsecular dipolar interactions and provides an axis for the nuclear spin states to align. The confined electron can cause relaxation of the nuclear spin polarisation on a timescale of ms [136] due to the the nuclear spins coupling through the electron spin and also depolarisation of the electron because of cotunnelling to electrons in the Fermi sea.

The electron to nuclear spin transfer rate w_s can be written as [135]

$$w_s \sim \frac{|A_j|}{\Delta_e^2 + \gamma_B^2/4}, \quad (2.27)$$

where $\Delta_e = \mu_B g_e (B_z + B_N)$ is the total Zeeman splitting of the electron and γ_B is the spin state broadening of the electron. The maximum DNP pumping rate occurs when the electronic Zeeman splitting is cancelled $B_N = -B_z$ and increasing B_z further actually reduces the magnitude of the Overhauser field. As the magnetic field is changed, significant non-linear effects are observed because of the dependence on the total splitting. As the field is swept the nuclear polarisation can be aligned or anti-aligned to the field and provides a feedback mechanism to the rate at which the nuclei can be polarised. Several examples of non-linear effects have been observed such as a bi stability with applied power or magnetic field or through “dragging” effects [137, 138].

2.3.5 Nuclear magnetic resonance and spin relaxation

It is important for spin qubit applications that the spin is sufficiently isolated from its surroundings so that the information that has been created by initializing the spin state is

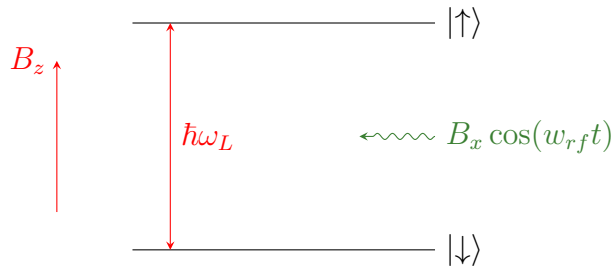


FIGURE 2.12: Simple illustration of an NMR experiment for a spin half nucleus. In an external static magnetic field B_z , the two Zeeman split nuclear levels are separated by the Larmor frequency ω_L . The population of the two levels can be manipulated using an oscillating transverse rf field B_x , oscillating at frequency ω_{rf} and is resonantly driven when $\omega_{rf} = \omega_L$.

not lost to the environment [19]. The ways in which the spin state decays can be categorized and was given a theoretical framework in the field of nuclear magnetic resonance (NMR). Initially, the historic Stern-Gerlach experiment in 1922 [139] first showed that different discrete quantized spin states exist by looking at deflected beams in a magnetic field. Then, the first experiment in the field of NMR was a modified Stern-Gerlach experiment by Rabi in 1939 [140] in which radio frequency (rf) excitations resonant with nuclear transitions were used to measure the magnetic moment directly. The pioneering work of Bloch [141] and Purcell et al. in 1946 [142] proved to be important advancements in the field particularly for solid state systems.

The experiments involved using rf fields applied through a coil to create a net non-equilibrium magnetization in the sample and studying the decay of this magnetization back to the equilibrium state by detecting a current in another pickup coil. Here we will look at a two level system of a spin $1/2$ nuclear spin, but the general concepts still apply for spin $> 1/2$. If a static external magnetic field is applied in the \hat{z} direction $\mathbf{B}_0 = B_z \hat{z}$, the system is split into two eigenstates with energy $E_0 = \mp \hbar \omega_L / 2$, where the Larmor frequency $\omega_L = -\gamma B_z$ is the precession frequency of the nuclear spin about the external field.

If a linearly polarized oscillating field $\mathbf{B}_x = B_x \hat{x}$ is now applied through the use of an NMR coil, the field can be split into two counter rotating components [143]

$$\mathbf{B}_1 = B_x \cos(\omega_{rf} t) \hat{x} = \frac{B_x}{2} (e^{i\omega_{rf} t} + e^{-i\omega_{rf} t}) \hat{x}, \quad (2.28)$$

where the oscillating frequency is of the applied transverse field is ω_{rf} . The effective amplitude of the two counter rotating components is $B_1 = B_x/2$ with a corresponding Larmor frequency $\omega_1 = -\gamma B_1$. The components can be treated separately, but the component

rotating at close to the nuclear resonance (Larmor frequency) is the most important and the component rotating in the opposite direction is negligible and is usually ignored in what is known as the “rotating wave approximation” [113].

By transforming into the rotating frame, the populations of the two states p_{\uparrow} and p_{\downarrow} can be written as

$$p_{\uparrow} = \frac{\Delta^2}{\Omega^2} + \frac{\omega_1^2}{\Omega^2} \cos^2\left(\frac{\Omega t}{2}\right) \quad (2.29)$$

$$p_{\downarrow} = \frac{\omega_1^2}{\Omega^2} \sin^2\left(\frac{\Omega t}{2}\right), \quad (2.30)$$

where the initial populations have been assumed to be $p_{\uparrow} = 1$ and $p_{\downarrow} = 0$, the detuning is $\Delta = \omega_{rf} - \omega_L$ and the Rabi frequency is defined $\Omega = \sqrt{\Delta^2 + \omega_1^2}$. In an NMR experiment, the NMR signal we measure is proportional to the difference in the populations of the two states $p_{\uparrow} - p_{\downarrow} = \frac{\Delta^2}{\Omega^2} + \frac{\omega_1^2}{\Omega^2} \cos(\Omega t)$.

Each nuclear spin in the bath experiences a slightly different magnetic field in space and can also vary in time. These can be caused by inhomogeneities in the magnet applying the external field, the fields from other nuclei that possess a dipole moment, hyperfine interactions with the electron and quadrupolar interactions caused by strain [143]. The relaxation of the magnetization can be split into two rates that characterize relaxation parallel and perpendicular to the applied magnetic field. The Bloch equations of motion [143] describe the precession of a magnetization vector \mathbf{M} (which is the sum over all nuclear spins) in the total magnetic field $\mathbf{B} = \mathbf{B}_0 + \mathbf{B}_1$,

$$\frac{d\mathbf{M}_{x,y}}{dt} = \gamma |\mathbf{M} \times \mathbf{B}|_{x,y} - \frac{M_{x,y}}{T_2} \quad (2.31)$$

$$\frac{d\mathbf{M}_z}{dt} = \gamma |\mathbf{M} \times \mathbf{B}|_z + \frac{(M_0 - M_z)}{T_1}, \quad (2.32)$$

where M_0 is the magnetization reached at equilibrium, T_1 is the spin-lattice or longitudinal relaxation time and T_2 is the spin-spin or transverse relaxation time. The longitudinal component tends to the equilibrium magnetization M_0 and the transverse components relax to zero. Using the Bloch equation model, the relaxation is exponential

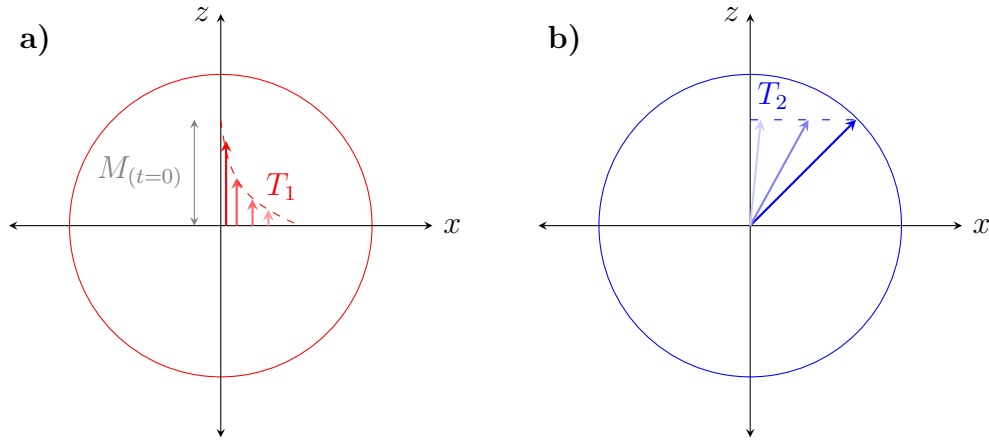


FIGURE 2.13: Representation of the a) longitudinal and b) transverse spin relaxation mechanisms on the Bloch sphere. The arrows represent the magnetization vector at various points in time and the left panel shows the longitudinal relaxation (characterized by the lifetime T_1) to the horizontal plane ($M_0 = 0$) from an initial magnetization $M_{(t=0)}$ along z and the right panel shows the transverse relaxation (governed by the coherence time T_2), which does not change the z component of the magnetization.

$$M_{x,y}(t) = M_{x,y}(0)e^{-\frac{t}{T_2}} \quad (2.33)$$

$$M_z(t) = M_0 - (M_0 - M_z(0))e^{-\frac{t}{T_1}}, \quad (2.34)$$

and if the relaxation is not observed to be a purely exponential function, then the times can be used as an approximate measure of the relaxation dynamics.

The longitudinal component T_1 involves exchanging energy with the environment (also called ‘lattice’) and involves the probability of a spin flip occurring parallel to the quantization axis (see Figure 2.13). It characterizes the time scale over which the polarisation averaged over many spins in an ensemble or many measurements of an individual spin, decays back to its equilibrium value. In subsequent chapters, the T_1 time of the nuclear polarisation in a QD is measured by looking at the decay of the OHS and fitted with an exponential function to extract the characteristic time.

The transverse component T_2 , called the coherence time, does not involve a transfer of energy to the environment and can be thought of as a type of destructive interference between nuclear spins as each spin precesses at a different rate. This type of process is usually associated with a broadening of the NMR linewidths. Additionally, the transverse magnetization of a spin ensemble can usually be seen to decay at a much faster rate, called the ensemble dephasing time T_2^* , due to variations in the magnetic field. But this coherence information is not lost completely and can be refocussed using pulse sequences

that cleverly reverse the oscillation direction such as the spin-echo sequence [143] and the true coherence time T_2 can be measured. In fact, the times are related through the simple expression [144]

$$\frac{1}{T_2} = \frac{1}{2T_1} + \frac{1}{T_2^*} \quad (2.35)$$

and strictly $T_2 \leq 2T_1$ and T_2^* is always less than T_2 . Both T_2 and T_2^* depend strongly on the nuclear isotope and we can measure the values through the linewidths of the homogeneous and inhomogeneous NMR spectra (see Section 6).

These time scales are measured experimentally in this work, but we will describe here the general processes associated with the relaxation of nuclear spins. At low temperature, the small coupling to phonons [145] ensures that the nuclear spin polarisation is stable and long lifetimes T_1 of hours have been observed [7, 135]. However T_1 depends on the number of electrons in the dot. It changes over many orders of magnitude as the applied bias is swept through regimes where cotunnelling effects or long range nuclear spin diffusion via the electron are strong [7]. The transverse times can be measured using pulse sequences and depend strongly on the properties of the isotope being measured (namely their spin, quadrupolar moments and the strain in the QD). The ensemble dephasing time T_2^* is in the range of $\sim 10 \mu\text{s}$ [146] and the coherence times are a few ms [147].

Such relaxation times also apply to the electron spin magnetization. At zero external magnetic fields, the evolution of the electron is determined by the fluctuation of the nuclear field via the hyperfine interaction (see Section 2.3.4). The system can be described by partial relaxation over three distinct timescales (Merkulov-Efros-Rosen model [55]). At large magnetic field in Faraday geometry, an electron spin lifetime of $T_1 = 20 \text{ ms}$ was measured for InGaAs dots and the limiting factor is single-phonon scattering processes via the spin orbit interaction which has a characteristic $T_1 = B^{-5}$ dependence with magnetic field [148]. The ensemble dephasing time (also called pure dephasing time) for the electron T_2^* is a few ns [118, 149], again due to the random directions that the nuclear field is pointing. But using spin echo pulse sequences, the pure dephasing can be suppressed and the coherence time of $T_2 = 1 \mu\text{s}$ has been observed [150, 151]. Another decoherence mechanism has been related to the coherent precession of the nuclear spins around a quadrupolar axis which causes electron spin decoherence at timescales of 750 ns [152]. The hole spin lifetime is also limited by a phonon relaxation with measured values of $T_1 = 1 \text{ ms}$ [153] at low fields and a reduced $T_1 = 11 \mu\text{s}$ at high fields [154]. The transverse relaxation times for the hole are found to be similar to the electron with a pure dephasing

time of $T_2^* = 20$ ns [155] that can again be extended by pulse sequences to T_2 in the microsecond scale [96].

Chapter 3

Experimental techniques

As an outline for this chapter, the important experimental techniques and hardware used throughout this work are described. Using single self assembled quantum dots, the properties of this mesoscopic nuclear spin system are explored. Two samples were used for the work in Chapter 5 both of which were InGaAs/GaAs quantum dot samples. One of the samples (“Low Temp Cap”) is embedded in a p-i-n diode structure which allows for the tuning of the QD charge state. The other InGaAs/GaAs sample (“In-flush”) has no charge tuning capabilities. We are able to analyze the structure of single QDs from both of these samples using novel experimental NMR techniques. In Chapter 6, the effect of a single electron on the nuclear spin properties in a single dot is explored. The sample used in Chapter 6 is the same as the “Low Temp Cap” diode sample used in Chapter 5, but a different QD was studied. We will describe the properties of the self assembled InGaAs/GaAs QD samples used in Chapters 5 and 6 (see Section 3.1).

The work in Chapter 4 concerns a different system of II-VI CdTe/ZnTe QDs. These were studied to see how the nuclear spin properties change when most of the nuclear isotopes have zero spin and the confined carriers interact with a dilute nuclear spin bath. To keep the work on CdTe/ZnTe QDs self contained, these samples will not be described here but rather within Chapter 4 itself.

The hardware required for these experiments are discussed next. The raw data comes from optical photoluminescence (PL) spectra and we require low temperatures and high magnetic fields. Hence, the sample is contained in a liquid helium bath cryostat (see Section 3.2) which contains a superconducting magnet. The optical components required to measure PL spectra are described in Section 3.3. For the measurements concerning the II-VI QDs, many of the components needed to be changed because the nuclear spins

properties were observed over much quicker timescales. Again to create a self contained chapter, any changes to the experimental setup that were made to measure the II-VI samples will be described explicitly in Chapter 4.

Next, we describe how the NMR experiments were conducted. The fundamental requirement is the so called pump-rf-probe technique which allows for the preparation, manipulation and readout of the nuclear spin state (see Section 3.4.1). Also, explained in more detail in Sections 3.4.2, 3.4.3 and 3.4.4 are the hardware and radio frequency waveforms required to perform our continuous wave (cw) inverse NMR technique.

3.1 Self assembled quantum dot samples

The growth techniques for self assembled QDs have been described previously in Section 2.1. Here, more specific details are given about the InGaAs/GaAs QD samples used in this work (for the CdTe/ZnTe samples, see Chapter 4). The experimental measurements in Chapter 5 were performed on two samples: an ungated “In-flush” sample that is nominally undoped and a charge tunable diode “Low Temp Cap” sample. A different dot from the same “Low Temp Cap” sample was used for the experiments in Chapter 6, so this sample will only be described here once.

3.1.1 Ungated InGaAs/GaAs quantum dot “In-flush” sample

The first “In-flush” sample contains InGaAs/GaAs QDs grown in Sheffield by M. Hopkinson with MBE at the National Epitaxy Facility and has been used in previous work in our group [146, 156]. This sample contains a single InAs dot layer which is embedded in a microcavity structure that allows the enhancement of the photoluminescence signal from part of the inhomogeneous spread of QD emission energies. This sample was grown using the “indium flush” technique [157, 158] and will be labelled “In-flush” when referring to it in the text. This consists of depositing a pure InAs layer (additional indium is used to form large mature dots), briefly interrupting the growth to form the initial QDs and then depositing a thin GaAs layer and increasing the temperature. This removes any surface resident indium and causes the tops of the QDs to be flattened as the indium can evaporate. Then, the temperature is decreased back to the original growth temperature and GaAs is deposited again to completely form the capping layer. This results in the formation of shallow disc-shaped dots, which is explored further in Chapter 5.

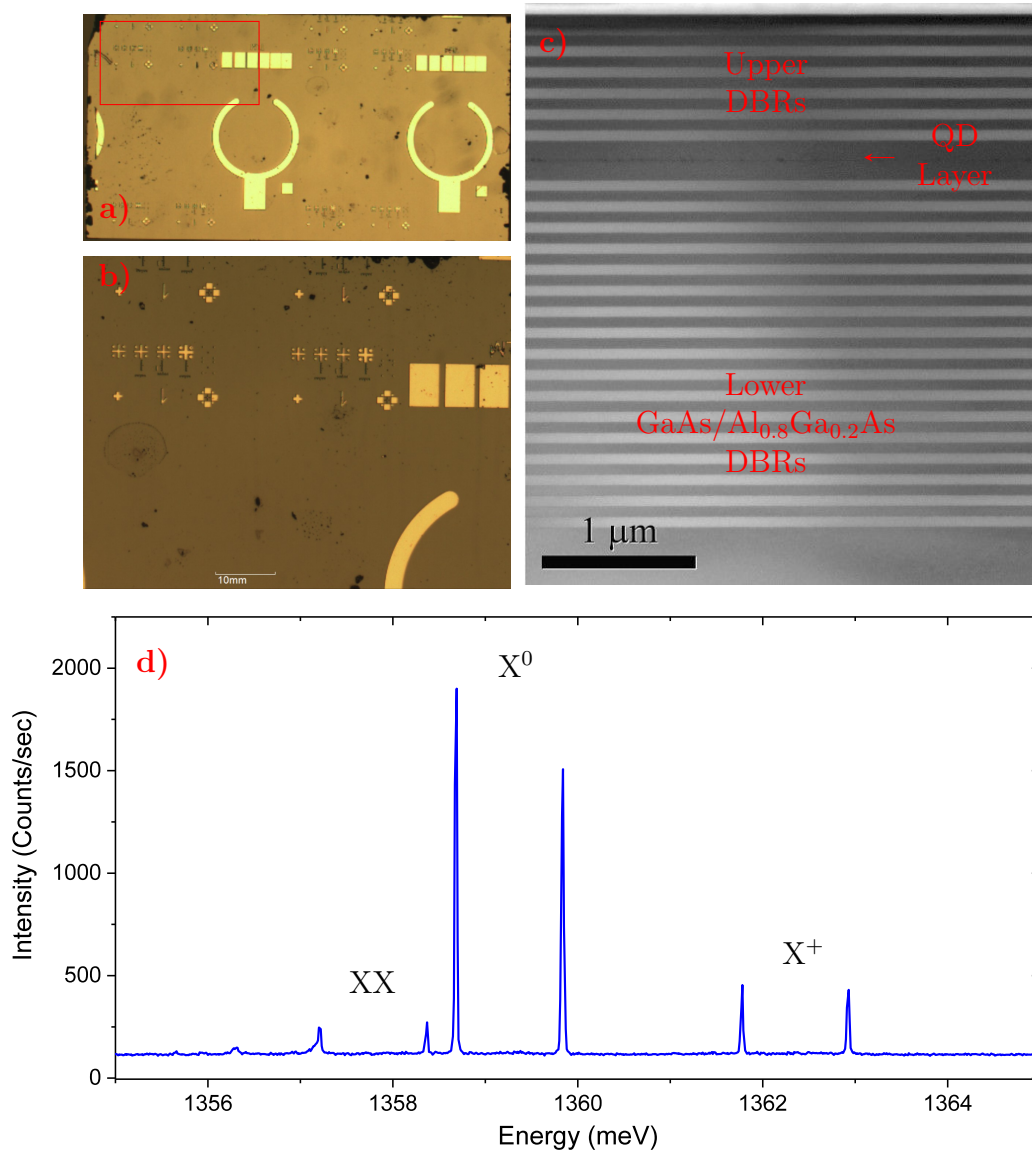


FIGURE 3.1: a) Optical microscope image of the surface of the sample grown using the In-flush technique (4 by 2 mm in dimensions). b) Zoomed in section of the sample marked by the red rectangle in a) where the QDs studied in this work were found. The features visible on the surface are markers which can be used as a reference when relocating specific dots. c) Bright field TEM image of a cross section of the “In-flush” sample with 3000 times magnification. The asymmetric DBR cavity is clearly visible around the dot layer (courtesy of Richard Beanland). d) Representative PL spectrum of a dot measured in this work at an external magnetic field of $B_z = 8$ T. The excitation power of the non-resonant laser is $1 \mu\text{W}$, the polarisation is linear and the wavelength of the laser is 850 nm. The dominant exciton line is the Zeeman split neutral exciton (X^0), but other exciton lines from the same dot are also visible (X^+ and XX).

The dot layer is created by depositing 1.85 monolayers (MLs) of InAs at a growth temperature of 510 °C and a growth rate of 0.1 ML/s. This thickness is chosen to be above the value required for QD nucleation (about 1.65 MLs), but below that required for a mature distribution of QDs. Hence, we observe a low density of infant QDs of about 1 dot / μm^2 , which are small and flat with a relatively low concentration of indium. Note that there must be some larger dots present in the sample but bright emission lines from such dots are not observed in PL spectra because the cavity is designed to enhance emission at around 920 nm.

The cavity layers around the QDs are created using an asymmetric set of DBR pairs of GaAs/ $\text{Al}_{0.8}\text{Ga}_{0.2}\text{As}$ layers, with 17 pairs below the dot layer and 6 pairs above (see Figure 3.1c). This allows for preferential emission vertically up from the dots ($+\hat{z}$) and the cavity has a resonant wavelength of around 920 nm at liquid helium temperatures and a cavity Q factor of ~ 250 [81]. The dot is protected from charges tunnelling in from impurities by using a short-period superlattice of GaAs/AlAs immediately surrounding the QD layer and both the superlattice and the DBR cavity are grown at 620 °C. Using non-resonant PL spectra, narrow emission lines (limited by the resolution of the spectrometer) are observed (see Figure 3.1d). The dominant emission line is from the neutral exciton (X^0) because the dot is nominally undoped, but other excitons from the same dot are also visible since a non-resonant excitation is used.

A series of markers are patterned onto the surface of the sample using optical lithography and depositing a gold layer. These markers can be used to navigate across the sample and relocate a specific dot with respect to the position of the marker. Dot emission is very weak through the markers so the laser spot must be moved away from a marker to locate QDs. The surface of the sample is shown in the images in Figure 3.1a and 3.1b.

3.1.2 InGaAs/GaAs quantum dot diode “Low Temp Cap” sample

The InGaAs/GaAs QDs were embedded in a p-i-n diode structure in the second “Low Temp Cap” sample and were grown using MBE. Acknowledgements go to our collaborators at the Cambridge Research Laboratory, namely R. M. Stevenson, A. J. Bennett and A. J. Shields at Toshiba Research Europe Limited for design of the structure, I. Farrer and D. A. Ritchie for sample growth and J. Nilsson for processing in the Cavendish Laboratory at the University of Cambridge. A single layer of InGaAs QDs are grown which is displaced from an electron doped layer by a 30 nm tunnelling barrier. This sample is capped with

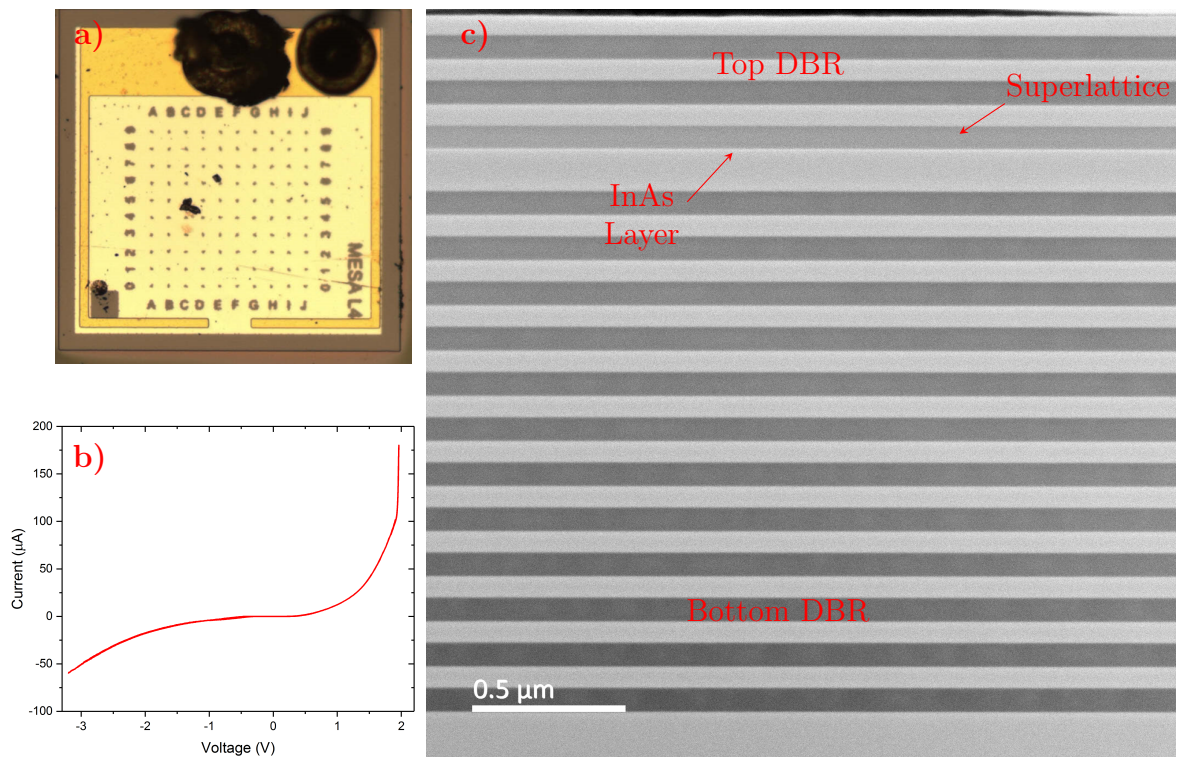


FIGURE 3.2: a) Optical microscope image of the surface of the “Low Temp Cap” p-i-n diode sample. The 10 by 10 array of apertures are labelled and can be used to easily relocate a particular QD. The two dark spots towards the top are used for bonding of the wires to the diode to allow for bias tuning. b) The current-voltage (IV) curve measured for one of the diodes shows characteristic diode behaviour. The data was measured with no optical illumination and at $T = 4.2$ K. c) Annular dark field TEM images to show the cross section of the sample with 80000 times magnification. A thin InAs layer is just visible as the bright layer beneath the AlGaAs superlattice.

GaAs at a lower temperature relative to the ungated “In-flush” sample and will be labelled “Low Temp Cap” when referring to it in the text. The signal here is also enhanced by a GaAs/AlGaAs DBR cavity with 2 pairs above and 12 pairs below the dot layer. Emission of QD signal is efficient at similar wavelengths (~ 920 nm) to the other sample and the PL signal in saturation reaches a similar intensity.

There is a short period AlGaAs superlattice barrier layer just above the dots which is used to prevent charges from tunnelling out of the dot and the p-contact is located on the surface of the sample. This configuration allows us to control the native charge in the QD by changing the applied bias between the p-contact and the n-contact below the dot layer. The IV curve in Figure 3.2b shows a typical characteristic diode shape where the current increases (under forward bias) rapidly after reaching a threshold voltage - the built-in voltage is around $V_{int} \approx 1.8$ V. With reverse bias, the current increases significantly less than the forward bias configuration. The electric field can be calculated

from the applied bias using $F = (V - V_{int})/d$, where d is the intrinsic region [103]. By performing a quadratic fit (using Equation 2.4 from Section 2.2.4) of the X^0 transition line (shown in Figure 2.8), the parameters of $p = -9.85 \times 10^{-4}$ [meV kV⁻¹ cm] and $\beta = -7.82 \times 10^{-7}$ [meV kV⁻² cm²] are obtained for the dipole moment and the polarisability respectively. These values (adapting the same units) are similar to previously reported values in diode structures for InGaAs QDs [103].

In Chapter 5, only the neutral exciton state is used to analyse the structure, but in Chapter 6, we compare a dot which is empty to when it contains a single electron. For some dots, we are able to tune the charge occupation from empty (X^0) to single electron (X^-) to two electrons (X^{2-}) over the voltage range of about 0.5 V. PL emission can be safely observed over a range of about 2-3 V beyond which the forward current through the diode starts to increase. When a negative bias is applied, the dot is flushed of all charges and can be used to reproducibly empty the dot. Narrow, resolution limited spectral lines are visible for all the charge states depending on the exact bias applied and whether this creates a charge in a stable portion of the charging bias plateau. This will be investigated for the single electron charged plateau in Chapter 6.

This sample is patterned with a series of apertures on the surface which are in a 10 by 10 array (see Figure 3.2a). In contrast with the markers from the other sample, the dots here are only found within an aperture. These are smaller than the laser spot and so reduce the number of QDs that can be controlled with the laser. The advantage here is that the PL spectra are clearer as there are less lines from other dots and it is trivial to relocate a particular dot. The disadvantage is that throughout most of the sample, there is no visible dot emission. Typically in one aperture, emission from 1 to 3 dots are visible depending on the applied bias and the emission wavelength being observed.

3.2 Sample control and cryostat

There are many pieces of experimental equipment that are essential to perform the optically detected NMR measurements presented in this thesis. We start by describing the cryogenic chamber that holds the sample. Most experiments using self assembled InGaAs/GaAs QDs require low temperatures (< 50 K) to ensure that the spacing between the confined energy levels is larger than the thermal energy of the electrons and holes. Once the electron spin state is initialized at low temperatures, the state can be manipulated and detected before the information is destroyed by interactions with phonons (see Section 2.2.1). This

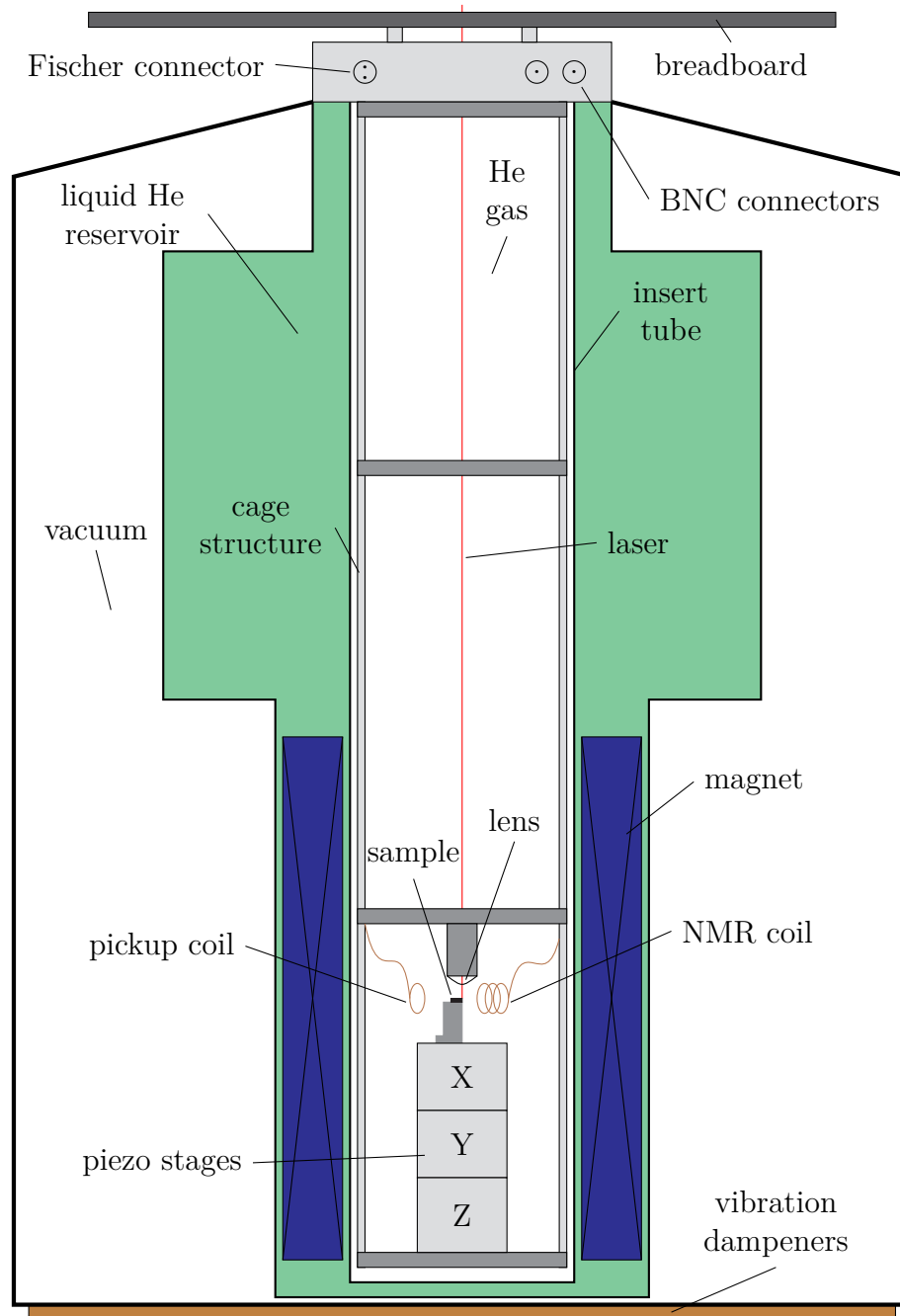


FIGURE 3.3: Simplified schematic diagram of the cryogenic system. The cryostat holds a liquid He reservoir that allows for the use of a superconducting magnet with fields up to 8 T along the vertical axis. A laser can pass through the system and is focussed onto the sample surface with an aspheric lens, which is also used to collect the emitted dot signal. The sample is mounted on a non magnetic holder that can be positioned precisely using 3 piezoelectric nanopositioners. The sample is not in contact with the liquid He, but instead is contained within an insert tube filled with a low pressure He gas used for exchange gas cooling. There is a copper coil near the sample used to apply radiofrequency excitations to the quantum dots and another coil used as a pickup coil to monitor the waveforms. Wires are fed through the cage structure and the electrical components can be controlled externally through the electrical connectors at the top of the insert. A breadboard housing important optical components sits on top of the cryostat and the structure is damped to minimize vibrations and maintain optical alignment.

is possible in the laboratory by placing the sample in a cryostat filled with liquid helium which has a boiling point of $T = 4.2$ K. A summary of the cryogenic system discussed in this section is illustrated in Figure 3.3.

In this work, an Attocube LTSys-He liquid helium bath cryostat was used to hold the sample. This is essentially a large cryogenic dewar which has insulated vacuum layers that prevent the heating of the liquid helium reservoir. The cryostat also houses a superconducting magnetic coil which is used to apply an external static magnetic field (of up to a maximum persistent field of $B_z = 8$ T) to the sample along the vertical (\hat{z}) direction. The field can be adjusted through an external power supply that controls the current flowing through the coils and can also be configured to create a persistent field. The sample can be mounted so that the optical direction is along the field axis (Faraday geometry) or perpendicular (Voigt geometry), but all measurements were performed in Faraday configuration. The chamber can hold a reservoir of upto about 50 litres of liquid helium and the sample could be kept cold for several months at a time by refilling the cryostat every 4 days, beyond which the helium level would drop below the coil. This creates a stable system and avoids issues with a different QD charge environment when the sample heats up and cools down. The reservoir is suspended from the external casing of the cryostat through vibration dampeners which enforce mechanical stability and allow us to perform measurements over night with only small drift corrections in the excitation laser path.

The sample itself is mounted on a copper holder on an aluminium pedestal (both of which are non-magnetic) through the use of silver paint which provides a good thermal conductive contact. The sample holder is glued onto a stack of 3 Attocube piezo-electric nanopositioners which are used to move the sample with high precision (sub micron). The two “x” and “y” stages can control the position of the sample with respect to the fixed excitation laser and the third “z” stage controls the focussing of the laser spot onto the surface. The sample, holder and piezo stack rest on a cage plate which is fixed onto a Thorlabs cage structure which comprises 4 long stainless steel rods with more cage plates at various locations across the rods. The cage plates provide stability to the structure and access points to feed the various cables and wires required for the sample (bias control and temperature sensor) and experiments (controlling the piezo positioners and the NMR coil). One of the cage plates just above the sample holds an aspheric objective lens (with focal length $f \approx 2$ mm and numerical aperture $NA \approx 0.5$), which focusses the laser down to a small micrometer sized spot onto the sample surface and also collimates the PL emission from the dot into a beam so that it can be detected in confocal PL spectroscopy. This small spot is what allows us to perform “micro-PL” measurements where individual spectral PL

lines can be identified (as opposed to “macro-PL” spectroscopy which detects a broadened ensemble).

The entire cage structure is inserted into a cylindrical stainless steel tube which has a glass window in the top of the tube allowing free space optical access for the laser and the QD signal. This “insert” tube is pumped to a high vacuum and a small amount of low pressure He gas (< 1 mbar) is added into the tube. This tube is then immersed into liquid helium in the cryostat and through the central hole (bore) in the magnetic coil, where the sample will sit approximately level with the center of the coil. The sample does not make contact with the liquid He; the sample is surrounded by the low pressure He gas within the insert tube and the exterior surface of the tube is in contact with the liquid He. This means the sample cools down in a slower controlled way and together with the inert atmosphere does not allow for contamination of the surface due to condensation.

Finally, to perform NMR experiments, a small multi-winding copper coil is used to generate oscillating radio-frequency (rf) magnetic fields which interact with the nuclear isotopes in the sample. The coil is aligned to be as close as possible to the edge of the sample to provide the maximum rf field on the nuclei in the sample. An additional single loop copper coil is placed on the other side of the sample and is used as a pickup coil to monitor the transmitted rf waves from the excitation coil. The NMR signal for the main experiment is detected optically and the pickup coil is only used during calibrations to check the intensity and distortions of the applied rf waveform. Both coils are wired to BNC connectors connected near the top of the insert tube via coaxial cables. Also near the top of the tube is a specially designed Fischer connector socket to which the other wires for diode bias, temperature sensors and piezo stages are connected. Above the insert tube, an optical breadboard is mounted which holds the various optical components used for the pump-probe PL measurements.

3.3 Optical photoluminescence spectroscopy

Spectroscopy is a very broad technique used to analyze the transitions between energy levels of a certain entity through emission or absorption of electromagnetic waves. Here we detect the light emitted from a QD ground state exciton which is typically in the infrared part of the electromagnetic spectrum (~ 920 nm). In the previous section, the cryostat part of the experimental setup was described which holds the sample and magnet. Now, we will describe the rest of the optical components and the arrangement that is required

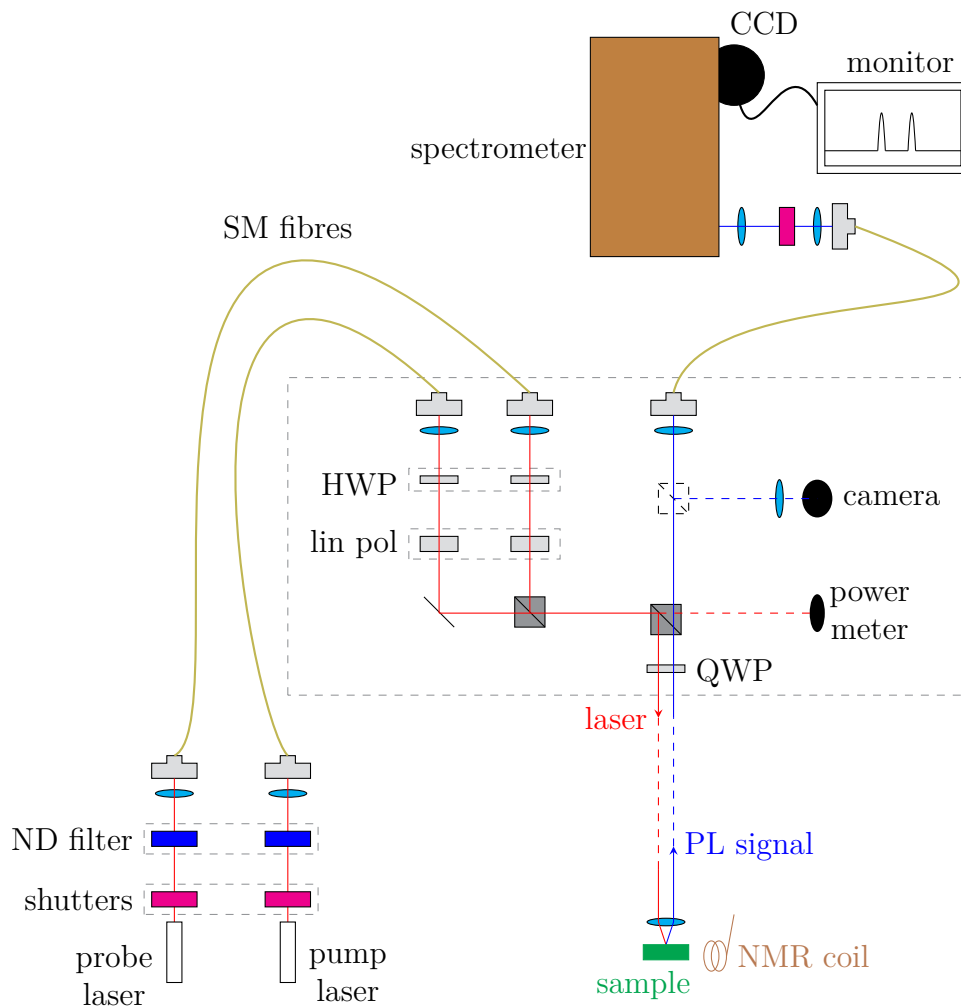


FIGURE 3.4: Diagram of experimental setup for optical photoluminescence spectroscopy. Two diode lasers are used to realize the pump-probe technique and pass through shutters and a series of polarisation optics via single mode (SM) fibres to create a high power, circularly polarised pump laser that polarises the nuclear spin bath and a low power, linear probe laser that detects the quantum dot signal. The emitted signal from the sample is directed through a high resolution double spectrometer and onto a CCD to measure the spectra. Also, the laser power and the location on the sample can be monitored by deflecting part of the beam onto a power meter and an imaging camera respectively. The components located on the breadboard above the cryostat are shown by the dotted rectangle.

to perform confocal photoluminescence spectroscopy. We will look at the components located on the breadboard above the cryostat as well as the lasers used for pump-probe experiments and the hardware for detection of the PL signal.

The entire experimental setup is illustrated in Figure 3.4. For the pump-probe scheme required for initialization and detection of the nuclear spin polarisation, two 850 nm diode lasers are used. This wavelength lies within the InAs wetting layer bandgap and allows

us to perform non-resonant PL and see the entire ensemble of QD emission lines. The current through the laser diode can be adjusted with an external power supply to change the power of the emitted beam. However, we choose a constant current value above the threshold value for lasing and we maintain this current in order to keep the power stable. Instead the power of the two lasers can be controlled individually by passing the beam through variable ND (neutral density) filters with an exponential gradient allowing for attenuation of the laser upto 3 orders of magnitude. If more dynamic range is needed, two such filters can be used in series. The experimental cycle typically consists of pump pulses and probe pulses where part of the time the dot is illuminated by the high power pump laser (to polarise the nuclei) and part of the time by a low power probe laser (to detect the polarisation). Each laser can be turned “on” and “off”, by allowing the beam to pass through or be blocked by a mechanical shutter. The time it takes for the shutters to open or close limits the width of the pulses and the shutters used here had a minimum operating time of ~ 1 ms. This is sufficient for most of our experiments on InGaAs/GaAs QDs but the CdTe/ZnTe system had faster dynamics and different hardware was used (see Chapter 4).

Due to limited space and ease of access, the lasers are on a separate optical table to the breadboard that is mounted above the cryostat. To transport the light from the lasers to the breadboard, the beams are focussed by lenses into single mode optical fibres. The fibres guide the beam to a pump path and a probe path located on the breadboard. In the pump path, the laser passes through a half wave plate (HWP) and a linear polariser. The half wave plate here is used to rotate the polarisation axis of the light coming out of the fibre to be aligned with the axis of the linear polariser so that a maximum intensity passes through. The linear polariser is oriented to create a linearly polarised beam parallel to the plane of the breadboard. This light is then directed towards a 50:50 non-polarising beam splitter cube. The horizontal polarisation of the beam here is aligned to the axis of the beam splitter to ensure that it does not create any ellipticity in the polarisation. Half of the light passes to a power meter and half is deflected down to the sample where the beam is focussed into a spot (of size $\sim 1 \mu\text{m}^2$) on the sample surface by an aspheric lens. A quarter wave plate (QWP) is placed just below the central beam splitter before the light reaches the cryostat. This is mounted on a mechanical rotation stage which is calibrated to change the polarisation state of the light to be circularly polarised (σ^+/σ^-).

The idea of the probe laser is to detect clearly the Zeeman splitting of the QD without influencing the nuclear polarisation state itself. This is done by using a low power (well below the saturation power of the exciton ground state) and by using linearly polarised light. The probe path also contains the combination of a HWP and a linear polariser, but

requires an additional pellicle beam splitter to deflect the probe laser into the path of the pump (the pump laser passes through the pellicle before reaching the beam splitter cube). Here the polarisation axis of the light is setup to be aligned with one of the optical axes of the QWP and this ensures a linear polarisation is incident on the sample surface.

The light emitted from the dot is then collimated by the objective lens in the cryostat and is passed back through the central beam splitter cube to the detection path. In the detection path, there is another beam splitter mounted on a flipper-mirror that can intercept some of the light and direct it to a digital camera connected to a TV monitor. This is used to look at the image of the sample and allows us to align the probe laser spot to the pump laser spot so that the same location of the sample is excited efficiently. The piezo nanositioners also allows for fine tuning of the focussing of the beams and to navigate around on the sample surface to relocate specific dots relative to the surface markers. The detection path on the breadboard concludes by focussing the light into another single mode (and occasionally multi mode) fibre.

The light from the detection path fibre is then sent to a 1 m double spectrometer (Ramanor U-1000 Monochromator). The double spectrometer has a pair of gratings (900 lines/mm), which allow for high resolution spectroscopy. The gratings can be rotated together to detect different wavelengths of light and are calibrated so that the energies of the QD lines can be derived. Finally, the light from the spectrometer falls onto a liquid nitrogen cooled charge coupled device (CCD) Princeton Instruments camera that is connected to a computer to record the spectra. There is another mechanical shutter before the entrance to the spectrometer, which is used to select the portion of the experimental cycle that light is allowed to pass to the CCD. For example, in pump-probe measurements, the shutter only opens when the dot is illuminated by the probe laser. The light is carefully focussed onto the entrance slit of the spectrometer using an adjustable lens so that the maximum signal and minimum linewidth is detected on the CCD. In this way, the resolution of the spectrometer is about $20 \mu\text{eV}$ and several tens of thousands of counts per second of QD signal is measured with non resonant PL at saturation powers. The integration times are of the order of ~ 1 s for a single spectra so the detected lines are actually time-averaged over the conditions that the QD experiences.

It should be mentioned that all the optical components discussed here (as well as various mirrors throughout the setup omitted for simplicity) are not perfect and will contribute to distortions in the beam profile, imperfections in the polarisation and losses in the beam throughput. However, these effects are relatively small for the requirements of our experiments. The beam shape of both lasers are circular and a diffraction limited $\sim 1 \mu\text{m}^2$

spot size is achieved on the sample surface. Perfect circular polarisation is not needed because asymmetry in the dot itself causes the nuclear spin polarisation to be a maximum when the polarisation is slightly different from σ^+ or σ^- (and is calibrated for each dot). There are losses in the intensity of the beam, but the pump laser reaches up to a few mW in power (at the power meter location) and the probe laser up to tens of μW , both of which are sufficient to polarise the nuclear spin bath and detect the PL signal. The alignment can also drift in time due to various external factors including vibrations and temperature fluctuations in the lab. On rare occasions, the data is discarded and remeasured, but usually measurements can be reliably performed over several days with brief interruptions to correct for small drifts.

3.4 Nuclear magnetic resonance techniques

Nuclear magnetic resonance is a branch of radiofrequency spectroscopy [113] where the spacing between energy levels is in the radiofrequency part of the electromagnetic spectrum - as is the case for most nuclear species. In this work, we only utilize cw NMR techniques to interact with the nuclear spin system in the frequency domain, as opposed to pulsed NMR which governs the time domain. In this section, we describe the experimental components required for the optical detection of the NMR signal.

3.4.1 Optically detected NMR: the Pump-RF-Probe technique

The fundamental concept of optically detected NMR in single self assembled QD systems is to measure changes in the Zeeman splitting of the QD lines. This is caused by changes in the net magnetic field acting on the electron as the Overhauser field due to the nuclear spin polarisation changes (see Section 2.3.4). Single QDs are particularly suited for optical observation of DNP because the linewidths of the QD emission are very narrow and a change in Zeeman splitting can be detected directly. This is in contrast to the equivalent bulk systems where linewidths are much larger than the energy shift from the nuclear field.

In our experiments, we apply repeated cycles of a three stage procedure: pump to polarise the nuclear spins, rf to manipulate the spins and probe to read out the final state. This is the basic scheme for most of the measurements and a schematic illustration of what happens to the nuclear spins is presented in Figure 3.5.

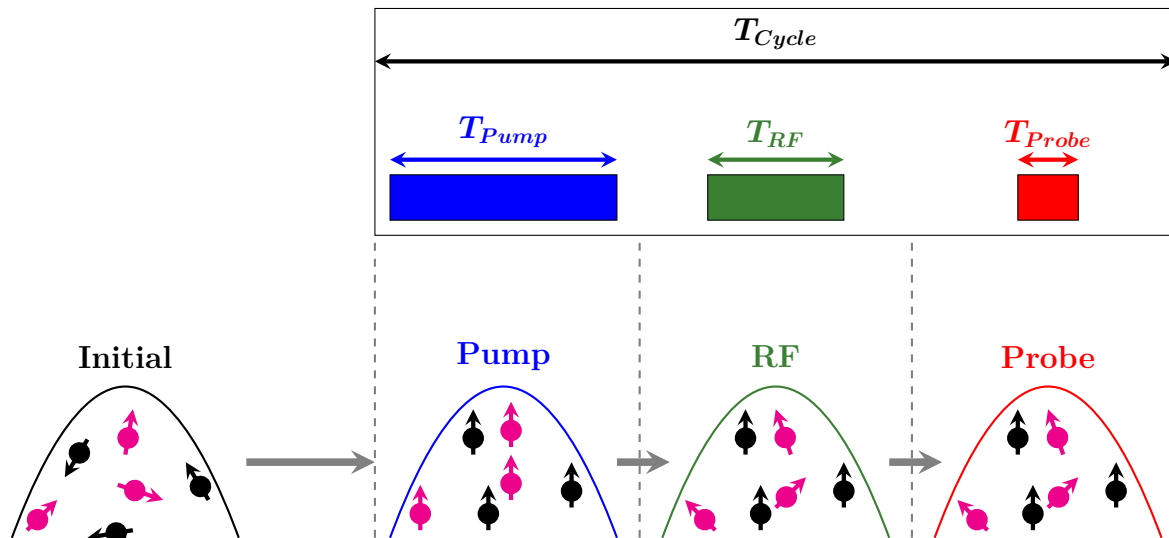


FIGURE 3.5: Schematic illustration of the Pump-RF-Probe technique used for optically detected NMR measurements. The initially randomly fluctuating nuclear spins are polarised by a high power pump laser. Nuclei of a particular isotope are depolarised by applying a cw radiofrequency excitation and the final nuclear spin state is detected optically in the PL spectra with a low power probe laser. A change in splitting in the PL spectra is observed as the nuclear polarisation is altered.

Initially without external excitation, the nuclear spins fluctuate randomly and reach some thermal equilibrium where no net nuclear spin polarisation is present when averaging over the ensemble. In the initial part of Figure 3.5, this is represented by all the nuclear spins (denoted by the black and purple arrows) pointing in random directions.

The first step requires the polarisation of the nuclear spins. This is done by applying a high power, circularly polarised laser onto a QD. Using an 850 nm non resonant pump laser, polarised electrons and holes are generated in the wetting layer and are quickly captured by relaxation into the dot (see Section 2.2.1). As the polarised electron spin tries to relax back to equilibrium, it can interact with the surrounding nuclear spins via the contact hyperfine interaction and a spin flip can occur between the electron spin and the nuclear spin. Due to the high power of the pump laser, the electron is polarised again very quickly and transfers its spin to another nucleus. This process repeats to create a net non-zero nuclear spin polarisation, where only nuclei that are covered by wavefunction of the electron trapped in the QD become polarised. This process is called optically induced dynamic nuclear polarisation (as introduced in Section 2.3.4) and was first realized in silicon [159] and later in doped GaAs samples [120]. All nuclei are polarised because all the isotopes present in our InGaAs sample have a non-zero hyperfine constant (see Table 2.1) and this is shown in Figure 3.5 by all arrows pointing in the same direction during the pump step. The sign of the nuclear polarisation depends on which circular polarisation is used for pumping; σ^+ acts to increase the overall Zeeman splitting and σ^- acts to reduce

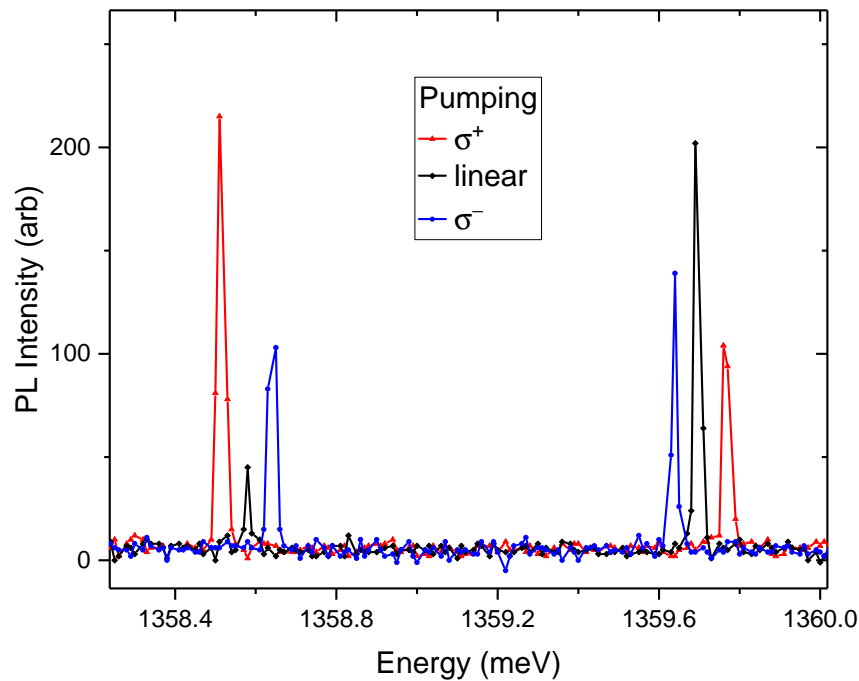


FIGURE 3.6: PL spectra recorded using the pump-probe technique from the X^0 transition of a quantum dot from the In-flush sample at $B_z = 8$ T. The sample is pumped with different polarisations of light for a few seconds before recording the spectra and a clear Overhauser shift ΔE_{OHS} is visible. With linear pumping, the Zeeman splitting is 1.124 meV and under σ^+ (σ^-) pumping, a shift of $\Delta E_{OHS} = +125\mu\text{eV}$ ($-125\mu\text{eV}$) is observed.

the Zeeman splitting (in InGaAs dots where all hyperfine constants are positive). This is visible in the PL spectra where an Overhauser shift (OHS) of upto $\pm 125\mu\text{eV}$ was observed under σ^+/σ^- pumping compared to the pure Zeeman splitting with linear pumping. This can be seen in the PL spectra in Figure 3.6 from the In-flush sample. Note here that for this simple explanation, all nuclear spins have been shown to be polarised (all arrows point in the same direction after the pump step in Figure 3.5), but in reality the maximum achieved polarisation is about 70 % in this InGaAs QD.

In the second step, we manipulate the nuclear spins using a low power cw radiofrequency pulse through the rf coil. The rf pulses have a specially designed spectral shape (see Section 3.4.3) and they are used to selectively depolarise nuclei of a particular isotope. Thus we observe a change in the Overhauser shift (seen as a change in the Zeeman splitting of the PL spectra) due to some nuclei being depolarised. This is shown in the rf step of Figure 3.5 by the purple arrows (which have been driven by the rf field) pointing in random directions, whilst all the other isotopes (denoted by the black arrows) remain polarised.

In the final step, a linear probe laser is applied. There is a compromise in the choice of parameters for this pulse so that a sufficient PL signal is obtained, but not affecting the

nuclear spin polarisation. We calibrate the pulse by looking at different powers and pulse lengths and ensure that the Overhauser shift does not fall below 95% of its original value.

These three steps form one cycle in our experiment. Typically for InGaAs/GaAs QDs, the pump time is $T_{Pump} = 6$ s and is the dominant part of the cycle and limits the total length of the experiment. The rf pulse time T_{RF} varies between isotopes from tens of milliseconds to a few seconds and the probe time is about $T_{Probe} = 30$ ms.

The measurements are all automated by connecting all the relevant controls for the shutters, laser power and polarisation controllers to a series of interconnected function generators that create the pulse cycles with TTL (transistor-transistor logic) signals. The cycle is repeated (usually around 10-20 times) for each datapoint until a PL signal of > 500 counts is obtained. The Zeeman split peaks are then fitted with a Gaussian function and the centre of mass is determined. Other fitting parameters such as the width and the amplitude of the peak are monitored to check for drift over time, but the most important parameter is the peak position and energy shifts as small as $\sim 1\mu\text{eV}$ can be measured. Additionally, the noise in the data is reduced further by taking multiple spectral repeats per datapoint and averaging the signal. Many calibration measurements are typically required before an NMR measurement can be performed such as determining all of the pulse times, the polarisations and powers for the lasers and any dependence on bias in the diode sample and these are discussed in the experimental chapters.

3.4.2 Inverse NMR technique

In order to understand the properties of the nuclear isotopes present in a single QD containing only 10^5 spins, we use an optically detected NMR (ODNMR) technique. The aim is to map out how the nuclear spin magnetisation changes with frequency and this powerful technique allows us to determine the chemical composition and the strain distribution in a particular dot. Early ODNMR work was measured by detecting the change in electron spin polarisation [160–162]. Then, the signal was detected by looking at changes in the Zeeman splitting through “saturation” NMR methods, where the NMR spectra for ^{69}Ga and ^{75}As were measured by stepping through the radiofrequency of the transverse field [56]. In our research group, we have advanced this technique further [163], and created a novel “inverse NMR” technique which uses a specially designed rf waveform [146]. The saturation method is used to detect the signal from spin $I = 1/2$ nuclei or quadrupolar nuclei in low strain systems. But in our self-assembled InGaAs QD system, there is a large

inhomogeneously broadened ensemble due to the in-built strain and the inverse NMR technique can be used to significantly enhance the extracted signal. In previous sections, we have discussed that a rf pulse is used to depolarise certain nuclei, and here we will explain the spectral shape of these pulses in the context of saturation and inverse NMR.

We have seen in Section 2.3.3, that the nuclear spin level structure of a quadrupolar nucleus in a large external magnetic field is dominated by the Zeeman effect and the states have a well defined spin projection m (from $-I_z$ to $+I_z$) along the field axis (\hat{z}). Quadrupolar shifts induced by strain give additional shifts and since the only dipole-allowed transitions are $m \leftrightarrow m + 1$, we find for the example case of a spin $I = 3/2$, three allowed resonance peaks (called the central transition CT between $-1/2 \leftrightarrow 1/2$, and side/satellite transitions ST $-3/2 \leftrightarrow -1/2$ or $1/2 \leftrightarrow 3/2$).

After the optical pump step of the experimental cycle and before any rf pulse is applied, most of the nuclear spins will have been polarised. For spin $I = 3/2$ isotopes in our InGaAs dots, this means that under σ^- pumping, the probability p_m of finding a nucleus with a projection $I_z = +3/2$ is much higher than $I_z = -3/2$ (and vice versa for σ^+ pumping). The population probabilities p_m depend on I_z and follow the canonical Boltzmann distribution [9, 146],

$$p_m = \frac{e^{m\beta}}{\sum_{m=-I}^{+I} e^{m\beta}}, \quad (3.1)$$

where the dimensionless inverse temperature is defined $\beta = \hbar\omega_L/k_B T_e$, \hbar and k_B are the Planck and Boltzmann constants, $\omega_L = -\gamma_N B_z$ is the Larmor frequency (see Section 2.3.3) and T_e is the spin temperature of the electrons inducing DNP.

Then, the total nuclear spin polarisation degree is

$$P_N = \sum_{m=-I}^{+I} \frac{m p_m}{I}, \quad (3.2)$$

which can be detected optically by detecting the total OHS.

For saturation NMR in its simplest form, rf excitation at a single frequency ν_{sat} is applied to the sample. This will alter P_N only when ν_{sat} is in resonance with one of the transitions of an isotope present in the system. P_N changes under a sufficiently long rf excitation because the population of the two spin levels equalize. Especially for an inhomogeneously

broadened spectrum, the number of nuclei of a given isotope with the same resonance frequency is small so the signal detected through a single frequency ν_{sat} rf pulse is low. To improve the signal (but at the risk of lower resolution), a distribution of frequencies that form a spectral band of width w_{sat} may be applied instead and now more nuclei will have their spin state populations equalized.

However the maximum signal achievable here is still low because it is limited by the difference in the initial populations between the two levels. For the example of the $1/2 \leftrightarrow 3/2$ transition, the signal is proportional to $\propto p_{+3/2} - p_{+1/2}$ and the rf waveform has no effect on the populations of the other spin levels. This is shown schematically in Figure 3.7b where a rf pulse resonant with the $1/2 \leftrightarrow 3/2$ transition equalizes their populations and does not change the other levels.

This is why the inverse NMR technique was developed, as it provides a large enhancement in the detectable changes in P_N for quadrupolar spins $I > 1/2$. Here, two broad cw radiofrequency bands are applied separated by a gap. The total width of the bands is calibrated to cover the entire width of the resonance (CT and ST) for a particular isotope. If there is no gap, all of the populations are equalized (see Figure 3.7c) and the nuclear spin polarisation is fully erased. When a gap is introduced, the width of the gap is carefully chosen to balance the amount of signal versus the resolution of the spectra. The gap is narrow to detect high resolution CT spectra (see experimental Chapter 5) and is much broader for the ST spectra that suffer from quadrupolar broadening. If the gap is in resonance with the $I_z \leftrightarrow I_{z+1}$ transition, this transition is not excited and hence the populations equalize in two separate groups of levels with $m \leq I_z$ and $m \geq I_{z+1}$. This is shown in Figure 3.7d, where a gap resonant with the $1/2 \leftrightarrow 3/2$ ST causes the equalization of the populations of the $-3/2, -1/2$ and $+1/2$ states and the $+3/2$ level remains at a large population. The central gap frequency f_{gap} is moved across the resonance and the more nuclei that lie within the gap, the larger the signal and the NMR spectra can be traced out.

For a saturation NMR measurement, a spectra is taken with no rf waveform applied (Figure 3.7a) and the Overhauser shift is detected $\Delta E_{OHS}^{no,rf}$ and this acts as a reference splitting value (where the nuclei are in a polarised state). Spectra are then taken with the rf band applied ΔE_{OHS}^{sat} (Figure 3.7b) and the difference in splitting $|\Delta E_{OHS}^{no,rf} - \Delta E_{OHS}^{sat}|$, caused by the difference in the nuclear spin polarisation, provides the NMR signal. For an inverse NMR measurement, the reference level of splitting is provided by a “no gap” spectra $\Delta E_{OHS}^{no,gap}$ where a single band depolarises the entire isotope (Figure 3.7c) and the signal comes from the splitting ΔE_{OHS}^{gap} measured when a gap is introduced (Figure 3.7d).

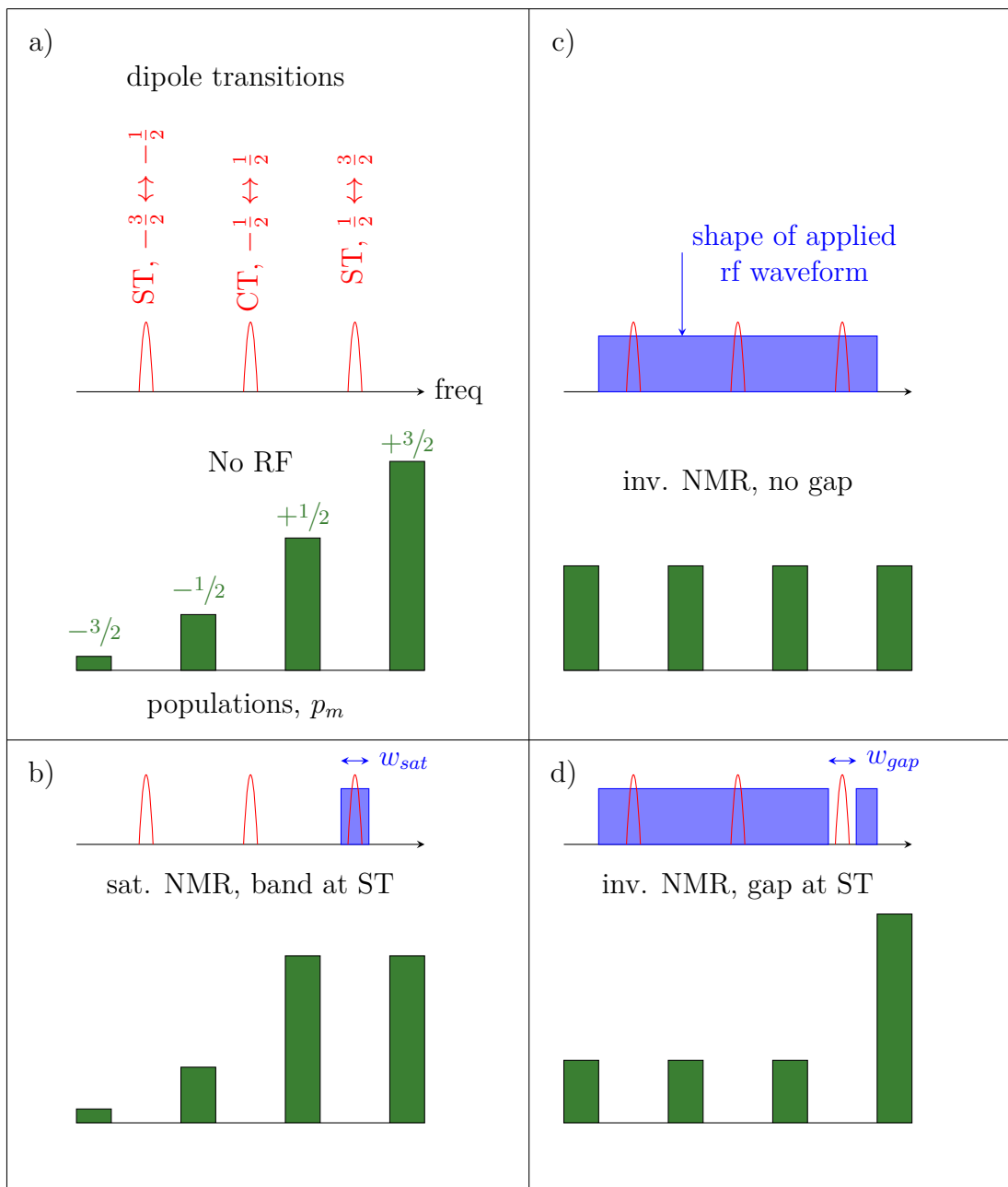


FIGURE 3.7: Schematic comparison of the saturation and inverse NMR techniques for quadrupolar nuclei with the example case chosen as spin $I = 3/2$. a) Shows how the populations (green bars) of the various spin states of a single nuclear isotope follow the Boltzmann distribution after strong optical pumping (with polarisation of $\sim 70\%$) and with no rf applied. b) Using the saturation NMR method, a narrow band with width w_{sat} is applied for a sufficient time in resonance with the $1/2 \leftrightarrow 3/2$ ST and equalizes the populations between these two states. The other spin states are unaffected. c) If a single broadband cw pulse is applied covering all three transitions (spectrum indicated by the blue rf waveform) the populations of all 3 states are equalized. d) In the inverse NMR method, two broad rf bands are applied separated by a gap of width w_{gap} . When applied to the ST, all levels are affected and the populations are equalized separately for two groups of levels $m \leq +1/2$ and $m = +3/2$, resulting in a larger overall change in polarisation and enhancement of the detected NMR signal.

Again the final NMR signal is the difference between the two $|\Delta E_{\text{OHS}}^{\text{no,gap}} - \Delta E_{\text{OHS}}^{\text{gap}}|$. It can be seen visually from Figure 3.7 that the difference in populations between $\Delta E_{\text{OHS}}^{\text{no,gap}}$ and $\Delta E_{\text{OHS}}^{\text{gap}}$ through the inverse NMR method is much larger than $\Delta E_{\text{OHS}}^{\text{no,rf}}$ and $\Delta E_{\text{OHS}}^{\text{sat}}$ from the saturation method and this is what provides the larger signal. It can be derived [146] that the CT signal is enhanced with the inverse method by a factor of $(I + 1/2)^3$ compared to the saturation method. As the formula suggests, the signal scales with the nuclear spin, so it is particularly useful for nuclear isotopes with large spin such as ^{115}In with spin $I = 9/2$. However, it makes no difference for spin $I = 1/2$ nuclei (with no quadrupolar moment) and so in Chapter 4, we measure the NMR spectra of Cd and Te (both having only $I = 1/2$ isotopes) using the saturation method.

3.4.3 Frequency combs

To perform such inverse NMR measurements, we have thus far discussed aperiodic rf spectral “bands” which are used to depolarise a nuclear isotope in the sample. Due to the large inhomogeneous broadening in self-assembled QDs, a band can reach up to 20 MHz in width. Such a broad continuum of rf excitation could not be created by our digital devices in the lab and instead we approximate such a band by using rf frequency combs. The idea is to have a large number of densely spaced discrete modes with equal separation (mode spacing $f_{MS} \sim 125$ Hz) such that each nuclear resonance of an isotope is being driven uniformly by multiple modes and are depolarised. The mode spacing of $f_{MS} \sim 125$ Hz is significantly smaller than the homogeneous NMR linewidth, which results in fast nuclear spin depolarisation [8] (this will be discussed in more detail in Chapter 6).

To introduce schematically how the frequency combs can be created and applied at some arbitrary frequency range, let's first consider a much simpler system of just 2 sine waves. The first sine wave is denoted as the carrier and the frequency f_{car} can be chosen to be resonant with a particular isotope - in our experiments, this is usually 50 – 110 MHz for the InGaAs isotopes at $B_z = 8$ T. The second sine wave acts as a modulating waveform (with frequency f_{mod}) and it is well known in the field of rf electronics that when two sine waves are mixed together, a low and high frequency side band are created. This can be derived explicitly using the trigonometric identity

$$A \sin(f_{carr}t) * B \sin(f_{mod}t) = \frac{AB}{2} \left(\cos[(f_{carr} - f_{mod})t] - \cos[(f_{carr} + f_{mod})t] \right), \quad (3.3)$$

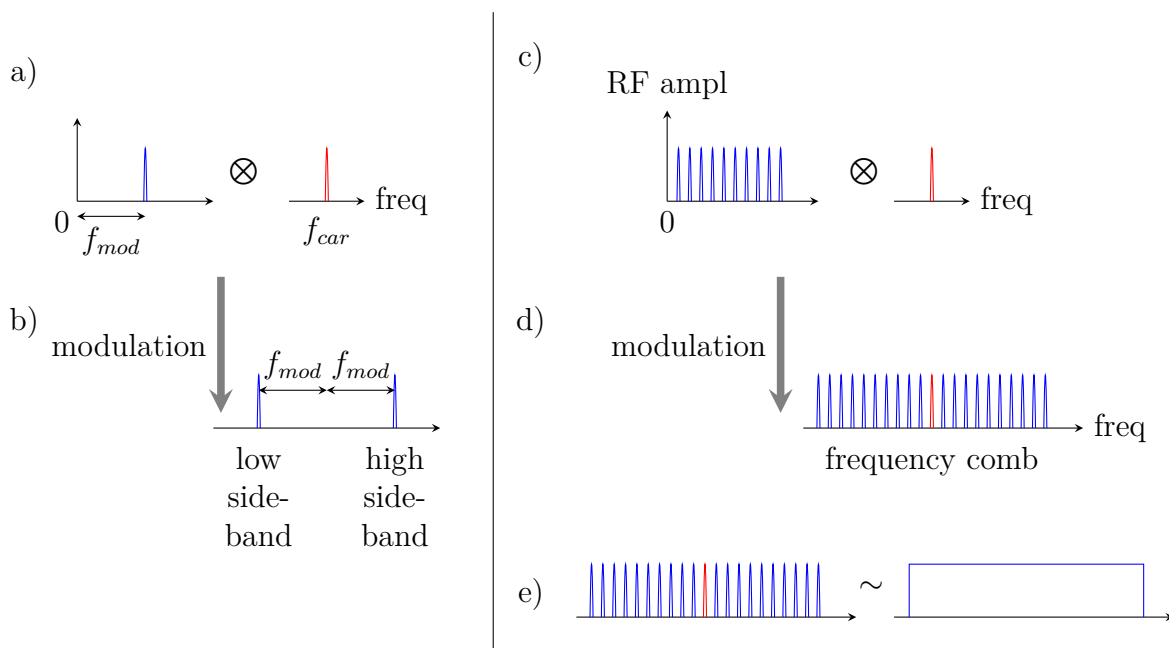


FIGURE 3.8: Schematic illustration of the generation of a rf frequency comb that is used in inverse NMR experiments. First, in a) we consider a simple case of two rf sine waves with frequency f_{car} and f_{mod} being modulated. b) A high and low frequency side band is formed either side of f_{car} and are separated by f_{mod} . c) Now, we consider modulating the carrier with an arbitrary waveform, which has a frequency comb shape that consists of a large number of closely spaced modes. d) Again high and low frequency sidebands are formed. e) This final frequency comb waveform approximates a spectral frequency band and can be arbitrarily positioned for use in inverse NMR experiments.

where A and B are arbitrary amplitudes and the low frequency side band has frequency $(f_{carr} - f_{mod})$ and the high frequency band has frequency $(f_{carr} + f_{mod})$. The remaining waveform is two sin waves separated by twice the modulation frequency centred on the carrier frequency (see the left half of Figure 3.8).

Now if we consider the modulating waveform as an arbitrary waveform with the shape of a frequency comb, which is itself computed by a summing over a series of sine curves. Again when the carrier is multiplied by the frequency comb using analogue modulation, we obtain low and high frequency side bands either side of the carrier. The carrier here is then typically suppressed to have the same spectral amplitude as the other modes (shown in the right half of Figure 3.8). In this way, we can create a rf frequency comb with densely spaced modes centred on the carrier frequency and this approximates a wide spectral band (Figure 3.8e). The rf signal must have a finite power and is designed to be evenly distributed over the entire spectral width of the comb w_{comb} . The number of modes in the comb is $N_m = w_{comb}/f_{MS} + 1$ and can range from a few hundred to a few hundred thousand modes.

We can create and sum two such frequency combs and one is used as the rf band on the low frequency side of the gap and one on the high frequency side to form the inverse NMR waveform (see Figure 3.7d). We can control the total width of the excitation so that it covers an entire nuclear isotope's resonance and the width of the gap (which dictates the resolution) by carefully choosing the width and carrier frequency of the two combs. The phases $\delta\phi_m = (m - 1)/(2N_m)$ of each mode are chosen to minimize the peak envelope power compared to the average power (known as the crest factor). The amplitude of the applied rf field used in the inverse NMR measurements had a peak value of $B_{rf} \lesssim 0.3$ mT and the root mean square value was $\sqrt{\langle B_{rf}^2 \rangle} \approx 0.15$ mT, which caused the sample to heat up by < 1 K.

3.4.4 NMR hardware

In this section, we describe the physical equipment required to apply the frequency combs to the sample in inverse NMR measurements. A schematic circuit diagram summarizing the important components are shown in Figure 3.9. As mentioned in the last section, two combs are required - one for the low frequency and one for the high frequency side of the gap. The carriers and arbitrary waveform envelopes are created and stored in the memory of two arbitrary waveform generators (Agilent 81150 and Agilent 33600). The applied rf signal is created by using external analogue mixers with “carrier 1” and “envelope 1” mixed together to form the low frequency spectral band and “carrier 2” and “envelope 2” mixed to form the high frequency band. The final shape of the applied rf waveform is achieved by using an analogue summator to add together the two bands.

The waveform is then sent to a 30 W class A power amplifier and a directional coupler. Most of the time the signal passes straight through this coupler but for some calibration tests for the matching, the reflected signal can be measured. The amplified rf excitation is coupled to the rf excitation coil through 50 Ω coaxial cables. The pickup coil can then be used to monitor the transmitted rf waveform with an Agilent EXA spectrum analyser in the frequency domain (or an oscilloscope for the time domain).

The rf excitation coil is placed very close to the sample < 1 mm and the amplitude of the rf field at the position of a dot depends on the transmission and reflection coefficient of the coil. This depends on the load impedance which in turn depends on the frequency of the applied rf field. This is not equivalent to the 50 Ω impedance of the coaxial cables and so the system is “mismatched” and a significant amount of rf signal will be reflected back to the source and not transmitted to the sample. To match the coil, an additional

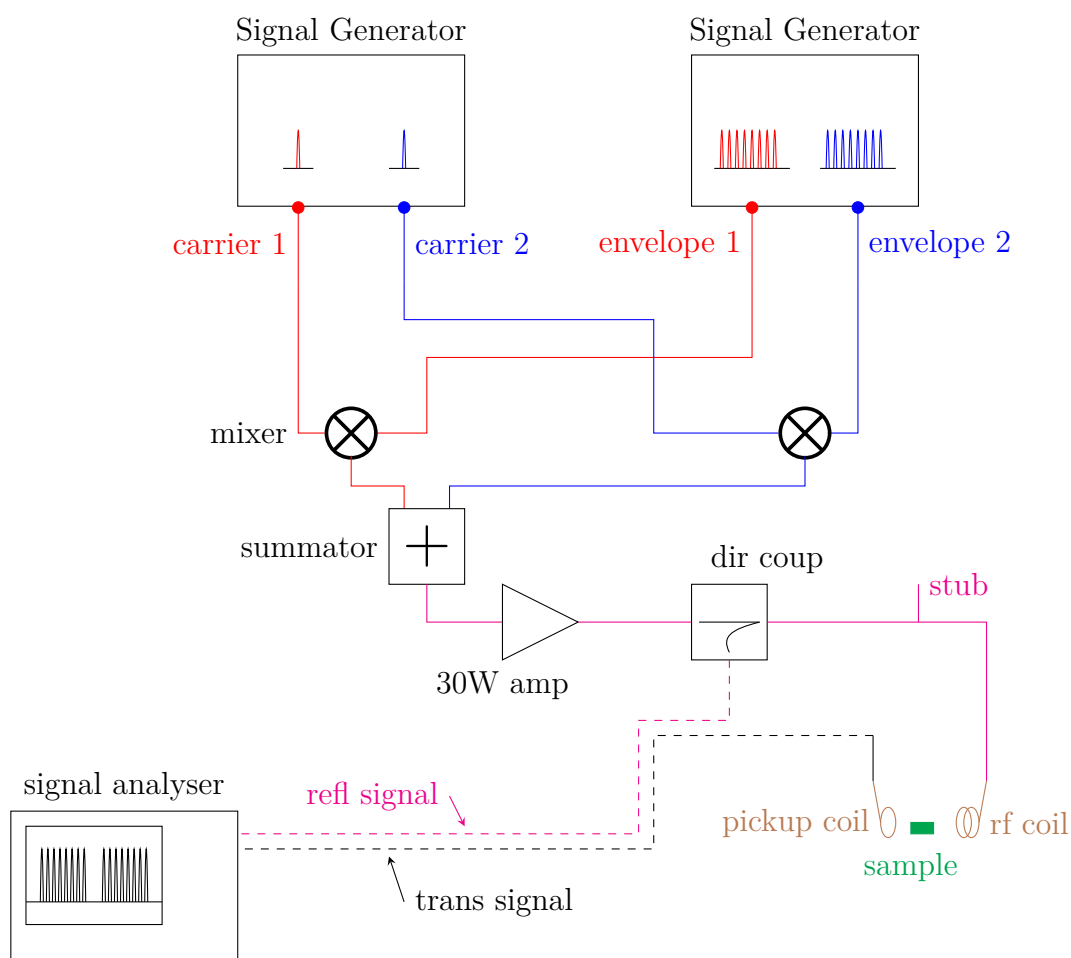


FIGURE 3.9: Circuit diagram for the applied rf waveform in inverse NMR experiments. Two sets of carriers and envelopes are stored in arbitrary waveform generators. The final shape of the waveform is created using external analogue mixers and a summator and then passed through a 30 W amplifier. This amplified rf field is applied through an rf coil placed near the sample via a variable length of $50\ \Omega$ coaxial cable to ensure broadband matching. The reflected signal (through the directional coupler) and the transmitted signal (through the pickup coil) can be monitored with a signal analyser.

“stub” line was added to the circuit, which consists of another coaxial cable connected in parallel to the main cable going to the coil. By applying a rf broadband noise waveform (> 100 MHz bandwidth) and changing the various lengths of cable through an iterative procedure, good matching can be achieved by monitoring the transmitted rf spectrum through a signal analyser. We require matching over a broad range of upto 30 MHz and this is not possible to execute perfectly with a real rf circuit. However, we adjust the cable lengths until the mismatched circuit forms a flat transmission profile within about 2 dB over the width of the frequency combs.

The shape that is created in the inverse NMR waveform is supposed to have no spectral amplitude within the gap and an evenly distributed amplitude across all the modes. But

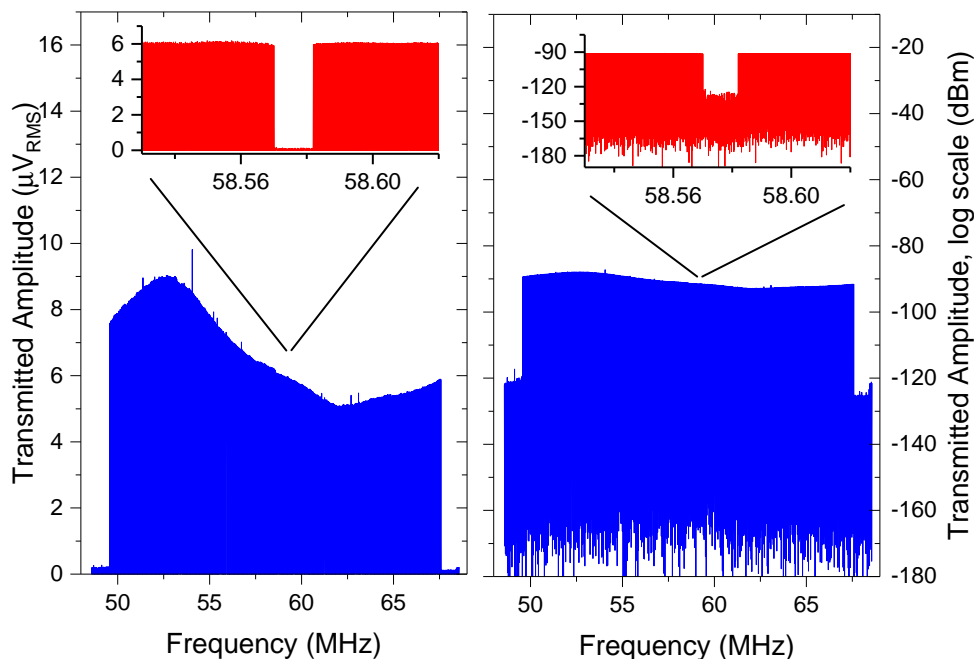


FIGURE 3.10: Transmitted radiofrequency waveform detected using a signal analyser via the pickup coil, which was used to measure the ^{75}As isotope in the In-flush sample. The gap is centered on the ^{75}As resonance frequency at $B_z = 8$ T which is 58.576 MHz and the total width of the band is 18 MHz and the gap width is 12 kHz. Left panel: The transmitted waveform on a linear amplitude scale and a broad frequency scale with a span of about 20 MHz (inset shows a zoomed in spectra with span ≈ 100 kHz to explicitly monitor the narrow gap). Right panel: The same transmitted waveform as the left panel but shown with a logarithmic amplitude scale. The matching can not be perfect across the whole 18 MHz range but on the log scale, the entire band is flat to within about ~ 2 dB. There is a small rf power within the gap due to imperfections with the amplifier but the power spectral density of the band is at least 30 dB (1000 times) larger than the power density within the gap (see inset of right panel). The waveforms appear as bands because the modes of the frequency comb are closely spaced - here a mode spacing of $f_{MS} = 125$ Hz was used.

because of noise in the rf circuit and non-linear intermodulation distortions of the amplifier, the rf amplitude in the gap is not strictly zero. Here we calibrate the applied power so that the spectral power density in the gap is at least 1000 times smaller (30dB) than the spectral density in the comb. An example of the broadband matching and the depth of the gap achieved for inverse NMR measurements of ^{75}As on the In-flush sample is shown in Figure 3.10.

Chapter 4

Nuclear spin properties of single CdTe/ZnTe quantum dots

Due to the large quantum confinement and the strong light matter interaction in self assembled semiconductor quantum dots, a lot of research in the last few decades has gone into attempting to store, process and transmit information in these quantum systems. However, the large nuclear spin fluctuations in Group III-V semiconductor, self assembled quantum dots present significant challenges in using the spin of the trapped electron for qubit applications as it suffers from fast spin decoherence [10, 54–57]. Another alternative system of group IV semiconductors such as defects in silicon and diamond have large coherence times exceeding 200 μs [164, 165], but they do not couple efficiently to optical fields due to their indirect band gap.

Here, we attempt to combine the advantages of both systems by using a system of optically active self assembled quantum dots where most nuclear isotopes have no nuclear spin. We study the II-VI system of CdTe/ZnTe quantum dots which contain isotopes that are mostly spin free, while the dot can still be populated optically as both CdTe and ZnTe are direct bandgap semiconductors (as is the case for InGaAs QDs).

A lot of research has been done into the nuclear spin system in III-V QDs and advanced experimental techniques now exist to control and detect the nuclear spin polarisation (some of them will be covered in the other experimental chapters of this thesis). However, studies of the nuclear spin properties in II-VI dots are few and this is directly related to the fact that there are fewer nuclear spins. The total achievable spin polarisation in such a dilute nuclear spin bath is small and it is difficult to detect any signal from changes in this small magnetization. The previous work on this topic have studied the nuclear spin

properties indirectly by detecting changes in the electron spin dynamics [166–169]. Such experiments can only be performed at low magnetic fields of $B < 0.5$ T.

Here we present the first direct observations of the Overhauser shifts in the photoluminescence spectra of single self assembled CdTe/ZnTe dots at high magnetic fields. This regime of large fields is of interest because the nonsecular electron-nuclear spin interactions are suppressed and this extends the electron spin lifetime. We explore important fundamental properties of the nuclear spin polarisation, its dynamics and the NMR spectra of the individual nuclear isotopes, which are detected optically.

4.1 Comparison of nuclear environment in II-VI and III-V quantum dots

We begin by looking at the important differences between the II-VI QD system and the III-V dot system specifically with regards to the properties of the nuclear spins. Firstly, the self assembled CdTe/ZnTe dots that are formed are much smaller than in InGaAs dots. It is estimated in our CdTe/ZnTe samples (see Section 4.2) that a typical dot contains approximately 5000 nuclei, which is at least an order of magnitude less than in a InGaAs dot, where there are usually $10^4 - 10^5$ nuclei.

Secondly and most importantly, the most abundant naturally occurring nuclear isotopes in CdTe/ZnTe have no nuclear spin $I = 0$. The small fraction of nuclei that do possess a spin are all isotopes with spin $I = 1/2$ and therefore have no nuclear quadrupolar moments. It can be seen from Table 2.1 in Section 2.3.4 that for cadmium there are two stable isotopes ^{111}Cd with abundance $\rho_{(^{111}\text{Cd})} = 12.8\%$ and ^{113}Cd with $\rho_{(^{113}\text{Cd})} = 12.22\%$ and only one isotope for tellurium ^{125}Te with $\rho_{(^{125}\text{Te})} = 7.07\%$. The other isotope for tellurium ^{123}Te has such a small fraction $\rho_{(^{123}\text{Te})} = 0.89\%$ that it will not be possible to detect with the methods used in this work and it is ignored. Also note that there will be a small amount of zinc present in the dot due to intermixing and its isotope ^{67}Zn is a quadrupolar isotope ($I = 5/2$), but it too has a small abundance of 4.1% [11]. For a quadrupolar isotope which will experience significant quadrupolar broadening and with such a low abundance, it will be very difficult to detect any NMR signal and will not contribute significantly to the overall nuclear spin polarisation. Additionally, ^{67}Zn has a smaller gyromagnetic moment and is lighter than Cd and Te, which reduces the hyperfine constant.

This CdTe/ZnTe dot, where only a fraction of all nuclei present in the sample have a spin, can be thought of as a dilute nuclear spin bath as opposed to the dense and strongly

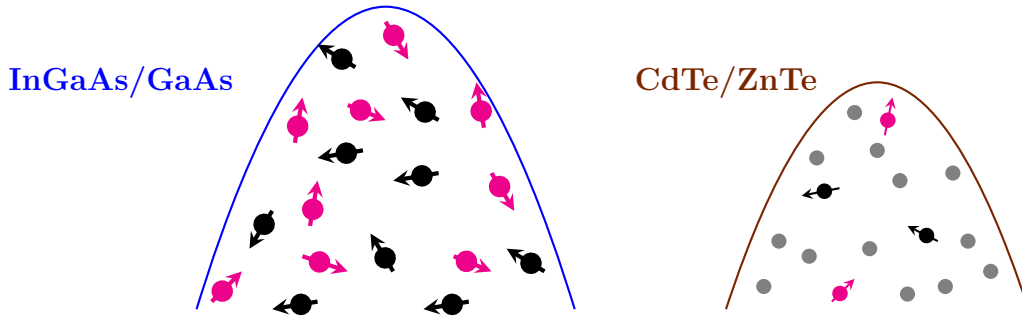


FIGURE 4.1: Schematic illustration comparing the nuclear spin baths in semiconductor quantum dots. On the left (in blue) is the dense nuclear spin bath found in InGaAs/GaAs dots and all the quadrupolar nuclear spins $I \geq 3/2$ are shown with thick arrows. On the right (in brown) is the dilute nuclear spin bath found in CdTe/ZnTe dots, which are smaller (contain less nuclei) and only a fraction of them possess a nuclear spin; most nuclei have no spin $I = 0$ (shown as grey dots) and the few nuclei with a spin are spin $I = 1/2$ isotopes (depicted with thin arrows).

fluctuating nuclear spin bath in InGaAs dots where all nuclei possess quadrupolar isotopes. A schematic comparison of the two systems is shown in Figure 4.1. It is also possible that the bath can be diluted further by selection of specific isotopes with $I = 0$ and this is not possible in III-V dots.

The obvious consequence of there being less nuclear spins is that there will be a much smaller maximum nuclear spin polarisation that can be created. In InGaAs dots the maximum Overhauser shift is $> 100 \mu\text{eV}$ and it is observed as a clear effect. In our CdTe/ZnTe dots, the maximum OHS achievable is estimated to be only a few μeV , so we expect to observe a change in the Zeeman splitting which is much smaller than the PL linewidths of these dots which can be as narrow as $\sim 20 \mu\text{eV}$. This is the main reason it is so difficult to measure the nuclear spin properties directly as the maximum available hyperfine shift is so low.

Finally, there can be a significant effect due to the Knight field which is caused by the small dot size and low nuclear spin density. The maximum field is estimated in the literature to be $B_e^{max} \approx 100 \text{ mT}$ for the Cd nuclei [169] whereas in InGaAs dots, the typical Knight field is of the order $\sim 10 \text{ mT}$ [131]. The Knight field amplitude varies across the dot and follows the shape of the electron wave function density and so is different for each nuclear site. We will see in Section 4.7, that the Knight field strongly influences the shape of the optically detected NMR spectra of the nuclear isotopes.

4.2 CdTe/ZnTe self assembled quantum dot samples

Here we describe the two samples used in this work. Both samples were grown with MBE in the University of Warsaw in Poland and acknowledgements go to our collaborators W. Pacuski for growth and especially Jakub Kobak who was involved in the sample growth as well as directly involved in the experimental work here at Sheffield. The general procedure is similar to that described for III-V QDs (see Section 2.1 and 3.1), but we will describe the specific properties and differences here.

Sample A contained a low density of single self assembled quantum dots and Sample B contained single dot lines as well as emission from a quantum well. Note that most experimental results on the nuclear spin phenomena were from sample B (with the quantum well), but sample A was measured first and unexpected shifts in the PL spectra were observed that resembled an Overhauser shift but were not caused by the nuclear spins. We briefly describe this effect in Section 4.4.1, before a full discussion is presented for the nuclear spin properties in Sample B.

Fabrication of the first sample (sample A) was performed on a GaAs:Si (100) substrate. After deposition of 1 μm ZnTe buffer layer, a CdTe film was grown by Atomic Layer Epitaxy. Though the lattice mismatch between CdTe/ZnTe (5.8 %) is only slightly smaller than InAs/GaAs (6.7 %), the formation energy for dislocations is lower[170]. Hence, to assist with 3 dimensional QD formation (as opposed to forming dislocations), an additional step is required which is not needed for III-V dot growth. For the first structure, such a step was realized with the commonly applied amorphous Te technique[170], where the substrate is strongly cooled (to ~ 100 °C) whilst Te is deposited onto the dot layer. This leads to a decrease of the surface energy and the thin CdTe film layer subsequently forms a low density of single quantum dots.

The second sample (sample B) was fabricated slightly differently. This sample contains not only QDs but also a quantum well (QW). First a GaAs:Zn (100) oriented substrate is covered by a 1.3 μm ZnTe buffer layer and then a 2 nm CdTe dot layer is deposited. Next, to induce formation of QDs and at the same time keep the QW in the structure, the substrate cooling time was reduced under a Te flux and so the deposition of amorphous Te was avoided. Finally, a 100 nm ZnTe cap layer is deposited. This procedure of sample fabrication results in a higher density of QDs compared to the first sample and can be seen from the broad PL spectra in Figure 4.2.

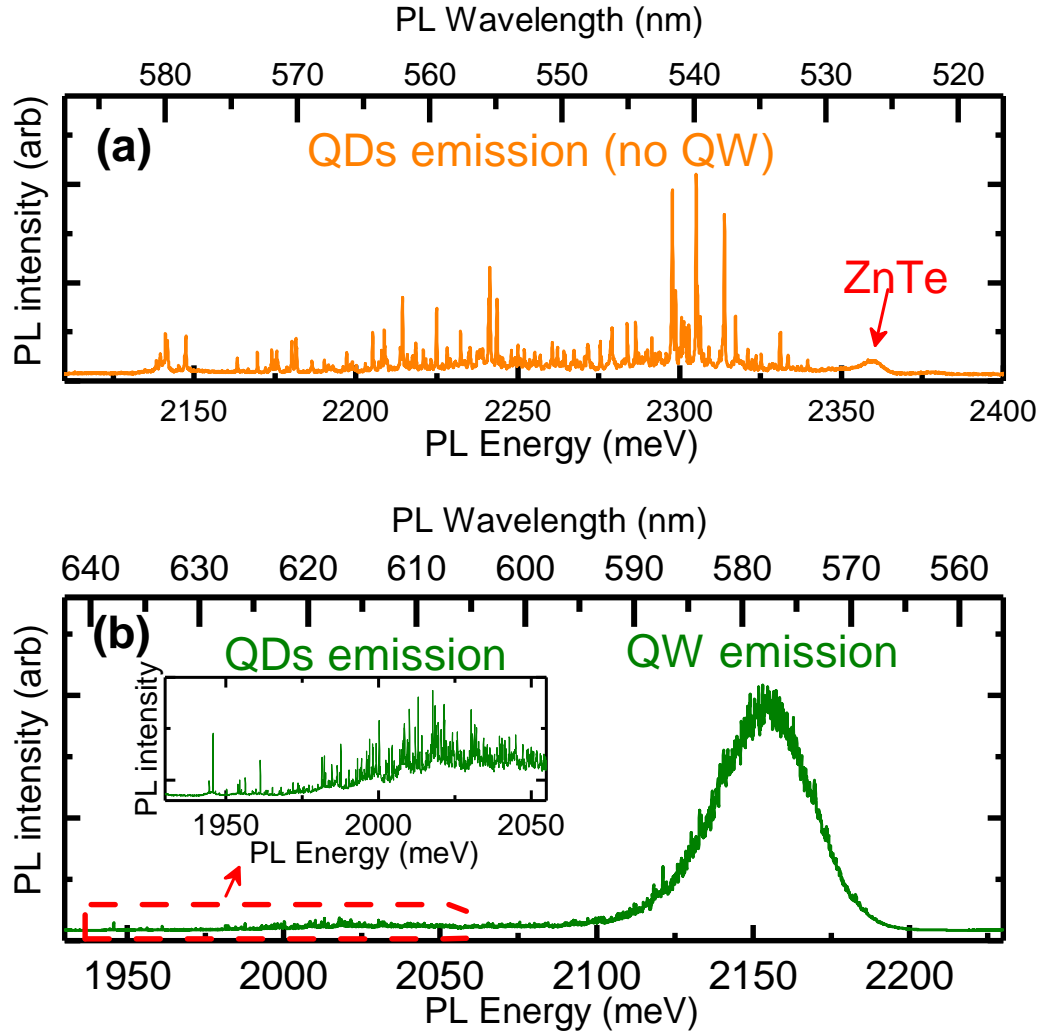


FIGURE 4.2: Broad range photoluminescence spectra taken from the CdTe/ZnTe QD samples used in this work at $B_z = 0$ T using 405 nm excitation. a) Sample A contains a low density of single dot lines and b) Sample B has a higher density of dots (the inset shows the magnified signal from the single dot region) accompanied by a quantum well.

Both samples are nominally undoped and are not embedded into any kind of cavity. This results in a lower PL signal compared to the III-V dots studied in the other chapters of this thesis. The broad range PL spectra measured for both samples are shown in Figure 4.2 and for Sample A, we observe a low density of single dot lines between 2130–2330 meV (\sim 530–580 nm) and for sample B, a higher density of lines is seen between 1930–2100 meV (\sim 590–640 nm) and a broad quantum well peak at \sim 2150 meV.

The additional step in the growth of these CdTe/ZnTe dots to assist with 3D dot formation (compared to the growth of InGaAs QDs) makes this a challenging material to obtain good quality single dot PL spectral lines. The charge environment surrounding the dot is more

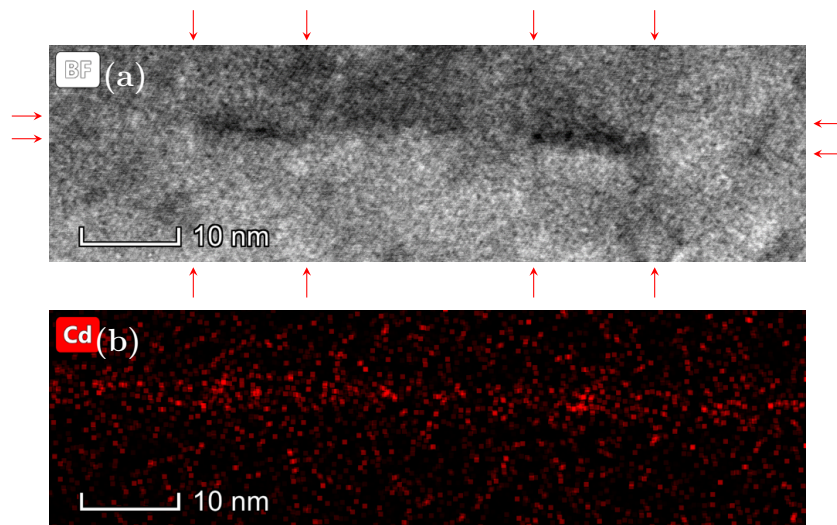


FIGURE 4.3: a) Bright field transmission electron microscopy (TEM) image of a cross section of Sample B. The dark regions indicate the presence of CdTe and the arrows show the approximate boundaries of two regions representing single CdTe quantum dots. b) Energy-dispersive X-ray (EDX) image of the same region as a) with the red dots (cadmium nuclei) showing there is an inhomogeneity in the distribution of cadmium atoms. An almost horizontal (with $\sim 2^\circ$ tilt) layer rich in Cd is seen in the EDX image and is attributed to the quantum well layer in Sample B.

disordered and there is significant evidence (as we shall see later in this chapter) of charge fluctuations surrounding the dot and intermittent occupation of the dot with carriers. This has a large impact of the noise in the spectral measurements as the emission lines are shown to exhibit spectral wandering [171] (see Appendix A).

Some basic analysis was performed using TEM images of the cross sections of the samples and acknowledgements go to our collaborators K. Sobczak and J. Borysiuk from the Faculty of Chemistry in the University of Warsaw for the TEM images. For sample A, only a small fraction of cadmium is detected and makes it difficult to obtain qualitative results. This complements the low density of QD lines observed in the PL spectra. For sample B (see Figure 4.3), a clear Cd rich region is observed and fluctuations of the Cd within the quantum well layer allow for the approximate size of the dots to be derived. The dots appear to be approximately cylindrical in shape and have a diameter of ~ 10 nm and a height of ~ 2.5 nm (marked by arrows in Figure 4.3a). The lattice constant of CdTe is $a_0 = 0.648$ nm and there are 8 atoms per unit cell, so we can estimate that the dot contains ~ 5000 atoms. This includes nuclei from all isotopes including those without any spin ($I = 0$) and is similar to the value of ~ 8000 nuclei in a single dot that was estimated from similar samples [169].

4.3 Experimental hardware changes to measure nuclear spin properties in CdTe/ZnTe dots

The general experimental setup described in Chapter 3 still applies to these measurements on CdTe/ZnTe QD samples. The samples are kept at $T = 4.2$ K in a liquid He bath cryostat and external magnetic fields upto $B_z = 8$ T can be applied. Most of the nuclear spin work on sample B is done at $B_z = 2.5$ T and we use the Faraday configuration. Most measurements still involve the use of pump-probe techniques and we measure micro photoluminescence spectra of the neutral exciton line X^0 and detect changes in the Zeeman split lines. In this section, we describe the main differences in the experimental setup that are required to measure the nuclear spin properties of CdTe/ZnTe dots compared to InGaAs dots.

One important difference is the change in the emission wavelength region of the dots. The InGaAs dots emit in the infra-red part of the electromagnetic spectrum from $\sim 890 - 960$ nm, while the dots studied in the CdTe/ZnTe sample B show PL emission from $590 - 640$ nm which is visible light. Hence, all of the necessary optical components (waveplates, polarisers, mirrors and lenses) were changed to have efficient transmission at this wavelength of light. Here we also use non-resonant excitation, but unlike the 850 nm diode lasers used for InGaAs dots, we used a diode pumped solid state (DPSS) laser emitting at 532 nm for sample A and a Vortran Stradus 561 nm (with higher energy than the quantum well emission), 50 mW laser for sample B.

The other main difference is that the nuclear spin dynamics are much faster (see Section 4.6) for the II-VI quantum dot system. So the equipment used, needed to have quicker response times so that the various experimental parameters could be changed faster than the evolution of the nuclear spin polarisation. To achieve the pump-probe type cycles, a single 561 nm laser was used and the power was changed between the nominal pump power (about $\sim 160 \mu\text{W}$ to polarise the nuclear spins), the nominal probe power (about $\sim 20 \mu\text{W}$ to detect the splitting) and no power (during the dark time). Analogue modulation of the diode current in the 561 nm laser allows us to control the power with a fast response time of $< 1 \mu\text{s}$. This is in contrast with the \sim ms response time of the mechanical shutters for the individual pump/probe laser for III-V dots. The polarisation of the laser is controlled using a Leysop low voltage electro optical light modulator (EOM) with response time ≈ 500 ns. This is essentially a Pockels cell where a voltage applied to the EOM rotates the polarisation axis of the beam that passes through. The pump pulse is circularly polarised, so the beam passes through a linear polariser, then the EOM and then through a

quarter-wave plate (QWP) and a voltage is applied to the EOM such that the polarisation axis of the beam is 45° to the QWP axis. The probe pulse is linearly polarised, so a voltage is applied to the EOM so that the polarisation axis is rotated to be along the QWP axis. To detect the PL signal with a fast switching time, we use an acousto-optical modulator (AOM) with a faster response time of $\approx 1.1 \mu\text{s}$ or a liquid crystal shutter with a slower response time of $\approx 4.5 \text{ ms}$ (but a higher transmission of light). Unlike a mechanical shutter that blocks all of the beam from passing through, these components have a characteristic on/off extinction ratio which was measured to be > 1000 for the AOM and > 5000 for the liquid crystal shutter. The appropriate component was chosen depending on the experiment, for example in dynamics measurements, the AOM was used for the faster response, but for the NMR spectra, the liquid crystal shutter was used to ensure a better extinction ratio and a better signal.

It was anticipated that any spectral shifts due to the Overhauser shift in such a dilute nuclear spin bath were small (on the order of a few μeV). The narrowest linewidths measured for the CdTe/ZnTe QDs in sample B were about $20 \mu\text{eV}$ and were limited by the resolution of the spectrometer. This spectral width of light falls onto about 2 pixels on the CCD camera (out of a total of 1340 pixels) and it was found to be very inaccurate to measure changes in splitting of a small fraction of a linewidth due to the inability to resolve the spectral spot within one pixel. So after the exit of the spectrometer, we placed a pair of achromatic doublet lenses with focal lengths ($f = 40 \text{ mm}$ and $f = 150 \text{ mm}$) pointing in opposite directions, which magnifies the light coming out of the spectrometer and onto the CCD by a factor of 3.75. These magnifying lenses, along with taking multiple spectral repeats, averaging and Gaussian fitting provides sufficient spectral resolution for the direct detection of splitting changes less than $0.5 \mu\text{eV}$.

4.4 Experimental observations in CdTe/ZnTe QD sample A

4.4.1 Large spectral shifts in continuous wave spectra

The first sample studied was sample A and initially only cw PL measurements were performed by applying a non-resonant laser with either σ^- or σ^+ excitation and observing the change in splitting. An example of such a spectrum of a single CdTe/ZnTe dot in sample A and sample B is shown in Figure 4.4. Both samples show narrow spectral lines

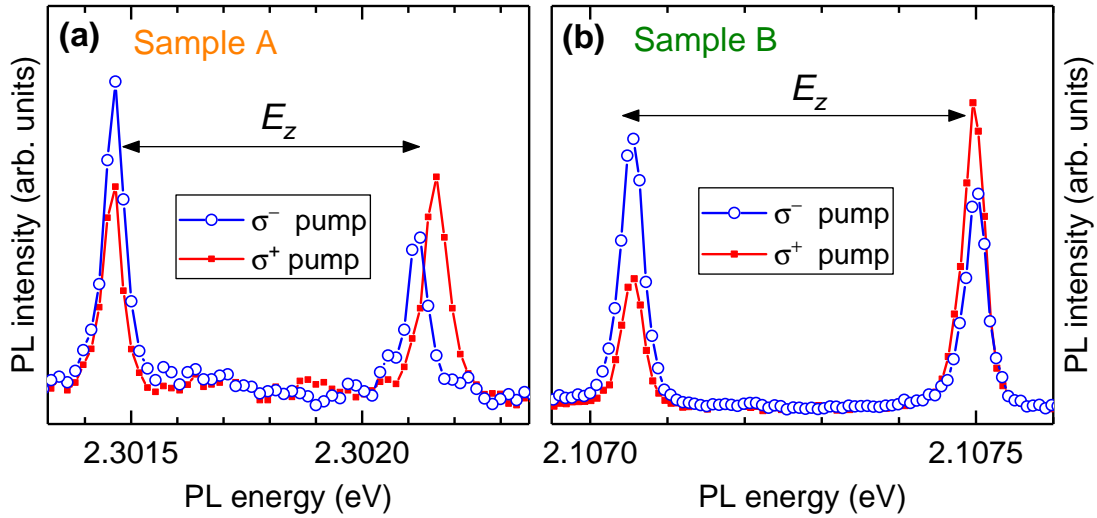


FIGURE 4.4: a) Continuous wave (cw) PL spectra of the neutral exciton X^0 of a single CdTe/ZnTe QD from sample A at $B_z = 4$ T using a non-resonant 532 nm excitation and a power of 2.2 mW. b) Similar cw PL spectra of a dot in sample B with 200 μ W, 561 nm excitation at $B_z = 2.5$ T. Circularly polarised light was used and blue circles represent σ^- excitation and the red squares represent σ^+ excitation. For sample A, a clear change in splitting is visible of $(E_Z^{\sigma^-} - E_Z^{\sigma^+})/2 \approx -22$ μ eV which is unrelated to nuclear spin effects, but for sample B a small change of $(E_Z^{\sigma^-} - E_Z^{\sigma^+})/2 \approx 1.5$ μ eV is measured when the data is fit with Gaussian lineshapes and is related to the nuclear spin polarisation.

from individual excitons and the narrowest dot lines have a full width at half maximum FWHM measured to be 30 μ eV in sample A and 20 μ eV in sample B.

For the dot in sample A, a clear change in splitting of $(E_Z^{\sigma^-} - E_Z^{\sigma^+})/2 \approx -22$ μ eV is visible. This was initially unexpected as such a large change in splitting is thought to be impossible even for a fully polarised nuclear spin bath in these dots (calculated to be about ± 4 μ eV in Section 4.7). However when such a measurement was conducted using the pump-probe technique, no measurable change in splitting was observed with either 532 nm or 561 nm pumping. To investigate further, the excitation polarisation was switched rapidly between σ^+ and σ^- in sample A and the measured change in splitting was found to occur on a timescale quicker than 500 ns. This was the fastest timescale that was investigated and was limited by the response time of the EOM. This is too quick to be caused by the dynamics associated with the nuclear spin polarisation and the exact cause of this effect would require additional measurements to deduce. In sample A, out of approximately 90 individual dots that were measured using cw PL spectra, at least 10 dots showed a clear change in splitting (> 5 μ eV). This effect is only observed (when using 532 nm excitation and only for QDs with a ground state energy emission in a small range of wavelengths between $\sim 537 - 539$ nm with a small detuning from the laser. It is possible that the fast timescales are related to electron/hole spins which recombine on a timescale on the order

of 300 ps in CdTe/ZnTe QDs [172]. It may also involve the dipolar or exchange interaction with charge spins in nearby dots or defects. In any case, this result shows that a change in the Zeeman splitting observed in the PL spectra alone is not an unambiguous signature of dynamic nuclear polarisation and additional measurements such as the pump-probe cycle or nuclear magnetic resonance techniques are required to verify the effects of the nuclear spins.

In sample B, a similar cw PL spectrum reveals a much smaller change in splitting of $(E_Z^{\sigma^-} - E_Z^{\sigma^+})/2 \approx 1.5 \mu\text{eV}$, but crucially is also observed in pump-probe spectra and so this change in splitting survives for much longer than the effect measured in sample A and is attributed to nuclear spin polarisation effects, which was confirmed by NMR measurements (see Section 4.7). Another point of note is that in both samples, cw excitation using circularly polarised light produces a non-zero spin polarisation of the excitons. This is visible in the PL spectra of Figure 4.4 as an increase (decrease) of the low (high) energy peak using σ^- (σ^+) polarised excitation. However, non-zero nuclear spin polarisation occurs only in sample B and this provides evidence that the mechanism of DNP is not related to electron-nuclear couplings during the radiative recombination of the ground state exciton (it is related to the quantum well states, see Section 4.5).

4.4.2 Electron and hole g-factors and assignment of the sign of nuclear spin polarisation

In Sample A, the dark exciton states could be observed and were used to calculate the g-factors for the electron and hole, which were then used to determine the sign of the hyperfine shift. Figure 4.5 shows the cw PL spectra of a single quantum dot in sample A under a large magnetic field $B_z = 8 \text{ T}$. When a large excitation power is applied ($P_{exc} = 400 \mu\text{W}$, Figure 4.5a), two Zeeman split bright exciton states are observed ($\uparrow\downarrow$ and $\downarrow\uparrow$, where \uparrow/\downarrow represents the hole spin and \uparrow/\downarrow the electron spin). However when a low power is applied ($P_{exc} = 7 \mu\text{W}$, Figure 4.5b), two additional lines can be seen, which correspond to the dark exciton states ($\uparrow\uparrow$ and $\downarrow\downarrow$, see Section 2.2.1). These states become optically active by mixing with the bright states because of the asymmetry potential in the quantum dot [173] and have previously been observed in CdTe/ZnTe QDs [174]. These states can only be observed at low power as they are only weakly optically active and have a small dipole moment. It is observed that one type of circular polarisation enhances one bright and one dark transition. For example, the low energy bright and the high energy dark transition states (the two middle peaks in Figure 4.5b) are enhanced by σ^- excitation

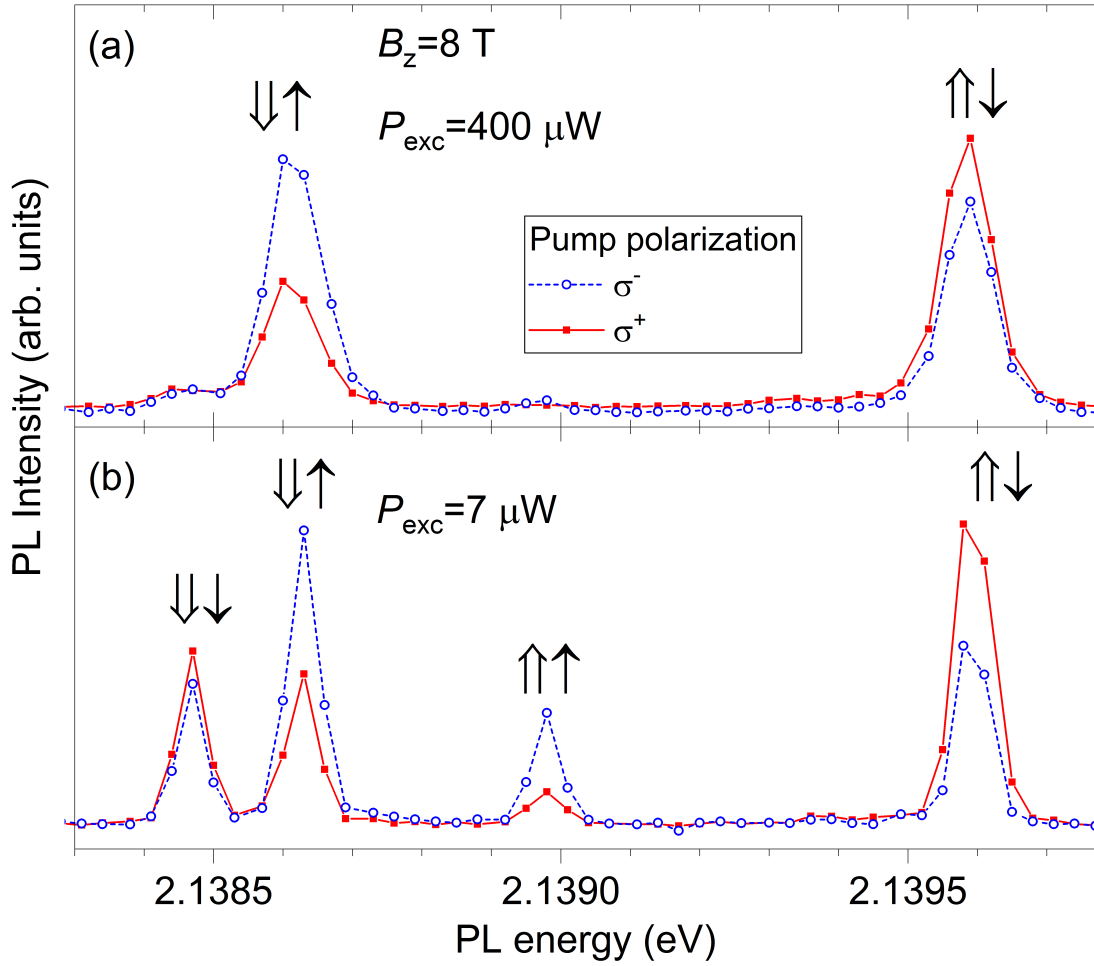


FIGURE 4.5: a) Continuous wave PL spectra of the neutral exciton in a single dot in sample A at $B_z = 8$ T using σ^- (blue dashed lines) and σ^+ (red solid lines) excitation. a) At high power $P_{exc} = 400 \mu\text{W}$, two Zeeman split bright exciton states are observed and b) at low power $P_{exc} = 7 \mu\text{W}$, both bright and dark exciton states are seen. Note \Uparrow/\Downarrow represents the hole spin and \Uparrow/\Downarrow the electron spin projection.

and these two states must have the same electron spin projection since the hole spin is usually lost during relaxation. This only tells us which two states share an electron spin projection and there are two possible options for the spin states - the one labelled in Figure 4.5 and another one with all electron and hole spin projections reversed.

The correct assignment of the exciton state to the spectral lines can be deduced by calculating the electron and hole g -factors. We use the energies of the bright and dark exciton states (explicitly written out in Equations 2.6 and 2.7 in Section 2.2.5) and calculate the g -factors for the dot in sample A. Since we only want to assign the states, the calculation was simplified by ignoring the small contributions from the dark exciton fine structure splitting δ_D . From PL spectra measured in a low magnetic field, we observe that $\delta_B \approx 60 \mu\text{eV}$ and we calculate that $g_e \approx \mp 0.49$ and $g_h \approx \pm 1.59$. The bulk electron g -factor in CdTe is

$g_e \approx -1.59$ [175] and ZnTe is $g_e \approx -0.6$ [176], which suggests it should be negative in CdTe/ZnTe quantum dots, as was confirmed in previous work [177]. So we can conclude that $g_e \approx -0.49$ and $g_h \approx +1.59$ and the spin states are labelled correctly in Figure 4.5.

Such spectra on several individual QDs in sample A revealed similar values of g_e and g_h and the dark exciton states are not observed in sample B. However, the Zeeman splitting of the bright states which is governed by $g_h - g_e$ is very similar to sample A, suggesting the individual g_e and g_h values are also similar. Also, when the $\uparrow\downarrow$ state recombines, it emits a circularly polarised photon with a $+1$ momentum (σ^+) and the $\downarrow\uparrow$ state, a photon with -1 momentum (σ^-). Hence in the PL spectra, σ^+ polarised excitation enhances emission from the $\uparrow\downarrow$ state, whereas σ^- polarised excitation enhances emission from the $\downarrow\uparrow$ state.

Having assigned the correct labels to the exciton spin states, we can now identify the sign of the nuclear spin polarisation. The Hamiltonian for the hyperfine interaction between the electron spin $\hat{\mathbf{s}}$ in the conduction band and nuclear spin $\hat{\mathbf{I}}$ has the form $\hat{H}_{hf} \propto A(\hat{\mathbf{s}} \cdot \hat{\mathbf{I}})$ (see Section 2.3.1), where A is the hyperfine constant whose sign depends on the sign of the gyromagnetic ratio γ_N (see Section 2.3.1). The primary DNP mechanism in quantum dots is the spin conserving electron-nuclear spin flips through the hyperfine interaction [9]. Because of this spin conserving property of the interaction, the signs of the non-equilibrium electron and nuclear spin polarisations are the same. So for example, if the electron spin state is initialised with a positive \uparrow (negative \downarrow) spin projection, the average nuclear spin polarisation will also be positive ($\langle I_z \rangle > 0$) (negative $\langle I_z \rangle < 0$), hence the product $(\hat{\mathbf{s}} \cdot \hat{\mathbf{I}})$ is always positive. Therefore, the sign of the Overhauser shift which acts on the exciton state is only determined by the sign of the hyperfine constant A .

For III-V semiconductors, all isotopes have positive γ_N and so $A > 0$ (see Table 2.1). So if a cw circularly polarised excitation enhances an exciton transition line, that line shifts to higher energy due to the Overhauser shift and this occurs regardless of the electron spin projection $s_z = \pm 1/2$ [178]. But for CdTe/ZnTe dots, the most abundant non-zero spin isotopes of Cd and Te have negative γ_N and $A < 0$, so the exciton state whose PL signal is enhanced with a given circular polarisation will shift to lower energy as a result of the Overhauser shift. Using the pump-probe technique, we measure for sample B that σ^+ polarisation decreases the Zeeman splitting E_Z and σ^- increases E_Z , which agrees well with this analysis and shows that DNP is produced by secular electron-nuclear spin flips.

4.5 Basic properties of the dynamic nuclear polarisation in CdTe/ZnTe dots: power and magnetic field dependence

The nuclear spin polarisation in a single CdTe/ZnTe dot was only observed in sample B using pump-probe techniques (see Figure 4.6b). Unless otherwise stated, the typical pump time used was $T_{Pump} = 40$ ms with a power of $160 \mu\text{W}$ and a typical probe time used was $T_{Probe} = 1$ ms with a power of $20 \mu\text{W}$. Between the pump and probe pulse, there was typically a delay of $T_{Wait} = 4.5$ ms (limited by the liquid crystal shutter response) and hence only effects that are persistent over such a timescale were measured (as should be the case for nuclear spin polarisation). The detected Overhauser shift is much smaller than the linewidth of the dot, but out of ~ 120 dots that were measured in sample B, about ~ 20 showed a clear OHS signal of $> 2 \mu\text{eV}$ (most dots showed a small OHS $\leq 2 \mu\text{eV}$).

The raw pump-probe PL spectrum is shown in Figure 4.6 for a single dot. The measured change in splitting is only $(E_Z^{\sigma^-} - E_Z^{\sigma^+})/2 \approx 2 \mu\text{eV}$ and is much smaller than the PL linewidth of the transition line (FWHM $\approx 20 \mu\text{eV}$) but can be detected by Gaussian fitting of the peaks and averaging over spectral repeats.

To understand the mechanism of DNP further in CdTe/ZnTe QDs, a pump power dependence measurement was conducted where only the pump power was changed and the probe power and all other experimental parameters were kept constant and is shown in Figure 4.7. The total X^0 PL intensity is observed to saturate at $\approx 50 \mu\text{W}$ in this dot (under cw excitation) and is typical for all dots studied in this sample. The Zeeman splitting at low pump power does not depend on the pump polarisation and a splitting of $E_Z \approx 392 \mu\text{eV}$ is observed under both σ^+/σ^- pumping. As the power is increased, there is a clear increase (decrease) in splitting with σ^- (σ^+) pumping and this reaches a maximum (and saturates at $\Delta E_Z^{\sigma^-,max} \approx +2.3 \mu\text{eV}$ and $\Delta E_Z^{\sigma^+,max} \approx -2.4 \mu\text{eV}$) at approximately the same power as the PL signal saturates and again this is seen for most dots in the sample. This situation is very different to III-V QDs where DNP under non-resonant pumping is observed to be most efficient when the pump power is much higher than the saturation of the PL ground state recombination signal and this was attributed to the effect of multi-exciton and excited states within the QD that contribute to the mechanism of DNP [134, 173, 179]. Here in CdTe/ZnTe dots, we see DNP only in the sample containing the QW and DNP reaches a maximum with saturation of the X^0 PL intensity. This suggests that the method of DNP is through a relaxation cascade of the electron-hole pair, where the quantum well is

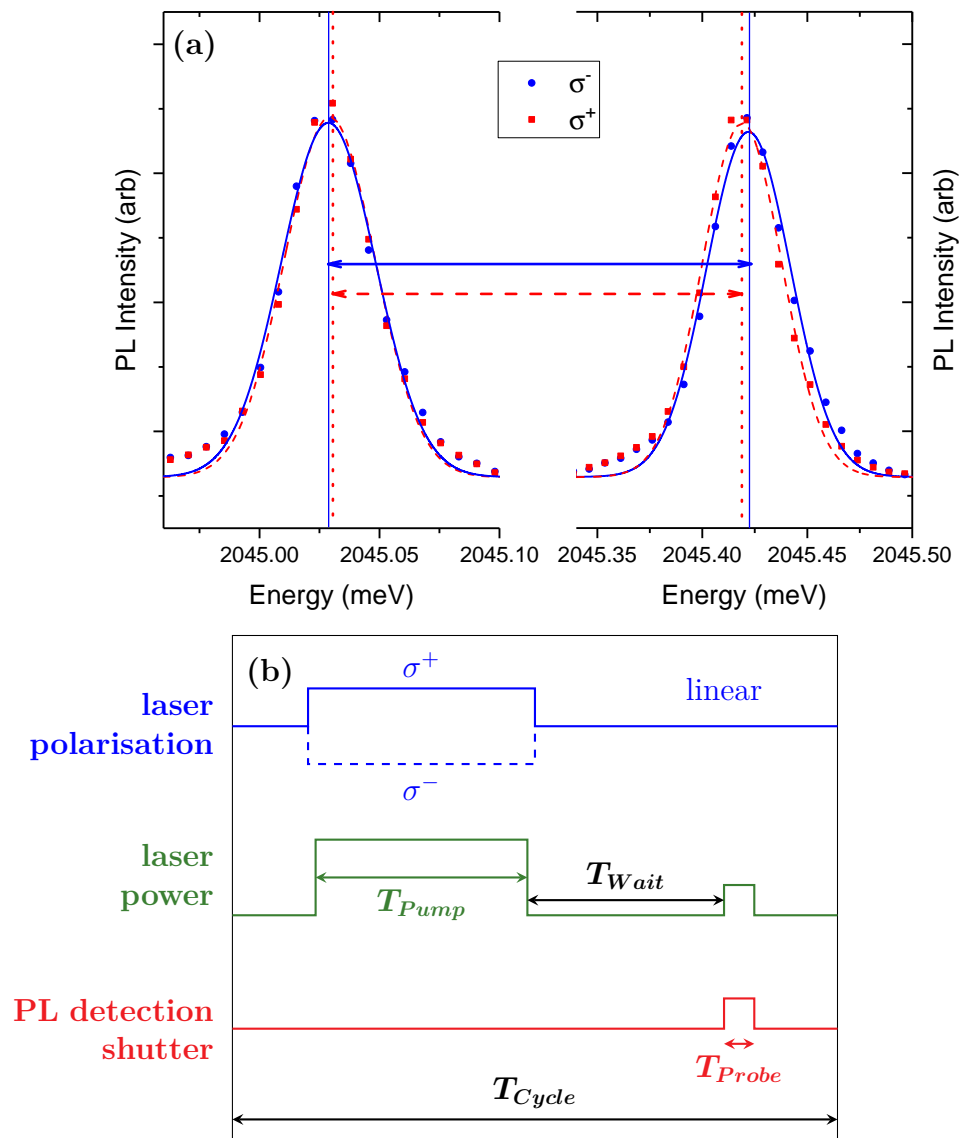


FIGURE 4.6: a) Pump-probe PL spectra of the neutral exciton X^0 in a single dot in sample B at $B_z = 2.5$ T using σ^- (blue circles, fit shown by solid lines) and σ^+ (red squares, fit shown by dashed lines), under excitation with a 561 nm laser. b) Pump-probe measurement cycle timing diagram used for CdTe/ZnTe dots.

an intermediate state and X^0 is the final state. Such broad energy intermediate states can assist with DNP by reducing the strict energy conservation required for nuclear spin flips [180].

Though the Overhauser shift increases approximately monotonically with pump power, a high power incident on to the sample causes severe fluctuations in the charge environment around the dot. So the pump power was chosen to be limited to $160 \mu\text{W}$, which induced an Overhauser shift below the maximum observed value but reduced the spectral wandering observed in the PL spectra. This is discussed in more detail in Appendix A.

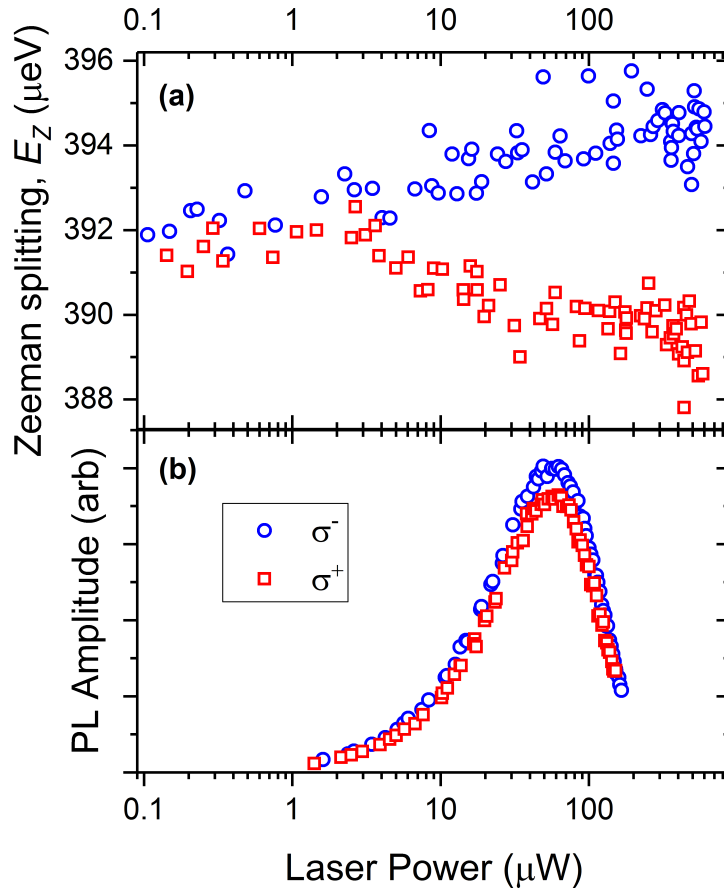


FIGURE 4.7: a) The detected X^0 Zeeman splitting E_Z as a function of the pump power for a single dot from sample B, measured at $B_z = 2.5$ T using the pump-probe scheme and pumped with a 561 nm laser with polarisation σ^- (blue circles) or σ^+ (red squares). The maximum Overhauser shifts observed at high power were $\Delta E_Z^{\sigma^-,max} \approx +2.3 \mu\text{eV}$ and $\Delta E_Z^{\sigma^+,max} \approx -2.4 \mu\text{eV}$. b) The total X^0 PL intensity (sum of the Zeeman split components), measured under cw conditions. The PL signal from the dot saturates at $\approx 50 \mu\text{W}$ under both σ^+/σ^- excitation.

Next, the Overhauser shift dependence on the external magnetic field is presented in Figure 4.8. Almost no DNP is observed at $B_z = 0$ T and this is due to exchange interaction between the electron and hole spin resulting in the fine structure splitting (see Section 2.2.2). This causes the bright states to become linearly polarised without an external magnetic field (with fine structure splitting $\delta_B \approx 115 \mu\text{eV}$ for this dot), no net electron spin polarisation can be induced with circularly polarised pumping and hence no nuclear polarisation is observed. As the external magnetic field is increased, the Zeeman splitting increases (by $\approx 150 \mu\text{eV/T}$ for this dot) and also the DNP increases and reaches a maximum at $B_z \approx 2.5$ T because the electron spin polarisation is restored along the \hat{z} axis through σ^-/σ^+ pumping and enables spin flips with the nuclear spins. There is still a clear observation of DNP upto the maximum field of $B_z = 8$ T, but there is a reduction beyond

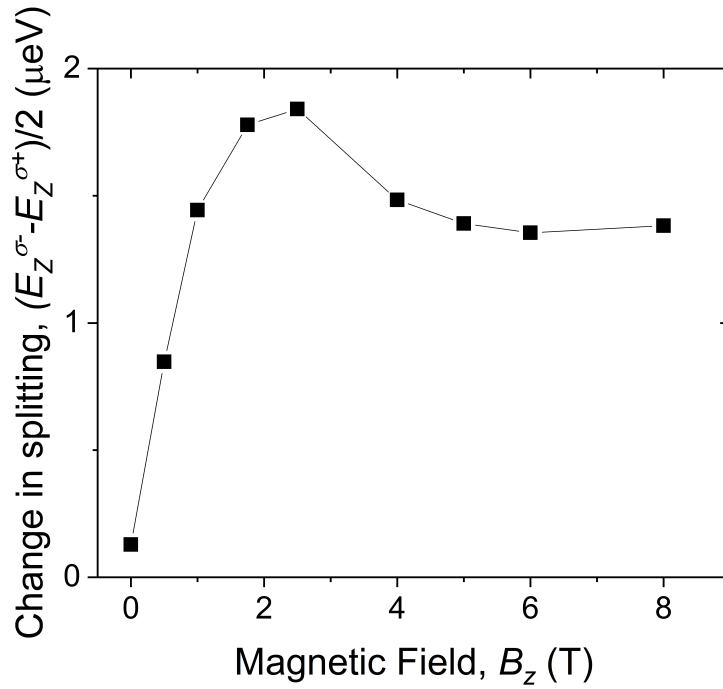


FIGURE 4.8: The detected change in splitting between σ^- and σ^+ pumping ($(E_Z^{\sigma^-} - E_Z^{\sigma^+})/2$) of X^0 as a function of the external magnetic field (in Faraday configuration) for a single dot from sample B using the pump-probe scheme.

$B_z \approx 2.5$ T which has also been observed for III-V dots [135]. The detailed analysis of the DNP at various external fields will depend on the polarisation and depolarisation rates of the electron, hole and nuclear spins, but as the field is increased, the electron Zeeman splitting increases much faster than the nuclear splitting and this mismatch in energy slows down the DNP. Since the intermediate QW states are very broad compared to the electron Zeeman splitting, we see that DNP is still detected at high fields. Due to the maxima at $B_z \approx 2.5$ T, this field was chosen for all subsequent dynamics and NMR measurements so that the maximum available change in splitting could be used.

4.6 Nuclear spin dynamics in CdTe/ZnTe dots

Now that the effect of DNP has been observed in CdTe/ZnTe QDs, we determine the timescales associated with the nuclear spin polarisation - that is how long it takes to buildup and how long it takes to decay. The observation of how the OHS builds up as a function of pump time under σ^-/σ^+ pumping is shown in Figure 4.9a. Before the pump pulse (only in this buildup dynamics measurement, see Figure 4.9c), a linear erase pulse with duration $T_{Erase} = 50$ ms and $160 \mu\text{W}$ power is applied so that the nuclear polarisation is erased between cycles and not built up over time. The data is fitted with an exponential

function of the form $E_Z(t) = E_Z(0) + \Delta E_Z(1 - \exp(-t/\tau))$ and the characteristic buildup time for the DNP is determined to be $\tau_{buildup} \sim 1$ ms. This is similar amongst several dots measured in the sample at $B_z = 2.5$ T and is about a factor of ~ 1000 smaller than the buildup time for III-V dots at similarly large fields (where $\tau_{buildup} \sim 0.5 - 3$ s [135, 179, 181, 182]). Since the only isotopes present in CdTe/ZnTe dots are spin $I = 1/2$ (unlike in III-V dots where $I \geq 3/2$) and only a fraction of the nuclei possess a spin (~ 25 % for Cd, ~ 8 % for Te, but 100 % for III-V), the buildup time for DNP is expected to be faster by about a factor of ~ 30 . The remainder of the difference is because of the smaller number of nuclei within the dot, which is estimated to be ~ 5000 nuclei from the TEM images for a CdTe/ZnTe dot (see Section 4.2) compared to $10^4 - 10^5$ in a typical III-V dot. Also, here we measure $\tau_{buildup} \sim 1$ ms at $B_z = 2.5$ T, which is at least an order of magnitude longer than times reported in the literature ($\tau_{buildup} < 100$ μ s) at low magnetic fields $B \lesssim 0.1$ T in CdTe/ZnTe [169] and CdSe/ZnSe [166] dots. This was expected, because at large magnetic fields, there is a large mismatch in the Zeeman energies between the electron and nuclear states and there is a lower probability of an electron-nuclear spin flip occurring.

In Figure 4.9b, we present the decay dynamics of the nuclear spin polarisation. Here, the nuclear spins are allowed to decay naturally by leaving the sample in the dark for different lengths of time T_{Wait} between the pump pulse and the probe pulse (see Figure 4.9d) and the final exciton spectral splitting is measured. Again the data is fit with an exponential decay function and the characteristic decay time of the nuclear spin polarisation is found to be $\tau_{decay} \sim 4$ s at $B_z = 2.5$ T. Similar times are measured for various dots in Sample B and are much longer (by 3 orders of magnitude) than the < 1 ms decay times in charged CdSe QDs in low external magnetic fields [167]. However these times are much shorter than the decay times (of $> 10^2$ s) measured in neutral [135, 181] and charged [7, 136] III-V dots at large magnetic fields. The decay times are large in III-V dots (on the timescale of hours [7]) because spin diffusion through the nuclear dipolar interaction is suppressed due to the strong quadrupolar broadening induced by strain. Due to the absence of quadrupolar effects for spin $I = 1/2$ nuclei, spin diffusion is expected to provide a significant contribution to nuclear polarisation decay in CdTe QDs (see supplementary of [183]) and additional relaxation mechanisms may include the hyperfine interaction with the fluctuating electron spin environment. These fluctuations are observed in this CdTe/ZnTe QD system through the spectral wandering effects (discussed in Appendix A) but additional measurements such as the depolarisation rates of individual isotopes would need to be performed for detailed analysis (and with dots embedded charge-tunable structures).

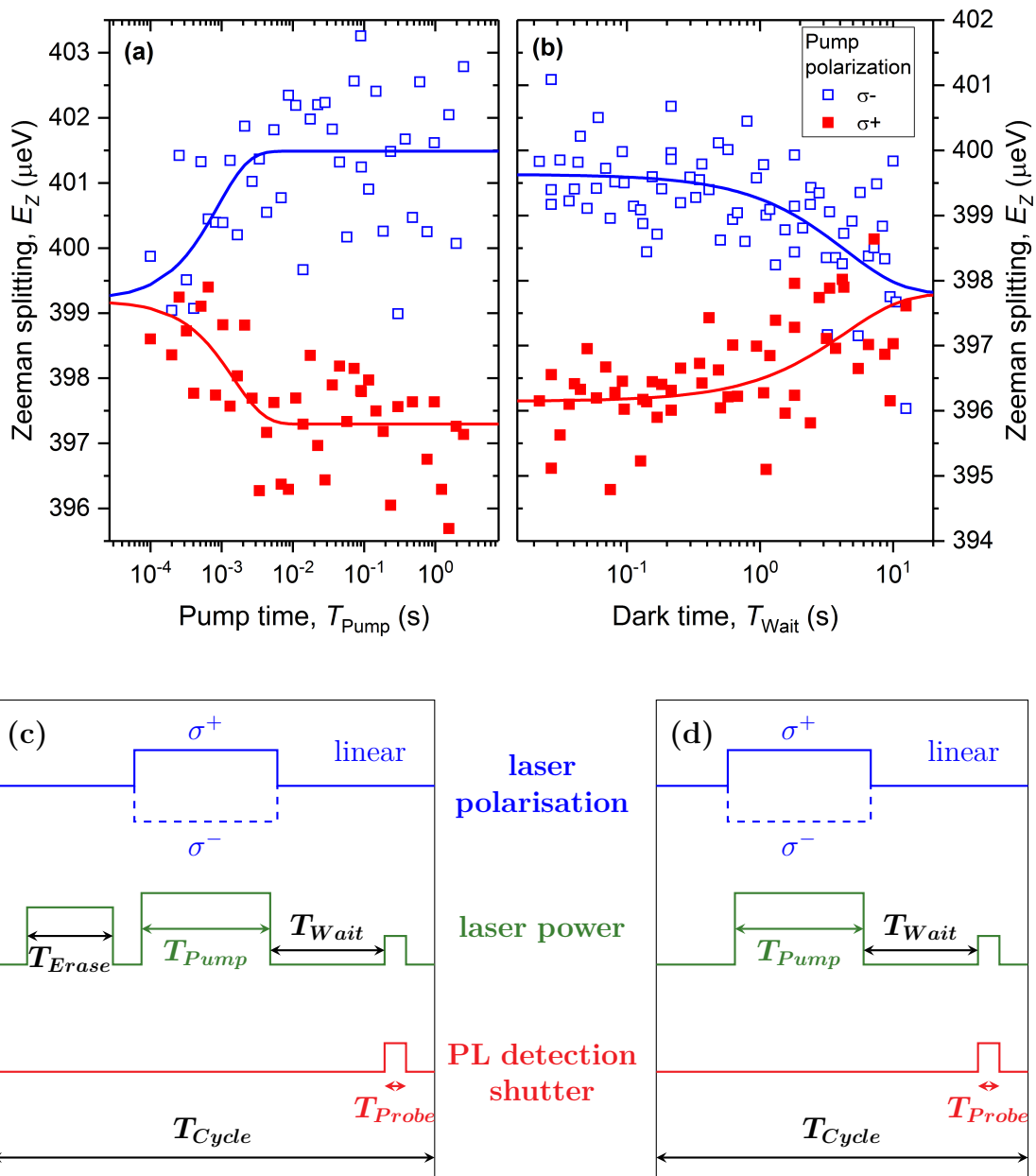


FIGURE 4.9: a) Nuclear spin polarisation buildup dynamics in a single CdTe/ZnTe QD from sample B using the pump-probe scheme at $B_z = 2.5$ T. The characteristic buildup time under σ^- pumping (blue, open symbols) is $\tau_{\text{buildup}} = 0.9_{-0.5}^{+1.3}$ ms and under σ^+ pumping (red, solid symbols) is $\tau_{\text{buildup}} = 1.5_{-1.0}^{+3.0}$ ms, where the 95 % confidence intervals are quoted. b) Nuclear spin polarisation decay in the dark of the same QD. A combined exponential fit gives the characteristic decay time $\tau_{\text{decay}} = 4.3_{-1.6}^{+2.5}$ s. c) Pump-probe measurement cycle timing diagram used for buildup dynamics where an extra linear erase pulse prevents buildup of DNP between cycles. d) Pump-probe timing diagram for decay dynamics measurement.

4.7 Optically detected NMR spectra of CdTe/ZnTe dots

So far we have shown that optical techniques can be used to initialize and detect the nuclear spin polarisation in single CdTe/ZnTe QDs. Now we discuss measurements of the NMR spectra, which require radiofrequency fields to control the nuclear spin polarisation. We use repeated cycles of pump-rf-probe (see Figure 4.11c) for the “saturation NMR” technique described in Section 3.4.2, by applying a rectangular band of excitation with width w_{sat} centred at a frequency f_{rf} , which is varied across a nuclear resonance. The width of the band is chosen to be between a few kHz to a few hundred kHz to balance the spectral resolution and the amplitude of the NMR signal (as discussed in Section 3.4.2). The pulse duration T_{RF} is calibrated separately where a large band with w_{sat} wide enough to cover the entire nuclear resonance is applied and T_{RF} is changed to detect the exponential depolarisation decay time due to applied rf pulse. The final pulse durations of $T_{RF} = 50 - 120$ ms used for the NMR spectra measurements were chosen so that $> 99\%$ of the nuclear spin polarisation is depolarised by the rf pulse. Note that the (natural) decay time of the nuclear spin polarisation was measured to be $\tau_{decay} \sim 4$ s in the previous section, so the proportion of nuclei that decay naturally over the applied $T_{RF} \sim 100$ ms will be low and a sufficient signal can be observed.

Additionally for the cadmium nuclei, there are two spin $I = 1/2$ isotopes of ^{111}Cd and ^{113}Cd that are distributed randomly within the QD so on average, both isotopes will experience the same fluctuations of the Knight field and chemical shifts. So the lineshape of the NMR spectrum of ^{113}Cd will be approximately the same as ^{111}Cd , but the resonance frequency will be offset by their gyromagnetic ratios $\gamma_{(^{113}\text{Cd})}/\gamma_{(^{111}\text{Cd})}$ (see Figure 4.10). In order to increase the magnitude of the observed NMR signal for cadmium, we depolarise both ^{111}Cd and ^{113}Cd simultaneously by applying 2 rf bands centred at frequencies f_{rf} and $(\gamma_{(^{113}\text{Cd})}/\gamma_{(^{111}\text{Cd})}) * f_{rf}$ and stepping through different f_{rf} so that the final measured NMR spectra is the sum of the ^{111}Cd and ^{113}Cd lineshapes.

The NMR spectra of two individual dots on sample B were measured and the results are shown in Figure 4.11. For QD1, there are two resolution limited peaks observed at resonance frequency ~ 22.6 MHz for ^{111}Cd and ~ 33.7 MHz for ^{125}Te as expected for the nuclei at $B_z = 2.5$ T (resonance frequency = $\gamma B_z/2\pi$).

The total observed hyperfine shift from both Cd isotopes is $|\Delta E_Z^{111\text{Cd}} + \Delta E_Z^{113\text{Cd}}| \approx 0.8 \mu\text{eV}$. The partial hyperfine shift, associated with a single isotope i can be written $\Delta E_Z^i =$

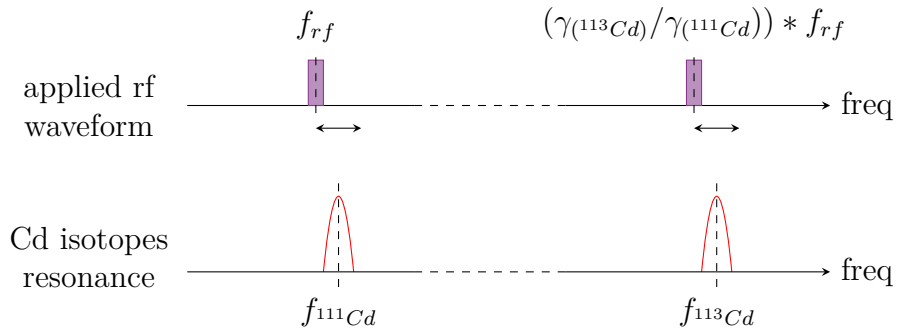


FIGURE 4.10: Schematic illustration of the shape of the rf waveform applied to excite both cadmium isotopes for the NMR spectra measurements in CdTe/ZnTe dots.

$k^i \rho^i A^i I^i P_N^i$, where $0 \leq k^i \leq 1$ is the element mole fraction that describes spatial non-uniformities within the electron envelope wave function, ρ^i is the natural abundance of the isotope and P_N^i is the average nuclear spin polarisation degree. Using the bulk hyperfine shifts [175], $A^{111Cd} \approx -31 \mu\text{eV}$ and $A^{113Cd} \approx -32 \mu\text{eV}$, so the product $\rho^i A^i I^i \approx -2.0 \mu\text{eV}$ for either Cd isotope. Using the bulk band gap values $E_0^{CdTe} = 1.60 \text{ eV}$ and $E_0^{ZnTe} = 2.38 \text{ eV}$, we can interpolate that QD1 with PL energy $\approx 2.05 \text{ eV}$ has roughly $k \approx 0.4$ for cadmium and so the average spin polarisation is $|P_N| \approx 0.5$. The average value of $|P_N| \approx 0.5$ should also apply to Te isotopes as the average spin polarisation is similar for all spin $I = 1/2$ isotopes (as seen in GaAs/AlGaAs dots [9]). Since we measure that the total hyperfine shift from all isotopes to be about $\Delta E_Z \approx \pm 2 \mu\text{eV}$ (see Figure 4.9), the maximum Overhauser shift we could observe with 100 % nuclear polarisation would be about $\approx \pm 4 \mu\text{eV}$.

NMR measurements from another dot (QD2 in Figure 4.11b) produce a more complex spectral lineshape. A resolution limited peak ($w_{sat} = 174 \text{ kHz}$) is only observed for the Cd isotopes under σ^- pumping (between 22.7 and 22.8 MHz with amplitude $\sim -0.5 \mu\text{eV}$), but is accompanied by a flat background offset of $\sim -0.3 \mu\text{eV}$ from the background splitting without rf (dashed horizontal line). An additional measurement was taken with the rf applied at a frequency range that does not correspond to the resonance frequency of any isotope in the sample (see middle panel in Figure 4.11b). Here, no obvious change in splitting is measured with respect to the dashed line without rf and it confirms the broad backgrounds observed in the Cd spectra under both σ^- and σ^+ pumping are real signals due to nuclei being depolarised by the rf and not related to any spurious experimental effects (such as rf heating of the sample).

Since there are no quadrupolar nuclei, the only source for such a large inhomogeneous broadening is the Knight field of the electron acting on the nuclei (see Section 2.3.4). The knight shift of the ^{111}Cd isotope can be written as $\gamma^{(111Cd)} B_e / 2\pi$ and the observed

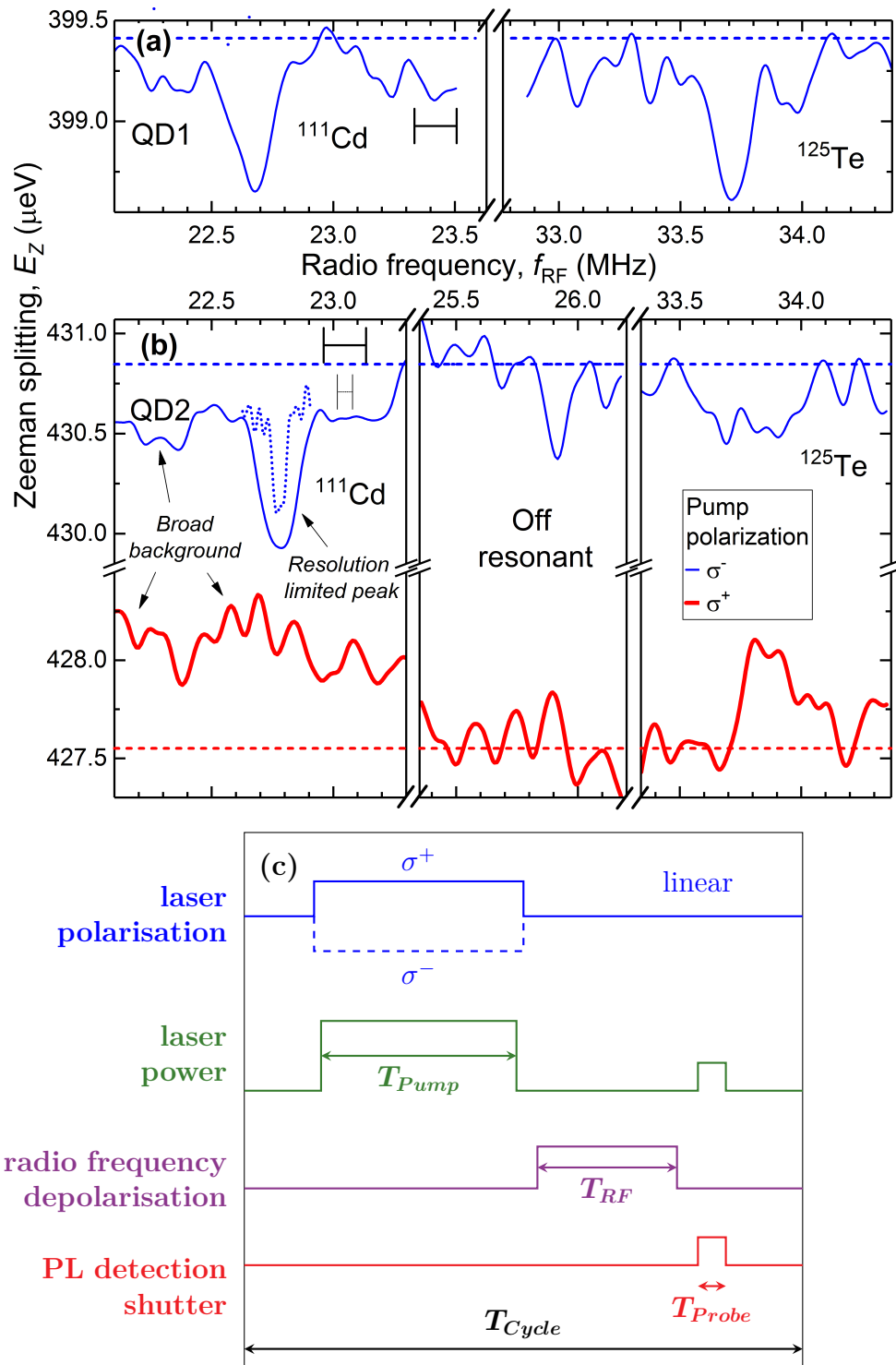


FIGURE 4.11: Optically detected NMR spectra at $B_z = 2.5$ T for the Cd and Te isotopes in two single CdTe/ZnTe quantum dots: a) QD1 and b) QD2 in sample B. Both σ^- (thin blue line) and σ^+ (thick red line) pumping are shown and the width of the rf waveform, which indicates the spectral resolution (also shown with horizontal bars), was 63 kHz (dotted line) or 174 kHz (solid line). The dashed horizontal lines show the measured splitting without any rf and indicate the “background” level of splitting and the “off resonant” spectra show a measurement with f_{RF} between ~ 25.3 and ~ 26.2 MHz where no nuclear isotopes are present. c) Pump-rf-probe measurement cycle timing diagram used to measure NMR spectra.

broadening in the NMR spectra of QD2 are at least ± 0.5 MHz, which leads to an estimate of the Knight field of $|B_e| \gtrsim 50$ mT, which can be created by electrons partially occupying the dot during the rf pulse in the dark. This is about a factor of ~ 5 larger than the Knight field $B_e \sim 10$ mT observed in III-V dots [131]. The detected NMR spectra of ^{111}Cd can then be thought of as the averaged sum of a narrow peak (when the dot is empty) and a broad background (when the dot is occupied by an electron). For a dot charged with an electron, the average Knight shift due to the polarised electron with spin $s = 1/2$ on the ^{111}Cd nuclei can be approximated as $\sim sI|A^{111\text{Cd}}|/N \approx 3$ neV $\approx h \times 0.75$ MHz, where $N \approx 2500$ is the number of group-II atoms (see Section 4.2) in the volume of the electron and h is the Planck constant. This value is close to the ± 0.5 MHz ($\approx \mu\text{s}$) observed from the NMR spectra, which indicates that the correlation time of the electron spin (trapped within the dot) is much longer than the nuclear spin precession period ($= 1/f_{rf} \approx 40$ ns). At any given time the nuclei may interact with a \uparrow (\downarrow) electron which produces a positive (negative) Knight field and appears as part of the NMR signal on the high (low) frequency side of the resonance. It can occur over a broad frequency range because of the inhomogeneity in the Knight field across the volume of the dot (the Knight field is strongest for nuclei near the center of the dot).

Also shown in Figure 4.11b (as the dotted line) is an attempt to measure the ^{111}Cd NMR peak with a narrower resolution of 63 kHz and this peak itself is a sum of a resolution limited peak and a broad ~ 100 kHz tail. Even narrower spectral resolution does not reliably produce a change in splitting. This time, the smaller broadening is likely due to the Knight field caused by electrons in nearby QDs or charge traps (that produce the spectral wandering effects discussed in Appendix A).

4.8 Summary

In this chapter, we have presented the first direct experimental observation of the Overhauser shift in CdTe/ZnTe quantum dots. This system consists of a dilute nuclear spin bath with only a few hundred nuclear spins, and in the regime of strong magnetic fields, hyperfine shifts of $\Delta E_Z \approx \pm 2$ μeV are observed corresponding to approximately 50 % nuclear polarisation. We see that DNP is only observed in a sample containing a quantum well suggesting that the quantum well states play a key role in the mechanism of DNP in this structure. We have shown the robust nature of this nuclear polarisation with an initialization time of ~ 1 ms and a decay time of $\gtrsim 1$ s (both of which are about two orders of magnitude quicker than their III-V counterparts) and the ability to manipulate

the nuclei using radiofrequency fields. The measurements revealed the strong Knight field of $|B_e| \gtrsim 50$ mT, which is an order of magnitude larger than in III-V dots. Severe spectral wandering effects due to charge fluctuations in the environment were also observed.

The optically active CdTe/ZnTe QD system has the potential to combine the advantages of III-V dots which have good optical properties and the long coherence times in nuclear spin free systems such as group IV semiconductors. The coherence time of the electron in InGaAs dots is limited to $\sim 1 \mu\text{s}$ [152] due to the nuclear spin fluctuations and by adapting the isotopic purification methods from silicon [60] and applying it to the II-VI QD system, it is possible in principle to have optically active QDs with electron spin coherence times in the millisecond timescale. Alternatively, the few nuclear spins themselves could be used as a resource to store and process quantum information. The strong electron-nuclear interaction (indicated by the Knight field shifts), and individual isotopic control could allow for the transfer of coherence between the electron and the nuclear spins and implementation of quantum registers based on electron-nuclear spin qubits [35], which is not possible in III-V dots. In any case, the crucial next step is to be able to control the charge environment of the dot and further samples need to be designed and fabricated in gated charge-tunable diode structures.

Chapter 5

Structural analysis of InGaAs/GaAs quantum dots using optically detected NMR

In this chapter, we present the experimental results in analysing the structure of individual self assembled InGaAs/GaAs QDs using optically detected NMR techniques. We have already discussed that such dots have favourable properties as fast, narrow linewidth, single photon sources [43, 44] that may be used for spin qubit applications [1, 40]. However, for this to become a scalable multi-qubit system, a detailed understanding of the underlying structure of the individual QDs is required. Most microscopy techniques [184, 185] used to analyse the structure are destructive and hence an individual QD will not be usable again after microscopy. Typically, a section of the sample needs to be cleaved to look at the cross section and it will most likely be a random dot in the sample. The important advantages of our NMR technique is that the structure of a specific QD of interest may be analysed and the technique is non-destructive so the same dot can be investigated for its structural properties as well as continue to be used for further experiments of its optical and spin qubit performance.

Here, we can detect NMR spectra optically from a system consisting of only $\sim 10^5$ nuclei, from which important structural information can be determined [124, 146]. We build upon previous studies [146] and present a direct comparison of the structure of individual dots in two different InGaAs/GaAs samples: the In-flush sample and the Low Temp Cap sample that were introduced in Section 3.1. We measure high resolution NMR spectra of the central transition (CT, between nuclear spin states $I_z = +\frac{1}{2} \leftrightarrow -\frac{1}{2}$) from which we extract

the chemical composition (the proportion of indium) within the dot. The novel aspect of this work involved designing a unique 3-band inverse NMR waveform to accurately measure the satellite transitions (ST, for a spin $I = 3/2$ nucleus, $I_z = +\frac{3}{2} \leftrightarrow +\frac{1}{2}$ or $-\frac{3}{2} \leftrightarrow -\frac{1}{2}$) which are sensitive to the distribution of strain within the QD. This revealed important structural information about nuclei within low strain areas of the QD that have previously not been detected.

We start by looking at the calibration experiments required for the inverse NMR spectra measured using the pump-rf-probe scheme. Then, we compare the high resolution spectra of the central transition for all four isotopes in both samples. Next we look at the newly developed 3-band inverse NMR technique, which was used to detect the satellite transitions of all four isotopes in both samples. Finally, we present some basic structural analysis using TEM images in comparison with the NMR measurements.

5.1 Calibration measurements for inverse NMR experiments

Before an optically detected NMR measurement can be performed, a number of important parameters must first be determined. The overall experimental setup and the pump-rf-probe technique have been discussed in Chapter 3. However, even before an rf pulse is applied, all of the parameters relating to the pump pulse and the probe pulse need to be calibrated in pump-probe type measurements. Unless otherwise stated, in this chapter all experiments were done with non-resonant lasers (850 nm) at large magnetic fields (Faraday geometry, $B_z = 8$ T) and only the neutral exciton line X^0 was used in the spectra.

Initially, both samples were searched for suitable QD candidates that showed a narrow linewidth in the PL spectra (limited by the resolution of the spectrometer of ~ 20 μeV) and a large PL amplitude. Such characteristics are not fundamental requirements but merely assist with the quality of the data. A large PL signal helps to limit the required measurement time and a narrow optical linewidth improves the accuracy of the fitting. We also select dots that have a large maximum Overhauser shift, which means a greater fraction of polarised nuclei and a larger available signal for NMR experiments.

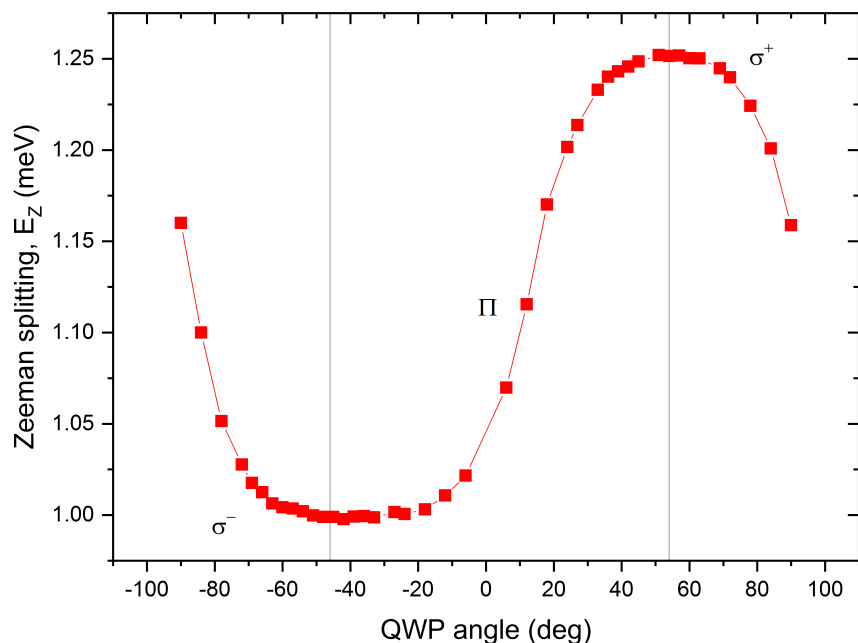


FIGURE 5.1: Dependence of the Zeeman splitting on the angle of a rotatable quarter wave plate (QWP). The data was measured on the neutral exciton X^0 line in a pump-probe scheme using the In-flush sample at $B_z = 8$ T. The other experimental parameters were $P_{\text{Pump}} = 1$ mW, $T_{\text{Pump}} = 6$ s, $P_{\text{Probe}} = 0.25$ μ W and $T_{\text{Probe}} = 30$ ms. With linear pumping Π , the Zeeman splitting is ~ 1.124 meV and under σ^+ (σ^-) pumping with a corresponding QWP angle of 54° (-46°), a shift of $\Delta E_{OHS} \approx +125$ μ eV (-125 μ eV) is observed.

5.1.1 Pump and probe pulse parameter calibration

There are several important parameters relating to the pump and probe pulse that need to be determined before optically detected NMR spectra can be detected. Calibration measurements are done to determine the polarisation, power and duration of the pump and probe pulses. The lifetime of the nuclear spin polarisation in the dark needs to be found, which is detected by changing the time in the dark between the pump and probe pulses. Additionally in the Low Temp Cap sample, which is embedded in a diode structure, the optimum bias during the pump/probe pulse and also in the dark time between pulses needs to be found. In this chapter, since we are only using the neutral exciton X^0 state, we will not discuss the bias dependant measurements, but just state the bias values used. In Chapter 6, the X^0 and X^- state are compared for a dot in the Low Temp Cap sample and the explicit bias dependant calibrations will be presented and discussed there.

The change in the observed Zeeman splitting with different polarisations of the pump laser is shown in Figure 5.1. This measurement is performed by changing the angle of the quarter wave plate (placed just above the entrance to the cryostat as described in Section

3.3) so that the polarisation of the pump laser changes from σ^+ to σ^- (through elliptically polarised states and including linearly polarised Π). We can see that the maximum change in the Overhauser shift occurs at an angle of 54° corresponding approximately to σ^+ circular polarisation and -46° for σ^- as indicated by the grey vertical lines. The maximum Overhauser shift does not occur at the pure circularly polarised states at angles $\pm 45^\circ$, likely due to distortion of the polarisation at the interface between the dot and the surrounding matrix. Additionally the angle of 0° does not correspond exactly to a linear polarisation, but this is just an offset due to the way the QWP is installed on its mount. The raw spectra for this measurement are shown in Figure 3.6 in Section 3.4.1. The pump polarisation for all subsequent measurements can now be set by rotating the QWP to the appropriate angle and similar angles are obtained for the Low Temp Cap sample. For the probe pulse, the polarisation is adjusted using the HWP and linear polariser in the probe arm of the optical setup (see Section 3.3). It is approximately aligned to have a linear polarisation incident on the sample, but the small power and duration of the probe pulse ensure that the precise polarisation should have little effect on the nuclear polarisation. Instead, the most important consideration is that the amplitudes of the two Zeeman split components are both approximately equal so that a Gaussian fit can be performed on both peaks to determine the splitting.

The time required to build up the DNP is not inconsequently short. To determine the duration of the pump pulse that is required, a pump-probe experiment is performed with varying pump time T_{Pump} and all other parameters are kept constant. The measured change in the Zeeman splitting from both pump polarisations are shown together in Figure 5.2a. Note that for this calibration measurement only, a linearly polarised erase pulse is included after the probe pulse in a pump-probe-erase type cycle. This pulse has the power of the probe pulse ($P_{\text{Probe}} = 0.25 \mu\text{W}$) and is applied for a long time of $T_{\text{Erase}} = 3.5 \text{ s}$. This ensures that no net nuclear polarisation is built up between cycles and that the nuclear spin bath is not polarised before a pump pulse is applied (similar considerations were made for the pump time measurement in II-VI dots, see Section 4.6). A clear increase (decrease) in the Zeeman splitting is observed under σ^+ (σ^-) pumping and reaches a maximum of approximately $\Delta E_{\text{OHS}} = \pm 125 \mu\text{eV}$ within a few seconds of optical pumping. Note that such a large polarisation is only achieved by using a pump power of $P_{\text{Pump}} = 1 \text{ mW}$ which is approximately 50 times the saturation power of the neutral exciton recombination PL line ($P_{\text{Sat}} \sim 20 \mu\text{W}$ for this dot). For NMR experiments, we choose $T_{\text{Pump}} = 6 \text{ s}$ which is sufficiently high to ensure that there is a reproducible nuclear spin bath polarisation. This long time of $T_{\text{Pump}} = 6 \text{ s}$ dominates the experiment cycle T_{Cycle} and controls how long it takes to measure a complete dataset.

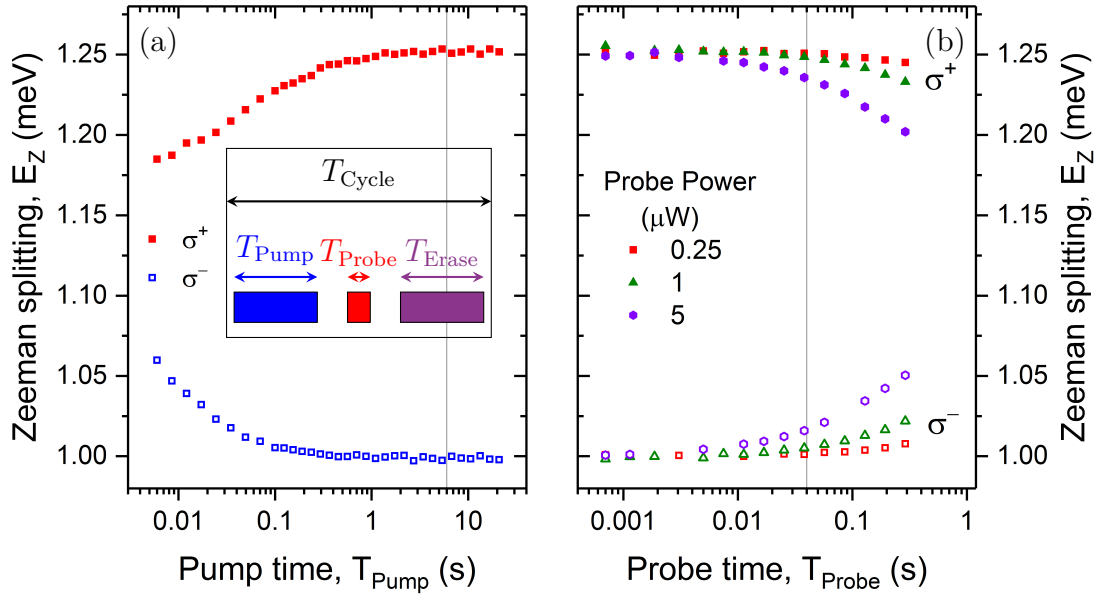


FIGURE 5.2: a) Dependence of the Zeeman splitting on the pump pulse duration T_{Pump} under both σ^+ (red solid squares) and σ^- (blue open squares) pumping at $B_z = 8$ T for a single dot in the In-flush sample. Inset shows the pump-probe-erase timing diagram used for this measurement only. A clear buildup in the Overhauser shift is observed and the vertical line shows the chosen pump time of $T_{\text{Pump}} = 6$ s for NMR experiments. The other experimental parameters for this measurement were $P_{\text{Pump}} = 1$ mW, $P_{\text{Probe}} = 0.25$ μW and $T_{\text{Probe}} = 10$ ms. b) Effect of the duration and power of the probe pulse on the Zeeman splitting. Three different probe powers were applied and both σ^+ (solid symbols) and σ^- (open symbols) pumping with $T_{\text{Pump}} = 6$ s and $P_{\text{Pump}} = 1$ mW are shown. A clear decay of the nuclear polarisation is observed which is faster for larger probe powers. Here, the vertical line shows the chosen probe time of $T_{\text{Probe}} = 40$ ms at a probe power of $P_{\text{Probe}} = 1$ μW for NMR experiments.

We also calibrate the effect of the probe pulse on the nuclear spin polarisation. An ideal probe pulse would have no effect on the nuclear spin bath and allow us to simply detect the final Zeeman splitting. However, a real linear probe pulse will always depolarise the spins over time and this is clearly observed in Figure 5.2b. The higher the probe power, the faster the decay of the polarisation and by 300 ms, a significant change in the splitting of ~ 50 μeV is observed for the highest probe power applied here of $P_{\text{Probe}} = 5$ μW ($\sim P_{\text{Sat}}/4$). However when using low probe powers and/or probe times, this reduces the PL signal that can be accumulated onto the CCD in a given pump-probe cycle and would require many more cycles to acquire enough signal for accurate Gaussian fitting and therefore leads to much longer measurements. Hence for NMR experiments, we choose a compromise of $P_{\text{Probe}} = 1$ μW ($\sim P_{\text{Sat}}/20$) and $T_{\text{Probe}} = 40$ ms, for which the OHS changes by no more than 5 % of the maximum observed value.

Though the data is not explicitly shown here, the same measurements were performed for the dot measured in the Low Temp Cap sample. The final pump parameters used in NMR

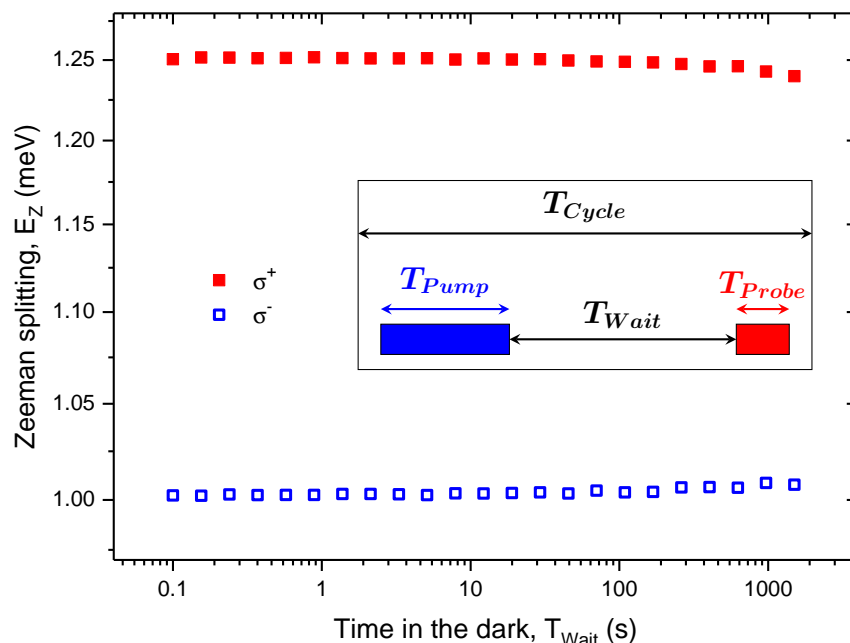


FIGURE 5.3: Dependence of the Zeeman splitting on the wait time T_{Wait} in the dark between the pump and probe pulse (shown schematically in the inset) under both σ^+ (red solid squares) and σ^- (blue open squares) pumping at $B_z = 8$ T for a single dot in the In-flush sample. The other experimental parameters were $P_{\text{Pump}} = 1$ mW, $T_{\text{Pump}} = 6$ s, $P_{\text{Probe}} = 1$ μ W and $T_{\text{Probe}} = 30$ ms.

experiments for this sample were also $T_{\text{Pump}} = 6$ s and $P_{\text{Pump}} = 1$ mW and for the probe pulse $T_{\text{Probe}} = 40$ ms and $P_{\text{Probe}} = 0.25$ μ W. Also in this sample, the diode bias values were chosen to be $V_{\text{Pump}} = 1.36$ V which was the value that provided the largest OHS and $V_{\text{Probe}} = 1.724$ V which provided the largest PL signal. For a more detailed analysis of such bias calibration measurements on another dot in this sample, see Chapter 6.

5.1.2 Nuclear spin lifetime

Another important consideration is to ensure the intrinsic lifetime of the nuclear spin polarisation (nuclear T_1 time) is sufficiently long. This means that the natural decay of the nuclei without any optical illumination is slow and the polarisation state can be manipulated, for example with an rf pulse, without having to correct for the T_1 decay.

The measured decay of the nuclear spin polarisation for a dot in the In-flush sample is shown in Figure 5.3. The large change in the splitting due to the Overhauser shift can be seen to survive even at very long times of > 1000 s under both circular polarisations of pumping. The longest time point measured in this experiment of 1500 s was limited to maintain a reasonable total measurement time. It was not possible to fit the data

and extract the nuclear lifetime T_1 because more datapoints (at longer T_{Wait}) would be necessary but we measure the Overhauser shift to drop to only 94 % of the maximum value after ~ 1000 s. Such long nuclear spin lifetimes indicate that the dot is absent of charge carriers and this can be deduced by looking at different biases applied to the diode (see Chapter 6) and agrees with the timescale measured by other groups [7].

Similar nuclear spin lifetimes of > 1000 s were found under reverse bias (where the dot is emptied of charges) in the Low Temp Cap sample. For the purposes of our NMR experiments, the requirement is that no significant nuclear spin polarisation decay occurs naturally when the rf pulse is applied. For all of the isotopes detected with the NMR spectra, the maximum duration of the applied rf pulse was $T_{\text{RF}} < 6$ s (see Section 5.1.3) and so only negligible DNP decay is expected.

5.1.3 Radiofrequency pulse parameter calibration for cw NMR

For the optically detected NMR spectra measurements, there are some important parameters relating to the applied rf pulse that must first be calibrated. As introduced in Section 3.4.2, the signal for an inverse NMR spectrum of a single isotope is given by the change in the Overhauser shift between a “no gap” and a “gap” measurement. For a “no gap” spectrum, a single rf spectral band is applied wide enough to cover the entire isotope resonance (CT and STs) which depolarises the isotope. Then for the “gap” measurement, a gap is introduced within this band and nuclei within the gap will not be depolarised and there will be a change in the nuclear spin state populations (see Figure 3.7). The gap width can be chosen to balance the spectral resolution and the amount of signal and is very different depending on whether the CT or the STs are being measured and the isotope. Therefore the important parameters here that must first be calibrated are the total width w_{Band} of the applied band for each isotope (indicating the total width of the resonance) and the amount of time T_{RF} that the rf pulse must be applied to depolarise the isotope.

The total inhomogeneous width of the nuclear resonance (CT and STs) changes considerably between isotopes in InGaAs/GaAs QDs. This is governed by the quadrupolar moment Q of each isotope (see Table 2.1) and the nuclear spin I through $\omega_Q \propto Q/(I(2I - 1))$. The quadrupolar moments interact with the electric field gradients caused by strain, as discussed in Section 2.3.3. The STs show a large inhomogeneous broadening (as they are affected by the first order quadrupolar shifts $\omega_Q^{(1)}$) and there are multiple STs for ^{115}In which has a spin $I = 9/2$.

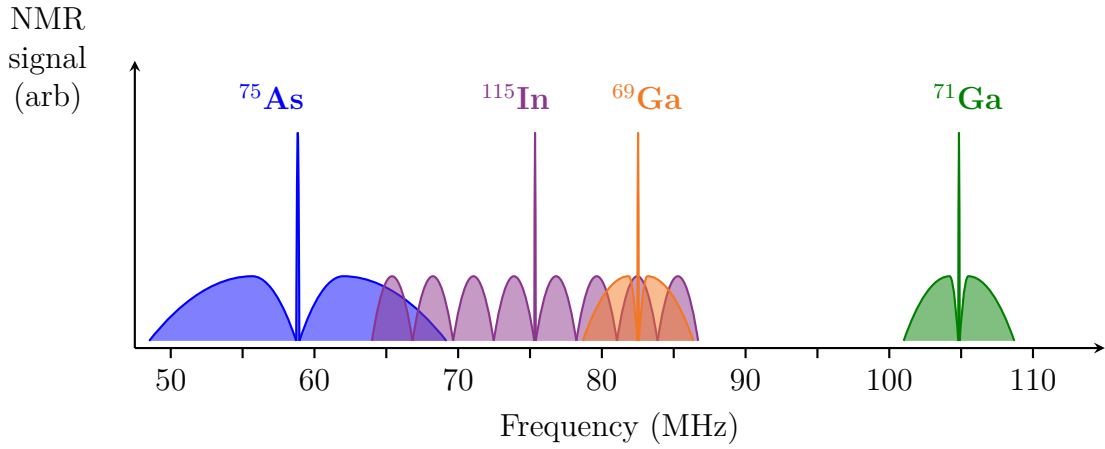


FIGURE 5.4: Nuclear resonance spectra schematic of the four studied isotopes in a single self assembled InGaAs/GaAs quantum dot at $B_z = 8$ T. There are narrow central transition peaks corresponding to the $-\frac{1}{2} \leftrightarrow +\frac{1}{2}$ spin states of each isotope. There are two satellite transitions for the spin $I = 3/2$ isotopes for Ga and As, but eight for the $I = 9/2$ isotope of ^{115}In .

To determine the width of the entire resonance, a pump-rf-probe type cycle is utilised and a single broad spectral rf band is applied during the “rf” part of the cycle. This rf band has its central frequency f_{Band} chosen to be at the middle of the CT resonance of a particular isotope. Whilst keeping the central frequency constant, the width of this band w_{Band} is varied and the change in the Overhauser shift ΔE_{OHS} between the “gap” and “no gap” measurements will be plotted. So here, we use the amplitude of the CT signal to determine the total width of the isotope. Note that the width of the gap w_{Gap} in all inverse NMR experiments is always less than w_{Band} .

The relative widths and frequencies of the four nuclear isotopes in InGaAs dots at $B_z = 8$ T are illustrated schematically in Figure 5.4. We ideally want to perform the width dependence separately for each isotope and this is possible for ^{71}Ga which has a central frequency of ~ 104.85 MHz at $B_z = 8$ T and so is well isolated from the other isotope resonances. Note that the resonance frequency is governed by the gyromagnetic ratio of the isotope (see Table 2.1) and depends on the magnetic field (resonant Larmor frequency $\omega_L = -\gamma B_z$). We can also measure the width of ^{75}As separately which has a resonance at ~ 58.84 MHz. There is only a small overlap between the low frequency ST of ^{115}In and the high frequency ST tail of ^{75}As but this should have a minimal effect on ^{115}In because the overlapping states are depopulated for a specific sign of optical pumping. This is due to the fact that ^{115}In and ^{75}As have opposite signs of quadrupolar splitting (see further discussion in Section 5.4). However, for ^{115}In (with frequency ~ 75.37 MHz), the high frequency ST overlaps with the entire ^{69}Ga resonance (with frequency ~ 82.52 MHz). These two isotopes can not be separated in frequency space at such large magnetic fields

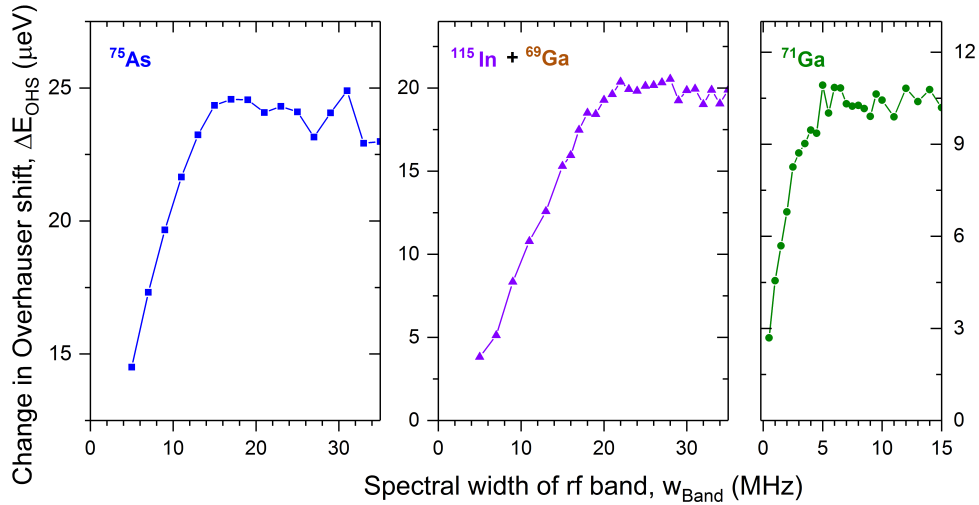


FIGURE 5.5: Calibration measurement to determine the total spectral width of each isotope in the In-flush sample at $B_z = 8$ T using σ^- pumping only. The change in Overhauser shift ΔE_{OHS} is between the “no gap” measurement where a single band of width w_{Band} depolarises the isotope and a “gap” measurement where a gap is introduced in the band. The gap widths (and length of rf pulse T_{RF}) used were 400 kHz (4.4 s) for ^{75}As (left panel), 200 kHz (3 s) for $^{115}\text{In} + ^{69}\text{Ga}$ centred on the ^{115}In resonance frequency (middle panel) and 100 kHz (1.28 s) for ^{71}Ga .

and the width dependence is done by applying the rf band centred on ^{115}In but changing the width until both isotopes (^{115}In and ^{69}Ga) are being depolarised.

The rf spectral band width dependence for each isotope in the In-flush sample is plotted in Figure 5.5. At small spectral band widths, not all nuclei and not all transitions of a particular isotope are being driven by the rf band. So less nuclei are being depolarised and there is a smaller detected change in the OHS between “gap” and “no gap” measurements. The signal (ΔE_{OHS}) then increases approximately monotonically until an rf spectral band width that covers the entire isotope is applied, beyond which the signal saturates. The first and most important point to note is that all isotopes show a significant total broadening on the order of several MHz (at $B_z = 8$ T) and indicate the severity of the inhomogeneous first order quadrupolar broadening $\omega_Q^{(1)}$ that affect the STs in these self assembled QDs. It can be seen that the narrowest total width is observed for ^{71}Ga where ΔE_{OHS} saturates when approximately $w_{\text{Band}} = 7$ MHz and this is because ^{71}Ga has a relatively small quadrupolar moment Q compared to the other isotopes (see Table 2.1). To be clear, this is $w_{\text{Band}} = 7$ MHz centred at ~ 104.85 MHz so the resonance extends from ~ 101.35 MHz to ~ 108.35 MHz and is illustrated schematically in Figure 5.4.

For the other isotope of gallium ^{69}Ga , the total resonance width will be about ~ 1.6 times broader (ratio of quadrupolar moments) than that of ^{71}Ga , but as discussed it

cannot be isolated from the broad ^{115}In resonance (which has the largest Q of all the studied isotopes, see Table 2.1). The $^{115}\text{In} + ^{69}\text{Ga}$ isotopes have a combined width of $w_{\text{Band}} = 24$ MHz (middle panel of Figure 5.5). Again this is centred around the ^{115}In frequency of ~ 75.37 MHz and so extends from ~ 63.37 MHz to ~ 87.37 MHz. The ^{69}Ga resonance is at ~ 82.52 MHz so the high frequency STs of ^{115}In which extend to ~ 87.37 MHz essentially cover the whole of the ^{69}Ga resonance, again illustrated in Figure 5.4.

For ^{75}As (left panel of Figure 5.5), the total width of the resonance is measured to be within $w_{\text{Band}} = 18$ MHz and this centred at ~ 58.84 MHz (so between ~ 49.84 MHz and ~ 67.84 MHz). We determine w_{Band} based on the signal that is detected above the noise but it is possible that there are some nuclei with even larger quadrupolar shifts but give too small a signal to detect. The ^{75}As resonance has been observed to have characteristic long “tails” in the ST spectra (discussed later in this chapter), which have a small contribution to the overall signal ΔE_{OHS} and extend over many MHz. Therefore the overlap between the high frequency ST of ^{75}As extending to ~ 67.84 MHz and the low frequency ST of ^{115}In down to ~ 63.37 MHz is minimal and the ^{75}As NMR spectra can be measured separately.

The applied spectral width of the band was usually chosen to be slightly higher than the measured saturation width to ensure that all isotopes are being depolarised under both circular polarisations of pumping. So for the In-flush sample, the final widths were $w_{\text{Band}}^{75\text{As}} = 18$ MHz, $w_{\text{Band}}^{115\text{In}+69\text{Ga}} = 30$ MHz and $w_{\text{Band}}^{71\text{Ga}} = 9$ MHz. Similar measurements on the Low Temp Cap sample yielded widths of $w_{\text{Band}}^{75\text{As}} = 20$ MHz, $w_{\text{Band}}^{115\text{In}+69\text{Ga}} = 27$ MHz and $w_{\text{Band}}^{71\text{Ga}} = 9$ MHz and are summarised in Table 5.1 for the In-flush sample and Table 5.2 for the Low Temp Cap sample.

Now that we have determined the spectral width of the rf band required for each isotope, the other important parameter that was calibrated in relation to the rf pulse was the duration of the pulse T_{RF} . Again this was measured using the inverse NMR “gap” minus “no gap” technique and was chosen based on the value that provided the largest signal ΔE_{OHS} as well as minimising the total experimental measurement time. The specific value was usually optimised for the gap width used in CT or ST NMR spectra and is inversely proportional to the amount of rf power applied for a given isotope and the quality of the rf matching achieved (which indicates how much power is transmitted to the coil and not reflected back along the cables, see Section 3.4.4).

The change in the Overhauser shift ΔE_{OHS} between “gap” and “no gap” waveforms measured as the rf time T_{RF} is varied is shown in Figure 5.6 for the In-flush sample for ^{75}As , ^{115}In and ^{71}Ga . The shape of the curves show that there is an optimal time required to

In-flush sample					
General parameters	T_{Pump} (s)	T_{Probe} (s)	P_{Pump} (μW)	P_{Probe} (μW)	rf mode spacing, f_{MS} (Hz)
	6	0.040	1000	1	120
High resolution CT spectra parameters					
Isotope	^{75}As	^{113}In	^{69}Ga	^{71}Ga	
Central frequency of band, f_{Band} (MHz)	58.84	75.37	82.52	104.85	
Width of band, w_{Band} (MHz)	18	30	14	9	
Gap width, w_{Gap} (kHz)	12	18	4	4	
RF time, T_{RF} (s)	3.5	3.0	1.7	1.28	
3 band inverse NMR ST spectra parameters					
Central frequency of band, f_{Band} (MHz)	58.84	75.37	82.52	104.85	
Width of band, w_{Band} (MHz)	18	30	30	9	
Gap width, w_{Gap} (kHz)	600	600	600	600	
RF time, T_{RF} (s)	4.4	3.0	3.0	1.28	
Width of 3rd CT satura- tion band, w_{CTband} (kHz)	503 [†]	81	39	39	

TABLE 5.1: List of all important experimental parameters used for the cw inverse NMR spectra measurements in the In-flush sample at $B_z = 8$ T. To account for the skewness in the ^{75}As lineshape, the 3rd band is offset to lower frequencies by [†]100 kHz, see Appendix C.

apply the rf pulse to obtain the most signal. At short times, the pulse does not fully depolarise the isotope, so the population change is small. At long times nuclei within the gap of the “gap” waveform are weakly excited due to imperfections in the waveform (for example due to distortions from the amplifier, see Section 3.4.4), so there is a smaller change between the “gap” and “no gap” waveforms (smaller change in the CT NMR signal amplitude). At even longer times, the decay of the nuclear spin polarisation (on a timescale of T_1) would be visible, but at the longest times measured here ~ 15 s, this decay is negligible (see Section 5.1.2). Hence there is an optimal value of T_{RF} which is

Low Temp Cap sample							
General parameters	V_{Pump} (V)	V_{Probe} (V)	T_{Pump} (s)	T_{Probe} (s)	P_{Pump} (μW)	P_{Probe} (μW)	rf mode spacing, f_{MS} (Hz)
	1.36	1.724	6	0.040	1000	0.25	120
High resolution CT spectra parameters							
Isotope	^{75}As	^{113}In	^{69}Ga	^{71}Ga			
Central frequency of band, f_{Band} (MHz)	58.84	75.37	82.52	104.85			
Width of band, w_{Band} (MHz)	20	27	14	9			
Gap width, w_{Gap} (kHz)	12	18	4	4			
RF time, T_{RF} (s)	2.9	3.2	0.36	0.36			
3 band inverse NMR ST spectra parameters							
Central frequency of band, f_{Band} (MHz)	58.84	75.37	82.52	104.85			
Width of band, w_{Band} (MHz)	20	27	27	9			
Gap width, w_{Gap} (kHz)	600	600	600	600			
RF time, T_{RF} (s)	2.9	2.5	2.5	0.5			
Width of 3rd CT sat- uration band, w_{CTband} (kHz)	503*	81	27	39			

TABLE 5.2: List of all important experimental parameters used for the cw inverse NMR spectra measurements in the Low Temp Cap sample at $B_z = 8$ T. To account for the skewness in the ^{75}As lineshape, the 3rd band is offset to lower frequencies by *30 kHz, see Appendix C.

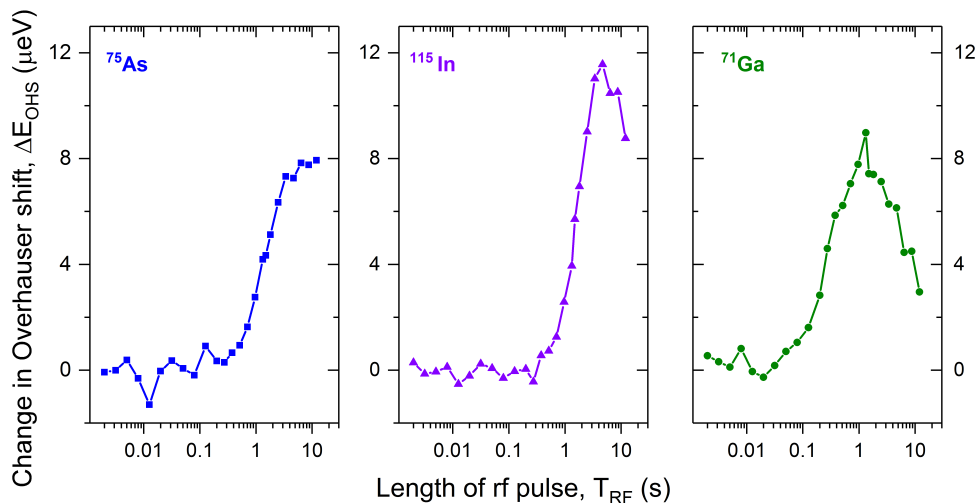


FIGURE 5.6: The difference in Overhauser shift ΔE_{OHS} produced by the “no gap” and “gap” waveforms (which provides the amplitude of the CT NMR signal) as the duration of the rf pulse T_{RF} is varied. The data is taken for each isotope in the In-flush sample at $B_z = 8$ T using σ^- pumping only. The chosen widths of the gap are similar to those used in the high resolution inverse NMR CT spectra i.e. 30 kHz for ^{75}As (left panel), 30 kHz for ^{115}In (middle panel) and 10 kHz for ^{71}Ga .

visible in the data as a peak in the NMR signal ΔE_{OHS} .

The ^{71}Ga calibration (right panel of Figure 5.6) shows a clear peak in the signal and an optimal rf time of $T_{\text{RF}} = 1.28$ s is chosen for the NMR spectra measurements. For ^{75}As and ^{115}In (left and middle panel), the maxima of the peak occurs at quite large rf times. In order to keep the total measurement time reasonable, a compromise time of $T_{\text{RF}} = 3.5$ s for ^{75}As and $T_{\text{RF}} = 3.0$ s for ^{115}In was chosen at the cost of some signal ΔE_{OHS} . Note that this data was measured using narrow gap widths (≤ 30 kHz) such as those used for the CT spectra measurements and more data was taken for large gap widths to determine the optimal T_{RF} for ST spectra. This was repeated for the other Low Temp Cap sample and all of the relevant control parameters used for the cw inverse NMR spectra dataset is summarised in Table 5.1 for the In-flush sample and Table 5.2 for the Low Temp Cap sample.

Finally, another important parameter that can be extracted from the T_{RF} calibration is the total Overhauser shift per isotope. Here we take only the change in splitting from “no gap” minus “no rf” (see Figure 5.7) where a single rf band is applied that is wide enough to cover the entire resonance and depolarises the entire isotope. We can see that the signal saturates at long rf times T_{RF} for all isotopes and this corresponds to the maximum available OHS for that particular isotope. The isotopic Overhauser shifts are $\Delta E_{\text{OHS}}(^{71}\text{Ga}) \approx 17 \mu\text{eV}$, $\Delta E_{\text{OHS}}(^{75}\text{As}) \approx 37 \mu\text{eV}$ and again $^{115}\text{In} + ^{69}\text{Ga}$ are depolarised

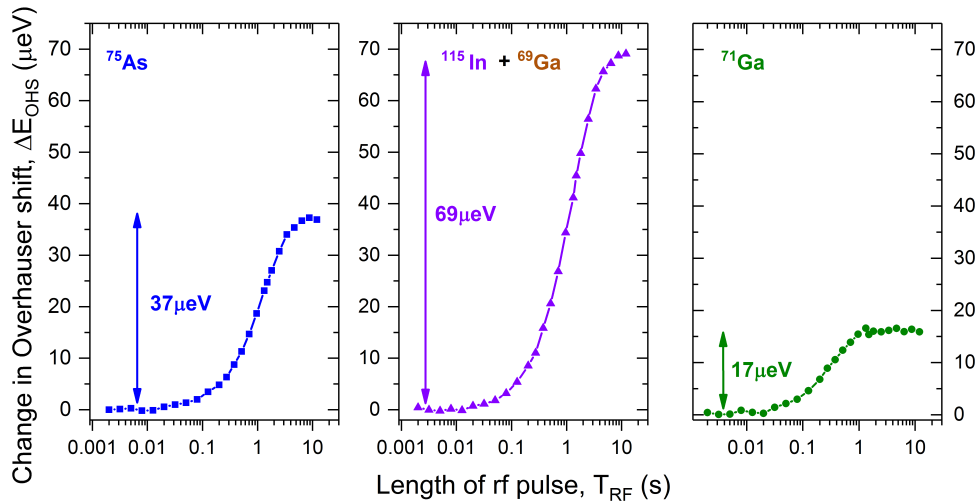


FIGURE 5.7: The change in Overhauser shift ΔE_{OHS} observed by applying a single rf band only (“no gap”) to depolarise the entire isotope as the length of the rf pulse T_{RF} is varied. This measurement allow us to determine the total Overhauser shift per isotope: $37 \mu\text{eV}$ for ^{75}As (left panel), $69 \mu\text{eV}$ for $^{115}\text{In} + ^{69}\text{Ga}$ (middle panel) and $17 \mu\text{eV}$ for ^{71}Ga . The data is taken for each isotope in the In-flush sample at $B_z = 8 \text{ T}$ using σ^- pumping only.

together with a total $\Delta E_{\text{OHS}}(^{115}\text{In} + ^{69}\text{Ga}) \approx 69 \mu\text{eV}$. The sum of all of these shifts is $17 + 37 + 69 = 123 \mu\text{eV}$, which is very close to the total OHS (using σ^-) measured directly after the pump pulse (see Figure 5.2a) of $125 \mu\text{eV}$ which polarises all isotopes. This tells us that our rf pulse can essentially depolarise all of the available nuclear spin polarisation built up by optical pumping. The corresponding measurements in the Low Temp Cap sample showed that $\Delta E_{\text{OHS}}(^{71}\text{Ga}) \approx 14 \mu\text{eV}$, $\Delta E_{\text{OHS}}(^{75}\text{As}) \approx 27 \mu\text{eV}$ and $\Delta E_{\text{OHS}}(^{115}\text{In} + ^{69}\text{Ga}) \approx 38 \mu\text{eV}$. These values can be used (together with the amplitudes of the CT NMR peaks, see Section 5.3) to calculate the indium fraction ρ_{In} within the dot.

5.2 Inverse NMR CT spectra example

Now that all of the important experimental parameters have been determined, we can measure the NMR spectra using the inverse NMR pump-rf-probe scheme discussed in Section 3.4.2. As a summary, a low power, cw radiofrequency waveform is applied to the sample. First a single rf spectral band (“No Gap”) waveform is applied that is wide enough to cover the entire resonance (CT and ST) of a particular isotope and depolarise those nuclei. Then a gap is introduced within the band (“Gap”) which is achieved by applying two rf bands - the width of the gap provides the resolution and since the CT is narrow, high resolution spectra require a narrow gap width w_{Gap} . Nuclei with resonance

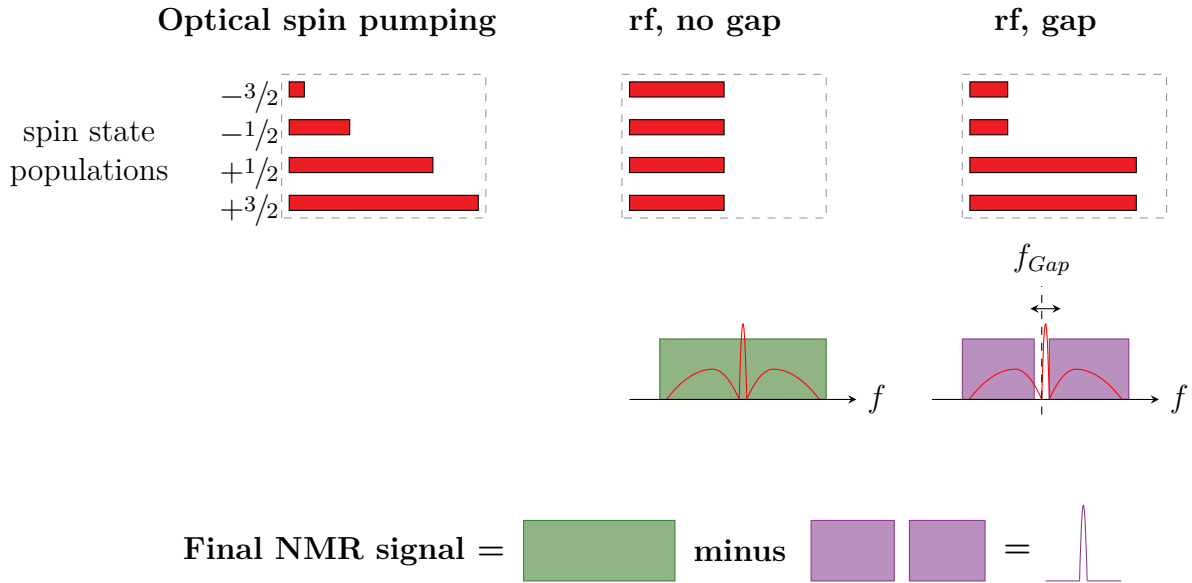


FIGURE 5.8: The optical pump pulse polarises all isotopes and the populations of the nuclear spin states for a spin $I = 3/2$ follow the Boltzmann distribution where most nuclei are initialised into the $I_z = +3/2$ for σ^- pumping. The “no gap” waveform depolarises all nuclei of a specific isotope so the populations of all states are the same. The “gap” waveform (with the gap centred on the CT) creates a population probability distribution with different probability values based on I_z and a change in the Overhauser shift is detected due to nuclei within the gap. The final NMR signal is obtained by taking the change in splitting between the “no gap” minus “gap” measurements as f_{Gap} moves across the resonance. For σ^+ pumping the changes in splitting are reversed and the final NMR signal is from “gap” minus “no gap”.

frequencies [energy difference between the $I_z = +\frac{1}{2} \leftrightarrow -\frac{1}{2}$ (CT) states] within the bands are depolarized and nuclei within the gap remain polarized and we detect a change in Zeeman splitting of the exciton PL line. The central frequency of the gap f_{Gap} is then moved across the isotope’s resonance to trace out the shape of the nuclear resonance spectra. The schematic illustration of the optically detected NMR signal together with how the populations of the nuclear spin states change is shown in Figure 5.8.

To provide an experimental example of how the nuclear resonance is measured, we present the change in the exciton Zeeman splitting as the $w_{\text{Gap}} = 18$ kHz gap is moved across the ^{115}In resonance (with σ^- pumping) in the In-flush sample (see Figure 5.9). The unfiltered data is shown in Figure 5.9a and the data filtered with a Gaussian averaging filter is shown in Figure 5.9b together with a Gaussian fit. For a typical measurement we take four PL spectral repeats with the “Gap” waveform applied at a given frequency and two spectral repeats for the “No Gap” waveform and the plotted data points are the averaged PL spectral splitting. The data shown here is unfiltered, but in the final CT spectra shown in Section 5.3 and ST spectra in Section 5.4, the data is filtered using a Gaussian average filter with a width less than a third of the resolution of the measurement (filter width $< w_{\text{Gap}}/3$,

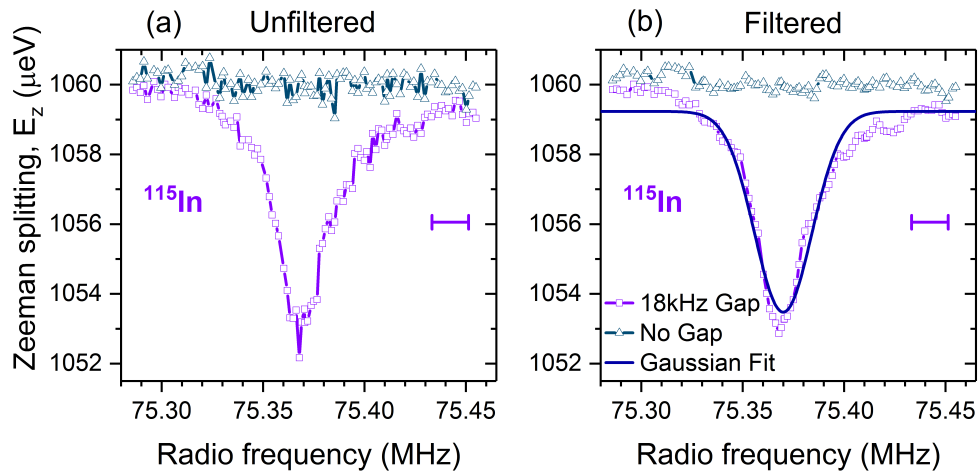


FIGURE 5.9: Inverse NMR CT spectra of ^{115}In in the In-flush sample at $B_z = 8$ T using σ^- pumping only. The “No Gap” waveform provides a background level of splitting and the change in splitting observed when applying a $w_{\text{Gap}} = 18$ kHz (which is the resolution and shown by the horizontal bar) provides the NMR signal. a) shows the unfiltered Zeeman splitting and b) shows the data filtered with a Gaussian averaging filter with a filter width of $w_{\text{Gap}}/3 = 6$ kHz. Also shown in b) is an example of a Gaussian fit which is used to extract the approximate width of the peak w_{inh} .

see comparison between filtered and unfiltered data in Figure 5.9). This allows for a clearer detection of the features in the spectrum such as peaks in the NMR signal as well as the extent of the tails (see Section 5.4). Additionally, this data is corrected for the decay of the external magnetic field from the magnet. The superconducting magnet is not a perfectly isolated system and when the current (field) of the magnet is ramped to the desired value ($B_z = 8$ T) and switched to persistent mode, we observe a slow decrease of the magnetic field over long time scales (of days/weeks). This is detectable as the resonance frequency of a nuclear isotope shifts to lower frequencies and this decay of the magnetic field is approximately linear with a rate of approximately $(dB/dt)/B = 1.2 \times 10^{-4}$ per day (which corresponds to 10 kHz/day for ^{71}Ga). A single detailed NMR spectrum can take several days to acquire a complete dataset and we cannot ignore this drift over such a time scale as the nuclear resonance would shift away from the central frequency of the gap f_{Gap} in the rf bands and no signal would be detected. We know the drift rate of the magnetic field as a function of the wall clock time and the wall clock time is recorded for each datapoint in the NMR spectrum. Hence we correct for this drift by appropriately rescaling the frequency of each datapoint ($f_{\text{Corrected}} = f_{\text{Raw}} + f_{\text{Raw}} \times (\text{elapsedtime} \times \text{driftrate})$) to determine the true NMR spectral profile. We also rescale the datasets between individual NMR spectra so that the resonance frequencies are the same (for a single isotope) and the shape of the resonance can readily be compared between samples or pump polarisations.

The “No Gap” measurement should be a flat horizontal line that denotes the splitting when

all ^{115}In nuclei have been depolarised. This is indeed observed from Figure 5.9, where the “No Gap” dataset is at a splitting of about 1.060 meV and shows a fluctuation of $< 1 \mu\text{eV}$. We observe that as the gap is moved across the ^{115}In CT resonance frequency of 75.37 MHz there is a decrease in the observed splitting of about $8 \mu\text{eV}$. This is illustrated schematically in Figure 5.8 and is because σ^- pumping was used in the measurement. This σ^- pumping creates a negative change in the total OHS. Then the “No Gap” rf waveform depolarises one isotope to induce a positive change in the OHS relative to the “ σ^- pumping” value. Finally, the “Gap” rf waveform provides a decrease in the Zeeman splitting relative to the “No Gap” value. Note that the opposite is true for σ^+ pumping and we can compare datasets by taking the absolute value of the splitting change.

The width of the peak is the inhomogeneously broadened linewidth of the central transitions for all nuclei of a given isotope in the dot. It is measured by fitting the peak with a Gaussian function and the FWHM is derived to be $w_{\text{inh}}(^{115}\text{In}) \approx 33 \text{ kHz}$. Note that this is just an approximation for the linewidth because the NMR lineshape is not perfectly Gaussian and is asymmetric. Though the amplitude can also be extracted from the fit, it is more reliable, particularly for ^{75}As whose signal has a peak that is accompanied by a broad tail (see Section 5.3), to integrate the area under the curve S_{CT} . To compare with other isotopes (and between samples) where different gap widths were used, S_{CT} is divided by w_{Gap} and the total “normalised” signal of the CT peak will be quoted as $\Delta E_{\text{CT}} = S_{\text{CT}}/w_{\text{Gap}}$ ($= 18.7 \mu\text{eV}$ for the ^{115}In CT peak in the In-flush sample).

5.3 Comparison of all inverse NMR CT spectra

The inverse NMR CT spectra discussed in the previous section were measured for the four most abundant nuclear isotopes (^{75}As , ^{115}In , ^{69}Ga , ^{71}Ga) in both InGaAs QD samples (In-flush and Low Temp Cap sample). The full dataset was measured for a single dot from each sample. Certain NMR spectra were repeated for several other dots from each sample and similar spectral shapes were obtained (but full datasets were not repeated for detailed comparisons). To obtain spectra with non resolution limited linewidths, the gap widths w_{Gap} had to be chosen as narrow as possible for each isotope whilst still being able to resolve enough signal. All of the important experimental parameters are listed in Table 5.1 and 5.2, and the final inverse NMR CT spectra are shown in Figure 5.10.

The amplitudes and widths of the peaks extracted from the CT NMR spectra are shown in Table 5.3. It can be seen that the width of both Ga isotopes are narrow $< 10 \text{ kHz}$

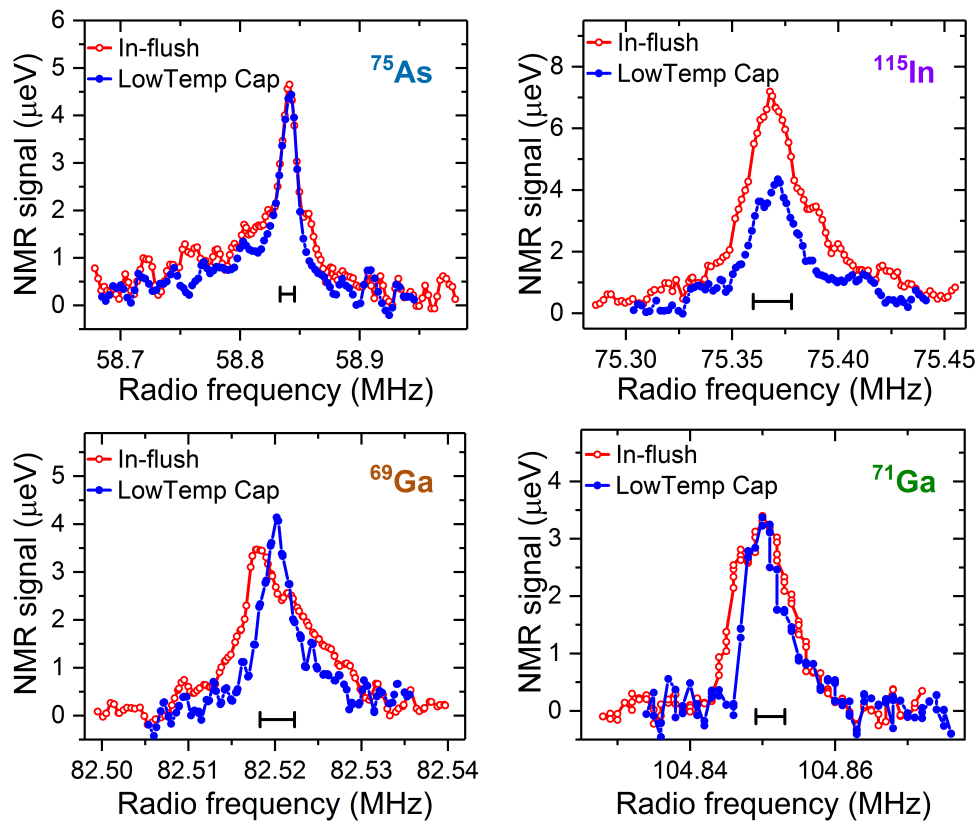


FIGURE 5.10: High resolution central transition (CT) NMR spectra of all nuclear isotopes in both InGaAs/GaAs QD samples. All spectra were taken at $B_z = 8$ T and using σ^- polarized pumping. The horizontal bars indicate the resolution which in these experiments are given by the width of the gap in the inverse NMR radiofrequency waveform and differ by isotope ($w_{Gap} = 4$ kHz for both Ga isotopes, $w_{Gap} = 12$ kHz for ^{75}As and $w_{Gap} = 18$ kHz for ^{115}In).

Low temp Cap sample	^{75}As	^{115}In	^{69}Ga	^{71}Ga
w_{Gap} (kHz)	12	18	4	4
w_{inh} (kHz)	20.6	25.9	4.5	6.3
ΔE_{CT} (μeV)	17.7	9.7	6.7	6.0
In-flush sample				
w_{Gap} (kHz)	12	18	4	4
w_{inh} (kHz)	29.5	33.1	10.4	8.9
ΔE_{CT} (μeV)	23.9	18.7	9.6	8.0

TABLE 5.3: The inhomogeneous linewidths (FWHM) of CT peaks (w_{inh}) from fitting NMR CT spectra and the normalised integrated CT signal (ΔE_{CT}) for all isotopes in both InGaAs/GaAs QD samples.

in both samples. However, both In and As are a factor of 3-5 times broader. This is in agreement with previous work (see [146]). This width of the CT is governed by the inhomogeneous second order quadrupolar interaction ($\omega_Q^{(2)}$, see Section 2.3.3). For the case of ^{115}In , this broadening occurs because it has a larger quadrupole moment Q (see Table 2.1) than the other isotopes which manifests in a more severe broadening in the CT spectra. The ^{75}As resonance is also broad but this is because of the compositional disorder around the As nuclei. For example in the zincblende crystal lattice for InGaAs dots, each ^{75}As nucleus can be surrounded by exactly four In nearest neighbours, exactly four Ga nearest neighbours or some combination of In and Ga. However, Ga or In may only be surrounded by exactly four As neighbours in a tetragonal configuration. This creates an additional source of local strain at the atomic length scale that is felt by the ^{75}As nuclei and they show larger quadrupolar shifts than Ga [146, 186].

Additionally, the ensemble dephasing time of the nuclei T_2^* which arise from the widths of these inhomogeneously broadened spectra are related through the equation $T_2^* = 1/(2\pi w_{\text{inh}})$. We can therefore estimate for the Low Temp Cap sample $T_2^*(^{75}\text{As}) \approx 7.7 \mu\text{s}$ and $T_2^*(^{71}\text{Ga}) \approx 25.3 \mu\text{s}$ and for the In-flush sample $T_2^*(^{75}\text{As}) \approx 5.4 \mu\text{s}$ and $T_2^*(^{71}\text{Ga}) \approx 17.9 \mu\text{s}$. Such times (calculated by measuring in the frequency domain with cw NMR) are in good agreement with previous work using pulsed NMR (in the time domain) techniques [147].

The amplitudes of the peaks are similar between samples when comparing the isotopes of ^{75}As , ^{69}Ga and ^{71}Ga . However, for the ^{115}In CT peak, the amplitude in the In-flush sample (integrated signal $\Delta E_{\text{CT}}(^{115}\text{In}) = 18.7 \mu\text{eV}$) is much higher than in the Low Temp Cap sample ($\Delta E_{\text{CT}}(^{115}\text{In}) = 9.7 \mu\text{eV}$). This reflects the differences in the chemical compositions and agrees with the growth methods of the two samples – the In-flush technique requires deposition of more indium before the growth temperature is increased (see Section 3.1).

We see a distinct CT NMR signal from both Ga and In isotopes and so there is a clear substitution of Ga nuclei by In nuclei within the QD. We can estimate the relative concentrations of indium ρ_{In} and gallium ρ_{Ga} within the specific InGaAs QDs in both samples. Being more specific, this corresponds to all the nuclei that overlap with the wavefunction of the electron trapped within the QD. We obtain numerical values for ρ_{In} and ρ_{Ga} in both samples by combining the measurements of the total Overhauser shift per isotope ΔE_{OHS} (see Figure 5.7) and the normalised integrated CT signal ΔE_{CT} (see Table 5.3). The detailed calculation is described in Appendix B) and we find for the In-flush sample $\rho_{\text{In}} = 19.2 \%$ and $\rho_{\text{Ga}} = 80.8 \%$, and for the Low Temp Cap sample $\rho_{\text{In}} = 9.9 \%$ and $\rho_{\text{Ga}} = 90.1 \%$. Immediately we recognize the sample grown with the Indium flush technique does indeed contain more indium because more indium was deposited during the

In-flush technique, but the dots from both samples have significantly more Ga than In. Also in the Low Temp Cap sample, the dots are observed to be smaller (see Section 5.5) as an indium rich core surrounded by GaAs. The spread of the electron wavefunction means that the average contribution of In observed in the NMR spectra is small.

This all indicates that the wavefunction of the electron trapped in the QD overlaps significantly more Ga nuclei than In. The information gained from these CT spectra provide hints that the electron wavefunction is significantly penetrating into the surrounding GaAs barrier layers in both samples and we actually corroborate this idea further with observations from inverse NMR ST spectra as well as analysis of TEM images.

5.4 Novel 3-band inverse NMR technique to measure ST spectra

The ST spectra (transitions between $I_z = +3/2 \leftrightarrow +1/2$ or $-3/2 \leftrightarrow -1/2$ for $I = 3/2$ nuclei) are much broader than the CT ($I_z = +1/2 \leftrightarrow -1/2$) due to strong 1st order quadrupolar shifts $\omega_Q^{(1)}$ induced by strain in self-assembled QDs on the spin $I = 3/2$ nuclear isotopes (and $I = 9/2$ for In). The individual resonance frequency of the ST nuclear transition depends on the position of the nucleus in the dot and the different combinations of neighbouring nuclei leading to different local strain environments.

To be able to detect any signal from the STs, the width of the gap in the inverse NMR waveform has to be much larger. As shown in previous work [146], when measuring such spectra using large gap widths for each isotope, a broad, resolution limited peak is observed together with additional secondary peaks and long tails. The resolution limited peak in the middle is observed because the large gap overlaps both the CT and any STs that have a small frequency offset. A change in splitting is observed due to both transitions and it is not possible to isolate the signal of the ST alone since the CT contribution dominates. This is an unwanted side effect of this technique and masks any ST signal with small frequency offsets from the CT frequency coming from nuclei with small total elastic strain.

In order to isolate the ST signal close to the central frequency of an isotope's resonance, we propose a novel 3-band inverse NMR waveform where a 3rd narrow band is positioned (at frequency f_{CTband}) to saturate the CT as the large gap ($w_{Gap} > w_{CTband}$, with central frequency f_{Gap}) is moved across the resonance. The width of the 3rd CT band w_{CTband} is chosen based on extensive measurements of the CT NMR spectra (see Appendix C and Figure 5.10 above) to cover at least 90% of the width of the CT for each isotope.

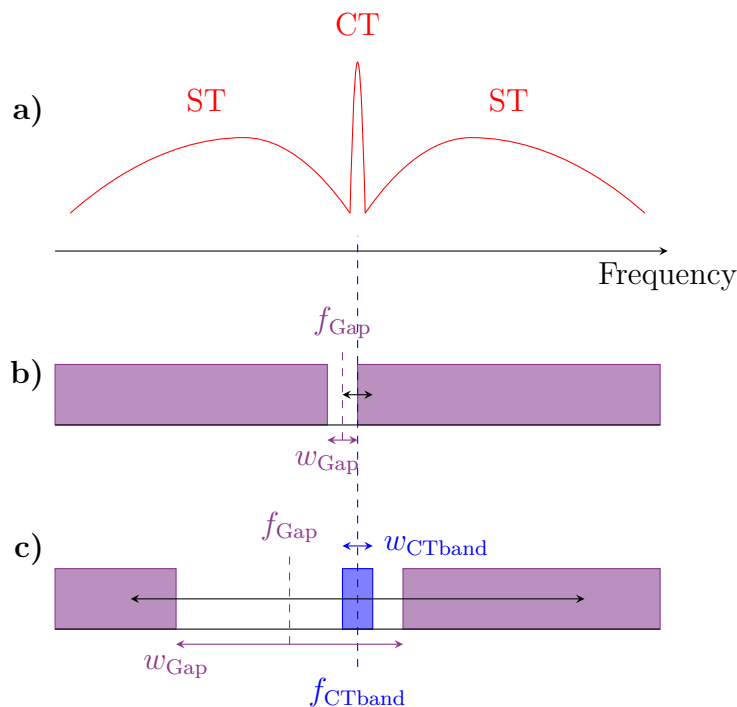


FIGURE 5.11: Comparison of the 2 and 3 band inverse NMR technique. a) Schematic illustration of the shape of the NMR signal from a spin $I = 3/2$ quadrupolar nuclear isotope. A narrow central transition ($I_z = +\frac{1}{2} \leftrightarrow -\frac{1}{2}$) is accompanied by 2 broad satellite transitions ($I_z = +\frac{3}{2} \leftrightarrow +\frac{1}{2}$ or $-\frac{3}{2} \leftrightarrow -\frac{1}{2}$) due to the strain distribution in single quantum dots. b) The shape of the inverse NMR radiofrequency waveform used to manipulate the isotope to measure the CT spectra. Two broad bands that are wide enough to cover the entire resonance are accompanied by a narrow gap and the central frequency of the gap f_{Gap} is moved across the CT resonance peak to measure the CT signal. c) The shape of the rf waveform for the new 3-band inverse NMR technique used to measure the STs. The gap between the bands is large and if the gap overlaps the CT transition, a 3rd narrow CT band ($w_{\text{CTband}} < w_{\text{Gap}}$) is applied to saturate the CT signal. The position of the 3rd band f_{CTband} remains fixed and the width of the 3rd band is chosen to cover at least 90% of the CT resonance peak.

The shapes of the applied rf waveforms are compared between the 2 band method used to measure the CT spectra and the new 3 band method for the ST spectra in Figure 5.11. Note that this technique only affects datapoints where the gap position f_{Gap} is close to the central frequency. The inclusion of the 3rd band can lead to the effective gap width w_{Gap} being reduced and in order to compare all datapoints equally, the NMR signal was rescaled. The rescaling procedure based on different gap positions relative to the 3rd CT band is comprehensively described in Appendix D and provides only a small correction to the signal of the order $w_{\text{CTband}}/w_{\text{Gap}}$.

To explicitly show the experimental effect of the 3rd CT band on the inverse NMR ST spectra, we performed a measurement of the ST spectra for ^{71}Ga in the Low Temp Cap sample. A set of spectra were taken (both σ^+ and σ^- pumping) using the new 3 band

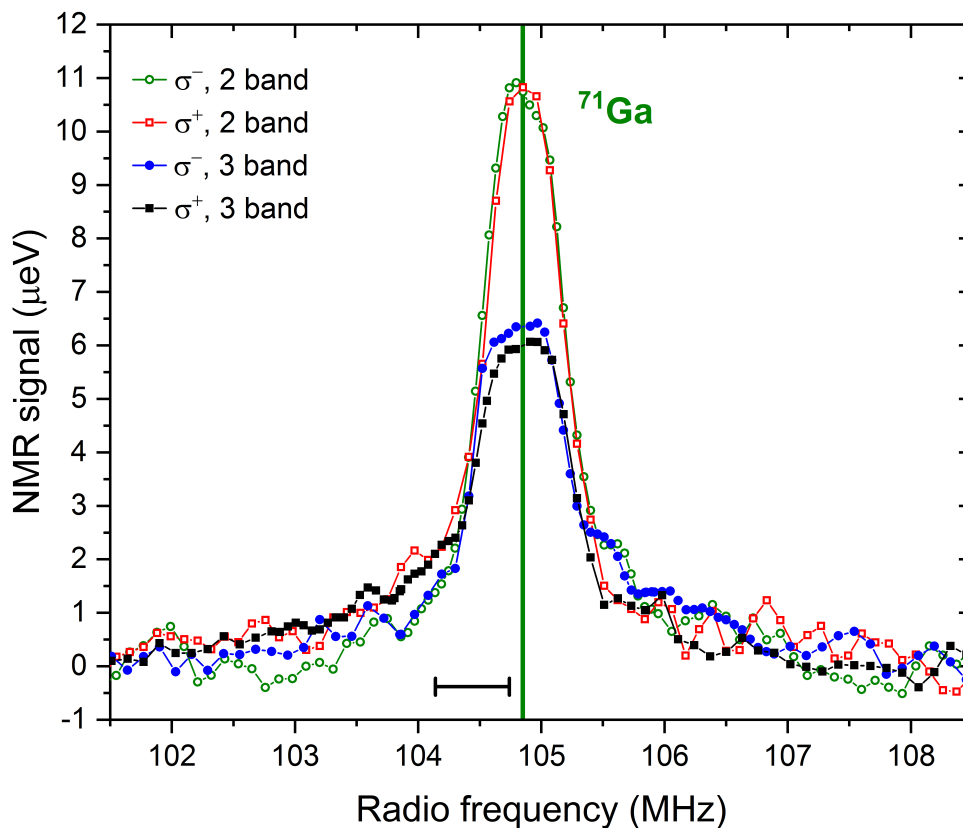


FIGURE 5.12: The inverse NMR ST spectra of ^{71}Ga in the Low Temp Cap sample. Both pump polarizations are shown for both 2 and 3 band techniques and a clear reduction in peak amplitude is visible in the 3 band measurement due to saturation of the CT signal. All spectra were taken at $B_z = 8$ T with a gap width (resolution) of $w_{\text{Gap}} = 600$ kHz.

technique with a gap width $w_{\text{Gap}} = 600$ kHz and a CT band with width $w_{\text{CTband}} = 39$ kHz, and a set of spectra were taken without the 3rd band (regular inverse NMR “2 band” technique) with a gap width $w_{\text{Gap}} = 600$ kHz. This allows for a direct comparison and the sole effect of the 3rd band can be investigated. Both sets of spectra for a single QD in the Low Temp Cap sample are shown in Figure 5.12 and it can be seen that far away from the central resonance, the spectra are almost identical. Characteristic features in the spectra are visible with both techniques including the “tails” at both the high and low frequency side of the spectra and also secondary peaks away from the central peak such as the “shoulder” shaped feature at the higher frequency of ≈ 105.55 MHz for σ^- and at a lower frequency of ≈ 103.98 MHz for σ^+ . Near the CT frequency, the difference between the two methods is clearly visible. The 3 band technique reduces the amplitude of central peak from ~ 11 μeV (maxima with the regular inverse NMR “2 band” technique) to ~ 6 μeV . The fact that the peak near the CT frequency still persists with the 3 band method indicates that some of the signal near the CT frequency is due to the ST signal. These are due to nuclei with a small quadrupolar shift and this new 3 band technique has

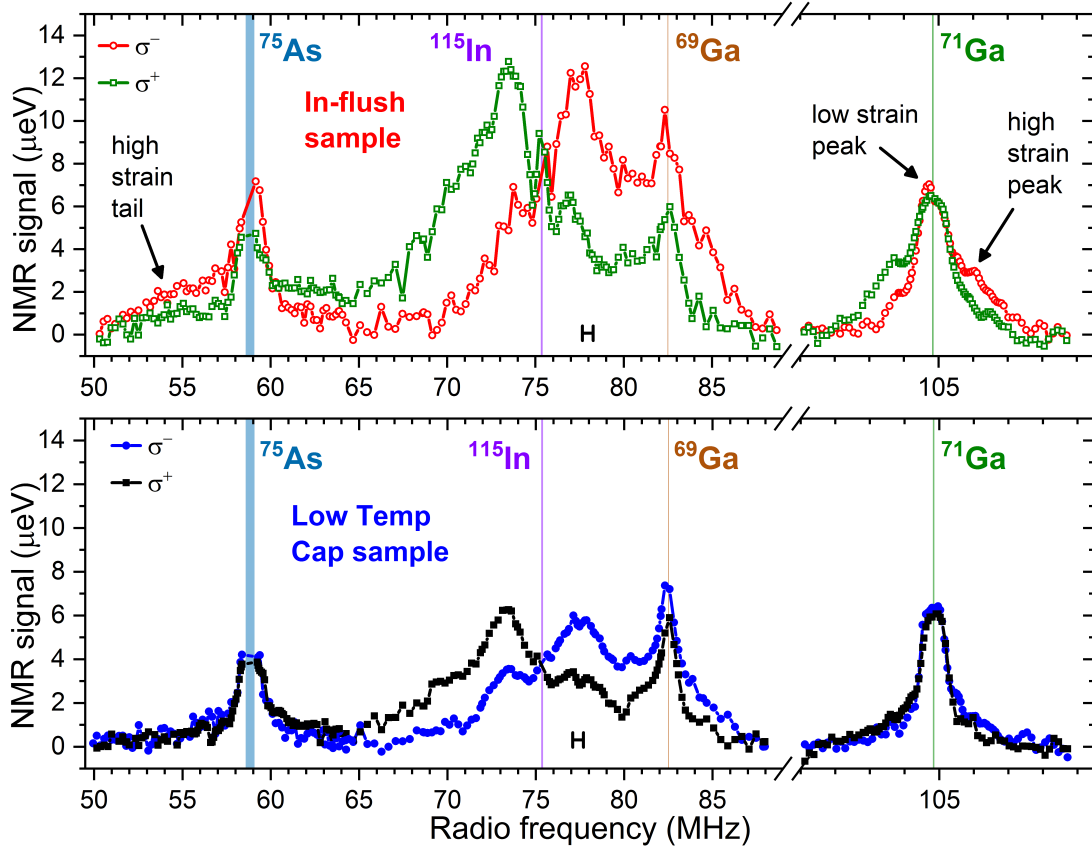


FIGURE 5.13: Inverse NMR satellite transition (ST) spectra of all nuclear isotopes in both QD samples using the novel 3-band inverse NMR technique and pumping with either σ^+ or σ^- circularly polarized pumping. All spectra were taken at $B_z = 8$ T and an inverse NMR gap width of $w_{\text{Gap}} = 600$ kHz which is the resolution of the spectra. Top Panel: ST spectra from a single QD in the sample grown with In-flush. Bottom Panel: ST spectra from a dot in the Low Temp Cap sample. The shaded lines at frequency 58.84 MHz, 75.37 MHz, 82.52 MHz and 104.85 MHz indicate the width of the CT-band used to saturate the CT of each of the 4 nuclear isotopes: ^{75}As ($w_{\text{CTband}} = 503$ kHz), ^{115}In ($w_{\text{CTband}} = 81$ kHz), ^{69}Ga ($w_{\text{CTband}} = 39$ kHz) and ^{71}Ga ($w_{\text{CTband}} = 39$ kHz) respectively.

allowed us to directly detect these low strain nuclei.

Now we present the full 3 band inverse NMR ST spectra for all isotopes in two individual QDs from the two studied samples under both σ^+ or σ^- pumping (shown in Figure 5.13). A gap width of $w_{\text{Gap}} = 600$ kHz was used in the inverse NMR waveform and the vertical shaded lines show the position and width of the 3rd CT saturation band (all of the other important experimental parameters are shown in Tables 5.2 and 5.1). The width of this CT band is broad ($w_{\text{CTband}} = 503$ kHz) for ^{75}As because analysis of the CT spectra (see Appendix C) shows that ^{75}As has a broad low frequency tail (see top left panel in Figure 5.10). This arises due to the additional compositional disorder around the As nuclei as discussed in Section 5.3 and is further evidenced by the long ST tails as wide

as ± 10 MHz visible in the ST spectra for both samples (see Figure 5.13). Again, as seen from the CT spectra, the widths of 3rd CT saturation bands chosen for the other three isotopes are relatively narrow (about 40 – 80 kHz) compared to $w_{\text{Gap}} = 600$ kHz.

Comparing the NMR spectra between samples, the shapes and distributions (for each polarisation) of the ST signal are remarkably similar for each dot in the two samples even though their growth procedure was quite different. The fact that the frequency offsets created by the quadrupolar shifts are similar indicates the distribution of strain felt by the nuclei is also similar in each sample. Even secondary peaks such as the pronounced maxima at 73.4 MHz and 77.4 MHz for ^{115}In are visible in both samples at approximately the same frequencies. The peaks in the ST spectra reach similar amplitudes for all isotopes except for ^{115}In which has a maximum of about $12 \mu\text{eV}$ for the In-flush sample and $6 \mu\text{eV}$ for the Low Temp Cap sample. This is consistent with the data from the CT spectra and is a consequence of the indium flush growth technique that deposited more indium. Note that there are a few noticeable differences in the ST spectra as well. The high strain tail in the ^{75}As ST signal and the high strain peaks at approximately ~ 103.7 MHz and ~ 106.0 MHz in the ^{71}Ga ST signal (labelled in the top panel in Figure 5.13) have larger amplitudes in the In-flush sample. Again, this is caused by the larger dots observed in the In-flush sample (see Section 5.5), which allows for the detection of a larger ST NMR signal compared to the smaller dot in the Low Temp Cap sample.

Since ^{115}In is a spin $I = 9/2$ isotope, the ST spectra extend over large ranges in frequency of about ± 15 MHz. However, the individual transitions between the higher order states ($I_z = +3/2 \leftrightarrow +5/2$, $I_z = +5/2 \leftrightarrow +7/2$, etc.) are not individually resolved and the strong variation in strain smooths out the signal into a single inhomogeneously broadened spectrum. Note that the secondary peaks in the ^{115}In ST spectra at about 73.4 MHz and 77.4 MHz are from the $I_z = -3/2 \leftrightarrow -1/2$ and $1/2 \leftrightarrow 3/2$ transitions because they have the smallest quadrupolar shifts and therefore the smallest inhomogeneous broadening. The high frequency side of the ^{115}In spectra also overlaps the ^{69}Ga spectra so the signal from the two isotopes were measured together (as discussed in Section 5.1.3). The broad bands in the inverse NMR waveform are chosen to cover the entire resonance of both isotopes and when the gap is moved near the ^{69}Ga frequency, the observed NMR signal is the sum of ST signals from both ^{115}In and ^{69}Ga .

The other important characteristic of the system that can be probed with these NMR techniques is the elastic strain magnitude and distribution. It must be noted however, that strain inside a QD is a complicated 3D function and the NMR spectrum that we measure is a convolution of the strain profile with the electron wavefunction [124, 126, 146]. We

can use the change in radio frequency between the CT and the ^{115}In ST peaks to estimate values for the biaxial strain in the dots. The $+1/2 \leftrightarrow +3/2$ and $I_z = -1/2 \leftrightarrow -3/2$ ST of ^{115}In has the smallest frequency offset and also the smallest inhomogeneous broadening and are responsible for the ST peaks at 73.4 MHz and 77.4 MHz (which are offset by -1.97 and +2.03 MHz from the CT frequency). From Section 2.3.3, we can obtain that for biaxial strain (with the electric field gradient axis pointing along B_z) the frequency offset between the $m \leftrightarrow m + 1$ transition and the CT ($-1/2 \leftrightarrow 1/2$) is $\Delta f_Q = f_Q(m + 1/2)$, where

$$f_Q = \frac{3eS_{11}Q\epsilon_B}{2hI(2I - 1)} \quad (5.1)$$

and Q is the quadrupolar moment, S_{11} is the gradient elastic tensor component and ϵ_B is the biaxial strain parameter. Using the measured frequency offsets of $|\Delta f_Q|$ from the ^{115}In ST spectra, $Q = 81.0 \times 10^{-30} \text{ m}^2$ for ^{115}In (see Table 2.1) and $S_{11} = 5.0 \times 10^{22} \text{ V/m}^2$ (measured for indium in bulk InAs [125]), the peak value of biaxial strain can be estimated. With $|\Delta f_Q| \approx 1.99 \text{ MHz}$ for the Low Temp Cap sample, we find $|\epsilon_B| \approx 4.9 \%$ and for the In-flush sample with $|\Delta f_Q| \approx 1.89 \text{ MHz}$, $|\epsilon_B| \approx 4.6 \%$.

Similarly, the maximum biaxial strain can be estimated using the ^{71}Ga ST peak which is separated in frequency from the other isotopes. The maximum offsets from the ^{71}Ga ST signal is found to be within $|\Delta f_Q| \approx 2.90 \text{ MHz}$ for the In-flush sample and $|\Delta f_Q| \approx 3.16 \text{ MHz}$ for the Low Temp Cap sample. Using the quadrupolar moment for ^{71}Ga of $Q = 10.7 \times 10^{-30} \text{ m}^2$ and $S_{11} = 2.7 \times 10^{22} \text{ V/m}^2$ (measured for gallium in bulk GaAs [125]), the maximum biaxial strain is $|\epsilon_B| \lesssim 8.3 \%$ for the In-flush sample and $|\epsilon_B| \lesssim 9.1 \%$ for the Low Temp Cap sample, which is consistent with the peak values ($\approx 4.9 \%$ for Low Temp Cap sample and $\approx 4.6 \%$ for In-flush sample) calculated above.

As observed previously [146], there is an asymmetry in the ST peaks depending on the polarization of the pump laser. This is because of the high degree of polarization of the nuclear spin bath, so transitions involving positive (negative) I_z spin states show a higher signal in the high (low) frequency side of the resonance under σ^- (σ^+) pumping for In and Ga. For As the situation is reversed and the low frequency side is enhanced under σ^- pumping and this is due to the direction of the electric field gradients being reversed for anions (As) from cations (Ga and In).

The new 3-band technique shows that the NMR signal from the STs with small quadrupolar shifts (close to the CT frequency) is a significant fraction of the overall signal. There is a non-zero ST signal for all of the isotopes in both samples and indeed in isotopes such as ^{71}Ga , the large peak within $\pm 0.5 \text{ MHz}$ of the CT forms most of the ST signal for

the isotope. This was a surprising result for gallium - it was assumed that some nuclei would have little to no strain but once the CT signal was eliminated, the remaining ST signal still shows such a large peak. It is possible for the biaxial strain to be completely relaxed to zero near the centre of the dot [85, 187] and $\Delta f_Q = 0$ for some nuclei. But such a large ST signal with small Δf_Q indicates that the electron wavefunction must have a significant penetration into the surrounding GaAs barrier layers where there is no intermixing with InAs and the elastic strain on the Ga nuclei is small. There is more evidence for this interpretation from the chemical composition of the dot obtained from the CT inverse NMR spectra which show that there is a small indium content in both samples ($\rho_{In} \approx 19.2\%$ for the In-flush sample and $\rho_{In} \approx 9.9\%$ for the Low Temp Cap sample) so most of the cations are gallium atoms. But most importantly, the ^{115}In ST signal shows a dip at the CT frequency as opposed to the peak for both gallium isotopes, which suggests that the large $\Delta f_Q = 0$ peak is from nuclei outside of the dot centre (where no ^{115}In nuclei are present). This new 3 band method has allowed us to extract these minute structural details of single QDs, which so far have not been observed experimentally.

5.5 TEM image analysis of InGaAs/GaAs QD samples

To obtain a comprehensive picture of the internal structure of the QD, we can use the complementary properties from the NMR spectra as well as TEM images. Using TEM images, we can extract information about the indium fraction ρ_{In} , as well as the size and shape of the QDs. Using the annular dark field technique [188], which provides a strong contrast in the measured image based on the chemical composition of the material, TEM images were recorded for both samples (see Figure 5.14 and 5.15a-b). In the In-flush sample, clear QD islands of InAs are visible and both large pyramid shaped (about 30 nm wide and 5 nm high) dots and shallow disc shaped dots (20 nm wide and 2 nm high) have formed (also visible just below the dot layer is the short-period GaAs/AlAs superlattice around the QD layer used to enhance the photoluminescence). However, in the Low Temp Cap sample, there are no obvious islands of InGaAs that can be identified as clear QD candidates. Instead the InGaAs layer is seen as a bright layer with only small scale fluctuations (on the order of tens of nanometres).

An example of a small shallow dot in the In-flush sample is shown in Figure 5.14b and a large pyramidal dot in Figure 5.14c. The wetting layer is also visible in the images as the

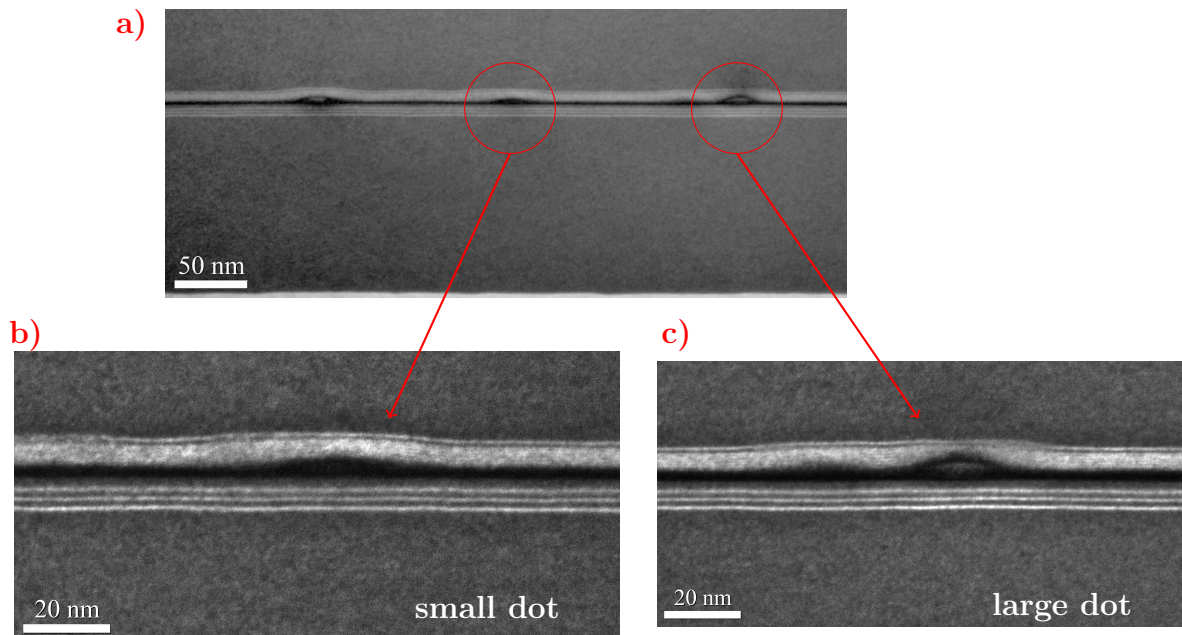


FIGURE 5.14: a) Transmission electron microscope (TEM) 002 dark field images of a cross section of the In-flush sample with 50000 times magnification. Both larger pyramidal shaped dots and shallower disc like dots both visible. b) Shows a magnified TEM image of a shallow dot and c) a large dot in the In-flush sample with 150000 times magnification.

thin horizontal dark layer and its thickness is seen to vary between $\sim 2.6 - 3.1$ nm. For this In-flush sample, we do not have very high resolution TEM images (unlike in the Low Temp Cap sample, see Figure 5.15b), but ρ_{In} may still be estimated by looking at the brightness of the various layers. Using the analysis presented in previous work analysing TEM images [189], the small dot (Figure 5.14b) which is essentially a thickened region of the dark wetting layer has a ρ_{In} value between $\sim 15 - 30$ %. This agrees well with the findings from the NMR CT spectra, where for the In-flush sample, we found that $\rho_{In} = 19.2$ %. The much brighter region in the centre of the large dot (Figure 5.14c) corresponds to a higher indium content with $\rho_{In} \sim 50$ %. But from the work by Gerthsen et al. [190] such large pyramidal dots are observed to emit at a much higher PL wavelength (~ 1200 nm) than the dots studied here in the In-flush sample (~ 920 nm). Additionally, simulations of the NMR spectra for these large pyramidal dots [126] reveal a clearly different shape to that measured in the inverse NMR ST spectra in Figure 5.13. Hence, although both small and large dots are visible in the TEM images, only the NMR spectra (and PL emission) from the small dots are studied here and we can approximate that the dots are about 20 nm wide and 2 nm high.

To explore the small scale fluctuations in the InGaAs layer of the Low Temp Cap sample, the very high resolution image (Figure 5.15b) was analysed to extract the In content

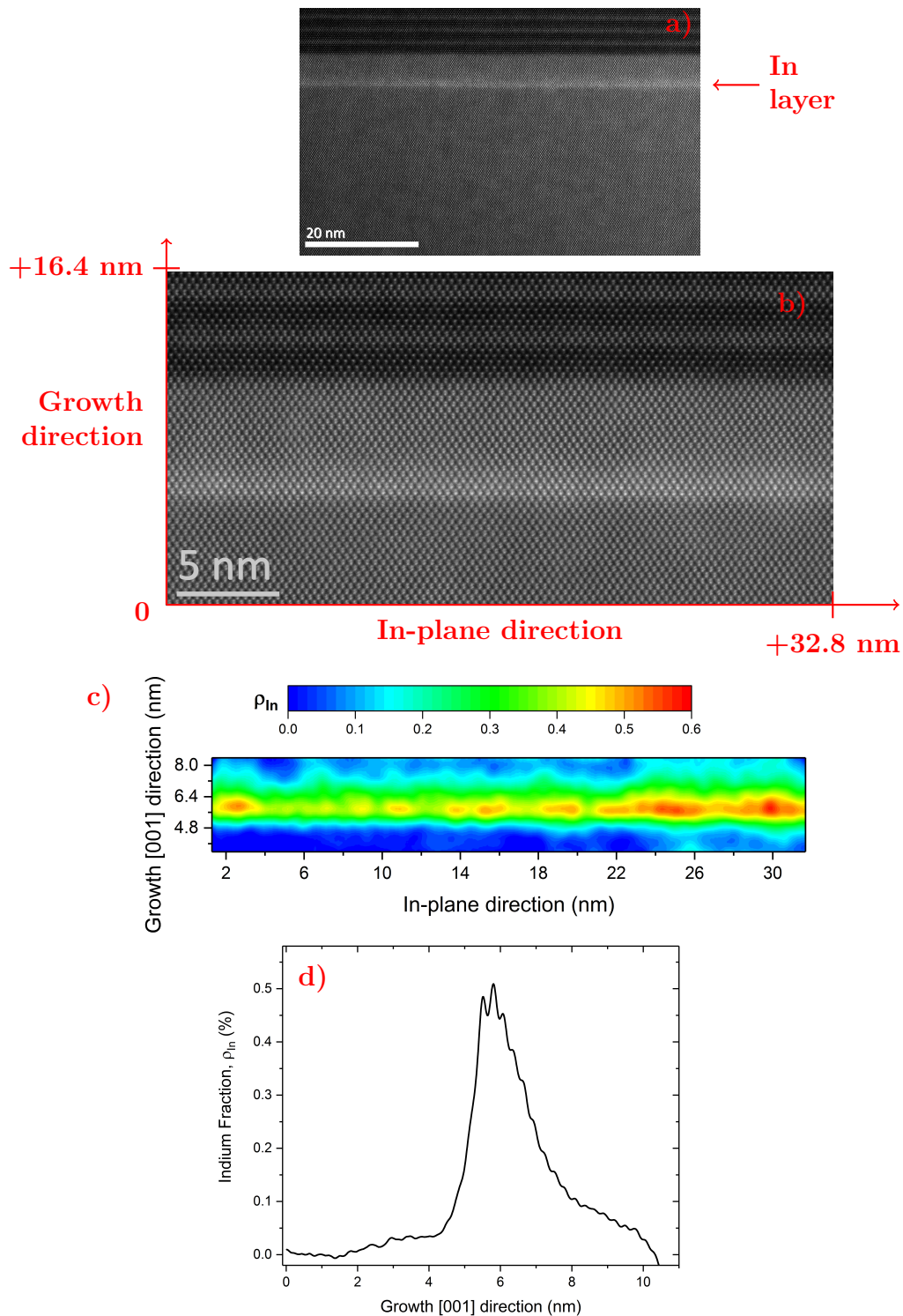


FIGURE 5.15: a) Annular dark field TEM image of Low Temp Cap sample with 2.5×10^6 times magnification. An indium layer is clearly visible (as the bright layer), but no obvious quantum dot like structures are found. b) Very high resolution TEM image of InAs layer in the Low Temp Cap sample with 6×10^6 magnification. The image growth axis and in plane axis are labelled with dimensions and these values are used for the axes scales in the plots in c) and d). c) In plane variation of ρ_{In} calculated from the intensity values of the high resolution TEM image (shown in b)) of the Low Temp Cap sample. Note that $\rho_{In} = 0$ corresponds to pure GaAs and $\rho_{In} = 1$ is pure InAs. d) The variation of the fraction of In ρ_{In} in the growth direction by averaging over rows of pixels in the high resolution TEM image (shown in b)). Thanks to Richard Beanland from the University of Warwick for the TEM images.

surrounding the InGaAs layer. In these dark field TEM images, the intensity I of the detected light (that has been scattered from the sample) at any point in the image is proportional to $Z^{1.5}$, where Z is the proton number of a nucleus. The exponent of 1.5 is a good approximation for a realistic image but in the ideal case of Rutherford scattering, the proportionality would be to Z^2 . To get some numerical estimates of the In concentration ρ_{In} , the image was filtered to smooth out atomic scale fluctuations and the intensity at any given pixel can be written

$$I = I_0 + k \sum_i \rho_i Z_i^{1.5}, \quad (5.2)$$

where I_0 is a background intensity, k is an intensity proportionality coefficient and the sum is over all isotopes i present at that pixel with an abundance ρ_i . There are two unknowns (I_0 and k) in the equation and thus require two reference points. The reference points used were the intensity of the GaAs layer I_{GaAs} and that of the AlAs I_{AlAs} layer and were estimated by averaging the intensities over a region of GaAs pixels (below the InAs layer) and AlAs pixels (in the GaAs/AlAs superlattice above the InAs layer). So the solution to Equation 5.2 is

$$\rho_{In} = \left(\frac{I_{InGaAs} - I_{GaAs}}{I_{GaAs} - I_{AlAs}} \right) \left(\frac{Z_{Ga}^{1.5} - Z_{Al}^{1.5}}{Z_{In}^{1.5} - Z_{Ga}^{1.5}} \right). \quad (5.3)$$

First, an approximate analysis was performed to visualise how the In fraction ρ_{In} varies in the growth direction (see Figure 5.15d) using the very high resolution TEM image shown in Figure 5.15b. For each pixel in the vertical growth direction, the entire row of pixel intensities were averaged to obtain I_{InGaAs} in Equation 5.3. This is then used to calculate ρ_{In} as an average for that row. We observe that the InAs to GaAs interface below the dot layer (at ~ 4.5 nm) is quite abrupt and the cations have changed over a thickness of about 1 nm in the growth direction, whereas above the dot layer (at ~ 6.5 nm) the interface is much more smooth as the InAs diffuses into the GaAs capping layer (this change occurs over a length scale of 3 nm).

To get a better understanding of the in-plane variation of ρ_{In} , instead of averaging over rows of pixels, the intensity value of each pixel in a region around the InAs layer was used to find ρ_{In} . A density plot showing the variation of ρ_{In} over a 2D cross section is plotted in Figure 5.15c. Though there are no clear dots identified in the TEM images, the in-plane In fraction plot shows there are regions of higher In content within the In layer. We ascribe that these fluctuations on the atomic scale in the InGaAs layer create the confinement

required to form QDs. There is a small “core” region with a large proportion of Indium ($\rho_{In} > 50\%$, such as the red region in Figure 5.15c at position (25.5 nm, 5.2 nm) with an approximate height of 0.7 nm and width of 10 nm) and the indium spreads into the surrounding GaAs layer. Also there appear to be regions where a maxima of $\rho_{In} > 60\%$ is observed but from the experimental NMR CT spectra for the Low Temp Cap sample $\rho_{In} = 9.9\%$. These two observations imply that the dot confines an electron whose wavefunction penetrates significantly into the surrounding GaAs layers.

This technique to calculate ρ_{In} was a simplified approach and there are a few sources of uncertainty to consider. The sample itself is of finite thickness (estimated to be 20-30 nm thick for the piece in Figure 5.15b) and the intensity detected at a given pixel is the sum of all the atoms present at that point. This includes nuclei behind the surface that are visible at the cleaved edge of the cross section (so called channelling effects). This is of particular significance near the interfaces between InAs and GaAs layers where the In nuclei at the surface may have some Ga nuclei behind (and vice versa). Also the variation of the measured brightness in the in-plane direction can be due to a combination of impurities, variations in the thickness of the sample as well as actual changes in ρ_{In} . These effects were checked by performing the same analysis except using a similar sized region of pure GaAs (below the InGaAs layer) and the variations in brightness were much less than that of the In layer so that the majority of the change in brightness can be attributed to a change in the indium fraction ρ_{In} . Other procedures in the literature using high angle annular dark field (HAADF) images take into account the vacuum intensity [191] and use intensity ratios of the form I_{InGaAs}/I_{GaAs} [192, 193] for various sample thicknesses. But these effects are only of major significance when the In fraction is small, whereas for large In fractions (as high as 60% we see here), they only provide a small correction to the numerical values. The overall conclusions drawn from this analysis will still remain: the indium concentration is high in the InAs layer, the indium atoms diffuse into the GaAs cap above the dots and the In content is not uniform across the InAs layer and they segregate together to form pockets of InAs sufficient to provide QD confinement.

5.6 Summary

Optically detected NMR techniques have been used to analyse the structure of single, self-assembled QDs in two different InGaAs/GaAs samples. The experimental results together with TEM images have shown that the dots are very shallow and have disc-like shape (as opposed to large pyramids). The TEM images indicate that the InAs deposition layer is

abundant in indium at the centre of the layer and that there is a significant intermixing between In and Ga particularly in the interface above the dot layer (during the capping process). However the data from the NMR experiments suggest that the dot contains little In on average and the majority of the cations in the InGaAs dot are Ga. Moreover the majority of the Ga nuclei are shown to have very little quadrupolar shift and thus originate from regions of low strain in the dot. The electron wavefunction that is confined by the InAs layer penetrates significantly into the surrounding GaAs barrier layers where the total elastic strain felt by the Ga nuclei is small. This new technique has allowed for the first direct, in-situ measurement of the NMR signal from these low strain nuclei. Further work to verify the experimental conclusions would involve a computational study to model different quantum dot structures and strain distributions and see the effect on the NMR spectra (this is similar to previous studies [124, 126] by our collaborator C. Bulutay of Bilkent University).

The cw NMR techniques performed here are very versatile and the only requirement is that it is possible to detect the optical Overhauser shift via the hyperfine interaction between nuclei and electron, which means that it can be used for other structures such as quantum wells or nanowires. Furthermore it can be used in-situ to measure a specific QD of interest (rather than another representative QD in the sample through TEM analysis) and requires no specific preparation of the sample. The applied rf field is of relatively low power and so provides only a minimal heating of the sample at liquid helium temperatures, which causes no deterioration of the optical quality of the QD for any subsequent measurements. It allows us to analyse the structure of small nanoscale structures (with only 10^5 nuclei) which will be crucial to understand if these structures are to be combined for multi qubit applications.

Chapter 6

Effect of a single electron on the nuclear spin properties in an InGaAs/GaAs quantum dot

The experiments thus far have involved measuring a single neutral self assembled quantum dot that is empty of trapped charge carriers. Under such conditions, the nuclear spin bath can be optically pumped to show a large stable nuclear polarisation. However for the real implementation of a spin qubit in this system, a dot would need to have a trapped charge and its spin states would form the two logical states of a qubit [40]. In the work by Wüst et al. in 2016 [194] using pulsed NMR Hahn Echo measurements, it was shown that the coherence times T_2 of the nuclear spins in an InGaAs dot are reduced from a few ms in the neutral state to tens of μs with a single trapped electron state and recovers back to a few ms when a second electron is trapped. This is the only direct study and there is no complete picture of the nuclear spin coherence properties in a central spin system.

In this chapter, we address the problem from an alternative perspective and see what the effect of a single electron is on the key properties of the nuclear spins. Here instead of the pulsed NMR techniques used in [194], we employ our cw NMR frequency comb techniques to directly compare a single InGaAs dot with no electrons and one trapped electron. Using a dot in the Low Temp Cap p-i-n diode sample (see Section 3.1) and changing the diode gate voltage, we can preferentially allow charges to tunnel into the dot and control the charge state.

First we discuss the bias dependent photoluminescence spectra and see how the bias can be adjusted to observe the different QD exciton states and show calibration measurements

to determine the optimal bias to observe the maximum Overhauser shift. The aim of this work is to directly compare three important nuclear spin timescales T_1 , T_2 and T_2^* between a neutral and singly charged dot. The nuclear spin lifetime T_1 is measured by looking at the decay in the dark of the OHS, the ensemble dephasing time T_2^* is extracted from the inhomogeneous linewidth measured using the optically detected inverse NMR technique and the nuclear coherence time T_2 is deduced from the homogeneous linewidth which is observed by manipulating the mode spacing f_{MS} of the frequency combs used for rf excitation.

6.1 Bias dependant photoluminescence spectra and Overhauser shift of InGaAs quantum dots

For the main experimental results in this chapter, we will again be utilising pump-probe cycles for the optically detected measurements. In Chapter 5, we showed how the calibration measurements are performed to determine some of the key parameters in pump-probe measurements such as T_{Pump} and T_{Probe} . Chapter 5 consisted of comparing QDs from an ungated, undoped sample (In-Flush) to the p-i-n diode Low Temp Cap sample. In that chapter for the Low Temp Cap diode sample, we simply stated the bias values that were used.

Now in this chapter, we will be showing the calibration measurements explicitly to determine the optimal bias for the various pulses in the pump-probe cycle: the bias applied during the pump pulse (V_{Pump}), the bias applied during the probe pulse (V_{Probe}) and the bias applied in the dark time between the pump and probe pulses (V_{Dark}). Here in Chapter 6, we use a different dot from the Low Temp Cap diode sample (as opposed to the dot used in Chapter 5), but the logic used to deduce the bias parameters was similar.

Figure 6.1 shows the bias dependant PL spectrum for the dot studied in this chapter. As previously discussed (in Section 2.1 and Section 2.2.4), a change in bias between the top contact and the back contact of the diode, changes the dot energy with respect to the Fermi level allowing for the control of the QD charge state. We see that below ~ 1.58 V, no emission is observed and the dot is empty, between about $\sim 1.58 - 1.68$ V an electron-hole pair can be photoexcited and their recombination emits X^0 and finally between about $\sim 1.68 - 1.88$ V an additional electron can now tunnel in to be resident in the dot and emission of the X^- state is observed. As discussed in Section 2.2.3, the transition lines are observed at different energies because of the different magnitudes of the Coulomb

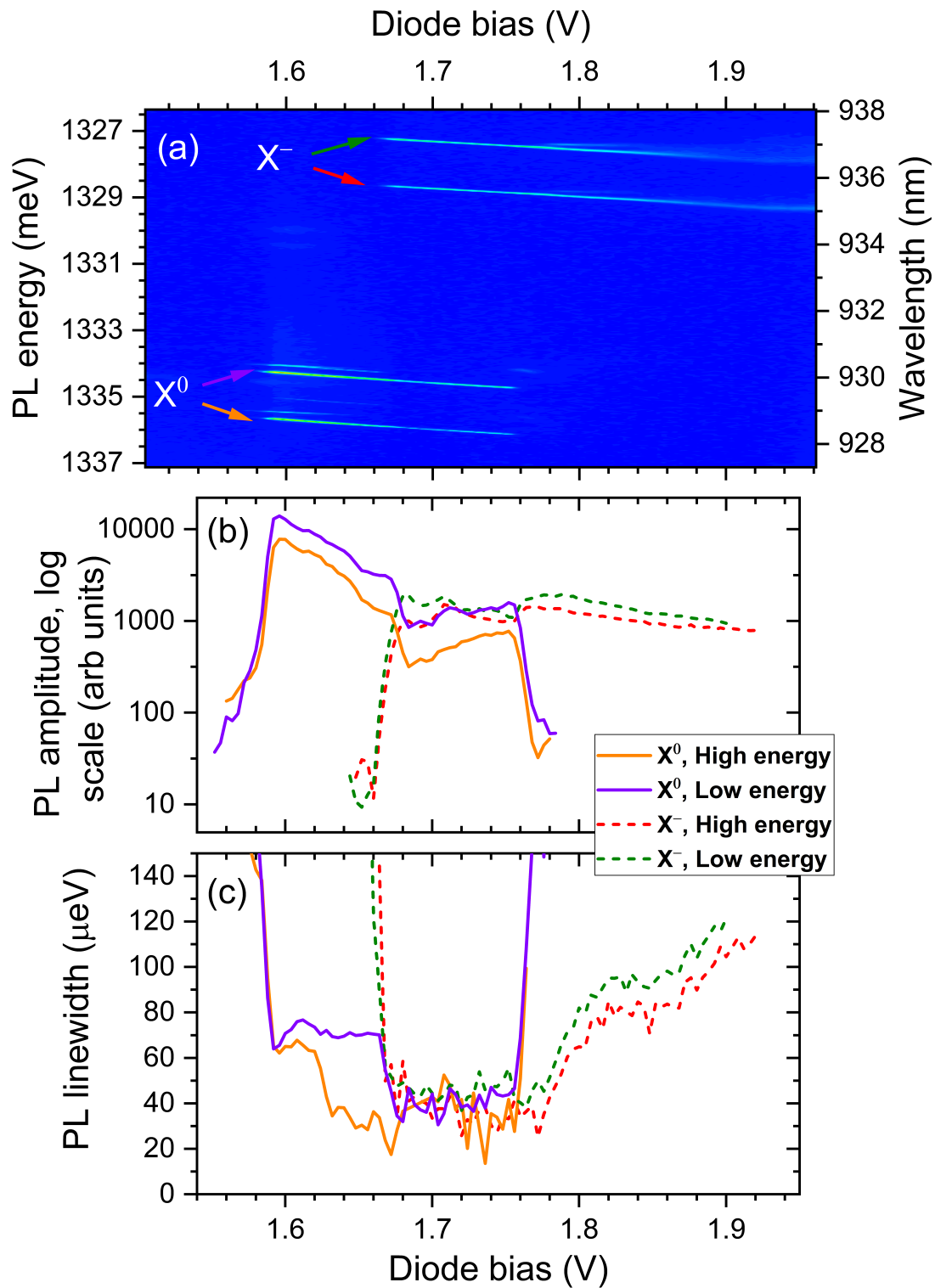


FIGURE 6.1: Bias dependant photoluminescence spectra of a single dot from the Low Temp Cap sample at $B_z = 8$ T with low power ($0.3 \mu\text{W}$) non-resonant 850 nm excitation. a) PL map showing the appearance of different exciton (X^0 and X^-) states as the bias is changed. b) The measured PL amplitudes and c) the detected linewidths of each exciton line as the bias is changed.

interaction between the different combinations of carriers. The fact that the 2e electron state is at a higher energy and the 1e state is stable (no extra electron can tunnel into the dot) is referred to as the Coulomb blockade [1].

Each peak in the bias dependant PL spectrum is fit with a Gaussian function and the amplitudes and widths (FWHM) are plotted as a function of the bias in Figure 6.1b and Figure 6.1c. There is a clear range in bias where the PL signal from the X^0 exciton lines (orange and purple in Figure 6.1) are strong between $\sim 1.59-1.67$ V and the corresponding linewidths are narrow in this range. Similarly the X^- exciton (red and green in Figure 6.1) shows the largest signal between $\sim 1.70-1.76$ V but doesn't emit as brightly as X^0 . The narrowest linewidths measured here of ~ 15 μeV are limited by the resolution of the double spectrometer and to measure the true transition linewidths, resonant excitation would be required (for resonance fluorescence measurements).

Note that within the range of bias where the X^- exciton is narrow ($\sim 1.70-1.76$ V), both X^- and X^0 are observed and this is because this is a cw PL spectrum recorded using non-resonant excitation. Since the excitation laser is at a higher energy (wetting layer) than the QD states and the sample is being continuously excited, the observed spectrum is essentially the time averaged emission from the QD. Within this bias range, for some fraction of the exposure time the dot may contain a resident electron (and emit at the energy of X^-) or the dot may be empty (emit at X^0). The dot can only truly be thought of as containing a single (stable) extra electron in the dark with no optical excitation (we can see the evidence for this in the nuclear spin lifetimes, see Section 6.2). Additionally, we have only shown the X^0 and X^- lines, but both X^+ and XX states were observed when investigating this dot. Detailed PL spectra were not taken of these states as the scope of this work is to specifically compare the neutral dot to a dot containing a single electron.

We use this data to determine the bias applied during the probe pulse V_{Probe} . The role of the probe laser is to accumulate PL signal to determine the final Zeeman splitting but not affect the nuclear polarisation during the probe pulse. It was found by performing a probe time calibration (similar to Figure 5.2 in Section 5.1.1) that a V_{Probe} applied to the X^0 maxima or the X^- maxima could both be used. A probe with a bias of $V_{\text{Probe}} = 1.76$ V (X^- maxima) was finally chosen because it affected the nuclear polarisation by a marginally lower amount than a probe voltage at the X^0 maxima.

Next, we can calibrate the bias required during the pump pulse to observe the maximum OHS. An explicit measurement is conducted (see Figure 6.2) where the voltage during the pump pulse V_{Pump} is varied and the OHS is detected under both σ^+ and σ^- pumping. An

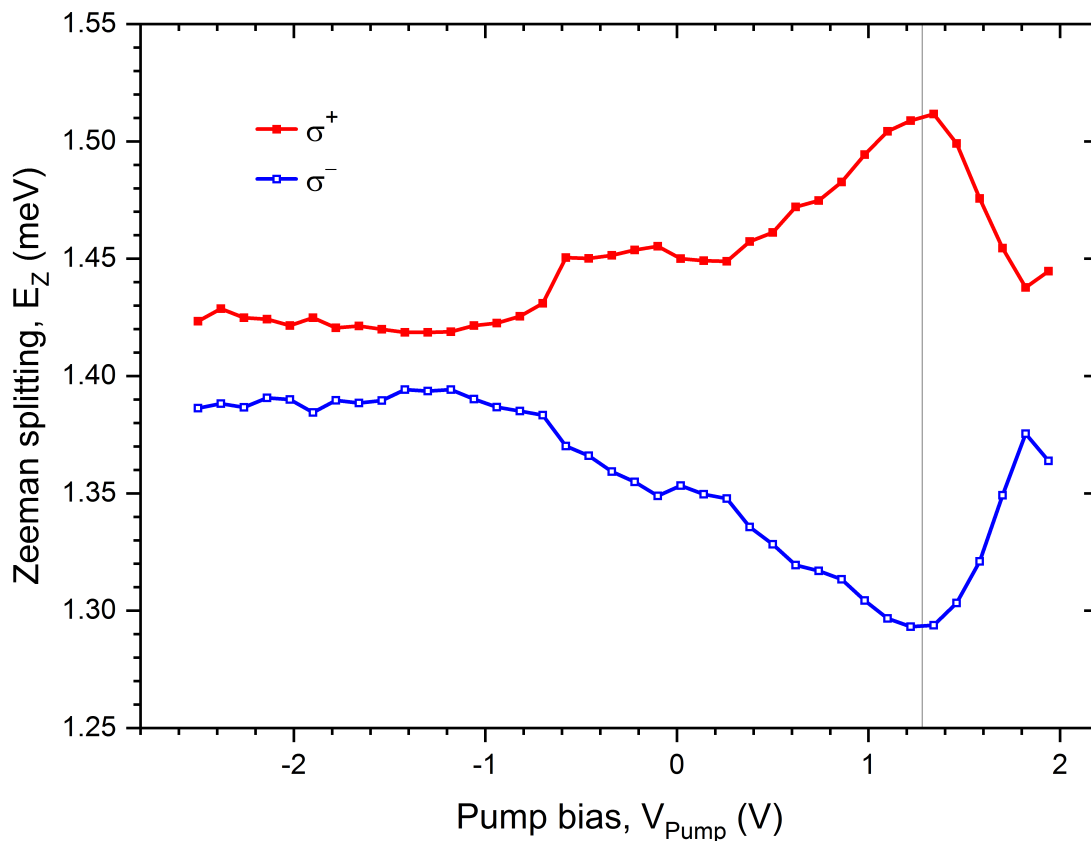


FIGURE 6.2: Dependence of the Zeeman splitting on the bias applied during the pump pulse V_{Pump} under both σ^+ (red solid squares) and σ^- (blue open squares) pumping at $B_z = 8$ T for a single dot in the Low Temp Cap sample. The vertical line shows the optimal pump bias of $V_{\text{Pump}} = 1.28$ V (which induces the largest Overhauser shift) used in NMR experiments. The other experimental parameters for this measurement were $P_{\text{Pump}} = 1$ mW, $T_{\text{Pump}} = 6.8$ s, $P_{\text{Probe}} = 0.25$ μ W and $T_{\text{Probe}} = 10$ ms.

OHS (of at least ± 15 μ eV) is detectable at all V_{Pump} but a clear maximum is observed of about ± 110 μ eV at a value of $V_{\text{Pump}} = 1.28$ V.

6.2 Bias dependant nuclear spin lifetime of InGaAs quantum dots

The optimal choices for V_{Pump} and V_{Probe} have been discussed in the previous section and the other remaining important bias in the pump-probe cycle is the bias applied in the dark time between the pump and probe pulses (V_{Dark}). In essence, this is the charging state that the QD will be kept at once the nuclear spin polarisation has been initialised (as well as the magnitude of the tunnelling rate). It should be emphasised that this charge state is only stable when the sample is kept in the dark. During optical excitation, the

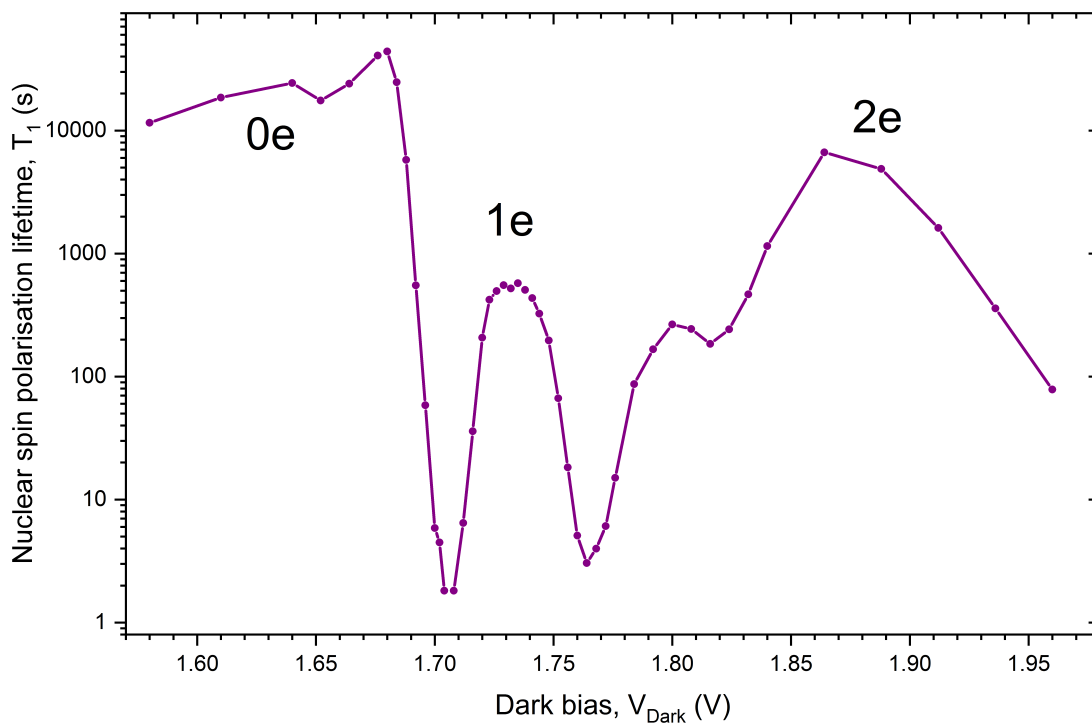


FIGURE 6.3: Bias dependence of the nuclear spin lifetime for a single InGaAs QD in the Low Temp Cap sample. The exponential decay of the nuclear polarisation is measured and the extracted T_1 times from the fit are plotted as the sample is kept at different biases in the dark V_{Dark} . Three distinct charging states of the QD are observed with long nuclear $T_1 > 10^4$ s for the empty (0e) and doubly charged (2e) states and a smaller $T_1 > 560$ s for a singly charged dot (1e). The other experimental parameters for this measurement were $B_z = 8$ T, $P_{\text{Pump}} = 1$ mW, $T_{\text{Pump}} = 10$ s, $P_{\text{Probe}} = 0.25$ μ W and $T_{\text{Probe}} = 25$ ms. Note that all T_1 values $> 10^4$ s are estimated values since long delay times $T_{\text{Wait}} > 900$ s were not explicitly measured.

charge state of the dot completely depends on the properties of the excitation laser. It is by changing the dark bias V_{Dark} that we can compare important nuclear spin timescales (set out at the start of this chapter as the nuclear T_1 , T_2 and T_2^*) between a neutral and singly charged QD.

We begin by measuring the lifetime (T_1) of the nuclear spin polarisation as V_{Dark} is varied. This is again done using a pump-probe scheme and is similar to the measurements done in previous chapters, where we measure the exponential decay of the nuclear polarisation as the delay (T_{Wait}) between the pump and probe pulse is varied (see Section 5.1.2 and Section 4.6). However in this bias-dependant measurement, we first measure the decay at a particular value of V_{Dark} , fit the data to extract the lifetime T_1 and then repeat at different dark biases V_{Dark} .

The final dataset showing how the extracted nuclear T_1 times change as the dark bias is varied is shown in Figure 6.3 and is similar to the observations from other groups [7, 194].

We observe three distinct charging states of the QD characterised by the values of the nuclear spin lifetimes T_1 . Below about $V_{\text{Dark}} \leq 1.67$ V, the T_1 is very long $> 10^4$ s and is when the (neutral) dot contains no electrons and hence the nuclear spin polarisation is very stable. Additionally, at a bias of $V_{\text{Dark}} \sim 1.87$ V, the lifetime T_1 recovers to similarly high values of $\sim 10^4$ s. This is again a stable spin configuration because the two electrons in the dot form a spin singlet with a total spin of zero and do not interact with the nuclei. Such long lifetimes are indicative of the suppression of nuclear spin diffusion due to the large strain induced quadrupolar shifts in the InGaAs/GaAs self assembled QD system (measured in Chapter 5). Hence the nuclear polarisation is robust and does not significantly diffuse out into the surrounding layers.

Once again, since the scope of this work is to compare a neutral and a singly charged dot, the doubly charged state beyond $V_{\text{Dark}} \sim 1.80$ V was not investigated in detail. We propose that the dot is charged with two resident electrons because of the recovery of the nuclear spin lifetime and the similar results presented by other groups [7, 194]. It is possible there are more than one (higher order) charged biexciton states and these could be investigated by exciting the dot with different polarisations and studying the polarisation of emission. The reduction of the nuclear spin lifetime beyond $V_{\text{Dark}} \sim 1.90$ V was a real effect and likely due to the current through the diode increasing rapidly beyond this bias value and thus creating an unstable QD charge environment.

The most interesting feature of the nuclear T_1 data is the bias range over which the QD is charged with a single electron. We observe a 1-electron (1e) charging plateau whose edges are given by two minima at about $V_{\text{Dark}} \sim 1.70$ V and $V_{\text{Dark}} \sim 1.76$ V where the nuclear T_1 is only a few seconds and a maximum at the centre of the 1e plateau at about $V_{\text{Dark}} = 1.732$ V with a maximum $T_1 \approx 560$ s. Note that similar results were obtained from several other dots in this sample where the maximum T_1 in the 1e plateau was > 100 s.

The electron in a QD in a charge tunable sample can interact with electrons in the broad continuum of electron states in the Fermi reservoir through the tunnelling barrier. The centre of the 1e plateau is where a QD populated with one electron is the ground state and the spin state is most stable because the cotunnelling rate with the electron reservoir is low. On the other hand, at the edges of the plateau is where the cotunnelling is strong and the optically initialised electron spin state is quickly lost by cotunnelling with the electron reservoir.

To be clear, as opposed to just tunnelling where a single carrier tunnels into or out of the dot, the effect of cotunnelling assisted nuclear spin relaxation is where a nuclear spin flip can occur without a flip of the confined electron spin, with the energy being provided by

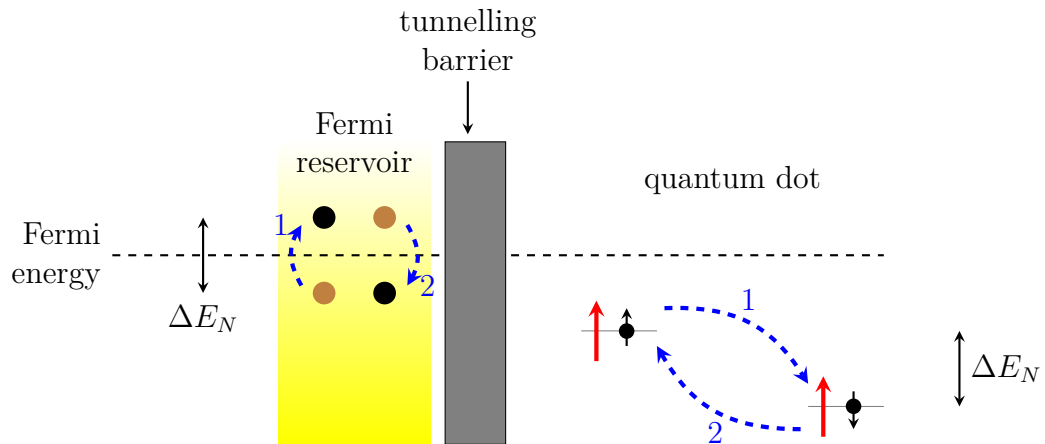


FIGURE 6.4: Schematic illustration of a nuclear spin flip via cotunnelling with the electron reservoir in the Fermi sea. The nuclear spin (black arrow) may be flipped without changing the confined electron spin (red arrow) with the energy difference ΔE_N 1) provided by electron-hole annihilation or 2) absorbed by electron-hole excitation in the Fermi reservoir. Adapted from [7].

carriers in the Fermi reservoir [7] (see Figure 6.4). Now the orientation of the nuclear spin has changed and so we observe a fast decay of the nuclear spin polarisation (low nuclear T_1). In the centre of the 1e plateau, the cotunnelling rate is smaller than plateau edges but the maximum nuclear $T_1 \approx 560$ s still doesn't reach the value of $\sim 10^4$ s observed for neutral dots. Though the effect of cotunnelling is smaller, it is still the dominant effect in our samples (due to the relatively narrow tunnelling barrier width of 32 nm).

In the work by Latta et al. [7], they propose an additional mechanism as to why the nuclear lifetime T_1 in the centre of the 1e plateau is lower due to the so called “electron mediated nuclear spin diffusion”. Usually dipolar nuclear spin flips only occur between nearest neighbour nuclei, but with an electron trapped in a QD, two distant nuclei (provided they both overlap with the electron wavefunction) can swap spins (see Figure 6.5). Because of the large quadrupolar shifts and the Knight field due to the electron, there can be a large distribution in the energy levels of the nuclei (as discussed in Chapter 5), so this is only possible for nuclei with a similar energy difference (Zeeman splitting). This second order process can effectively redistribute the nuclear spin polarisation and cause a decay of the Overhauser shift and thus reduce the nuclear T_1 for a dot charged with a single electron (compared to an empty dot). Latta et al. [7] measure much longer nuclear $T_1 \approx 4000$ s for the centre of the 1e plateau (at liquid helium temperatures) and perform resonant pumping experiments so this electron mediated nuclear spin diffusion plays a significant part in the nuclear spin relaxation. For our experiments, with non resonant pumping at 850 nm, we observe a maxima of nuclear $T_1 \approx 560$ s in the 1e plateau due to the cotunnelling assisted relaxation, though the electron mediated diffusion effect may provide some contribution to

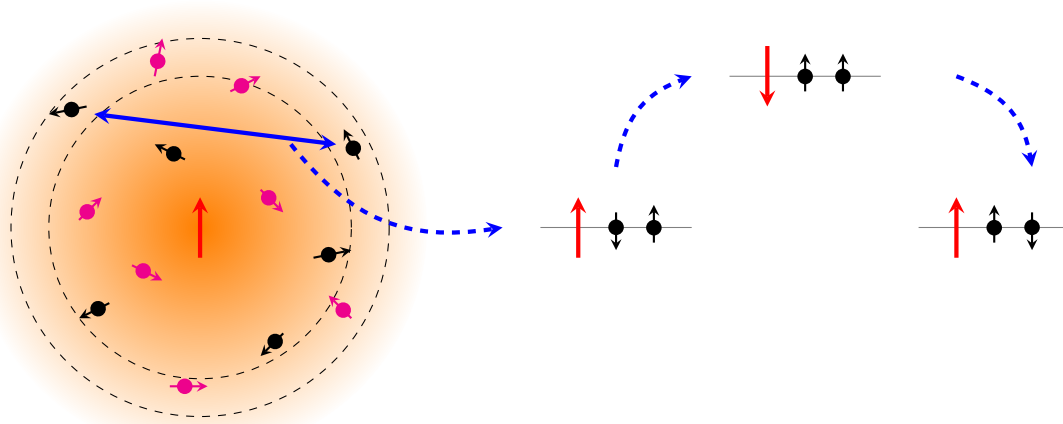


FIGURE 6.5: Schematic illustration of an electron mediated nuclear spin flip. Two distant nuclear spins (black arrows) that overlap the electron wavefunction (shaded orange area) and with a small difference in energy (shown within the dashed circles) can exchange their spins via a virtual second order spin flip with the electron spin (red arrow). This redistributes the nuclear spin polarisation and causes a faster decay of the nuclear spin lifetime in the 1-electron charging plateau. Adapted from [7].

the nuclear spin relaxation. These mechanisms could be investigated further, for example by investigating samples with different barrier thicknesses.

6.3 Inhomogeneous linewidth measurement using NMR spectra

Next we investigate the inhomogeneous linewidth of a nuclear isotope resonance and how it changes between an empty QD and when there is a single electron confined in the dot. Once again we utilise the cw, low power “inverse NMR” technique as we have done in Chapter 5 (for details, see Section 3.4 and 5.2) to measure the NMR spectra of a quadrupolar nuclear isotope. Again several NMR calibration measurements were performed to determine the width of the rf band w_{Band} and the length of the rf pulse T_{RF} but the methodology is similar to that of Section 5.1.3 and is omitted here.

Here in this chapter, we only present the NMR spectra for the one nuclear isotope of ^{71}Ga because of its relatively narrow transition linewidth (due to the small quadrupolar moment Q , see Table 2.1) and its isolation in frequency from the other isotopes in the dot (due to the large gyromagnetic ratio γ). This is convenient because it means that ^{71}Ga nuclei can be manipulated with negligible effect on the other nuclear isotopes. The aim is to directly compare the linewidth of the ^{71}Ga resonance between when the dot is empty and when a single electron is present. This is done by measuring the NMR spectra using

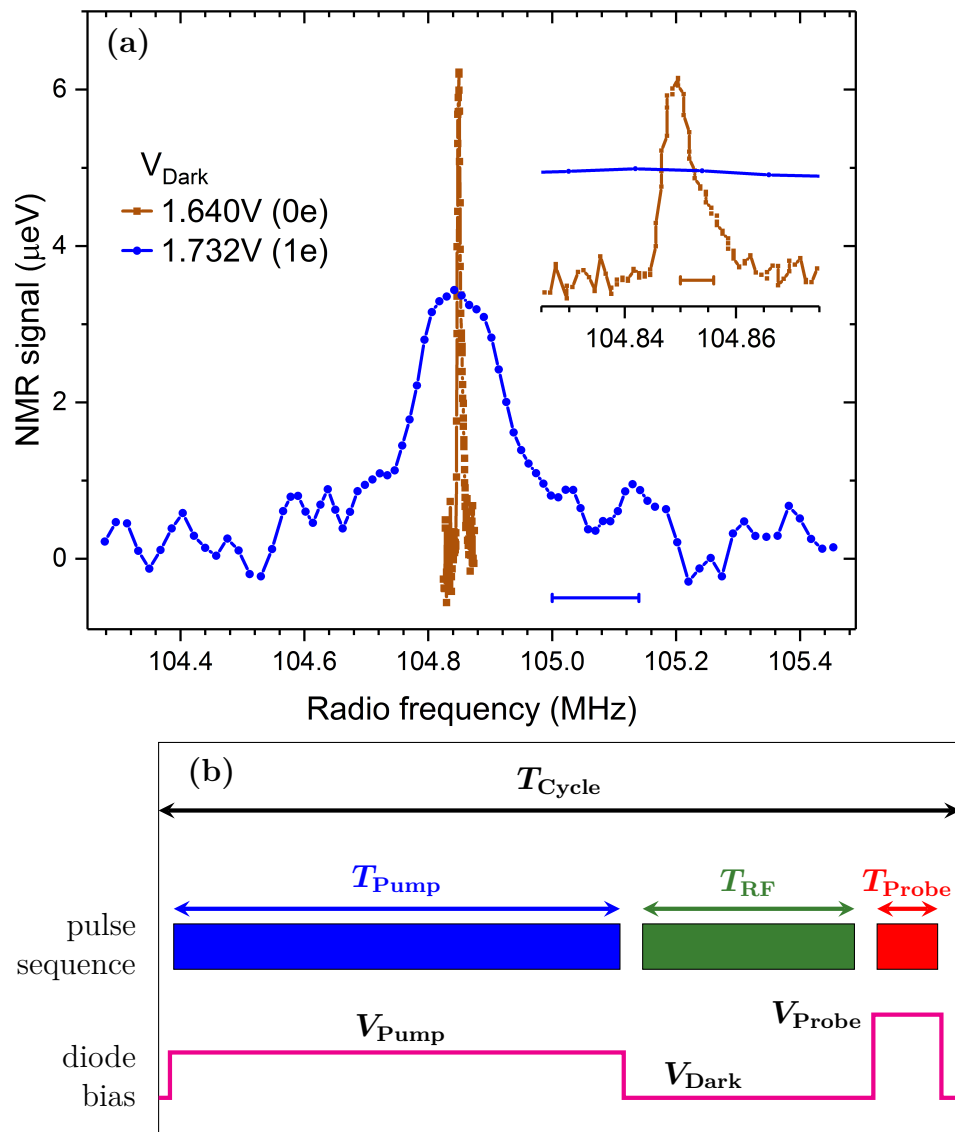


FIGURE 6.6: a) Inverse NMR CT spectra of ^{71}Ga for a single dot in the Low Temp Cap sample for an empty dot ($V_{\text{Dark}} = 1.64$ V, brown squares) and a singly charged dot ($V_{\text{Dark}} = 1.732$ V, blue circles). The inset shows a magnified version of the 0e peak. The data was taken at $B_z = 8$ T using σ^- pumping and the gap widths used in the inverse NMR waveform were $w_{\text{Gap}} = 6$ kHz for the 0e peak and $w_{\text{Gap}} = 140$ kHz for the 1e peak (shown by the horizontal bars). b) Timing diagram for NMR spectra measurements illustrating the bias values used for the various pulses in the cycle. By changing the bias applied in the dark V_{Dark} , we control the QD charge state during the rf pulse.

the pump-rf-probe cycle but by changing the bias applied to the diode in the dark V_{Dark} between the pump and probe cycles (i.e. during the rf pulse, see Figure 6.6b). A bias of $V_{\text{Dark}} = 1.64$ V was applied to measure the NMR spectra when the dot is empty and a bias of $V_{\text{Dark}} = 1.732$ V was chosen for the centre of the 1e plateau.

The CT NMR spectra of ^{71}Ga for both the 0e and 1e state are shown in Figure 6.6a. It is clear that the width of the ^{71}Ga peak measured when a single electron is present in the dot

($V_{\text{Dark}} = 1.732$ V) is much broader than the ^{71}Ga peak with an empty dot ($V_{\text{Dark}} = 1.64$ V). To obtain high resolution peaks, the width of the gap w_{Gap} (which provides the resolution for inverse NMR spectra) was chosen to be different for each of the two spectra. For the 0e state, $w_{\text{Gap}} = 6$ kHz and the width (FWHM) of the peak is measured to be $w_{\text{inh}} = 7.2$ kHz and for the 1e state, $w_{\text{Gap}} = 140$ kHz and the peak width is $w_{\text{inh}} = 170$ kHz. This is approximately a 25 times increase in linewidth and is a direct indication of the Knight field induced inhomogeneous broadening due to the extra confined electron.

Using a similar method to the calculation in Chapter 4 (for II-VI dots), we can estimate the magnitude of the Knight field in these InGaAs dots. The Knight shift of the ^{71}Ga can be written as $\gamma_{(^{71}\text{Ga})}B_e/2\pi$ and using the observed broadening of approximately ± 80 kHz, we can estimate that the peak Knight field is $|B_e| \approx 6.2$ mT. This is similar to previously reported values for III-V dots [131]. Again using similar arguments to Chapter 4, the symmetric character of the broadening occurs because at a specific time, the nuclei may interact with a \uparrow (\downarrow) electron which produces a positive (negative) Knight field. In the NMR spectrum, this appears as a signal on the high (low) frequency side of the resonance and because of the inhomogeneity in the Knight field across the dot (inhomogeneity in the electron envelope wavefunction), we observe a broadening of the NMR peak.

The corresponding ensemble nuclear spin dephasing times T_2^* are related to the inhomogeneous linewidths via $T_2^* = 1/(2\pi w_{\text{inh}})$. For the 0e state, $T_2^* = 22$ μs (which agrees with previously reported values [146]) and for the 1e state, $T_2^* = 0.94$ μs . Just as with the nuclear spin lifetime T_1 , there is a significant decrease in T_2^* for the 1e state compared to the 0e state. Our NMR techniques provides a way of measuring the ensemble timescale T_2^* by using cw measurements in the frequency domain (as opposed to pulsed NMR methods in the time domain).

The effect of a single electron trapped in a QD on the nuclear spin ensemble was investigated further by measuring the inverse NMR spectra for different biases across the 1e plateau (see Figure 6.7). Figure 6.7b shows part of the 1e plateau data from the bias dependent nuclear spin lifetime measurement in Figure 6.3. The vertical lines show 5 different biases chosen at various positions across the 1e plateau with $V_{\text{Dark}} = 1.732$ V being the middle of the plateau and where the electron spin is most stable. This is indicated by the longest nuclear $T_1 \approx 520$ s measured in the 1e plateau and is because the cotunnelling rate is small at this bias. The other bias values of $V_{\text{Dark}} = 1.720$ V and $V_{\text{Dark}} = 1.744$ V are located towards the edges of the plateau maxima where the nuclear T_1 is still long and

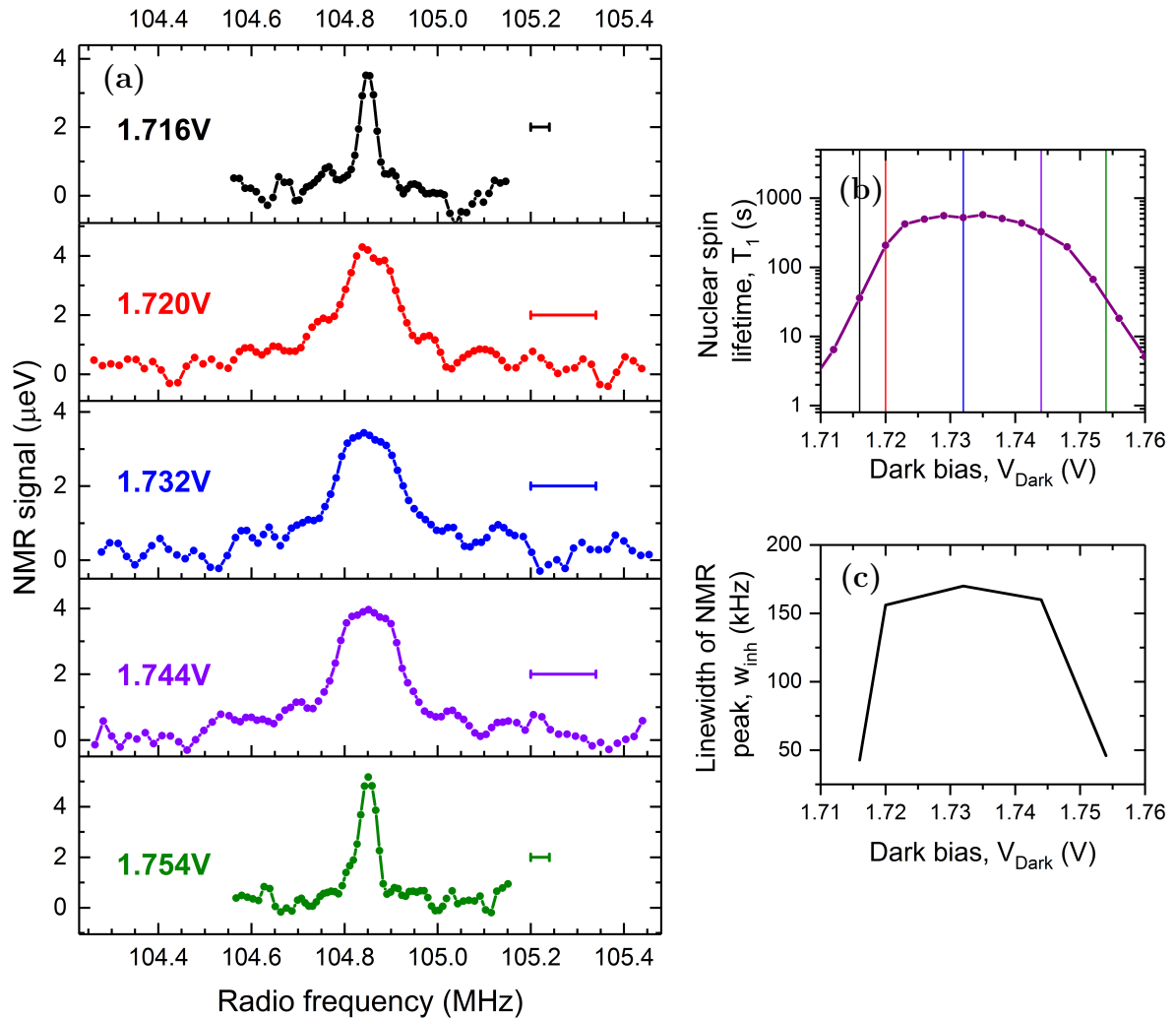


FIGURE 6.7: a) Inverse NMR CT spectra of ^{71}Ga for a single dot in the Low Temp Cap sample for different dark biases across the $1e$ plateau. The data was taken at $B_z = 8$ T using σ^- pumping and the gap widths used in the inverse NMR waveform were $w_{\text{Gap}} = 40$ kHz for $V_{\text{Dark}} = 1.716$ V and $V_{\text{Dark}} = 1.754$ V and $w_{\text{Gap}} = 140$ kHz for $V_{\text{Dark}} = 1.720$ V, $V_{\text{Dark}} = 1.732$ V and $V_{\text{Dark}} = 1.44$ V. b) A subset of the data shown in Figure 6.3 of how the nuclear spin lifetime T_1 varies across the $1e$ plateau. The vertical lines (with the corresponding colours) show the different V_{Dark} values used to measure the NMR spectra and their relative positions in the $1e$ plateau. c) The extracted NMR CT linewidths w_{inh} (FWHM from Gaussian fitting) for the different biases across the $1e$ plateau.

Dark bias, V_{Dark} (V)	1.716	1.720	1.732	1.744	1.754
w_{Gap} (kHz)	40	140	140	140	40
w_{inh} (kHz)	42.7	156	170	160	45.9

TABLE 6.1: The inhomogeneous linewidths (FWHM) of CT peaks (w_{inh}) at different dark biases V_{Dark} across the 1e plateau from fitting the inverse NMR ^{71}Ga CT spectra for the Low Temp Cap sample.

finally $V_{\text{Dark}} = 1.716$ V and $V_{\text{Dark}} = 1.754$ V were chosen to be part way down the decreasing edges of the 1e plateau where the nuclear T_1 has decreased significantly compared to the maxima at $V_{\text{Dark}} = 1.732$ V.

Figure 6.7a shows the inverse NMR spectra measured at the 5 different dark biases across the 1e plateau. It is observed that there is a clear change in the widths of the ^{71}Ga NMR peaks between the biases. The gap widths used w_{Gap} and the inhomogeneous linewidths detected w_{inh} from the spectra are summarised in Table 6.1. The largest linewidth of $w_{\text{inh}} = 170$ kHz is observed at the centre of the plateau and there is a small decrease to $w_{\text{inh}} \sim 160$ kHz towards the edges of the plateau maxima at $V_{\text{Dark}} = 1.720$ V and $V_{\text{Dark}} = 1.744$ V and a significant decrease to $w_{\text{inh}} \sim 45$ kHz at $V_{\text{Dark}} = 1.716$ V and $V_{\text{Dark}} = 1.754$ V. This indicates that the maximum Knight field induced broadening occurs only when the electron spin is most stable (largest electron spin lifetime) at the centre of the plateau. The electron spin is much less stable at the decreasing edges of the plateau ($V_{\text{Dark}} = 1.716$ V and $V_{\text{Dark}} = 1.754$ V) and the electron spin lifetime becomes comparable or shorter than the nuclear spin precession frequency (~ 100 MHz at $B_z = 8$ T). Here the nuclei start to feel a “time-averaged” electron spin Knight field rather than the discrete \uparrow (\downarrow) field in the centre of the 1e plateau. Hence this “time-averaged” amplitude of the Knight field felt by the nuclei is smaller and the NMR peaks are narrower at the edges of the plateau.

This interlinked electron-nuclear spin system indicates one of the fundamental problems in using a single trapped electron in self assembled QDs for spin qubit applications. For the electron spin to be stable (large electron spin lifetime), a bias is required at the centre of the 1e plateau, which in turn causes a large Knight field acting on the nuclei. This causes a broader nuclear spin ensemble and larger nuclear spin fluctuations. On the other hand, at the edges of the plateau, the time-averaged Knight field is small but the electron spin is less stable due to tunnelling effects. This anticorrelation between electron spin lifetime and the nuclear spin coherence is also discussed by Wust et al. [194], where pulsed NMR experiments are performed, and indicates a fundamental issue with the InGaAs QD system.

6.4 Homogeneous linewidth measurement using frequency combs

In this section, we describe how the nuclear spin coherence time T_2 is measured. In the previous section and in Chapter 5, we have seen that the strain and quadrupolar isotopes present in the system of self assembled InGaAs QDs lead to large inhomogeneous broadening of the NMR spectra. This large broadening is several MHz in width for the STs and the underlying nuclear spin coherence dynamics is masked by the ensemble dephasing.

One method to remove the inhomogeneous broadening is to use spin-echo pulse sequences [195]. However such pulsed NMR techniques including more sophisticated pulse sequences [196, 197] typically require a high power and can lead to issues such as spin locking or other interactions during the pulse itself [198–200].

Here, we use a low power, cw NMR technique that allows us to detect the underlying homogeneous linewidth of the nuclear spin transitions with rf excitation in the shape of frequency combs. This precise technique is adapted from the field of optical frequency metrology [201, 202] and we generate combs in the radiofrequency part of the electromagnetic spectrum to depolarise nuclear spins. We will first describe the methodology of how the frequency comb technique can be used to determine the homogeneous linewidth in Section 6.4.1 before discussing the experimental results comparing a neutral to a singly charged dot in Section 6.4.2.

6.4.1 Frequency comb technique

The overall experimental cycle for this measurement to determine the homogeneous linewidth w_{hom} of the nuclear transition is still the pump-rf-probe technique used in previous cw NMR measurements (see Section 3.4.1 for a full discussion). The important difference here is the shape of the applied rf excitation during the “rf” part of the cycle. For the NMR spectra measurements (both the “inverse” and “saturation” methods, see Section 3.4.2), we applied rf frequency combs with densely spaced modes that approximated a wide, uniform spectral frequency band to depolarise an inhomogeneously broadened isotope. The generation of these frequency combs and the hardware required to implement these rf experiments are described in Sections 3.4.3 and 3.4.4 respectively.

Importantly for the NMR spectra measurements, the mode spacing f_{MS} was kept constant at a small value of $f_{\text{MS}} = 120$ Hz and all nuclear transitions were excited uniformly within

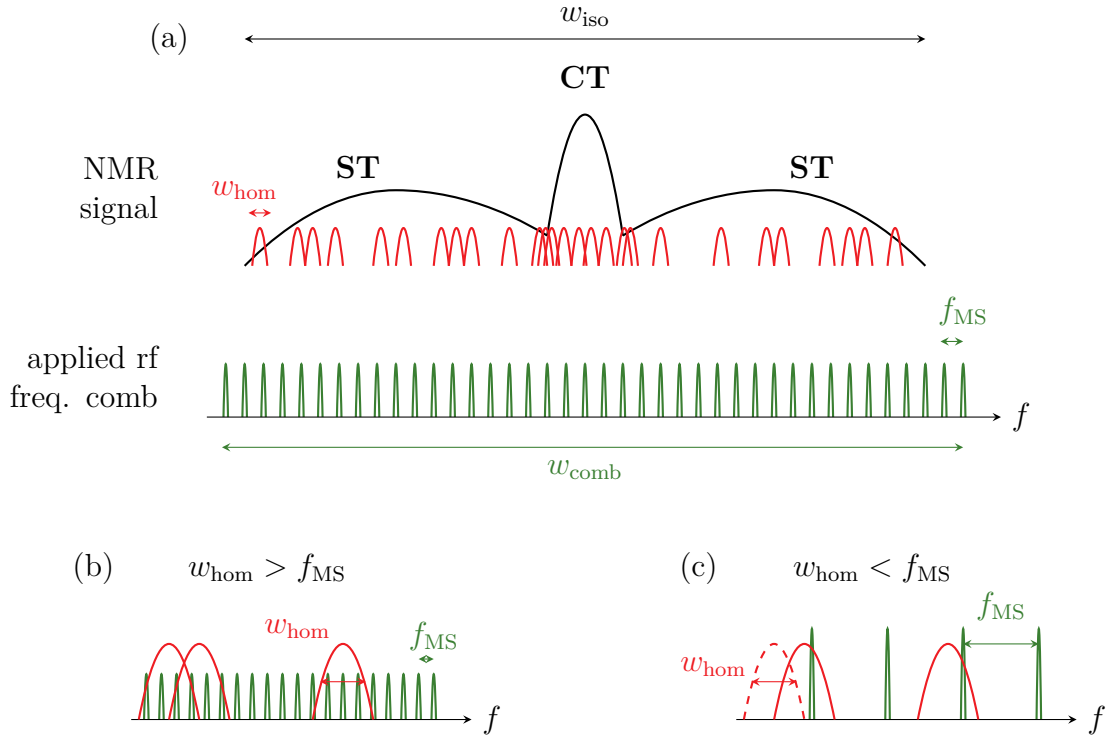


FIGURE 6.8: Schematic diagram to illustrate the frequency comb technique to measure the homogeneous linewidth w_{hom} of a nuclear spin ensemble. a) The inhomogeneously broadened NMR lineshape (with width w_{iso}) of a quadrupolar nuclear isotope (black line) showing both the central transition (CT, $I_z : -\frac{1}{2} \leftrightarrow \frac{1}{2}$) and the satellite transitions (ST, $I_z : -\frac{3}{2} \leftrightarrow -\frac{1}{2}$ or $+\frac{1}{2} \leftrightarrow +\frac{3}{2}$) is actually the spectral sum of a large number of individual nuclear transitions with width w_{hom} (red lines). Shown in green is the applied rf excitation in the shape of a frequency comb with a mode spacing f_{MS} and a width w_{comb} that covers the entire resonance ($w_{\text{comb}} > w_{\text{iso}}$). b, c) By changing the mode spacing f_{MS} we can experimentally determine the underlying homogeneous linewidth w_{hom} due to the effect on the rf induced nuclear spin depolarisation time. The two extreme cases are shown: b) either $w_{\text{hom}} > f_{\text{MS}}$, so all nuclear transitions are driven by the rf (and we observe fast depolarisation) or c) $w_{\text{hom}} < f_{\text{MS}}$, so some nuclear transitions (dashed red line) do not overlap with any of the modes of the comb and the depolarisation rate is slow. When the depolarisation begins to slow down, we can estimate w_{hom} because $w_{\text{hom}} \sim f_{\text{MS}}$. Adapted from [8].

the total width of the applied rf comb w_{comb} . Now to measure the narrow homogeneous nuclear linewidth w_{hom} from the inhomogeneously broadened ensemble, we apply a frequency comb and vary the mode spacing f_{MS} .

A conceptual diagram showing how this mode spacing experiment works is shown in Figure 6.8. The full inhomogeneously broadened NMR lineshape (black line in Figure 6.8a) of a quadrupolar nuclear isotope has a total width w_{iso} and is actually the spectral sum of a large number ($\sim 10^5$) of individual, narrower nuclear transitions with width w_{hom} (red lines). These all have some offset from the central frequency of the isotope due to the specific environment around each nuclear lattice site.

We apply a single frequency comb containing $N_m = w_{\text{comb}}/f_{\text{MS}} + 1$ equally spaced modes with amplitude B_1 and wide enough to cover the CT and STs of a nuclear isotope ($w_{\text{comb}} > w_{\text{iso}}$). We then change the mode spacing f_{MS} from between ~ 20 Hz to ~ 1 MHz so there can be between a few modes to a few 100000 modes. Because f_{MS} is being changed, to keep the total rf power constant, the ratio of B_1^2/f_{MS} is kept constant between datapoints (typically B_1 is in the $\sim \mu\text{T}$ range). The actual amplitudes of each mode that reach the sample cannot be totally uniform across the entire comb which is several MHz wide, because it is determined by the rf matching of the circuit (all mode amplitudes are within the same order of magnitude, see Section 3.4.4), but this has little effect on our experimental results.

If the mode spacing is small with respect to the homogeneous linewidth $f_{\text{MS}} < w_{\text{hom}}$ (see Figure 6.8b), all nuclear spin transitions are excited by multiple modes of the frequency comb and the nuclear spins depolarise rapidly from the non-coherent excitation. On the other hand if the mode spacing is larger than the homogeneous linewidth $f_{\text{MS}} > w_{\text{hom}}$ (see Figure 6.8c), some nuclear transitions (dashed red line) do not overlap with any of the modes of the comb. Hence these nuclei remain polarised and it takes longer to depolarise the entire nuclear isotope. We can determine the homogeneous linewidth w_{hom} as the mode spacing f_{MS} at which the depolarisation rate starts to slow down. This technique was originally introduced in [8], but applied only to neutral QDs. Here we apply it to compare the 0e state with the 1e state of a single dot.

6.4.2 Measurement of homogeneous NMR linewidths

From the discussion in the previous section, to be able to find w_{hom} , we must observe how the nuclear spin polarisation changes as a function of both the duration of the rf pulse T_{RF} (in the pump-rf-probe cycle) and the mode spacing f_{MS} of the comb. The experimentally measured decay curves for ^{71}Ga are shown in Figure 6.9 for both the empty dot and the dot confining a single electron. The signal plotted on the y-axis ΔE_{OHS} is the optically detected change in the Overhauser shift between applying the rf comb for duration T_{RF} and not applying the comb but instead leaving the sample in the dark for the same duration T_{RF} (“rf” minus “no rf”). In this way, $\Delta E_{\text{OHS}} = 0 \mu\text{eV}$ corresponds to no nuclear spin depolarisation and the maximum change in ΔE_{OHS} corresponds to when all of the ^{71}Ga nuclei have been depolarised by the rf comb.

The data is shown together with a compressed exponential fit of the form $(A_0 - A_1 \times \exp(-(T_{\text{RF}}/\tau)^k)) \times \exp(-(T_{\text{RF}}/T_1))$, where A_0 , A_1 and k are constants and τ characterises

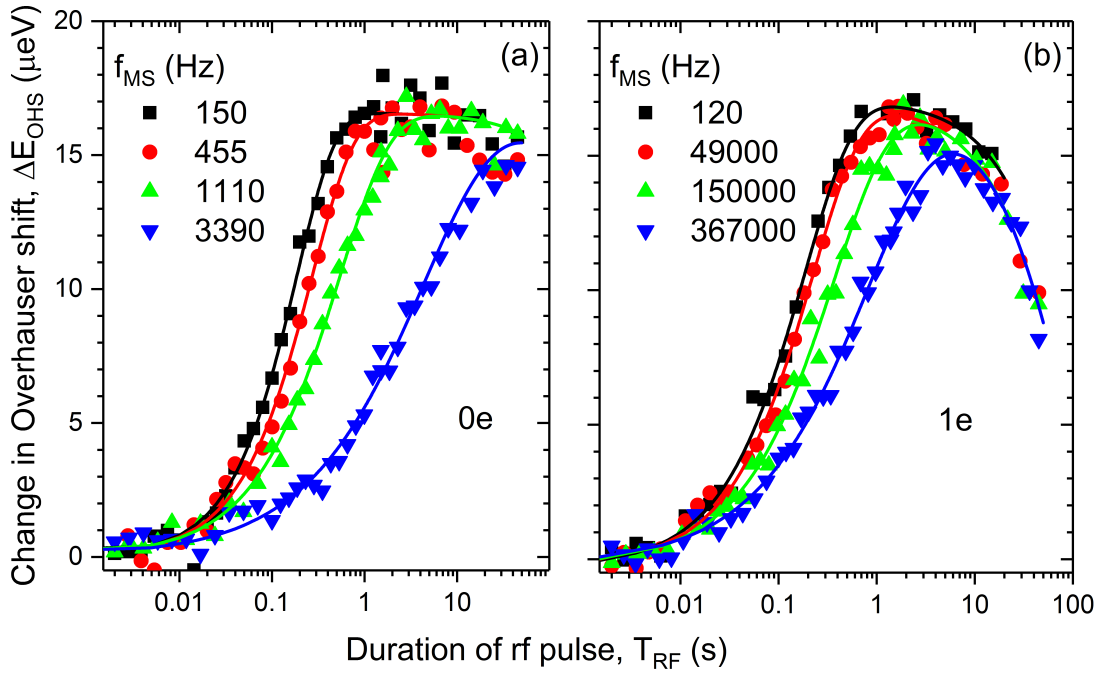


FIGURE 6.9: The change in the ^{71}Ga nuclear spin polarisation ΔE_{OHS} as the duration T_{RF} of the applied rf frequency comb is changed. Different modes spacings of the frequency comb f_{MS} are shown and a clear slow down of the nuclear spin depolarisation is observed for large f_{MS} whilst the sample is kept in a) the 0e state ($V_{\text{Dark}} = 1.64$ V) and b) the centre of the 1e plateau ($V_{\text{Dark}} = 1.732$ V) in the dark during the rf pulse. The data is taken at $B_z = 8$ T and using σ^- pumping and the solid lines show the exponential fitting.

the time it takes for the rf comb to depolarise the nuclei and T_1 is the nuclear spin lifetime (which is found from the natural decay of the nuclear spin polarisation in the dark, see Section 6.2). The height of the curve is $A_1 \approx 17 \mu eV$ and corresponds to the total Overhauser shift due to ^{71}Ga in the dot and agrees well with the rf calibration measurements performed in Section 5.1.3.

For small comb mode spacings f_{MS} , the polarisation decay due to the rf is fast with $\tau < 200$ ms regardless of the charging state of the dot. For an empty dot (Figure 6.9a), a significant slow down of the depolarisation rate is observed when the mode spacing is just $f_{\text{MS}} \approx 3400$ Hz and it now takes several seconds to reach the same change in splitting ΔE_{OHS} . However in the 1e plateau (Figure 6.9b), no slow down in the depolarisation is observed for f_{MS} of a few kHz. This indicates that the mode spacing required to avoid depolarisation of all ^{71}Ga nuclei (the nuclear homogeneous linewidth w_{hom} of ^{71}Ga) is much higher when a single electron is present in the dot.

Note that the effect of the natural decay of the nuclear spins is also visible in the long T_{RF} datapoints in Figure 6.9. When the dot is left in the 0e state, the nuclear spin

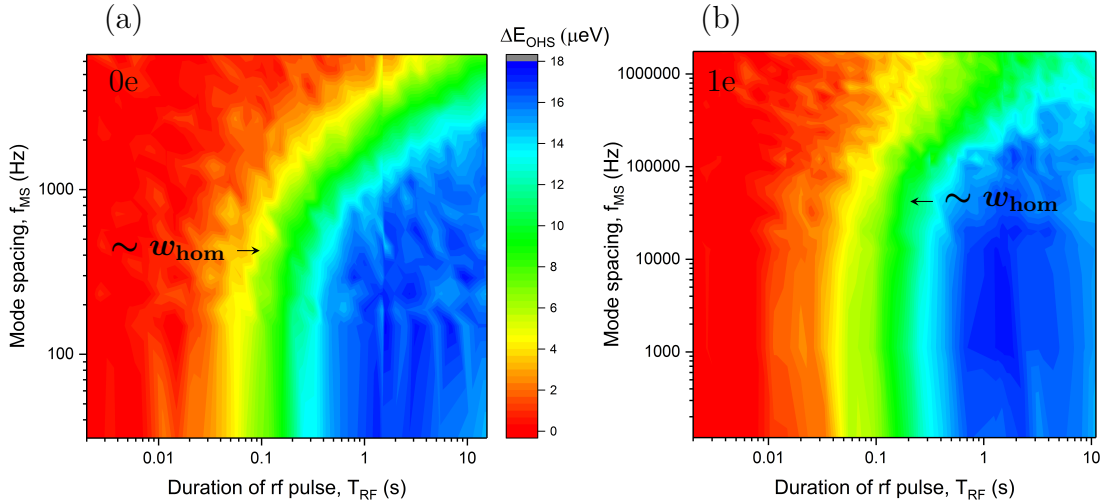


FIGURE 6.10: Two-dimensional density plot of how the Overhauser shift changes ΔE_{OHS} due to ^{71}Ga depolarisation with different mode spacing f_{MS} of the frequency comb and different durations of the rf pulse T_{RF} . The f_{MS} at which the depolarisation slows down gives an estimate of the homogeneous linewidth w_{hom} (indicated by black arrows) and this occurs a) for an empty dot ($V_{\text{Dark}} = 1.64$ V) at $w_{\text{hom}} \approx 400$ Hz and b) for a singly charged dot ($V_{\text{Dark}} = 1.732$ V) at a much larger $w_{\text{hom}} \approx 50000$ Hz.

lifetime is very long with $T_1 > 10^4$ s (see Section 6.2) at $V_{\text{Dark}} = 1.64$ V and there is only a small decrease in ΔE_{OHS} for $T_{\text{RF}} > 10$ s. However at the centre of the 1e plateau ($V_{\text{Dark}} = 1.732$ V), the nuclear spin lifetime is much shorter at $T_1 \approx 560$ s and the ΔE_{OHS} decreases significantly at long T_{RF} because the total nuclear polarisation has decayed and so there is a smaller change in splitting between “rf” and “no rf” datapoints.

The rf induced depolarisation curves were measured for many more values of mode spacings and over many orders of magnitude. To be able to visualize the f_{MS} at which the slow down occurs, a detailed color coded density plot is shown in Figure 6.10. Here, to determine the effect of the applied rf only, the data has been corrected for the natural decay of the spin polarisation by dividing the datapoints by $\exp(-(T_{\text{RF}}/T_1))$ and using the values from the fitted curves (such as those shown in Figure 6.9). The threshold value of f_{MS} , above which the slow down of the nuclear spin dynamics is observed, is shown by the black arrows and gives an estimate of w_{hom} . For the 0e state $w_{\text{hom}} \approx 400$ Hz and for the 1e state $w_{\text{hom}} \approx 50$ kHz. Note that the underlying individual nuclear transitions have a much narrower homogeneous linewidth than the inhomogeneously broadened ensemble (with total width $w_{\text{iso}} \approx 7$ MHz) and shows the severity of the strain induced quadrupolar broadening in self assembled InGaAs QDs.

Just as we did with the inhomogeneous linewidths w_{inh} to determine the ensemble nuclear spin dephasing times T_2^* , we can use the homogeneous linewidth w_{hom} to find the nuclear

spin coherence time T_2 . Using the relation $T_2 \approx 1/(\pi \times w_{\text{hom}})$, we obtain that $T_2 \approx 0.8$ ms (compared to $T_2^* = 22 \mu\text{s}$ calculated from Section 6.3) for the 0e state (which is similar to previous values for ^{71}Ga obtained using spin echo pulsed NMR measurements [147, 203] and using cw NMR [8]) and $T_2 \approx 6.4 \mu\text{s}$ (compared to $T_2^* = 0.94 \mu\text{s}$) for the 1e state. This corresponds to at least two orders of magnitude smaller nuclear spin coherence time due to the presence of the electron and agrees with the findings of Wüst et al. [194], who used pulsed NMR techniques to observe a two orders of magnitude decrease for arsenic and indium nuclear isotopes (for indium, they observed $T_2 = 3.3$ ms for 0e state and $T_2 = 25 \mu\text{s}$ for 1e state).

The electron spin lifetime at large magnetic fields has been measured to be on the order of $100 \mu\text{s}$ [204] and a flip of the electron spin at this timescale can lead to the measured homogeneous broadening of ≈ 50 kHz. Additionally, as discussed in Section 6.2, there may be a significant contribution due to the electron mediated nuclear spin coupling as well as coupling with the Fermi reservoir. Both our sample (32 nm tunnelling barrier) and the sample used by Wüst et al. [194] (25 nm barrier) have strong cotunnelling effects, so a systematic dependence of nuclear (and electron) spin dynamics on the tunnelling barrier thickness would be required to investigate weaker cotunnelling samples.

6.5 Summary

The ability to tune the charge state of InGaAs QDs using the Low Temp Cap diode sample has allowed for the direct experimental comparison of the nuclear spin dynamics for a QD with and without a confined electron. Having identified the individual charge states, the optimal bias values for the various part of the experimental pump-rf-probe cycle were obtained by performing bias dependent calibration measurements. Then experimental comparisons were shown between 0e and 1e states for the nuclear spin lifetime T_1 , the ensemble dephasing time T_2^* and the nuclear spin coherence time T_2 .

The first nuclear spin timescale of interest was the lifetime T_1 which was measured by looking at the natural decay of the nuclear spin polarisation in the dark at different biases. The nuclear polarisation is stable for the empty dot and the doubly charged singlet state (2e) where $T_1 > 10^4$ s, due to the large quadrupolar shifts in self assembled InGaAs dots that suppress spin diffusion. But in the centre of the 1e charging plateau, the lifetime is significantly reduced to $T_1 \approx 560$ s because of cotunnelling with electrons in the Fermi sea and the electron mediated hyperfine interaction that can couple two nuclear spins together

via the Fermi reservoir. The observation of minima in the nuclear T_1 at biases towards each edge of the 1e plateau indicate that the cotunnelling rate is a maxima at these bias values and this creates an unstable electron spin state.

By using our low power, cw NMR techniques to measure the inverse NMR spectra, the inhomogeneous linewidths and the ensemble dephasing time of the nuclear spins were compared between the 0e and 1e states. The presence of the electron once again caused faster nuclear spin dynamics with $T_2^* = 22 \mu\text{s}$ for the 0e state and $T_2^* = 0.94 \mu\text{s}$ for the 1e state. This was caused by the inhomogeneity in the Knight field due to the electron that is felt by the individual nuclei at each lattice site in the QD. Moreover, the broadest inhomogeneous linewidth (shortest T_2^*) was observed to be at the centre of the 1e plateau, where the electron spin is most stable, revealing the opposite tendencies between long electron spin lifetime and short nuclear dephasing times.

Finally, by utilising the frequency comb NMR technique, the homogeneous linewidths of a nuclear spin transition and the nuclear coherence time T_2 were investigated between the 0e and 1e states. Once more the presence of the additional electron causes a decrease in the nuclear T_2 by at least two orders of magnitude (agreeing well with pulsed NMR experiments [194]).

By all indications, the presence of a single electron spin trapped in a QD to be used for spin qubit applications [40], has a detrimental effect on the nuclear spin bath and highlights one of the fundamental problems in QDs with such a large strain variation across its volume. To improve the situation, optical nuclear spin pumping may be combined with various pulsed NMR sequences such as dynamical decoupling sequences [205] that suppress inhomogeneous broadening but suffer from instantaneous diffusion [206] or solid echo sequences [207] that average out the nuclear dipolar couplings but not inhomogeneous broadening. Recently, more sophisticated sequences such as the Combined Hahn and Solid Echo (CHASE) [203] that efficiently combines the features of both types of pulse sequences have been developed and may be applied to singly charged InGaAs dots to prolong the nuclear spin coherence times even in the presence of a confined electron. Additionally further work could involve looking explicitly at the effect of cotunnelling on both the electron and nuclear spin dynamics, for example by growing a series of samples with different tunnelling barrier thicknesses.

Chapter 7

Conclusion

The experimental measurements presented in this thesis have been used primarily to understand the fundamental properties of the nuclear spins in single self assembled QDs. By using optical pump-probe techniques and cw NMR, we have studied the dense quadrupolar ($I \geq 3/2$) nuclear spin system of III-V InGaAs/GaAs QDs and for the first time the dilute nuclear spin bath of II-VI CdTe/ZnTe QDs where most of the nuclei have no spin ($I = 0$). We have also developed a novel cw NMR method as a non-invasive way of analysing the structural properties of a single InGaAs dot consisting of only $\sim 10^5$ nuclei. Finally, direct comparisons have been made of the nuclear spin evolution timescales between neutral and singly charged dots. To conclude this thesis, we summarize the key results and potential directions of future research for the three experimental chapters.

In Chapter 4, we presented the first direct measurement of the Overhauser shift (upto $\Delta E_Z \approx \pm 2 \mu\text{eV}$) in the CdTe/ZnTe quantum dot system containing only a few hundred nuclear spins. We propose that DNP is formed via the quantum well states and we saw that this polarisation is robust with an initialisation time of ~ 1 ms and decay time of $\gtrsim 1$ s (both approximately two orders of magnitude faster than their III-V counterparts). Using cw NMR techniques, the first detection of Cd and Te NMR signals revealed the strong Knight field of $|B_e| \gtrsim 50$ mT present in this system as well as spectral wandering effects due to charge fluctuations in the environment. The promising optically active CdTe/ZnTe QD system has the potential to combine the advantages of III-V dots which have good optical properties and the long coherence times found in nuclear spin free systems such as group IV semiconductors. However a better understanding is required of the limits of the nuclear spin dynamics. This would require the design and fabrication of the next generation of samples in gated charge-tunable diode structures so that the charge environment of the dot may be controlled.

We saw in Chapter 5 how optically detected NMR techniques can be used to compare the structure of single, self-assembled QDs in two different InGaAs/GaAs samples. The cw NMR techniques used require no specific preparation of the sample and can be used to analyse (in-situ) the structure of small nanoscale structures (with only 10^5 nuclei) whilst not affecting the optical quality of the QD for any subsequent measurements. The newly developed 3-band inverse NMR technique has allowed for the first direct, measurement of the NMR signal from low strain nuclei. The experimental NMR results together with TEM images have revealed that the shape of the dots are very shallow and disc-like (as opposed to large pyramids) with the electron wavefunction penetrating significantly into the weakly strained surrounding GaAs barrier layers. Further work to verify the experimental conclusions would involve a computational study to model different quantum dot structures and strain distributions and see the effect on the NMR spectra (see Bultay et al. [124, 126]).

In Chapter 6 we provided a direct experimental comparison of the nuclear spin dynamics for a QD with and without a resident electron. The nuclear spin lifetime T_1 measurement showed a stable nuclear polarisation for the empty dot and the doubly charged singlet state ($2e$) where $T_1 > 10^4$ s, but for the $1e$ state, a reduction of the nuclear spin lifetime to $T_1 \approx 560$ s was observed due to the cotunnelling with electrons in the Fermi sea. Using the inhomogeneous linewidths from the inverse NMR spectra, the ensemble dephasing times were extracted and the $1e$ state showed much faster nuclear spin dynamics ($T_2^* = 0.94 \mu\text{s}$) than the $0e$ state ($T_2^* = 22 \mu\text{s}$). This was a direct measurement of the Knight field induced broadening due to the resident electron. Measurements at different bias values across the $1e$ plateau revealed a fundamental problem with the InGaAs/GaAs QD system – the opposite tendencies of long electron spin lifetime and short nuclear dephasing times. Finally, using the frequency comb NMR technique, the homogeneous linewidths of a nuclear spin transition were measured and the nuclear coherence time T_2 was compared between the $0e$ and $1e$ states. Once again the additional electron causes a decrease in the nuclear T_2 by at least two orders of magnitude. These measurements highlighted the detrimental effect on the nuclear spin bath due to the presence of a single confined electron. Further experiments could involve using recently developed, efficient pulse sequences (such as the Combined Hahn and Solid Echo (CHASE) [203] demonstrated so far on neutral dots) to prolong the nuclear spin coherence times even in the presence of a single electron. Furthermore, the effect of cotunnelling may be investigated further by growing a series of samples with different tunnelling barrier thicknesses and determining the effect on both the electron and nuclear spin dynamics.

Though self assembled QDs have been actively researched for a few decades now, there are many fundamental processes and basic properties that we do not fully understand yet. The research community should take caution in the approach towards spin qubit applications. Even from the insights gained in Chapter 5 of this work, we may have even misinterpreted what the shape and structure of a QD looks like. Particularly with the eventual ambition of combining 2, 3, 5, 10 or more QD qubits together, it is imperative to understand the fundamentals of a single dot first. Throughout this thesis, we have tried to gain some understanding from the perspective of the nuclear spins. Though the II-VI system of CdTe/ZnTe QDs show promise, a much more stable environment is necessary surrounding the single dot even just to understand the limiting mechanisms more clearly. Our collaborators at the University of Warsaw are now attempting to embed these QDs in diode structures, with the ambition of creating reproducible, stable QDs with even better optical properties. For the InGaAs system, one of the main issues we discussed in Chapter 6 is the true limiting mechanism of the nuclear spin lifetime at the centre of the single electron charging plateau. Various processes were described, but we now believe that though the tunnelling rate is suppressed at the centre of the plateau, there is still a significant contribution from electron cotunnelling with the Fermi reservoir. Our group is now conducting a comprehensive study of the lifetimes for both the electron and nuclear spins of the QD with samples of various tunnelling barrier thicknesses. Beyond that, in order to narrow the nuclear spin bath fluctuations further in the presence of a single electron, we will attempt to use pulsed NMR sequences [203] to prolong the nuclear spin coherence time. Once again, this will give an insight into what the ultimate limiting mechanisms are in the single electron and many nuclei central spin problem.

Appendix A

Appendix: Spectral wandering in CdTe/ZnTe quantum dots

In this appendix, we discuss the spectral fluctuations that were observed in the CdTe/ZnTe self assembled QD samples. The energy of the X^0 line in the PL spectra is plotted for two separate dots from sample B. It can be seen that the average energy varies over the time of the experiment (this data was recorded during the NMR spectra measurements) by $\sim 100 \mu\text{eV}$ over the time scale of hours. Part of this spectral fluctuation can be from external environment factors such as the drifts in the ambient temperature which can change the alignment of optical components in the spectrometer. However, in this CdTe/ZnTe sample, a significant amount of spectral wandering was observed, which could vary considerably between dots. Spectral wandering is caused by changes in the charge environment around the dot due to continuous optical excitation of the sample [171, 208]. This adds noise to the optically detected pump-probe measurements because it reduces the precision in measuring the splitting of the PL lines. This makes it very difficult to measure small changes in splitting, which is required for the NMR spectra, and we chose dots that have minimal spectral wandering.

There are also longer term variations of the detected Zeeman splitting in the PL spectra on the timescale of days or weeks. For example in the dynamics measurements in Figure 4.9, a small difference ($< 0.5 \%$) is observed between the initial splitting of $\approx 399.2 \mu\text{eV}$ in the nuclear spin buildup measurement and the final splitting of $\approx 397.8 \mu\text{eV}$ in the nuclear spin decay measurement. These datasets were measured 25 days apart but from the same QD in sample B. Such a slow variation can be caused by external factors such as the inability to reproduce the same static magnetic field or a change in the dispersion of the spectrometer due to the ambient temperature. Alternatively, it can also be attributed

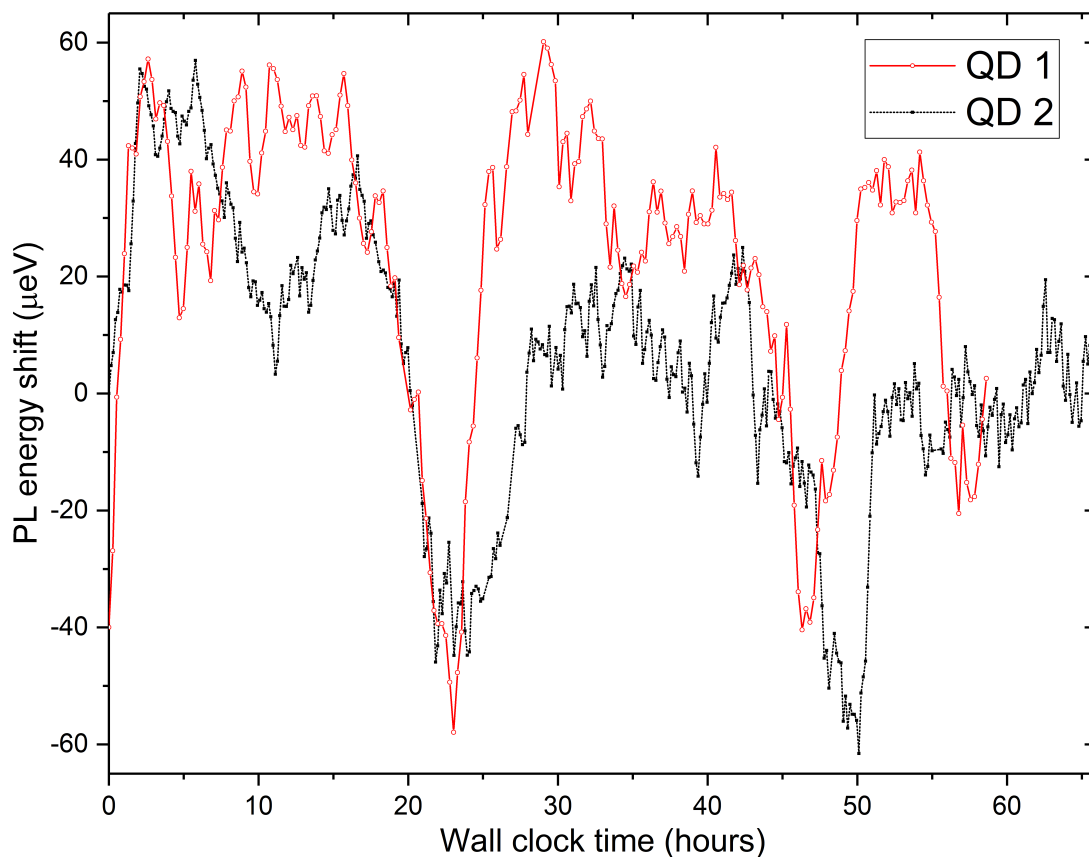


FIGURE A.1: The observed variation in the PL energy of the neutral X^0 state as a function of wall clock time passed in the lab, during NMR measurements. The average energies of the two Zeeman split peaks are plotted for two separate QDs in sample B.

to same charge fluctuations in the environment that cause the spectral wandering, which can induce an electric field that creates a small variation in the electron and hole g-factors. However, we can account for such fluctuations by designing the experiments to use differential measurements. For the measurement of the NMR spectra for example, multiple PL spectra are taken with rf (signal) and without rf (background) and the difference is taken to find the NMR signal. Though the absolute value of the splitting may drift with time, the change in splitting between rf and no rf can be used to reliably trace out the NMR signal. Additionally, all experiments are run so that we step through multiple sweeps (about 6-10) of the control variable from a low value to high, then high to low, then low to high again etc. This allows us to not only monitor the drift with time, but check for any hysteresis effects, and if a significant drift is observed, the data is discarded and remeasured.

Finally, fluctuations in the charge environment of the dot are most likely the reason for the broadening observed between the NMR spectra. A large broadening is clearly observed in QD2 for the Cd spectrum with σ^+ pumping and also for Te with σ^- pumping. However

under σ^- pumping for Cd and σ^+ pumping for Te a peak-like lineshape is observed. So the broadening of the NMR lineshape does not appear to depend on the sign of the circular polarisation and it is not obvious what the exact mechanism is for the observed broadening. Again, the likely cause is the slow fluctuations in the charge environment over the timescale of hours. So because the NMR spectra are measured for one isotope and one pump polarisation at a time, it is possible that for some of the measurements, there was a greater chance that an electron could be trapped by the dot and create a broadening of the peaks.

Appendix B

Appendix: Estimate of the average chemical composition of the InGaAs QDs

In this appendix, we present the numerical analysis used to determine the relative concentrations of indium ρ_{In} and gallium $\rho_{Ga} = 1 - \rho_{In}$ in the InGaAs QDs studied in both the In-flush sample and the Low Temp Cap sample. The signal is combined from two datasets to determine the final chemical compositions. We use both the maximum total OHS per isotope ΔE_{OHS} where a single band depolarises the entire isotope (see Figure 5.7) and the normalised, integrated, high resolution CT NMR signal ΔE_{CT} (see Table 5.3). The measured values of these shifts for both samples are summarised in Table B.1.

Low temp Cap sample	^{113}In	^{69}Ga	^{71}Ga
total OHS, ΔE_{OHS} (μeV)		38	14
normalised, integrated CT signal, ΔE_{CT} (μeV)	9.7	6.7	6.0
In-flush sample			
total OHS, ΔE_{OHS} (μeV)		69	17
normalised, integrated CT signal, ΔE_{CT} (μeV)	18.7	9.6	8.0

TABLE B.1: The experimentally measured total OHS (ΔE_{OHS}) and the normalised integrated CT signal (ΔE_{CT}) for In and Ga in both InGaAs/GaAs QD samples (using σ^- pumping only at $B_z = 8$ T). Note that ΔE_{OHS} for ^{113}In and ^{69}Ga is a combined value due to the total OHS from both isotopes.

As discussed in Section 3.4.2, the application of the cw rf pulse changes the populations of the nuclear spin states and this is detected by a change in the spectral splitting of the exciton PL lines. The total OHS of the j th isotope $\Delta E_{\text{OHS},j}$ can be related to the nuclear spin polarisation degree of that isotope $P_{N,j}$ via

$$\Delta E_{\text{OHS},j} = \rho_j A_j I_j P_{N,j}, \quad (\text{B.1})$$

where ρ_j is the average mole fraction sampled by the electron wavefunction of the j th isotope, A_j is the hyperfine constant and I_j is the nuclear spin. The polarisation degree $P_{N,j}$ was introduced in Section 3.4.2 and is defined as

$$P_{N,j} = \sum_{m=-I_j}^{+I_j} \frac{m p_m}{I_j}, \quad (\text{B.2})$$

where the population probabilities p_m follow the Boltzmann distribution when the DNP is formed through electron-nuclear spin flips [9, 146]

$$p_m = \frac{e^{m\beta}}{\sum_{m=-I}^{+I} e^{m\beta}} \quad (\text{B.3})$$

and β is the dimensionless inverse temperature.

For InGaAs dots, whilst the natural abundance of $\sigma_{^{115}\text{In}} \approx 1$, the two gallium isotopes have a natural abundance of $\sigma_{^{69}\text{Ga}} \approx 0.60$ and $\sigma_{^{71}\text{Ga}} \approx 0.40$ (see Table 2.1). We can account for this by writing $\rho_{^{69}\text{Ga}} = 0.60\rho_{\text{Ga}}$ and $\rho_{^{71}\text{Ga}} = 0.40\rho_{\text{Ga}}$. Also since each cationic site is either Ga or In, the concentration must sum to unity $\rho_{\text{In}} + \rho_{\text{Ga}} = 1$ (so $\rho_{\text{In}} = 1 - \rho_{\text{Ga}}$).

The full set of equations for the total OHS ΔE_{OHS} data can be written in terms of ρ_{Ga} and β as

$$\Delta E_{\text{OHS}}(^{115}\text{In} + ^{69}\text{Ga}) = \frac{9}{2}(1 - \rho_{\text{Ga}})A_{(^{115}\text{In})}P_{N,(^{115}\text{In})} + \frac{3}{2}(0.6 \times \rho_{\text{Ga}})A_{(^{69}\text{Ga})}P_{N,(^{69}\text{Ga})}, \quad (\text{B.4})$$

$$\Delta E_{\text{OHS}}(^{71}\text{Ga}) = \frac{3}{2}(0.4 \times \rho_{\text{Ga}})A_{(^{71}\text{Ga})}P_{N,(^{71}\text{Ga})} \quad (\text{B.5})$$

with P_N (which depends on β) substituted using Equations B.2 and B.3.

Similarly, the inverse NMR signal ΔE_{CT} , which corresponds to a change in the polarisation degree ΔP_N (as opposed to just P_N), can be written as

$$\Delta E_{\text{CT},j} = \rho_j A_j I_j \Delta P_{N,j}. \quad (\text{B.6})$$

To determine the change in the nuclear polarisation ΔP_N using the inverse NMR technique, we follow the derivation from the supplementary material of [146]. If the nuclear transition between the $m \leftrightarrow m + 1$ states lies within the gap in the rf waveform, the transition is not driven and the populations equalise for two sets of spin states ($I_z \leq m$ and $I_z \geq m + 1$) because the only dipole allowed transitions that can be induced by the rf field is between states I_z that differ by ± 1 . After rf excitation, the populations of the two sets of spin levels will be the average of their initial populations and can be written as

$$\Delta P_{N,j} = \frac{m - I_j}{2I_j} \sum_{k=-I_j}^m p_k + \frac{I_j + m + 1}{2I_j} \sum_{k=m+1}^{+I_j} p_k. \quad (\text{B.7})$$

Finally, to obtain the expression for the change in nuclear polarisation using the Inverse NMR technique, we substitute the Boltzmann distribution (Equation B.3) for p_k in Equation B.7 and $m = -1/2$ for a gap at the central transition ($-1/2 \leftrightarrow 1/2$), to obtain

$$\Delta P_{N,j} = \frac{(I_j + 1/2) + (I_j + 1/2)e^{(2I_j+1)\beta} - (2I_j + 1)e^{(I_j+1/2)\beta}}{2I_j(e^{(2I_j+1)\beta} - 1)}. \quad (\text{B.8})$$

The set of equations relating the measured inverse NMR signal ΔE_{CT} to the change in nuclear polarisation ΔP_N are analogous to Equations B.4 and B.5,

$$\Delta E_{\text{CT}}(^{115}\text{In}) + \Delta E_{\text{CT}}(^{69}\text{Ga}) = \frac{9}{2}(1 - \rho_{\text{Ga}})A_{(^{115}\text{In})}\Delta P_{N,(^{115}\text{In})} + \frac{3}{2}(0.6 \times \rho_{\text{Ga}})A_{(^{69}\text{Ga})}\Delta P_{N,(^{69}\text{Ga})}, \quad (\text{B.9})$$

$$\Delta E_{\text{CT}}(^{71}\text{Ga}) = \frac{3}{2}(0.4 \times \rho_{\text{Ga}})A_{(^{71}\text{Ga})}\Delta P_{N,(^{71}\text{Ga})}, \quad (\text{B.10})$$

but with substitution of Equation B.8 for $\Delta P_{N,j}$.

Finally to combine the datasets of both techniques, we define a χ^2 statistic as

$$\chi^2 = \sum_n (O_n - E_n)^2, \quad (\text{B.11})$$

where O is the observed value and E is the expected value. The observed value (actually measured from experiment) is taken to be the left hand side of Equations B.4, B.5, B.9 and B.10 and the expected value as the right hand side and we sum over the squares of the differences of the $n = 4$ equations. In essence, the entire dataset is fit with the Boltzmann distribution model for the populations and χ^2 (the sum of the fitting residuals) is minimised to obtain the best fit value for the fitting parameters of ρ_{Ga} and β .

By minimising the χ^2 , we find for the QD measured in the In-flush sample that $\beta = 0.93$, $\rho_{Ga} = 80.8\%$ and $\rho_{In} = 19.2\%$. For the dot in the Low Temp Cap sample, $\beta = 0.51$, $\rho_{Ga} = 90.1\%$ and $\rho_{In} = 9.9\%$. This indicates significantly more indium in the dot measured in the In-flush sample.

Appendix C

Appendix: Entire dataset for high resolution inverse NMR CT spectra

In order to determine the precise resonance frequency and the width of the CT for each isotope in both samples, more inverse NMR CT spectra were taken with larger gap widths (lower resolution) in the radiofrequency waveform than the highest resolution spectra shown in Figure 5.10. This provides a greater NMR signal as there are more nuclear resonances within a larger gap size and comparing results with different w_{Gap} allows us to see the true width of the CT resonance.

The full dataset that was measured for different gap sizes for all of the isotopes in both samples is shown in Figure C.1. By analysing the width of the CT resonances of all the spectra, different band widths were chosen for the 3rd CT band of each isotope for both samples. The width of the band w_{CTband} was chosen to cover approximately 90 % of the observed CT spectra and the chosen values for each isotope in each sample is shown in Table C.1.

For ^{75}As , a narrow peak is accompanied by a broader tail which is why the CT band width (of about 500 kHz) is much higher than the other isotopes. This also causes an asymmetric lineshape due to the fact that As can have different combinations of nearest neighbours and is discussed in the main text. The As CT spectra (shown in the top row of Figure C.1) were further processed to identify the skew of the lineshape. To make sure 90% of the CT is covered (including the tails), we estimate that the 3rd CT band should be offset from the true ^{75}As CT peak to lower frequencies - for the low temp. cap sample by 30 kHz and for the In-flush sample by 100 kHz.

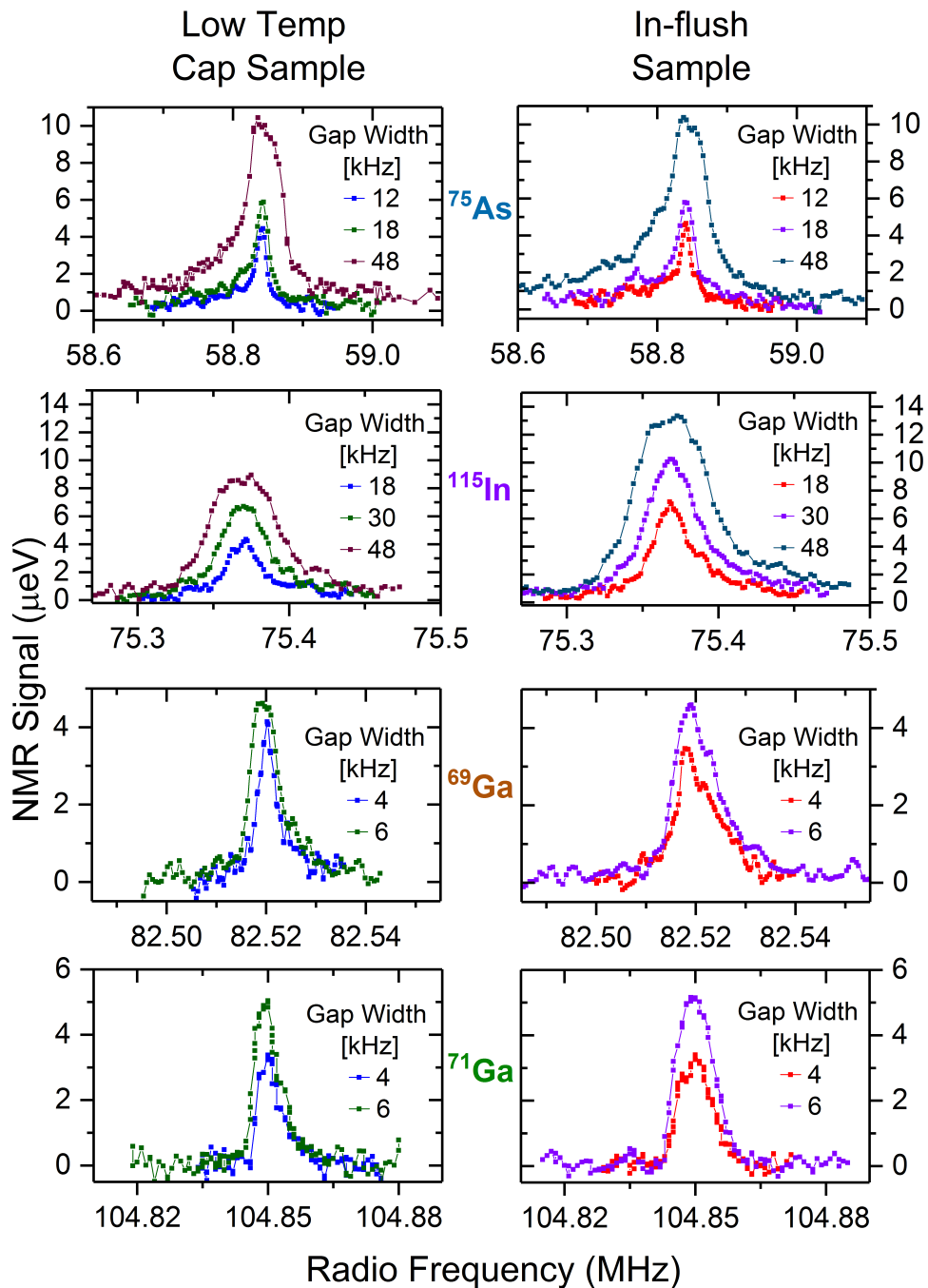


FIGURE C.1: The inverse NMR CT spectra of all 4 isotopes for both samples. The spectra were taken at $B_z = 8$ T and using σ^- pumping. The horizontal and vertical scales of each row (isotope) are set to be identical so that the equivalent lineshapes can be compared for a specific isotope between samples.

Sample	^{75}As	^{113}In	^{69}Ga	^{71}Ga
Low temp Cap	503*	81	27	39
In-flush	503 [†]	81	39	39

TABLE C.1: The chosen widths of the third CT saturation band w_{CTband} (in units of [kHz]) of each of the isotopes in the two samples used in this work. To account for the skewness in the ^{75}As lineshape, the 3rd band is offset to lower frequencies (compared to the ^{75}As CT frequency) by *30 kHz for the Low temp cap sample and [†]100 kHz for the In-flush sample.

Appendix D

Appendix: 3-band inverse NMR ST spectra data correction

In an Inverse NMR measurement, a datapoint is taken by measuring the Zeeman splitting of an exciton after depolarising nuclei of a particular isotope using an RF waveform. First, a ‘No Gap’ measurement is taken where rf excitation in the shape of a single spectral band is applied that is wide enough to cover the entire resonance (CT and STs) of a single isotope, which provides the background level of splitting where a single isotope has been fully depolarised. Then, a ‘Gap’ measurement is performed where a gap (with central frequency f_{Gap} and width w_{Gap}) is introduced within this single band and any nuclear resonances that lie within the band are depolarised and any resonances within the gap remain polarised. The final NMR signal is obtained by subtracting the splitting of the ‘Gap’ waveform from the splitting with the ‘No Gap’ waveform. The position of the gap is moved across the band and a NMR spectral lineshape is obtained.

To separate the ST signal from the CT in this paper, a 3rd CT saturation band was positioned to cover at least 90% of the CT signal of a particular isotope. The precise resonance frequency and the width of the isotope are determined using the inverse NMR CT spectra (using the full dataset shown in Appendix C). The central frequency of the 3rd band f_{CTband} , with a width w_{CTband} , is aligned to the central frequency of the isotope’s resonance in all cases apart from ^{75}As . This is because ^{75}As has an asymmetric CT line shape accompanied by a broad tail. So to fulfill the 90 % coverage of the CT resonance, the 3rd CT saturation band has to be offset from the resonance frequency to lower frequencies (by 30 kHz for the low temp. cap sample and 100 kHz for the In-flush sample).

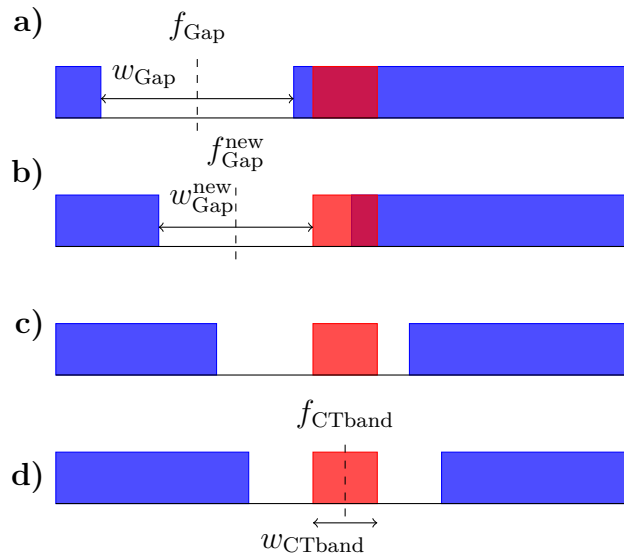


FIGURE D.1: Schematic illustration of various gap positions relative to the 3rd CT band in inverse 3-band NMR measurements.

To simplify the mathematical expressions that follow, we define the lower f_{CT}^L and higher edge f_{CT}^H of the 3rd CT band to be

$$f_{\text{CT}}^L = \left(f_{\text{CTband}} - \frac{w_{\text{CTband}}}{2} \right), \quad (\text{D.1a})$$

$$f_{\text{CT}}^H = \left(f_{\text{CTband}} + \frac{w_{\text{CTband}}}{2} \right), \quad (\text{D.1b})$$

and the lower f_{Gap}^L and higher edge f_{Gap}^H of the gap to be

$$f_{\text{Gap}}^L = \left(f_{\text{Gap}} - \frac{w_{\text{Gap}}}{2} \right), \quad (\text{D.1c})$$

$$f_{\text{Gap}}^H = \left(f_{\text{Gap}} + \frac{w_{\text{Gap}}}{2} \right). \quad (\text{D.1d})$$

As the gap is moved across the resonance, datapoints in the inverse NMR spectra can be separated into different categories.

1. Those with a whole gap positioned entirely to a lower frequency (see Figure D.1a) than the 3rd CT band

$$f_{\text{Gap}}^H \leq f_{\text{CT}}^L, \quad (\text{D.2a})$$

or entirely to a higher frequency

$$f_{\text{Gap}}^L \geq f_{\text{CT}}^H. \quad (\text{D.2b})$$

These datapoints require no rescaling and are unaltered. This is essentially equivalent to 2-band inverse NMR because the gap is far enough away from the CT resonance that there is no need to apply a 3rd CT saturation band.

2. Those with a gap partially overlapping the 3rd CT band (see Figure D.1b) on the low frequency side

$$f_{\text{CT}}^L < f_{\text{Gap}}^H \leq f_{\text{CT}}^H, \quad (\text{D.3a})$$

or the high frequency side

$$f_{\text{CT}}^L \leq f_{\text{Gap}}^L < f_{\text{CT}}^H. \quad (\text{D.3b})$$

These datapoints essentially have a narrower gap $w_{\text{Gap}}^{\text{new}}$ with a new central gap frequency $f_{\text{Gap}}^{\text{new}}$ that is shifted from the nominal gap frequency f_{Gap} from the corresponding experiment without the 3rd band. For the low frequency side, the new gap centre is the average of the lower edge of the gap and the lower edge of the 3rd CT band

$$f_{\text{Gap}}^{\text{new}} = \frac{f_{\text{Gap}}^L + f_{\text{CT}}^L}{2}, \quad (\text{D.3c})$$

with a narrower gap of

$$w_{\text{Gap}}^{\text{new}} = f_{\text{CT}}^L - f_{\text{Gap}}^L, \quad (\text{D.3d})$$

and for the high frequency side, the new gap centre is the average of the upper edge of the gap and the upper edge of the 3rd CT band

$$f_{\text{Gap}}^{\text{new}} = \frac{f_{\text{Gap}}^H + f_{\text{CT}}^H}{2}, \quad (\text{D.3e})$$

with a narrower gap of

$$w_{\text{Gap}}^{\text{new}} = f_{\text{Gap}}^H - f_{\text{CT}}^H. \quad (\text{D.3f})$$

In an inverse NMR spectra, a datapoint has an x coordinate f_{Gap} (central frequency of gap), and a y coordinate A_{sig} (amplitude of the NMR signal). The amplitude is proportional to the width of the gap (provided the NMR signal is not resolution limited by the gap width). For all datapoints to be compared equally, the amplitude is scaled by the ratio of the old gap width to the new reduced gap width. Hence the coordinates are recalculated to be

$$(f_{\text{Gap}}, A_{\text{sig}}) \rightarrow (f_{\text{Gap}}^{\text{new}}, \frac{w_{\text{Gap}}}{w_{\text{Gap}}^{\text{new}}} \times A_{\text{sig}}). \quad (\text{D.3g})$$

3. Those where the 3rd CT band is fully within the gap (so there is one gap on the low frequency side and one gap on the high frequency side of the CT band, see Figure D.1c)

$$(f_{\text{Gap}}^H > f_{\text{CT}}^H) \ \& \ (f_{\text{Gap}}^L < f_{\text{CT}}^L). \quad (\text{D.4a})$$

The new central gap frequency $f_{\text{Gap}}^{\text{new}}$ is calculated by taking into account the relative widths of the 2 gaps on either side of the CT band

$$\begin{aligned} f_{\text{Gap}}^{\text{new}} = f_{\text{CTband}} - \frac{f_{\text{CT}}^L - f_{\text{Gap}}^L}{w_{\text{Gap}} - w_{\text{CTband}}} \times (f_{\text{CTband}} - \frac{f_{\text{Gap}}^L + f_{\text{CT}}^L}{2}) \\ + \frac{f_{\text{Gap}}^H - f_{\text{CT}}^H}{w_{\text{Gap}} - w_{\text{CTband}}} \times (\frac{f_{\text{Gap}}^H + f_{\text{CT}}^H}{2} - f_{\text{CTband}}), \end{aligned} \quad (\text{D.4b})$$

and the new narrower gap width is given by

$$w_{\text{Gap}}^{\text{new}} = w_{\text{Gap}} - w_{\text{CTband}}. \quad (\text{D.4c})$$

For the same reasoning as category 2 above, the coordinates of the datapoints in the NMR spectra are recalculated as

$$(f_{\text{Gap}}, A_{\text{sig}}) \rightarrow (f_{\text{Gap}}^{\text{new}}, \frac{w_{\text{Gap}}}{w_{\text{Gap}}^{\text{new}}} \times A_{\text{sig}}). \quad (\text{D.4d})$$

4. Those with f_{Gap} within the 3rd CT band (a subset of category 3 above, see Figure D.1d)

$$f_{\text{CT}}^L \leq f_{\text{Gap}} \leq f_{\text{CT}}^H \quad (\text{D.5})$$

These datapoints are removed because their recalculated central gap frequency would lie within the 3rd CT band and no NMR signal can be detected from nuclei that are

covered by the CT saturation band, whether those resonances are from the CT or STs.

For completeness, the raw data where the procedure detailed in this appendix has not been applied is presented in Figure D.2. This is the counterpart to Figure 5.13 in the main text that shows the ST spectra for all isotopes in both samples. The effect of the above procedure becomes clear when the raw data (solid lines) is compared to the corrected data (dashed lines). The only datapoints that are affected are those that are close to the CT frequency and the change in signal is very small in most cases. The only exception is for ^{75}As because the CT is so wide, a large CT band width of 503 kHz is chosen and this is of comparable width to the inverse NMR gap width of 600 kHz, so many datapoints are removed (that fulfill condition 4 above) and the rescaling of the signal (via condition 2 and 3) can lead to relatively large changes in amplitude of a few μeV . The “dip” observed in the uncorrected dataset near the CT frequency is not a real feature of the ^{75}As spectrum and is removed by the data correction procedure.

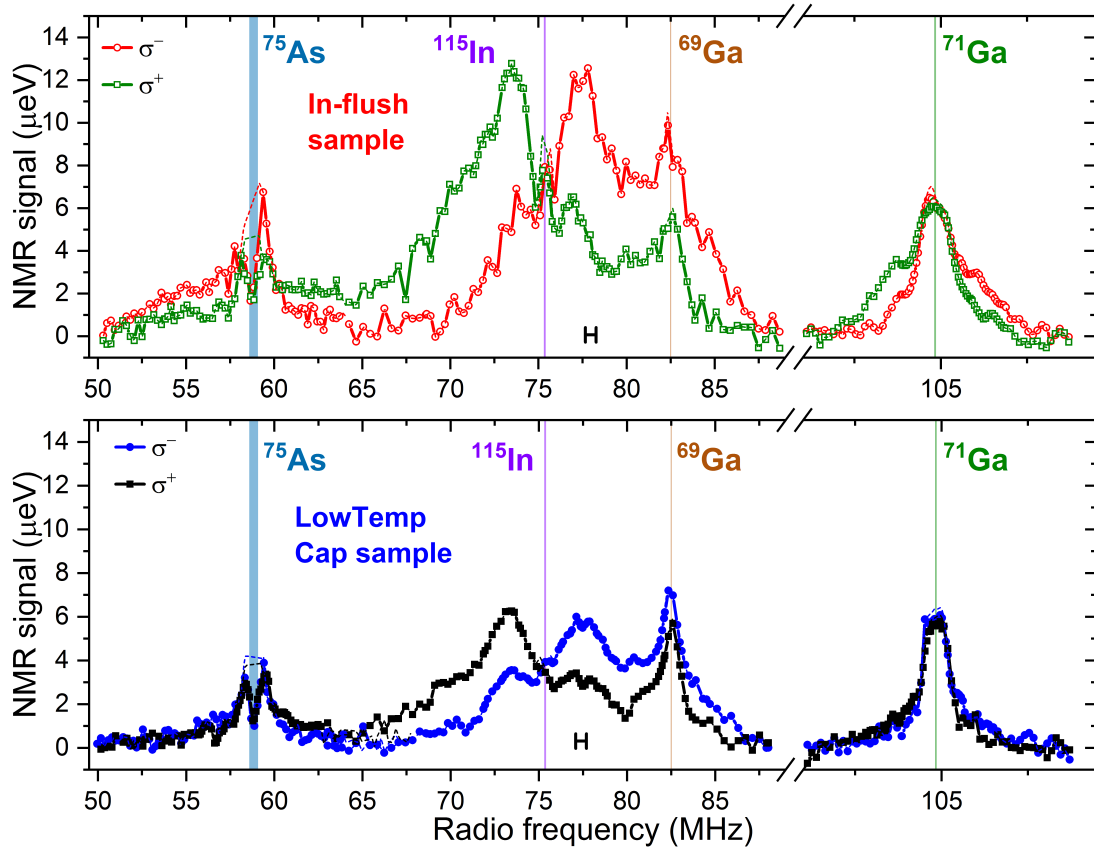


FIGURE D.2: Raw uncorrected data (solid lines) of the satellite transition (ST) NMR spectra from all nuclear isotopes in both QD samples using the new 3-band inverse NMR technique and pumping with either σ^+ or σ^- circularly polarised pump. Also shown in thin dashed lines are the corrected NMR ST dataset using the data correction procedure described in this appendix. All spectra were taken at $B_z = 8$ T and an inverse NMR gap width of 600 kHz which is the resolution of the spectra. Top Panel: ST spectra from the sample grown with In-flush. Bottom Panel: ST spectra from the sample capped at low temperature. The shaded lines at frequency 58.84 MHz, 75.37 MHz, 82.52 MHz and 104.85 MHz indicate the width of the CT-band used to saturate the CT of each of the 4 nuclear isotopes: ^{75}As ($w_{\text{CTband}} = 503$ kHz), ^{115}In ($w_{\text{CTband}} = 81$ kHz), ^{69}Ga ($w_{\text{CTband}} = 39$ kHz) and ^{71}Ga ($w_{\text{CTband}} = 39$ kHz) respectively.

Bibliography

- [1] Richard J. Warburton. Single spins in self-assembled quantum dots. *Nature Materials*, 12(6):483–493, 2013. ISSN 1476-1122. doi: 10.1038/nmat3585. URL <http://www.nature.com/doi/10.1038/nmat3585>.
- [2] Arkadiusz Wojs, Pawel Hawrylak, Simon Fafard, and Lucjan Jacak. Electronic structure and magneto-optics of self-assembled quantum dots. *Physical Review B*, 54(8):5604–5608, aug 1996. doi: 10.1103/PhysRevB.54.5604. URL <https://link.aps.org/doi/10.1103/PhysRevB.54.5604>.
- [3] M Bayer, O Stern, P Hawrylak, S Fafard, and A Forchel. Hidden symmetries in the energy levels of excitonic ‘artificial atoms’. *Nature*, 405(6789):923–926, 2000. ISSN 1476-4687. doi: 10.1038/35016020. URL <https://doi.org/10.1038/35016020>.
- [4] Peter Michler. *Single quantum dots : fundamentals, applications and new concepts*. Berlin : Springer, 2003, Berlin, 2003. ISBN 3540140220.
- [5] M. Bayer, G. Ortner, O. Stern, a. Kuther, a. Gorbunov, a. Forchel, P. Hawrylak, S. Fafard, K. Hinzer, T. Reinecke, S. Walck, J. Reithmaier, F. Klopff, and F. Schäfer. Fine structure of neutral and charged excitons in self-assembled In(Ga)As/(Al)GaAs quantum dots. *Physical Review B*, 65(19):1–23, 2002. ISSN 0163-1829. doi: 10.1103/PhysRevB.65.195315.
- [6] Peter Michler. *Single Semiconductor Quantum Dots*. Springer, 2009. ISBN 978-3-540-87445-4. doi: 10.1007/978-3-540-87446-1. URL <http://www.springerlink.com/content/m97527516r618634>.
- [7] Christian Latta, Ajit Srivastava, and Atac Imamoglu. Hyperfine interaction-dominated dynamics of nuclear spins in self-assembled InGaAs quantum dots. *Physical Review Letters*, 107(16):1–5, 2011. ISSN 00319007. doi: 10.1103/PhysRevLett.107.167401.

- [8] A. M. Waeber, M Hopkinson, I Farrer, D. A. Ritchie, J Nilsson, R. M. Stevenson, A. J. Bennett, A. J. Shields, G Burkard, A. I. Tartakovskii, M. S. Skolnick, and E. A. Chekhovich. Few-second-long correlation times in a quantum dot nuclear spin bath probed by frequency-comb nuclear magnetic resonance spectroscopy. *Nature Physics*, 12:688, mar 2016. URL <https://doi.org/10.1038/nphys3686><http://10.0.4.14/nphys3686><https://www.nature.com/articles/nphys3686#supplementary-information>.
- [9] E. A. Chekhovich, A. Ulhaq, E. Zallo, F. Ding, O. G. Schmidt, and M. S. Skolnick. Measurement of the spin temperature of optically cooled nuclei and GaAs hyperfine constants in GaAs/AlGaAs quantum dots. *Nature Materials*, 16(August), 2017. ISSN 1476-1122. doi: 10.1038/nmat4959. URL <http://www.nature.com/doifinder/10.1038/nmat4959>.
- [10] Bernhard Urbaszek, Xavier Marie, Thierry Amand, Olivier Krebs, Paul Voisin, Patrick Maletinsky, Alexander Högele, and Atac Imamoglu. Nuclear spin physics in quantum dots: An optical investigation. *Reviews of Modern Physics*, 85(1):79–133, 2013. ISSN 00346861. doi: 10.1103/RevModPhys.85.79.
- [11] Robin K. Harris, Edwin D. Becker, Sonia M. Cabral De Menezes, Robin Goodfellow, and Pierre Granger. NMR nomenclature: Nuclear spin properties and conventions for chemical shifts (IUPAC recommendations 2001). *Concepts in Magnetic Resonance Part A: Bridging Education and Research*, 14(5):326–346, 2002. ISSN 15466086. doi: 10.1002/cmr.10035.
- [12] Richard P Feynman. Simulating physics with computers. *International Journal of Theoretical Physics*, 21(6):467–488, 1982. ISSN 1572-9575. doi: 10.1007/BF02650179. URL <https://doi.org/10.1007/BF02650179>.
- [13] Y. I. Manin. Computable and Noncomputable. *Sovetskoe Radio*, 1980.
- [14] Paul Benioff. The computer as a physical system: A microscopic quantum mechanical Hamiltonian model of computers as represented by Turing machines. *Journal of Statistical Physics*, 22(5):563–591, 1980. ISSN 1572-9613. doi: 10.1007/BF01011339. URL <https://doi.org/10.1007/BF01011339>.
- [15] Deutsch David and Penrose Roger. Quantum theory, the Church–Turing principle and the universal quantum computer. *Proceedings of the Royal Society of London. A. Mathematical and Physical Sciences*, 400(1818):97–117, jul 1985. doi: 10.1098/rspa.1985.0070. URL <https://doi.org/10.1098/rspa.1985.0070>.

- [16] P Shor. Polynomial-Time Algorithms for Prime Factorization and Discrete Logarithms on a Quantum Computer. *SIAM Journal on Computing*, 26(5):1484–1509, oct 1997. ISSN 0097-5397. doi: 10.1137/S0097539795293172. URL <https://doi.org/10.1137/S0097539795293172>.
- [17] Lov K Grover. A Fast Quantum Mechanical Algorithm for Database Search. In *Proceedings of the Twenty-eighth Annual ACM Symposium on Theory of Computing, STOC '96*, pages 212–219, New York, NY, USA, 1996. ACM. ISBN 0-89791-785-5. doi: 10.1145/237814.237866. URL <http://doi.acm.org/10.1145/237814.237866>.
- [18] Andrew M Childs, Richard Cleve, Enrico Deotto, Edward Farhi, Sam Gutmann, and Daniel A Spielman. Exponential Algorithmic Speedup by a Quantum Walk. In *Proceedings of the Thirty-fifth Annual ACM Symposium on Theory of Computing, STOC '03*, pages 59–68, New York, NY, USA, 2003. ACM. ISBN 1-58113-674-9. doi: 10.1145/780542.780552. URL <http://doi.acm.org/10.1145/780542.780552>.
- [19] David P. DiVincenzo. The physical implementation of quantum computation, 2000. ISSN 00158208.
- [20] T. D. Ladd, F. Jelezko, R. Laflamme, Y. Nakamura, C. Monroe, and J. L. O'Brien. Quantum computers. *Nature*, 464(7285):45–53, 2010. ISSN 0028-0836. doi: 10.1038/nature08812. URL <http://www.nature.com/doi/10.1038/nature08812>.
- [21] J I Cirac and P Zoller. Quantum Computations with Cold Trapped Ions. *Physical Review Letters*, 74(20):4091–4094, may 1995. doi: 10.1103/PhysRevLett.74.4091. URL <https://link.aps.org/doi/10.1103/PhysRevLett.74.4091>.
- [22] D J Wineland, C Monroe, W M Itano, D Leibfried, B E King, and D M Meekhof. Experimental Issues in Coherent Quantum-State Manipulation of Trapped Atomic Ions. *Journal of research of the National Institute of Standards and Technology*, 103(3):259–328, 1998. ISSN 1044-677X. doi: 10.6028/jres.103.019. URL <https://www.ncbi.nlm.nih.gov/pubmed/28009379><https://www.ncbi.nlm.nih.gov/pmc/PMC4898965/>.
- [23] Rainer Blatt and David Wineland. Entangled states of trapped atomic ions. *Nature*, 453:1008, jun 2008. URL <https://doi.org/10.1038/nature07125><http://10.0.4.14/nature07125>.
- [24] David G Cory, Amr F Fahmy, and Timothy F Havel. Ensemble quantum computing by NMR spectroscopy. *Proceedings of the National Academy of Sciences*, 94(5):1634

- LP – 1639, mar 1997. doi: 10.1073/pnas.94.5.1634. URL <http://www.pnas.org/content/94/5/1634.abstract>.
- [25] Neil A Gershenfeld and Isaac L Chuang. Bulk Spin-Resonance Quantum Computation. *Science*, 275(5298):350 LP – 356, jan 1997. doi: 10.1126/science.275.5298.350. URL <http://science.sciencemag.org/content/275/5298/350.abstract>.
- [26] C Negrevergne, T S Mahesh, C A Ryan, M Ditty, F Cyr-Racine, W Power, N Boulant, T Havel, D G Cory, and R Laflamme. Benchmarking Quantum Control Methods on a 12-Qubit System. *Physical Review Letters*, 96(17):170501, may 2006. doi: 10.1103/PhysRevLett.96.170501. URL <https://link.aps.org/doi/10.1103/PhysRevLett.96.170501>.
- [27] M H Devoret and R J Schoelkopf. Superconducting Circuits for Quantum Information: An Outlook. *Science*, 339(6124):1169 LP – 1174, mar 2013. doi: 10.1126/science.1231930. URL <http://science.sciencemag.org/content/339/6124/1169.abstract>.
- [28] B D Josephson. Possible new effects in superconductive tunnelling. *Physics Letters*, 1(7):251–253, 1962. ISSN 0031-9163. doi: [https://doi.org/10.1016/0031-9163\(62\)91369-0](https://doi.org/10.1016/0031-9163(62)91369-0). URL <http://www.sciencedirect.com/science/article/pii/0031916362913690>.
- [29] P W Anderson and J M Rowell. Probable Observation of the Josephson Superconducting Tunneling Effect. *Physical Review Letters*, 10(6):230–232, mar 1963. doi: 10.1103/PhysRevLett.10.230. URL <https://link.aps.org/doi/10.1103/PhysRevLett.10.230>.
- [30] B E Kane. A silicon-based nuclear spin quantum computer. *Nature*, 393:133, may 1998. URL <https://doi.org/10.1038/30156><http://10.0.4.14/30156>.
- [31] Rutger Vrijen, Eli Yablonovitch, Kang Wang, Hong Wen Jiang, Alex Balandin, Vwani Roychowdhury, Tal Mor, and David DiVincenzo. Electron-spin-resonance transistors for quantum computing in silicon-germanium heterostructures. *Physical Review A*, 62(1):12306, jun 2000. doi: 10.1103/PhysRevA.62.012306. URL <https://link.aps.org/doi/10.1103/PhysRevA.62.012306>.
- [32] Kamyar Saeedi, Stephanie Simmons, Jeff Z Salvail, Phillip Dluhy, Helge Riemann, Nikolai V Abrosimov, Peter Becker, Hans-Joachim Pohl, John J L Morton, and Mike L W Thewalt. Room-Temperature Quantum Bit Storage Exceeding 39 Minutes Using Ionized Donors in Silicon-28. *Science*, 342(6160):830 LP – 833, nov 2013.

- doi: 10.1126/science.1239584. URL <http://science.sciencemag.org/content/342/6160/830.abstract>.
- [33] F Jelezko, I Popa, A Gruber, C Tietz, J Wrachtrup, A Nizovtsev, and S Kilin. Single spin states in a defect center resolved by optical spectroscopy. *Applied Physics Letters*, 81(12):2160–2162, sep 2002. ISSN 0003-6951. doi: 10.1063/1.1507838. URL <https://doi.org/10.1063/1.1507838>.
- [34] J Harrison, M J Sellars, and N B Manson. Measurement of the optically induced spin polarisation of N-V centres in diamond. *Diamond and Related Materials*, 15(4):586–588, 2006. ISSN 0925-9635. doi: <https://doi.org/10.1016/j.diamond.2005.12.027>. URL <http://www.sciencedirect.com/science/article/pii/S0925963505006266>.
- [35] M V Gurudev Dutt, L Childress, L Jiang, E Togan, J Maze, F Jelezko, A S Zibrov, P R Hemmer, and M D Lukin. Quantum Register Based on Individual Electronic and Nuclear Spin Qubits in Diamond. *Science*, 316(5829):1312 LP – 1316, jun 2007. doi: 10.1126/science.1139831. URL <http://science.sciencemag.org/content/316/5829/1312.abstract>.
- [36] R Hanson, L P Kouwenhoven, J R Petta, S Tarucha, and L M K Vandersypen. Spins in few-electron quantum dots. *Reviews of Modern Physics*, 79(4):1217–1265, oct 2007. doi: 10.1103/RevModPhys.79.1217. URL <https://link.aps.org/doi/10.1103/RevModPhys.79.1217>.
- [37] Graham H Carey, Ahmed L Abdelhady, Zhijun Ning, Susanna M Thon, Osman M Bakr, and Edward H Sargent. Colloidal Quantum Dot Solar Cells. *Chemical Reviews*, 115(23):12732–12763, dec 2015. ISSN 0009-2665. doi: 10.1021/acs.chemrev.5b00063. URL <https://doi.org/10.1021/acs.chemrev.5b00063>.
- [38] A Zrenner, L V Butov, M Hagn, G Abstreiter, G Böhm, and G Weimann. Quantum dots formed by interface fluctuations in AlAs/GaAs coupled quantum well structures. *Physical Review Letters*, 72(21):3382–3385, may 1994. doi: 10.1103/PhysRevLett.72.3382. URL <https://link.aps.org/doi/10.1103/PhysRevLett.72.3382>.
- [39] N Akopian, G Patriarche, L Liu, J.-C. Harmand, and V Zwiller. Crystal Phase Quantum Dots. *Nano Letters*, 10(4):1198–1201, apr 2010. ISSN 1530-6984. doi: 10.1021/nl903534n. URL <https://doi.org/10.1021/nl903534n>.

- [40] Daniel Loss and David P. DiVincenzo. Quantum Computation with Quantum Dots. *Physical Review A*, 57(1):12, 1998. ISSN 1050-2947. doi: 10.1103/PhysRevA.57.120. URL <http://arxiv.org/abs/cond-mat/9701055>.
- [41] A G Milnes and A Y Polyakov. Indium arsenide: a semiconductor for high speed and electro-optical devices. *Materials Science and Engineering: B*, 18(3):237–259, 1993. ISSN 0921-5107. doi: [https://doi.org/10.1016/0921-5107\(93\)90140-I](https://doi.org/10.1016/0921-5107(93)90140-I). URL <http://www.sciencedirect.com/science/article/pii/092151079390140I>.
- [42] D. Pinotsi and A. Imamoglu. Single photon absorption by a single quantum emitter. *Physical Review Letters*, 100(9), 2008. ISSN 00319007. doi: 10.1103/PhysRevLett.100.093603.
- [43] P Michler, A Kiraz, C Becher, W V Schoenfeld, P M Petroff, L Zhang, E Hu, and A Imamoglu. A quantum dot single-photon turnstile device. *Science*, 290(5500):2282–2285, 2000. ISSN 00368075. doi: 10.1126/science.290.5500.2282. URL <http://www.sciencemag.org/cgi/doi/10.1126/science.290.5500.2282>.
- [44] A. Kiraz, M. Atature, and A. Imamoglu. Quantum-dot single-photon sources: Prospects for applications in linear optics quantum-information processing. *Physical Review A - Atomic, Molecular, and Optical Physics*, 69(3):032305–1, 2004. ISSN 10502947. doi: 10.1103/PhysRevA.69.032305.
- [45] Charles Santori, David Fattal, Jelena Vuckovic, Glenn S Solomon, and Yoshihisa Yamamoto. Single-photon generation with InAs quantum dots. *New Journal of Physics*, 6:89, 2004. ISSN 1367-2630. doi: 10.1088/1367-2630/6/1/089. URL <http://dx.doi.org/10.1088/1367-2630/6/1/089>.
- [46] A Zrenner, E Beham, S Stuffer, F Findeis, M Bichler, and G Abstreiter. Coherent properties of a two-level system based on a quantum-dot photodiode. *Nature*, 418: 612, aug 2002. URL <https://doi.org/10.1038/nature00912><http://10.0.4.14/nature00912>.
- [47] T Lund-Hansen, S Stobbe, B Julsgaard, H Thyrrerstrup, T Sünner, M Kamp, A Forchel, and P Lodahl. Experimental Realization of Highly Efficient Broadband Coupling of Single Quantum Dots to a Photonic Crystal Waveguide. *Physical Review Letters*, 101(11):113903, sep 2008. doi: 10.1103/PhysRevLett.101.113903. URL <https://link.aps.org/doi/10.1103/PhysRevLett.101.113903>.
- [48] T Yoshie, A Scherer, J Hendrickson, G Khitrova, H M Gibbs, G Rupper, C Ell, O B Shchekin, and D G Deppe. Vacuum Rabi splitting with a single quantum

- dot in a photonic crystal nanocavity. *Nature*, 432:200, nov 2004. URL <https://doi.org/10.1038/nature03119><http://10.0.4.14/nature03119>.
- [49] Julien Claudon, Joël Bleuse, Nitin Singh Malik, Maela Bazin, Périne Jaffrennou, Niels Gregersen, Christophe Sauvan, Philippe Lalanne, and Jean-Michel Gérard. A highly efficient single-photon source based on a quantum dot in a photonic nanowire. *Nature Photonics*, 4:174, jan 2010. URL <https://doi.org/10.1038/nphoton.2009.287x><http://10.0.4.14/nphoton.2009.287x>.
- [50] A J Ramsay, Achanta Venu Gopal, E M Gauger, A Nazir, B W Lovett, A M Fox, and M S Skolnick. Damping of Exciton Rabi Rotations by Acoustic Phonons in Optically Excited InGaAs/GaAs Quantum Dots. *Physical Review Letters*, 104(1):17402, jan 2010. doi: 10.1103/PhysRevLett.104.017402. URL <https://link.aps.org/doi/10.1103/PhysRevLett.104.017402>.
- [51] Joanna Skiba-Szymanska, Ayesha Jamil, Ian Farrer, Martin B Ward, Christine A Nicoll, David J P Ellis, Jonathan P Griffiths, David Anderson, Geb A C Jones, David A Ritchie, and Andrew J Shields. Narrow emission linewidths of positioned InAs quantum dots grown on pre-patterned GaAs(100) substrates. *Nanotechnology*, 22(6):65302, 2011. ISSN 0957-4484. doi: 10.1088/0957-4484/22/6/065302. URL <http://dx.doi.org/10.1088/0957-4484/22/6/065302>.
- [52] Gediminas Juska, Valeria Dimastrodonato, Lorenzo O Mereni, Agnieszka Gocalinska, and Emanuele Pelucchi. Towards quantum-dot arrays of entangled photon emitters. *Nature Photonics*, 7:527, may 2013. URL <https://doi.org/10.1038/nphoton.2013.128><http://10.0.4.14/nphoton.2013.128><https://www.nature.com/articles/nphoton.2013.128#supplementary-information>.
- [53] André Strittmatter, André Holzbecher, Andrei Schliwa, Jan-Hindrik Schulze, David Quandt, Tim David Germann, Alexander Dreismann, Ole Hitzemann, Erik Stock, Irina A Ostapenko, Sven Rodt, Waldemar Unrau, Udo W Pohl, Axel Hoffmann, Dieter Bimberg, and Vladimir Haisler. Site-controlled quantum dot growth on buried oxide stressor layers. *physica status solidi (a)*, 209(12):2411–2420, dec 2012. ISSN 1862-6300. doi: 10.1002/pssa.201228407. URL <https://doi.org/10.1002/pssa.201228407>.
- [54] Alexander V Khaetskii, Daniel Loss, and Leonid Glazman. Electron Spin Decoherence in Quantum Dots due to Interaction with Nuclei. *Physical Review Letters*, 88(18):186802, apr 2002. doi: 10.1103/PhysRevLett.88.186802. URL <https://link.aps.org/doi/10.1103/PhysRevLett.88.186802>.

- [55] I. A. Merkulov, Al. L. Efros, and M. Rosen. Electron Spin Relaxation by Nuclei in Semiconductor Quantum Dots. *Physical Review B*, 65(20):205309, 2002. ISSN 1098-0121. doi: 10.1103/PhysRevB.65.205309. URL <http://link.aps.org/doi/10.1103/PhysRevB.65.205309>.
- [56] D Gammon, S W Brown, E S Snow, T A Kennedy, D S Katzer, and D Park. Nuclear spectroscopy in single quantum dots: Nanoscopic Raman scattering and nuclear magnetic resonance. *Science*, 277(5322):85–88, 1997. ISSN 00368075. doi: DOI10.1126/science.277.5322.85.
- [57] E A Chekhovich, M N Makhonin, A I Tartakovskii, A Yacoby, H Bluhm, K C Nowack, and L M K Vandersypen. Nuclear spin effects in semiconductor quantum dots. *Nature materials*, 12(6):494–504, 2013. ISSN 1476-1122. doi: 10.1038/nmat3652. URL <http://www.ncbi.nlm.nih.gov/pubmed/23695746>.
- [58] R Oulton, A Greulich, S Yu. Verbin, R V Cherbunin, T Auer, D R Yakovlev, M Bayer, I A Merkulov, V Stavarache, D Reuter, and A D Wieck. Subsecond Spin Relaxation Times in Quantum Dots at Zero Applied Magnetic Field Due to a Strong Electron-Nuclear Interaction. *Physical Review Letters*, 98(10):107401, mar 2007. doi: 10.1103/PhysRevLett.98.107401. URL <https://link.aps.org/doi/10.1103/PhysRevLett.98.107401>.
- [59] E A Chekhovich, M N Makhonin, K V Kavokin, A B Krysa, M S Skolnick, and A I Tartakovskii. Pumping of Nuclear Spins by Optical Excitation of Spin-Forbidden Transitions in a Quantum Dot. *Physical Review Letters*, 104(6):66804, feb 2010. doi: 10.1103/PhysRevLett.104.066804. URL <https://link.aps.org/doi/10.1103/PhysRevLett.104.066804>.
- [60] Eisuke Abe, Alexei M Tyryshkin, Shinichi Tojo, John J L Morton, Wayne M Witzel, Akira Fujimoto, Joel W Ager, Eugene E Haller, Junichi Isoya, Stephen A Lyon, Mike L W Thewalt, and Kohei M Itoh. Electron spin coherence of phosphorus donors in silicon: Effect of environmental nuclei. *Physical Review B*, 82(12):121201, sep 2010. doi: 10.1103/PhysRevB.82.121201. URL <https://link.aps.org/doi/10.1103/PhysRevB.82.121201>.
- [61] A.A.Onushchenko I. Ekimov. Quantum size effect in three-dimensional microscopic semiconductor crystals, 1981. ISSN 0370274X.
- [62] A Y Cho and J R Arthur. Molecular beam epitaxy. *Progress in Solid State Chemistry*, 10:157–191, 1975. ISSN 0079-6786. doi: <https://doi.org/10.1016/>

- 0079-6786(75)90005-9. URL <http://www.sciencedirect.com/science/article/pii/0079678675900059>.
- [63] R Nötzel, J Temmyo, A Kozen, T Tamamura, T Fukui, and H Hasegawa. Self-organized growth of quantum-dot structures. *Solid-State Electronics*, 40(1):777–783, 1996. ISSN 0038-1101. doi: [https://doi.org/10.1016/0038-1101\(95\)00363-0](https://doi.org/10.1016/0038-1101(95)00363-0). URL <http://www.sciencedirect.com/science/article/pii/0038110195003630>.
- [64] Ernst Bauer. Phanomenologische Theorie Der Kristallabscheidung An Oberflächen. II. *Zeitschrift für Kristallographie - New Crystal Structures*, 110(1-6):395–431, 1958. ISSN 00442968. doi: [10.1524/zkri.1958.110.1-6.395](https://doi.org/10.1524/zkri.1958.110.1-6.395).
- [65] F C Frank and J H van der Merwe. One-Dimensional Dislocations. II. Misfitting Monolayers and Oriented Overgrowth. *Proceedings of the Royal Society of London A: Mathematical, Physical and Engineering Sciences*, 198(1053):216–225, aug 1949. URL <http://rspa.royalsocietypublishing.org/content/198/1053/216.abstract>.
- [66] A. Weber M. Volmer. Keimbildung in übersättigten Gebilden. *Zeitschrift der physikalischen. Z. Physik. Chem.*, 119:277, 1926.
- [67] I N Stranski and L Krastanow. Zur Theorie der orientierten Ausscheidung von Ionenkristallen aufeinander. *Monatshefte für Chemie und verwandte Teile anderer Wissenschaften*, 71(1):351–364, 1937. ISSN 1434-4475. doi: [10.1007/BF01798103](https://doi.org/10.1007/BF01798103). URL <http://dx.doi.org/10.1007/BF01798103>.
- [68] D Leonard, M Krishnamurthy, C M Reaves, S P Denbaars, and P M Petroff. Direct formation of quantum-sized dots from uniform coherent islands of InGaAs on GaAs surfaces. *Applied Physics Letters*, 63(23):3203–3205, dec 1993. ISSN 0003-6951. doi: [10.1063/1.110199](https://doi.org/10.1063/1.110199). URL <https://doi.org/10.1063/1.110199>.
- [69] P B Joyce, T J Krzyzewski, G R Bell, B A Joyce, and T S Jones. Composition of InAs quantum dots on GaAs(001): Direct evidence for (In,Ga)As alloying. *Physical Review B*, 58(24):R15981–R15984, dec 1998. doi: [10.1103/PhysRevB.58.R15981](https://doi.org/10.1103/PhysRevB.58.R15981). URL <https://link.aps.org/doi/10.1103/PhysRevB.58.R15981>.
- [70] I Kegel, T H Metzger, A Lorke, J Peisl, J Stangl, G Bauer, J M García, and P M Petroff. Nanometer-Scale Resolution of Strain and Interdiffusion in Self-Assembled InAs/GaAs Quantum Dots. *Physical Review Letters*, 85(8):1694–1697, aug 2000. doi: [10.1103/PhysRevLett.85.1694](https://doi.org/10.1103/PhysRevLett.85.1694). URL <https://link.aps.org/doi/10.1103/PhysRevLett.85.1694>.

- [71] R J Warburton, C Schäfflein, D Haft, F Bickel, A Lorke, K Karrai, J M Garcia, W Schoenfeld, and P M Petroff. Optical emission from a charge-tunable quantum ring. *Nature*, 405(6789):926–929, 2000. ISSN 1476-4687. doi: 10.1038/35016030. URL <https://doi.org/10.1038/35016030>.
- [72] H Drexler, D Leonard, W Hansen, J P Kotthaus, and P M Petroff. Spectroscopy of Quantum Levels in Charge-Tunable InGaAs Quantum Dots. *Physical Review Letters*, 73(16):2252–2255, oct 1994. doi: 10.1103/PhysRevLett.73.2252. URL <https://link.aps.org/doi/10.1103/PhysRevLett.73.2252>.
- [73] S. M. Sze. *Physics of Semiconductor Devices*, 1969. ISSN 00135127.
- [74] O Gywat, H Krenner, and J Berezovsky. *Theory of Confined States in Quantum Dots*. Wiley Online Books. Wiley, dec 2009. ISBN 9783527628988. doi: doi:10.1002/9783527628988.ch3. URL <https://doi.org/10.1002/9783527628988.ch3>.
- [75] J S Blakemore. Semiconducting and other major properties of gallium arsenide. *Journal of Applied Physics*, 53(10):R123–R181, oct 1982. ISSN 0021-8979. doi: 10.1063/1.331665. URL <https://doi.org/10.1063/1.331665>.
- [76] W Porod and D K Ferry. Modification of the virtual-crystal approximation for ternary III-V compounds. *Physical Review B*, 27(4):2587–2589, feb 1983. doi: 10.1103/PhysRevB.27.2587. URL <https://link.aps.org/doi/10.1103/PhysRevB.27.2587>.
- [77] K. H. Goetz, D Bimberg, H Jurgensen, J Selders, A V Solomonov, G F Glinskii, and M Razeghi. Optical and crystallographic properties and impurity incorporation of $\text{Ga}_x\text{In}_{1-x}\text{As}$ ($0.44 < x < 0.49$) grown by liquid phase epitaxy, vapor phase epitaxy, and metal organic chemical vapor deposition. *Journal of Applied Physics*, 54(8):4543–4552, aug 1983. ISSN 0021-8979. doi: 10.1063/1.332655. URL <https://doi.org/10.1063/1.332655>.
- [78] C P Kuo, S K Vong, R M Cohen, and G B Stringfellow. Effect of mismatch strain on band gap in III-V semiconductors. *Journal of Applied Physics*, 57(12):5428–5432, jun 1985. ISSN 0021-8979. doi: 10.1063/1.334817. URL <https://doi.org/10.1063/1.334817>.
- [79] Charles Kittel. *Introduction to Solid State Physics, 8th Edition*. Wiley, 2004. ISBN 978-0-471-41526-8.
- [80] Michel Dyakonov. *Spin Physics in Semiconductors*, volume 1. Springer-Verlag Berlin Heidelberg, jul 2008. doi: 10.1007/978-3-540-78820-1.

- [81] E A Chekhovich, M M Glazov, A B Krysa, M Hopkinson, P Senellart, A Lemaître, M S Skolnick, and A I Tartakovskii. Element-sensitive measurement of the hole–nuclear spin interaction in quantum dots. *Nature Physics*, 9:74, dec 2012. URL <https://doi.org/10.1038/nphys2514><http://10.0.4.14/nphys2514><https://www.nature.com/articles/nphys2514#supplementary-information>.
- [82] S W da Silva, Yu A Pusep, J C Galzerani, D I Lubyshev, P P González-Borrero, and P Basmaji. Photoluminescence study of spin - orbit-split bound electron states in self-assembled InAs and quantum dots. *Journal of Physics: Condensed Matter*, 2002. ISSN 0953-8984. doi: 10.1088/0953-8984/9/1/003.
- [83] Y H Huo, B J Witek, S Kumar, J R Cardenas, J X Zhang, N Akopian, R Singh, E Zallo, R Grifone, D Kriegner, R Trotta, F Ding, J Stangl, V Zwiller, G Bester, A Rastelli, and O G Schmidt. A light-hole exciton in a quantum dot. *Nature Physics*, 10:46, nov 2013. URL <https://doi.org/10.1038/nphys2799><http://10.0.4.14/nphys2799><https://www.nature.com/articles/nphys2799#supplementary-information>.
- [84] Gabriel Bester and Alex Zunger. Cylindrically shaped zinc-blende semiconductor quantum dots do not have cylindrical symmetry: Atomistic symmetry, atomic relaxation, and piezoelectric effects. *Phys. Rev. B*, 71(4):45318, jan 2005. doi: 10.1103/PhysRevB.71.045318. URL <https://link.aps.org/doi/10.1103/PhysRevB.71.045318>.
- [85] M. Grundmann, O. Stier, and D. Bimberg. InAs/GaAs pyramidal quantum dots: Strain distribution, optical phonons, and electronic structure. *Physical Review B*, 52(16):11969–11981, 1995. ISSN 01631829. doi: 10.1103/PhysRevB.52.11969.
- [86] S Tarucha, D G Austing, T Honda, R J van der Hage, and L P Kouwenhoven. Shell Filling and Spin Effects in a Few Electron Quantum Dot. *Physical Review Letters*, 77(17):3613–3616, oct 1996. doi: 10.1103/PhysRevLett.77.3613. URL <https://link.aps.org/doi/10.1103/PhysRevLett.77.3613>.
- [87] P Hawrylak, G A Narvaez, M Bayer, and A Forchel. Excitonic Absorption in a Quantum Dot. *Physical Review Letters*, 85(2):389–392, jul 2000. doi: 10.1103/PhysRevLett.85.389. URL <https://link.aps.org/doi/10.1103/PhysRevLett.85.389>.
- [88] J. Hegarty, M. D. Sturge, C. Weisbuch, A. C. Gossard, and W. Wiegmann. Resonant Rayleigh Scattering from an Inhomogeneously Broadened Transition: A New Probe

- of the Homogeneous Linewidth. *Physical Review Letters*, 1982. ISSN 00319007. doi: 10.1103/PhysRevLett.49.930.
- [89] D Gammon, E S Snow, B V Shanabrook, D S Katzer, and D Park. Homogeneous Linewidths in the Optical Spectrum of a Single Gallium Arsenide Quantum Dot. *Science*, 273(5271):87 LP – 90, jul 1996. URL <http://science.sciencemag.org/content/273/5271/87.abstract>.
- [90] Paul A Dalgarno, Jason M Smith, Jamie McFarlane, Brian D Gerardot, Kahled Karrai, Antonio Badolato, Pierre M Petroff, and Richard J Warburton. Coulomb interactions in single charged self-assembled quantum dots: Radiative lifetime and recombination energy. *Physical Review B*, 77(24):245311, jun 2008. doi: 10.1103/PhysRevB.77.245311. URL <https://link.aps.org/doi/10.1103/PhysRevB.77.245311>.
- [91] M Bayer, S N Walck, T L Reinecke, and A Forchel. Exciton binding energies and diamagnetic shifts in semiconductor quantum wires and quantum dots. *Physical Review B*, 57(11):6584–6591, mar 1998. doi: 10.1103/PhysRevB.57.6584. URL <https://link.aps.org/doi/10.1103/PhysRevB.57.6584>.
- [92] S B Nam, D C Reynolds, C W Litton, R J Almassy, T C Collins, and C M Wolfe. Free-exciton energy spectrum in GaAs. *Physical Review B*, 13(2):761–767, jan 1976. doi: 10.1103/PhysRevB.13.761. URL <https://link.aps.org/doi/10.1103/PhysRevB.13.761>.
- [93] A Nick Vamivakas, Yong Zhao, Chao-Yang Lu, and Mete Atatüre. Spin-resolved quantum-dot resonance fluorescence. *Nature Physics*, 5:198, jan 2009. URL <https://doi.org/10.1038/nphys1182http://10.0.4.14/nphys1182https://www.nature.com/articles/nphys1182{#}supplementary-information>.
- [94] M Zieliński, Y Don, and D Gershoni. Atomistic theory of dark excitons in self-assembled quantum dots of reduced symmetry. *Physical Review B*, 91(8):85403, feb 2015. doi: 10.1103/PhysRevB.91.085403. URL <https://link.aps.org/doi/10.1103/PhysRevB.91.085403>.
- [95] Allan S Bracker, Daniel Gammon, and Vladimir L Korenev. Fine structure and optical pumping of spins in individual semiconductor quantum dots. *Semiconductor Science and Technology*, 23(11):114004, 2008. ISSN 0268-1242. doi: 10.1088/0268-1242/23/11/114004. URL <http://stacks.iop.org/0268-1242/23/i=11/a=114004>.

- [96] Kristiaan De Greve, Peter L McMahon, David Press, Thaddeus D Ladd, Dirk Bisping, Christian Schneider, Martin Kamp, Lukas Worschech, Sven Höfling, Alfred Forchel, and Yoshihisa Yamamoto. Ultrafast coherent control and suppressed nuclear feedback of a single quantum dot hole qubit. *Nature Physics*, 7:872, aug 2011. URL <https://doi.org/10.1038/nphys2078><http://10.0.4.14/nphys2078><https://www.nature.com/articles/nphys2078#supplementary-information>.
- [97] S Cortez, O Krebs, S Laurent, M Senes, X Marie, P Voisin, R Ferreira, G Bastard, J-M. Gérard, and T Amand. Optically Driven Spin Memory in n-Doped InAs-GaAs Quantum Dots. *Physical Review Letters*, 89(20):207401, oct 2002. doi: 10.1103/PhysRevLett.89.207401. URL <https://link.aps.org/doi/10.1103/PhysRevLett.89.207401>.
- [98] J J Finley, P W Fry, A D Ashmore, A Lemaître, A I Tartakovskii, R Oulton, D J Mowbray, M S Skolnick, M Hopkinson, P D Buckle, and P A Maksym. Observation of multicharged excitons and biexcitons in a single InGaAs quantum dot. *Physical Review B*, 63(16):161305, apr 2001. doi: 10.1103/PhysRevB.63.161305. URL <https://link.aps.org/doi/10.1103/PhysRevB.63.161305>.
- [99] D V Regelman, E Dekel, D Gershoni, E Ehrenfreund, A J Williamson, J Shumway, A Zunger, W V Schoenfeld, and P M Petroff. Optical spectroscopy of single quantum dots at tunable positive, neutral, and negative charge states. *Physical Review B*, 64(16):165301, sep 2001. doi: 10.1103/PhysRevB.64.165301. URL <https://link.aps.org/doi/10.1103/PhysRevB.64.165301>.
- [100] P W Fry, I E Itskevich, D J Mowbray, M S Skolnick, J J Finley, J A Barker, E P O'Reilly, L R Wilson, I A Larkin, P A Maksym, M Hopkinson, M Al-Khafaji, J P R David, A G Cullis, G Hill, and J C Clark. Inverted Electron-Hole Alignment in InAs-GaAs Self-Assembled Quantum Dots. *Physical Review Letters*, 84(4):733–736, jan 2000. doi: 10.1103/PhysRevLett.84.733. URL <https://link.aps.org/doi/10.1103/PhysRevLett.84.733>.
- [101] D A B Miller, D S Chemla, T C Damen, A C Gossard, W Wiegmann, T H Wood, and C A Burrus. Band-Edge Electroabsorption in Quantum Well Structures: The Quantum-Confined Stark Effect. *Phys. Rev. Lett.*, 53(22):2173–2176, nov 1984. doi: 10.1103/PhysRevLett.53.2173. URL <http://link.aps.org/doi/10.1103/PhysRevLett.53.2173>.
- [102] J J Finley, M Sabathil, P Vogl, G Abstreiter, R Oulton, A I Tartakovskii, D J Mowbray, M S Skolnick, S L Liew, A G Cullis, and M Hopkinson. Quantum-confined

- Stark shifts of charged exciton complexes in quantum dots. *Phys. Rev. B*, 70(20):201308, nov 2004. doi: 10.1103/PhysRevB.70.201308. URL <http://link.aps.org/doi/10.1103/PhysRevB.70.201308>.
- [103] Anthony J Bennett, Raj B Patel, Joanna Skiba-Szymanska, Christine A Nicoll, Ian Farrer, David A Ritchie, and Andrew J Shields. Giant Stark effect in the emission of single semiconductor quantum dots. *Applied Physics Letters*, 97(3):31104, jul 2010. ISSN 0003-6951. doi: 10.1063/1.3460912. URL <https://doi.org/10.1063/1.3460912>.
- [104] Raj B Patel, Anthony J Bennett, Ian Farrer, Christine A Nicoll, David A Ritchie, and Andrew J Shields. Two-photon interference of the emission from electrically tunable remote quantum dots. *Nature Photonics*, 4:632, jul 2010. URL <https://doi.org/10.1038/nphoton.2010.161><http://10.0.4.14/nphoton.2010.161><https://www.nature.com/articles/nphoton.2010.161#supplementary-information>.
- [105] A Laucht, F Hofbauer, N Hauke, J Angele, S Stobbe, M Kaniber, G Böhm, P Lodahl, M-C Amann, and J J Finley. Electrical control of spontaneous emission and strong coupling for a single quantum dot. *New Journal of Physics*, 11(2):23034, 2009. ISSN 1367-2630. doi: 10.1088/1367-2630/11/2/023034. URL <http://dx.doi.org/10.1088/1367-2630/11/2/023034>.
- [106] Andreas Muller, Wei Fang, John Lawall, and Glenn S Solomon. Creating Polarization-Entangled Photon Pairs from a Semiconductor Quantum Dot Using the Optical Stark Effect. *Physical Review Letters*, 103(21):217402, nov 2009. doi: 10.1103/PhysRevLett.103.217402. URL <https://link.aps.org/doi/10.1103/PhysRevLett.103.217402>.
- [107] M Bayer, O Stern, A Kuther, and A Forchel. Spectroscopic study of dark excitons in $\text{In}_x\text{Ga}_{1-x}\text{As}/\text{GaAs}$ self-assembled quantum dots by a magnetic-field-induced symmetry breaking. *Physical Review B*, 61(11):7273–7276, mar 2000. doi: 10.1103/PhysRevB.61.7273. URL <https://link.aps.org/doi/10.1103/PhysRevB.61.7273>.
- [108] A Kuther, M Bayer, A Forchel, A Gorbunov, V B Timofeev, F Schäfer, and J P Reithmaier. Zeeman splitting of excitons and biexcitons in single $\text{In}_{0.60}\text{Ga}_{0.40}\text{As}/\text{GaAs}$ self-assembled quantum dots. *Physical Review B*, 58(12):R7508–R7511, sep 1998. doi: 10.1103/PhysRevB.58.R7508. URL <https://link.aps.org/doi/10.1103/PhysRevB.58.R7508>.

- [109] T Nakaoka, T Saito, J Tatebayashi, and Y Arakawa. Size, shape, and strain dependence of the g factor in self-assembled In(Ga)As quantum dots. *Physical Review B*, 70(23):235337, dec 2004. doi: 10.1103/PhysRevB.70.235337. URL <https://link.aps.org/doi/10.1103/PhysRevB.70.235337>.
- [110] A Schwan, B.-M. Meiners, A Greilich, D R Yakovlev, M Bayer, A D B Maia, A A Quivy, and A B Henriques. Anisotropy of electron and hole g-factors in (In,Ga)As quantum dots. *Applied Physics Letters*, 99(22):221914, nov 2011. ISSN 0003-6951. doi: 10.1063/1.3665634. URL <https://doi.org/10.1063/1.3665634>.
- [111] Mete Atatüre, Jan Dreiser, Antonio Badolato, Alexander Högele, Khaled Karrai, and Atac Imamoglu. Quantum-Dot Spin-State Preparation with Near-Unity Fidelity. *Science*, 312(5773):551 LP – 553, apr 2006. doi: 10.1126/science.1126074. URL <http://science.sciencemag.org/content/312/5773/551.abstract>.
- [112] W. A. Coish and J. Baugh. Nuclear spins in nanostructures. *Physica Status Solidi (B)*, 246(10):2203–2215, 2009. ISSN 03701972. doi: 10.1002/pssb.200945229. URL <http://doi.wiley.com/10.1002/pssb.200945229>.
- [113] A. Abragam. *The Principles of Nuclear Magnetism*. Comparative Pathobiology - Studies in the Postmodern Theory of Education. Oxford University Press, Oxford, 1961. ISBN 9780198520146.
- [114] Charles Slichter. *Principles of magnetic resonance*. Springer-Verlag, 1989. doi: <https://doi.org/10.1007/BF00714632>.
- [115] D. Gammon, Al. L. Efros, T. A. Kennedy, M. Rosen, D. S. Katzer, D. Park, S. W. Brown, V. L. Korenev, and I. A. Merkulov. Electron and Nuclear Spin Interactions in the Optical Spectra of Single GaAs Quantum Dots. *Physical Review Letters*, 86(22):5176–5179, 2001. ISSN 0031-9007. doi: 10.1103/PhysRevLett.86.5176. URL <https://link.aps.org/doi/10.1103/PhysRevLett.86.5176>.
- [116] Albert W Overhauser. Polarization of Nuclei in Metals. *Physical Review*, 92(2):411–415, oct 1953. doi: 10.1103/PhysRev.92.411. URL <https://link.aps.org/doi/10.1103/PhysRev.92.411>.
- [117] W D Knight. Nuclear Magnetic Resonance Shift in Metals. *Physical Review*, 76(8):1259–1260, oct 1949. doi: 10.1103/PhysRev.76.1259.2. URL <https://link.aps.org/doi/10.1103/PhysRev.76.1259.2>.

- [118] P.-F. Braun, X Marie, L Lombez, B Urbaszek, T Amand, P Renucci, V K Kalevich, K V Kavokin, O Krebs, P Voisin, and Y Masumoto. Direct Observation of the Electron Spin Relaxation Induced by Nuclei in Quantum Dots. *Physical Review Letters*, 94(11):116601, mar 2005. doi: 10.1103/PhysRevLett.94.116601. URL <https://link.aps.org/doi/10.1103/PhysRevLett.94.116601>.
- [119] M Gueron. Density of the Conduction Electrons at the Nuclei in Indium Antimonide. *Physical Review*, 135(1A):A200–A205, jul 1964. doi: 10.1103/PhysRev.135.A200. URL <https://link.aps.org/doi/10.1103/PhysRev.135.A200>.
- [120] D Paget, G Lampel, B Sapoval, and V I Safarov. Low field electron-nuclear spin coupling in gallium arsenide under optical pumping conditions. *Physical Review B*, 15(12):5780–5796, jun 1977. doi: 10.1103/PhysRevB.15.5780. URL <https://link.aps.org/doi/10.1103/PhysRevB.15.5780>.
- [121] P Fallahi, S T Yilmaz, and A Imamoğlu. Measurement of a Heavy-Hole Hyperfine Interaction in InGaAs Quantum Dots Using Resonance Fluorescence. *Physical Review Letters*, 105(25):257402, dec 2010. doi: 10.1103/PhysRevLett.105.257402. URL <https://link.aps.org/doi/10.1103/PhysRevLett.105.257402>.
- [122] E A Chekhovich, A B Krysa, M S Skolnick, and A I Tartakovskii. Direct Measurement of the Hole-Nuclear Spin Interaction in Single InP/GaInP Quantum Dots Using Photoluminescence Spectroscopy. *Physical Review Letters*, 106(2):27402, jan 2011. doi: 10.1103/PhysRevLett.106.027402. URL <https://link.aps.org/doi/10.1103/PhysRevLett.106.027402>.
- [123] R G Shulman, B J Wyluda, and P W Anderson. Nuclear Magnetic Resonance in Semiconductors. II. Quadrupole Broadening of Nuclear Magnetic Resonance Lines by Elastic Axial Deformation. *Phys. Rev.*, 107(4):953–958, aug 1957. doi: 10.1103/PhysRev.107.953.
- [124] Ceyhun Bulutay. Quadrupolar spectra of nuclear spins in strained $\text{In}_x\text{Ga}_{1-x}\text{As}/\text{GaAs}$ quantum dots. *Physical Review B - Condensed Matter and Materials Physics*, 85(11):1–12, 2012. ISSN 10980121. doi: 10.1103/PhysRevB.85.115313.
- [125] R K Sundfors. Experimental gradient-elastic tensors and chemical bonding in III-V semiconductors. *Phys. Rev. B*, 10(10):4244–4252, nov 1974. doi: 10.1103/PhysRevB.10.4244.

- [126] Ceyhun Bulutay, E A Chekhovich, and A I Tartakovskii. Nuclear magnetic resonance inverse spectra of InGaAs quantum dots: Atomistic level structural information. *Phys. Rev. B*, 90(20):205425, nov 2014. doi: 10.1103/PhysRevB.90.205425.
- [127] R. V. Pound. Nuclear Electric Quadrupole Interactions in Crystals. *Phys. Rev.*, 79(4):685–702, aug 1950. doi: 10.1103/PhysRev.79.685. URL <https://link.aps.org/doi/10.1103/PhysRev.79.685>.
- [128] M. H. Cohen and F. Reif. Quadrupole Effects in Nuclear Magnetic Resonance Studies of Solids. *Solid State Physics*, 5:321–438, jan 1957. ISSN 0081-1947. doi: 10.1016/S0081-1947(08)60105-8.
- [129] T. P. Das and E. L. Hahn. *Nuclear quadrupole resonance spectroscopy*. Solid state physics. Supplement. Academic Press, 1958.
- [130] P. Maletinsky, M. Kroner, and A. Imamoglu. Breakdown of the nuclear-spin-temperature approach in quantum-dot demagnetization experiments. *Nature Physics*, 5(6):407–411, 2009. ISSN 17452473. doi: 10.1038/nphys1273.
- [131] C W Lai, P Maletinsky, A Badolato, and A Imamoglu. Knight-Field-Enabled Nuclear Spin Polarization in Single Quantum Dots. *Physical Review Letters*, 96(16):167403, apr 2006. doi: 10.1103/PhysRevLett.96.167403. URL <https://link.aps.org/doi/10.1103/PhysRevLett.96.167403>.
- [132] M S Kuznetsova, K Flisinski, I Ya. Gerlovin, I V Ignatiev, K V Kavokin, S Yu. Verbin, D R Yakovlev, D Reuter, A D Wieck, and M Bayer. Hanle effect in (In,Ga)As quantum dots: Role of nuclear spin fluctuations. *Physical Review B*, 87(23):235320, jun 2013. doi: 10.1103/PhysRevB.87.235320. URL <https://link.aps.org/doi/10.1103/PhysRevB.87.235320>.
- [133] F Klotz, V Jovanov, J Kierig, E C Clark, M Bichler, G Abstreiter, M S Brandt, J J Finley, H Schwager, and G Giedke. Asymmetric optical nuclear spin pumping in a single uncharged quantum dot. *Physical Review B*, 82(12):121307, sep 2010. doi: 10.1103/PhysRevB.82.121307. URL <https://link.aps.org/doi/10.1103/PhysRevB.82.121307>.
- [134] J. Puebla, E. A. Chekhovich, M. Hopkinson, P. Senellart, A. Lemaitre, M. S. Skolnick, and A. I. Tartakovskii. Dynamic nuclear polarization in InGaAs/GaAs and GaAs/AlGaAs quantum dots under nonresonant ultralow-power optical excitation. *Physical Review B - Condensed Matter and Materials Physics*, 88(4):1–9, 2013. ISSN 10980121. doi: 10.1103/PhysRevB.88.045306.

- [135] E. A. Chekhovich, M. N. Makhonin, J. Skiba-Szymanska, A. B. Krysa, V. D. Kulakovskii, M. S. Skolnick, and A. I. Tartakovskii. Dynamics of optically induced nuclear spin polarization in individual InP/GaInP quantum dots. *Physical Review B - Condensed Matter and Materials Physics*, 81(24), 2010. ISSN 10980121. doi: 10.1103/PhysRevB.81.245308.
- [136] P Maletinsky, A Badolato, and A Imamoglu. Dynamics of Quantum Dot Nuclear Spin Polarization Controlled by a Single Electron. *Physical Review Letters*, 99(5): 56804, aug 2007. doi: 10.1103/PhysRevLett.99.056804. URL <https://link.aps.org/doi/10.1103/PhysRevLett.99.056804>.
- [137] P Maletinsky, C W Lai, A Badolato, and A Imamoglu. Nonlinear dynamics of quantum dot nuclear spins. *Physical Review B*, 75(3):35409, jan 2007. doi: 10.1103/PhysRevB.75.035409. URL <https://link.aps.org/doi/10.1103/PhysRevB.75.035409>.
- [138] C Latta, A Högele, Y Zhao, A N Vamivakas, P Maletinsky, M Kroner, J Dreiser, I Carusotto, A Badolato, D Schuh, W Wegscheider, M Atature, and A Imamoglu. Confluence of resonant laser excitation and bidirectional quantum-dot nuclear-spin polarization. *Nature Physics*, 5:758, aug 2009. URL <https://doi.org/10.1038/nphys1363><http://10.0.4.14/nphys1363><https://www.nature.com/articles/nphys1363#supplementary-information>.
- [139] O.; Stern and W.; Gerlach. The experimental proof of the directional quantization in the magnetic field. *Zeitschrift für Physik*, 9, 1922. doi: <https://doi.org/10.1007/BF01326983>.
- [140] I I Rabi, J R Zacharias, S Millman, and P Kusch. A New Method of Measuring Nuclear Magnetic Moment. *Physical Review*, 53(4):318, feb 1938. doi: 10.1103/PhysRev.53.318. URL <https://link.aps.org/doi/10.1103/PhysRev.53.318>.
- [141] F Bloch, W W Hansen, and Martin Packard. Nuclear Induction. *Physical Review*, 69(3-4):127, feb 1946. doi: 10.1103/PhysRev.69.127. URL <https://link.aps.org/doi/10.1103/PhysRev.69.127>.
- [142] E M Purcell, H C Torrey, and R V Pound. Resonance Absorption by Nuclear Magnetic Moments in a Solid. *Physical Review*, 69(1-2):37–38, jan 1946. doi: 10.1103/PhysRev.69.37. URL <https://link.aps.org/doi/10.1103/PhysRev.69.37>.

- [143] Brian Cowan. *Nuclear Magnetic Resonance and Relaxation*. Cambridge University Press, 1997. ISBN 9780511524226. URL <http://dx.doi.org/10.1017/CB09780511524226>.
- [144] A J Ramsay. A review of the coherent optical control of the exciton and spin states of semiconductor quantum dots. *Semiconductor Science and Technology*, 25(10):103001, 2010. ISSN 0268-1242. doi: 10.1088/0268-1242/25/10/103001. URL <http://dx.doi.org/10.1088/0268-1242/25/10/103001>.
- [145] John A McNeil and W Gilbert Clark. Nuclear quadrupolar spin-lattice relaxation in some III-V compounds. *Physical Review B*, 13(11):4705–4713, jun 1976. doi: 10.1103/PhysRevB.13.4705. URL <https://link.aps.org/doi/10.1103/PhysRevB.13.4705>.
- [146] E. A. Chekhovich, K. V. Kavokin, J. Puebla, A. B. Krysa, M. Hopkinson, A. D. Andreev, A. M. Sanchez, R. Beanland, M. S. Skolnick, and A. I. Tartakovskii. Structural analysis of strained quantum dots using nuclear magnetic resonance. *Nature Nanotechnology*, 7(10):646–650, 2012. ISSN 1748-3387. doi: 10.1038/nnano.2012.142. URL <http://dx.doi.org/10.1038/nnano.2012.142>.
- [147] E A Chekhovich, M Hopkinson, M S Skolnick, and A I Tartakovskii. Suppression of nuclear spin bath fluctuations in self-assembled quantum dots induced by inhomogeneous strain. *Nat Commun*, 6, feb 2015. URL <http://dx.doi.org/10.1038/ncomms7348>.
- [148] Miro Kroutvar, Yann Ducommun, Dominik Heiss, Max Bichler, Dieter Schuh, Gerhard Abstreiter, and Jonathan J Finley. Optically programmable electron spin memory using semiconductor quantum dots. *Nature*, 432(7013):81–84, 2004. ISSN 1476-4687. doi: 10.1038/nature03008. URL <https://doi.org/10.1038/nature03008>.
- [149] M V Gurudev Dutt, Jun Cheng, Bo Li, Xiaodong Xu, Xiaoqin Li, P R Berman, D G Steel, A S Bracker, D Gammon, Sophia E Economou, Ren-Bao Liu, and L J Sham. Stimulated and Spontaneous Optical Generation of Electron Spin Coherence in Charged GaAs Quantum Dots. *Physical Review Letters*, 94(22):227403, jun 2005. doi: 10.1103/PhysRevLett.94.227403. URL <https://link.aps.org/doi/10.1103/PhysRevLett.94.227403>.
- [150] J R Petta, A C Johnson, J M Taylor, E A Laird, A Yacoby, M D Lukin, C M Marcus, M P Hanson, and A C Gossard. Coherent Manipulation of Coupled Electron Spins in Semiconductor Quantum Dots. *Science*, 309(5744):2180 LP – 2184, sep 2005.

- doi: 10.1126/science.1116955. URL <http://science.sciencemag.org/content/309/5744/2180.abstract>.
- [151] David Press, Kristiaan De Greve, Peter L McMahon, Thaddeus D Ladd, Benedikt Friess, Christian Schneider, Martin Kamp, Sven Höfling, Alfred Forchel, and Yoshihisa Yamamoto. Ultrafast optical spin echo in a single quantum dot. *Nature Photonics*, 4:367, apr 2010. URL <https://doi.org/10.1038/nphoton.2010.83><http://10.0.4.14/nphoton.2010.83>.
- [152] Alexander Bechtold, Dominik Rauch, Fuxiang Li, Tobias Simmet, Per-Lennart Ardel, Armin Regler, Kai Müller, Nikolai A Sinitsyn, and Jonathan J Finley. Three-stage decoherence dynamics of an electron spin qubit in an optically active quantum dot. *Nature Physics*, 11(12):1005–1008, 2015. ISSN 1745-2473. doi: 10.1038/nphys3470. URL <http://www.nature.com/doifinder/10.1038/nphys3470>.
- [153] Brian D Gerardot, Daniel Brunner, Paul A Dalgarno, Patrik Öhberg, Stefan Seidl, Martin Kroner, Khaled Karrai, Nick G Stoltz, Pierre M Petroff, and Richard J Warburton. Optical pumping of a single hole spin in a quantum dot. *Nature*, 451:441, jan 2008. URL <https://doi.org/10.1038/nature06472><http://10.0.4.14/nature06472><https://www.nature.com/articles/nature06472#supplementary-information>.
- [154] D Heiss, S Schaeck, H Huebl, M Bichler, G Abstreiter, J J Finley, D V Bulaev, and Daniel Loss. Observation of extremely slow hole spin relaxation in self-assembled quantum dots. *Physical Review B*, 76(24):241306, dec 2007. doi: 10.1103/PhysRevB.76.241306. URL <https://link.aps.org/doi/10.1103/PhysRevB.76.241306>.
- [155] S G Carter, Sophia E Economou, A Greilich, Edwin Barnes, T Sweeney, A S Bracker, and D Gammon. Strong hyperfine-induced modulation of an optically driven hole spin in an InAs quantum dot. *Physical Review B*, 89(7):75316, feb 2014. doi: 10.1103/PhysRevB.89.075316. URL <https://link.aps.org/doi/10.1103/PhysRevB.89.075316>.
- [156] E A Chekhovich, M M Glazov, A B Krysa, M Hopkinson, P Senellart, A Lemaître, M S Skolnick, and A I Tartakovskii. Element-sensitive measurement of the hole–nuclear spin interaction in quantum dots. *Nature Physics*, 9:74, dec 2012. URL <https://doi.org/10.1038/nphys2514><http://10.0.4.14/nphys2514><https://www.nature.com/articles/nphys2514#supplementary-information>.

- [157] Z R Wasilewski, S Fafard, and J P McCaffrey. Size and shape engineering of vertically stacked self-assembled quantum dots. *Journal of Crystal Growth*, 201-202:1131–1135, 1999. ISSN 0022-0248. doi: [https://doi.org/10.1016/S0022-0248\(98\)01539-5](https://doi.org/10.1016/S0022-0248(98)01539-5). URL <http://www.sciencedirect.com/science/article/pii/S0022024898015395>.
- [158] J P McCaffrey, M D Robertson, S Fafard, Z R Wasilewski, E M Griswold, and L D Madsen. Determination of the size, shape, and composition of indium-flashed self-assembled quantum dots by transmission electron microscopy. *Journal of Applied Physics*, 88(5):2272–2277, aug 2000. ISSN 0021-8979. doi: 10.1063/1.1287226. URL <https://doi.org/10.1063/1.1287226>.
- [159] Georges Lampel. Nuclear Dynamic Polarization by Optical Electronic Saturation and Optical Pumping in Semiconductors. *Physical Review Letters*, 20(10):491–493, mar 1968. doi: 10.1103/PhysRevLett.20.491. URL <https://link.aps.org/doi/10.1103/PhysRevLett.20.491>.
- [160] M. Krapf, G. Denninger, H. Pascher, G. Weimann, and W. Schlapp. Optically detected nuclear magnetic resonance and Knight shift in $\text{Al}_x\text{Ga}_{1-x}\text{As}/\text{GaAs}$ heterostructures. *Solid State Communications*, 1991. ISSN 00381098. doi: 10.1016/0038-1098(91)90704-Y.
- [161] J. A. Marohn, P. J. Carson, J. Y. Hwang, M. A. Miller, D. N. Shykind, and D. P. Weitekamp. Optical larmor beat detection of high-resolution nuclear magnetic resonance in a semiconductor heterostructure. *Phys. Rev. Lett.*, 75:1364–1367, Aug 1995. doi: 10.1103/PhysRevLett.75.1364. URL <https://link.aps.org/doi/10.1103/PhysRevLett.75.1364>.
- [162] G. Kamp, H. Obloh, J. Schneider, G. Weimann, and K. Ploog. Overhauser shift and nuclear spin relaxation in $\text{Al}_x\text{Ga}_{1-x}\text{As}/\text{GaAs}$ heterostructures. *Semiconductor Science and Technology*, 1992. ISSN 02681242. doi: 10.1088/0268-1242/7/4/017.
- [163] M. N. Makhonin, E. A. Chekhovich, P. Senellart, A. Lemaître, M. S. Skolnick, and A. I. Tartakovskii. Optically tunable nuclear magnetic resonance in a single quantum dot. *Physical Review B*, 82(16):161309, 2010. ISSN 1098-0121. doi: 10.1103/PhysRevB.82.161309. URL <http://link.aps.org/doi/10.1103/PhysRevB.82.161309>.
- [164] Jarryd J Pla, Kuan Y Tan, Juan P Dehollain, Wee H Lim, John J L Morton, David N Jamieson, Andrew S Dzurak, and Andrea Morello. A single-atom electron spin qubit in silicon. *Nature*, 489:541, sep 2012. URL

- <https://doi.org/10.1038/nature11449><http://10.0.4.14/nature11449><https://www.nature.com/articles/nature11449#supplementary-information>.
- [165] L Childress, M V Gurudev Dutt, J M Taylor, A S Zibrov, F Jelezko, J Wrachtrup, P R Hemmer, and M D Lukin. Coherent Dynamics of Coupled Electron and Nuclear Spin Qubits in Diamond. *Science*, 314(5797):281 LP – 285, oct 2006. doi: 10.1126/science.1131871. URL <http://science.sciencemag.org/content/314/5797/281.abstract>.
- [166] I. A. Akimov, D. H. Feng, and F. Henneberger. Electron spin dynamics in a self-assembled semiconductor quantum dot: The limit of low magnetic fields. *Physical Review Letters*, 97(5), 2006. ISSN 00319007. doi: 10.1103/PhysRevLett.97.056602.
- [167] D H Feng, I A Akimov, and F Henneberger. Nonequilibrium Nuclear-Electron Spin Dynamics in Semiconductor Quantum Dots. *Physical Review Letters*, 99(3):36604, jul 2007. doi: 10.1103/PhysRevLett.99.036604. URL <https://link.aps.org/doi/10.1103/PhysRevLett.99.036604>.
- [168] Jungtaek Kim, J Puls, Y S Chen, G Bacher, and F Henneberger. Electron-nuclear spin control in charged semiconductor quantum dots by electrical currents through micro-coils. *Applied Physics Letters*, 96(15):151908, apr 2010. ISSN 0003-6951. doi: 10.1063/1.3373591. URL <https://doi.org/10.1063/1.3373591>.
- [169] C. Le Gall, A Brunetti, H Boukari, and L Besombes. Electron-nuclei spin dynamics in II-VI semiconductor quantum dots. *Physical Review B*, 85(19):195312, 2012. ISSN 1098-0121. doi: 10.1103/PhysRevB.85.195312. URL <http://link.aps.org/doi/10.1103/PhysRevB.85.195312>.
- [170] F. Tinjod, B. Gilles, S. Moehl, K. Kheng, and H. Mariette. II-VI quantum dot formation induced by surface energy change of a strained layer. *Applied Physics Letters*, 82(24):4340–4342, 2003. ISSN 00036951. doi: 10.1063/1.1583141.
- [171] Sean A Blanton, Margaret A Hines, and Philippe Guyot-Sionnest. Photoluminescence wandering in single CdSe nanocrystals. *Applied Physics Letters*, 69(25):3905–3907, dec 1996. ISSN 0003-6951. doi: 10.1063/1.117565. URL <https://doi.org/10.1063/1.117565>.
- [172] J Suffczyński, T Kazimierzuk, M Goryca, B Piechal, A Trajnerowicz, K Kowalik, P Kossacki, A Golnik, K P Korona, M Nawrocki, J A Gaj, and G Karczewski. Excitation mechanisms of individual CdTe/ZnTe quantum dots studied by photon correlation spectroscopy. *Physical Review B*, 74(8):85319, aug 2006. doi: 10.1103/

- PhysRevB.74.085319. URL <https://link.aps.org/doi/10.1103/PhysRevB.74.085319>.
- [173] E A Chekhovich, A B Krysa, M S Skolnick, and A I Tartakovskii. Light-polarization-independent nuclear spin alignment in a quantum dot. *Physical Review B*, 83(12):125318, mar 2011. doi: 10.1103/PhysRevB.83.125318. URL <https://link.aps.org/doi/10.1103/PhysRevB.83.125318>.
- [174] T Smoleński, T Kazimierzczuk, M Goryca, T Jakubczyk, Ł Kłopotowski, Ł Cywiński, P Wojnar, A Golnik, and P Kossacki. In-plane radiative recombination channel of a dark exciton in self-assembled quantum dots. *Physical Review B*, 86(24):241305, dec 2012. doi: 10.1103/PhysRevB.86.241305. URL <https://link.aps.org/doi/10.1103/PhysRevB.86.241305>.
- [175] A Nakamura, D Paget, C Hermann, C Weisbuch, G Lampel, and B C Cavenett. Optical detection of electron spin resonance in CdTe. *Solid State Communications*, 30(7):411–414, 1979. ISSN 0038-1098. doi: [https://doi.org/10.1016/0038-1098\(79\)91177-3](https://doi.org/10.1016/0038-1098(79)91177-3). URL <http://www.sciencedirect.com/science/article/pii/0038109879911773>.
- [176] G Schmieder, W Maier, Liu Pu-Lin, and C Klingshirn. The magnetic field behavior of the neutral donor bound excitons in ZnTe. *Journal of Luminescence*, 28(4):357–365, 1983. ISSN 0022-2313. doi: [https://doi.org/10.1016/0022-2313\(83\)90004-2](https://doi.org/10.1016/0022-2313(83)90004-2). URL <http://www.sciencedirect.com/science/article/pii/0022231383900042>.
- [177] Y Léger, L Besombes, L Maingault, and H Mariette. Valence-band mixing in neutral, charged, and Mn-doped self-assembled quantum dots. *Physical Review B*, 76(4):45331, jul 2007. doi: 10.1103/PhysRevB.76.045331. URL <https://link.aps.org/doi/10.1103/PhysRevB.76.045331>.
- [178] E A Chekhovich, I M Griffiths, M S Skolnick, H Huang, S F Covre da Silva, X Yuan, and A Rastelli. Cross calibration of deformation potentials and gradient-elastic tensors of GaAs using photoluminescence and nuclear magnetic resonance spectroscopy in GaAs/AlGaAs quantum dot structures. *Physical Review B*, 97(23):235311, jun 2018. doi: 10.1103/PhysRevB.97.235311. URL <https://link.aps.org/doi/10.1103/PhysRevB.97.235311>.
- [179] A Ulhaq, Q Duan, E Zallo, F Ding, O G Schmidt, A I Tartakovskii, M S Skolnick, and E A Chekhovich. Vanishing electron g factor and long-lived nuclear spin

- polarization in weakly strained nanohole-filled GaAs/AlGaAs quantum dots. *Physical Review B*, 93(16):165306, apr 2016. doi: 10.1103/PhysRevB.93.165306. URL <https://link.aps.org/doi/10.1103/PhysRevB.93.165306>.
- [180] B Urbaszek, P.-F. Braun, T Amand, O Krebs, T Belhadj, A Lemaître, P Voisin, and X Marie. Efficient dynamical nuclear polarization in quantum dots: Temperature dependence. *Physical Review B*, 76(20):201301, nov 2007. doi: 10.1103/PhysRevB.76.201301. URL <https://link.aps.org/doi/10.1103/PhysRevB.76.201301>.
- [181] A E Nikolaenko, E A Chekhovich, M N Makhonin, I W Drouzas, A B Van'kov, J Skiba-Szymanska, M S Skolnick, P Senellart, D Martrou, A Lemaître, and A I Tartakovskii. Suppression of nuclear spin diffusion at a GaAs/Al_xGa_{1-x}As interface measured with a single quantum-dot nanoprobe. *Physical Review B*, 79(8):81303, feb 2009. doi: 10.1103/PhysRevB.79.081303. URL <https://link.aps.org/doi/10.1103/PhysRevB.79.081303>.
- [182] Thomas Belhadj, Takashi Kuroda, Claire-Marie Simon, Thierry Amand, Takaaki Mano, Kazuaki Sakoda, Nobuyuki Koguchi, Xavier Marie, and Bernhard Urbaszek. Optically monitored nuclear spin dynamics in individual GaAs quantum dots grown by droplet epitaxy. *Physical Review B*, 78(20):205325, nov 2008. doi: 10.1103/PhysRevB.78.205325. URL <https://link.aps.org/doi/10.1103/PhysRevB.78.205325>.
- [183] G Ragunathan, J Kobak, G Gillard, W Pacuski, K Sobczak, J Borysiuk, M. S. Skolnick, and E. A. Chekhovich. Direct Measurement of Hyperfine Shifts and Radio Frequency Manipulation of Nuclear Spins in Individual CdTe/ZnTe Quantum Dots. *Physical Review Letters*, 122(9):96801, mar 2019. doi: 10.1103/PhysRevLett.122.096801. URL <https://link.aps.org/doi/10.1103/PhysRevLett.122.096801>.
- [184] Ichiro Tanaka, Itaru Kamiya, H Sakaki, Naser Qureshi, S. J. Allen, and P. M. Petroff. Imaging and probing electronic properties of self-assembled InAs quantum dots by atomic force microscopy with conductive tip. *Applied Physics Letters*, 74(6):844–846, feb 1999. ISSN 0003-6951. doi: 10.1063/1.123402. URL <http://aip.scitation.org/doi/10.1063/1.123402>.
- [185] P S Sokolov, M Yu. Petrov, T Mehtens, K Müller-Caspary, A Rosenauer, D Reuter, and A D Wieck. Reconstruction of nuclear quadrupole interaction in (In,Ga)As/GaAs quantum dots observed by transmission electron microscopy. *Physical Review B*, 93(4):45301, jan 2016. doi: 10.1103/PhysRevB.93.045301. URL <https://link.aps.org/doi/10.1103/PhysRevB.93.045301>.

- [186] Paulus J Knijn, P Jan M van Bentum, Ernst R H van Eck, Changming Fang, Dennis L A G Grimminck, Robert A de Groot, Remco W A Havenith, Martijn Marsman, W Leo Meerts, Gilles A de Wijs, and Arno P M Kentgens. A solid-state NMR and DFT study of compositional modulations in $\text{Al}_x\text{Ga}_{1-x}\text{As}$. *Physical Chemistry Chemical Physics*, 12(37):11517–11535, 2010. ISSN 1463-9076. doi: 10.1039/C003624B. URL <http://dx.doi.org/10.1039/C003624B>.
- [187] A D Andreev, J R Downes, D A Faux, and E P O'Reilly. Strain distributions in quantum dots of arbitrary shape. *Journal of Applied Physics*, 86(1):297–305, jun 1999. ISSN 0021-8979. doi: 10.1063/1.370728. URL <https://doi.org/10.1063/1.370728>.
- [188] Richard Beanland, A Sanchez, Juan Hernandez-Garrido, Daniel Wolf, and P A MIDGLEY. Electron tomography of III-V quantum dots using dark field 002 imaging conditions. *Journal of Microscopy*, 237:148–154, feb 2010. doi: 10.1111/j.1365-2818.2009.03318.x.
- [189] A Wahra, C H Tan, J Xie, P Vines, and R Beanland. Three-dimensional measurement of composition changes in InAs/GaAs quantum dots. *Journal of Physics: Conference Series*, 326:12048, 2011. ISSN 1742-6596. doi: 10.1088/1742-6596/326/1/012048. URL <http://dx.doi.org/10.1088/1742-6596/326/1/012048>.
- [190] D Gerthsen, H Blank, D Litvinov, R Schneider, A Rosenauer, T Passow, A Grau, P Feinäugle, H Kalt, C Klingshirn, and M Hetterich. On the incorporation of indium in InAs-based quantum structures. *Journal of Physics: Conference Series*, 209:12006, 2010. ISSN 1742-6596. doi: 10.1088/1742-6596/209/1/012006. URL <http://dx.doi.org/10.1088/1742-6596/209/1/012006>.
- [191] Thorsten Mehrtens, Knut Müller, Marco Schowalter, Dongzhi Hu, Daniel M Schaadt, and Andreas Rosenauer. Measurement of indium concentration profiles and segregation efficiencies from high-angle annular dark field-scanning transmission electron microscopy images. *Ultramicroscopy*, 131:1–9, 2013. ISSN 0304-3991. doi: <https://doi.org/10.1016/j.ultramic.2013.03.018>. URL <http://www.sciencedirect.com/science/article/pii/S0304399113000880>.
- [192] Andreas Rosenauer, Katharina Gries, Knut Müller, Angelika Pretorius, Marco Schowalter, Adrian Avramescu, Karl Engl, and Stephan Lutgen. Measurement of specimen thickness and composition in AlGaIn/GaN using high-angle annular dark field images. *Ultramicroscopy*, 109(9):1171–1182, 2009. ISSN 0304-3991. doi:

- <https://doi.org/10.1016/j.ultramic.2009.05.003>. URL <http://www.sciencedirect.com/science/article/pii/S030439910900117X>.
- [193] V Grillo, E Carlino, and F Glas. Influence of the static atomic displacement on atomic resolution Z-contrast imaging. *Physical Review B*, 77(5):54103, feb 2008. doi: 10.1103/PhysRevB.77.054103. URL <https://link.aps.org/doi/10.1103/PhysRevB.77.054103>.
- [194] Gunter Wüst, Mathieu Munsch, Franziska Maier, Andreas V. Kuhlmann, Arne Ludwig, Andreas D. Wieck, Daniel Loss, Martino Poggio, and Richard J. Warburton. Role of the electron spin in determining the coherence of the nuclear spins in a quantum dot. *Nature Nanotechnology*, 11(July):1–6, 2016. ISSN 1748-3387. doi: 10.1038/nnano.2016.114. URL <http://dx.doi.org/10.1038/nnano.2016.114>.
- [195] E L Hahn. Spin Echoes. *Physical Review*, 80(4):580–594, nov 1950. doi: 10.1103/PhysRev.80.580. URL <https://link.aps.org/doi/10.1103/PhysRev.80.580>.
- [196] N Bar-Gill, L M Pham, C Belthangady, D Le Sage, P Cappellaro, J R Maze, M D Lukin, A Yacoby, and R Walsworth. Suppression of spin-bath dynamics for improved coherence of multi-spin-qubit systems. *Nature Communications*, 3:858, may 2012. URL <https://doi.org/10.1038/ncomms1856><http://10.0.4.14/ncomms1856><https://www.nature.com/articles/ncomms1856#supplementary-information>.
- [197] Michael J Biercuk, Hermann Uys, Aaron P VanDevender, Nobuyasu Shiga, Wayne M Itano, and John J Bollinger. Optimized dynamical decoupling in a model quantum memory. *Nature*, 458:996, apr 2009. URL <https://doi.org/10.1038/nature07951><http://10.0.4.14/nature07951><https://www.nature.com/articles/nature07951#supplementary-information>.
- [198] María Belén Franzoni and Patricia R Levstein. Manifestations of the absence of spin diffusion in multipulse NMR experiments on diluted dipolar solids. *Physical Review B*, 72(23):235410, dec 2005. doi: 10.1103/PhysRevB.72.235410. URL <https://link.aps.org/doi/10.1103/PhysRevB.72.235410>.
- [199] Clark D Ridge, Lauren F O’Donnell, and Jamie D Walls. Long-lived selective spin echoes in dipolar solids under periodic and aperiodic pi-pulse trains. *Physical Review B*, 89(2):24404, jan 2014. doi: 10.1103/PhysRevB.89.024404. URL <https://link.aps.org/doi/10.1103/PhysRevB.89.024404>.

- [200] Dale Li, Yanqun Dong, R G Ramos, J D Murray, K MacLean, A E Dementyev, and S E Barrett. Intrinsic origin of spin echoes in dipolar solids generated by strong pi pulses. *Physical Review B*, 77(21):214306, jun 2008. doi: 10.1103/PhysRevB.77.214306. URL <https://link.aps.org/doi/10.1103/PhysRevB.77.214306>.
- [201] J. N. Eckstein, A. I. Ferguson, and T. W. Hänsch. High-resolution two-photon spectroscopy with picosecond light pulses. *Physical Review Letters*, 40(13):847–850, 1978. ISSN 00319007. doi: 10.1103/PhysRevLett.40.847.
- [202] Th. Udem, R Holzwarth, and T W Hänsch. Optical frequency metrology. *Nature*, 416(6877):233–237, 2002. ISSN 1476-4687. doi: 10.1038/416233a. URL <https://doi.org/10.1038/416233a>.
- [203] A M Waeber, G Gillard, G Ragunathan, M Hopkinson, P Spencer, D A Ritchie, M S Skolnick, and E A Chekhovich. Pulse control protocols for preserving coherence in dipolar-coupled nuclear spin baths. *Nature Communications*, 10(1):3157, 2019. ISSN 2041-1723. doi: 10.1038/s41467-019-11160-6. URL <https://doi.org/10.1038/s41467-019-11160-6>.
- [204] C.-Y. Lu, Y Zhao, A N Vamivakas, C Matthiesen, S Fält, A Badolato, and M Atatüre. Direct measurement of spin dynamics in InAs/GaAs quantum dots using time-resolved resonance fluorescence. *Physical Review B*, 81(3):35332, jan 2010. doi: 10.1103/PhysRevB.81.035332. URL <https://link.aps.org/doi/10.1103/PhysRevB.81.035332>.
- [205] Gonzalo A Álvarez, Ashok Ajoy, Xinhua Peng, and Dieter Suter. Performance comparison of dynamical decoupling sequences for a qubit in a rapidly fluctuating spin bath. *Physical Review A*, 82(4):42306, oct 2010. doi: 10.1103/PhysRevA.82.042306. URL <https://link.aps.org/doi/10.1103/PhysRevA.82.042306>.
- [206] Alexei M Tyryshkin, Shinichi Tojo, John J L Morton, Helge Riemann, Nikolai V Abrosimov, Peter Becker, Hans-Joachim Pohl, Thomas Schenkel, Michael L W Thewalt, Kohei M Itoh, and S A Lyon. Electron spin coherence exceeding seconds in high-purity silicon. *Nature Materials*, 11:143, dec 2011. URL <https://doi.org/10.1038/nmat3182><http://10.0.4.14/nmat3182><https://www.nature.com/articles/nmat3182#supplementary-information>.
- [207] J S Waugh, L M Huber, and U Haeberlen. Approach to High-Resolution nmr in Solids. *Physical Review Letters*, 20(5):180–182, jan 1968. doi: 10.1103/PhysRevLett.20.180. URL <https://link.aps.org/doi/10.1103/PhysRevLett.20.180>.

- [208] J Houel, A V Kuhlmann, L Greuter, F Xue, M Poggio, B D Gerardot, P A Dalgarno, A Badolato, P M Petroff, A Ludwig, D Reuter, A D Wieck, and R J Warburton. Probing Single-Charge Fluctuations at a GaAs/AlAs Interface Using Laser Spectroscopy on a Nearby InGaAs Quantum Dot. *Physical Review Letters*, 108(10):107401, mar 2012. doi: 10.1103/PhysRevLett.108.107401. URL <https://link.aps.org/doi/10.1103/PhysRevLett.108.107401>.